A study of thermal components in gamma-ray burst afterglows

Samuel. W. K. Emery

A dissertation submitted in partial fulfillment
of the requirements for the degree of
Doctor of Philosophy
of
University College London.

Mullard Space Science Laboratory
Department of Space and Climate Physics
University College London

April 22, 2024

I, Samuel. W. K. Emery, confirm that the work presented in this thesis is my own. Where information has been derived from other sources, I confirm that this has been indicated in the work.

Abstract

The thesis presents a comprehensive analysis of thermal components observed in the afterglows of gamma-ray bursts (GRBs) via multi-wavelength observations. The primary objective is to unravel the mechanisms and characteristics that shape the early afterglow emission phases. The study predominantly focuses on three specific GRB events: GRB 100316D, GRB 060218, and GW170817. For GRB 100316D, it was determined that UV/optical/X-ray emissions within 33-52 ks intervals indicate a blackbody component, potentially suggesting a cooling envelope post-shock-breakout. A similar thermal emission pattern observed in GRB 060218 hints at potential commonalities in their underlying processes. Upon re-examination of GRB 060218, a synchrotron component in the initial 1350s of the UV/optical spectra was identified, indicating a low-luminosity jet interaction after a core collapse. This phase is succeeded by dominant thermal radiation, with spectral data between 1350-10,000s aligning most accurately with a spherically outflowing blackbody model and an additional power-law component at X-ray wavelengths. In the case of GW170817, the simultaneous detection of a short gamma-ray burst coupled with a gravitational wave from a binary neutron star merger solidified the prevailing theory that such mergers can be precursors to short gamma-ray bursts. It was observed that immediate UV emissions, followed by UV/optical thermal emissions, support the hypothesis of an r-process event post-merger. Additionally, the thesis explores the influence of redshift on the detectability of thermal components in GRBs associated with supernovae. Higher redshift GRBs tend to show thermal detection in the XRT spectrum, possibly a result of cosmological dimming. The potential universality of thermal components in GRBs, occasionally overshadowed by the afterglow's luminosity, underscores the importance of multi-wavelength observations. The research endeavours to deepen the understanding of the origins, intricate characteristics, and wider ramifications of thermal emissions in GRBs.

Acknowledgements

First and foremost, I would like to express my profound gratitude to my primary supervisor, Prof. Mat Page. His unwavering guidance and support have been instrumental in my successful completion of this doctorate journey.

Special thanks are due to my secondary supervisor, Prof. Kinwah Wu. Our enlightening discussions have greatly enriched my research process.

I am also indebted to Dr. Denis González Caniulef and Dr. Monica Tress Barojas. Collaborating with them has been a privilege, and their friendship has been a beacon of light throughout my Ph.D. journey.

I am honored to have been a part of the UVOT team at SWIFT within MSSL. My heartfelt appreciation goes to Dr. Alice Breeveld, Dr. Paul Kuin, Dr. Samantha Oates and Dr. Massimiliano De Pasquale. Their expertise in the analysis of UVOT data, coupled with their unwavering support and cherished friendship, has significantly enhanced my Ph.D. experience.

For efficiently managing the administrative intricacies of my Ph.D., I extend my sincere thanks to Philippa Elwell and Samantha Babister. Their dedication made my journey smoother.

On a personal note, my deepest gratitude goes to my partner Yusheng. Their constant encouragement and support have been my bedrock. I would also like to thank my parents Chris and Gill Emery for their never-ending motivation and support throughout this expedition.

Finally, to all my friends and colleagues at MSSL: thank you for the stimulating discussions, enduring friendship, and unwavering support. You have all played a vital role in making this journey memorable.

UCL Research Paper Declaration Form: referencing the doctoral candidate's own published work(s)

1. **1. For a research manuscript that has already been published** (if not yet published, please skip to section 2)**:**

   (a) **What is the title of the manuscript?** The early optical afterglow and non-thermal components of GRB 060218

   (b) **Please include a link to or doi for the work:** https://doi.org/10.1093/mnras/stz373

   (c) **Where was the work published?** Monthly Notices of the Royal Astronomical Society

   (d) **Who published the work?** Oxford University Press

   (e) **When was the work published?** February 2019

   (f) **List the manuscript's authors in the order they appear on the publication:** S. W. K. Emery, M. J. Page, A. A. Breeveld, P. J. Brown, N. P. M. Kuin, S. R. Oates, M. De Pasquale.

   (g) **Was the work peer reviewd?** Yes

   (h) **Have you retained the copyright?** No

   (i) **Was an earlier form of the manuscript uploaded to a preprint server (e.g. medRxiv)? If 'Yes', please give a link or doi**
   If 'No', please seek permission from the relevant publisher and check the box next to the below statement:

   ☒ *I acknowledge permission of the publisher named under 1d to include in this thesis portions of the publication named as included in 1c.*

2. **For a research manuscript prepared for publication but that has not yet been published** (if already published, please skip to section 3)**:**

   (a) **What is the current title of the manuscript?**

   (b) **Has the manuscript been uploaded to a preprint server 'e.g. medRxiv'?**

   If 'Yes', please please give a link or doi:

   (c) **Where is the work intended to be published?**

   (d) **List the manuscript's authors in the intended authorship order:**

   (e) **Stage of publication:**

3. **For multi-authored work, please give a statement of contribution covering all authors** (if single-author, please skip to section 4)**:** S. W. K Emery: Lead-author, carried out all data reduction and analysis, wrote whole text and provided discussion. M. J. Page: Was the supervisor of S. W. K Emery, and therefore provided support and discussion, and also provided a critical reading and review of the text. P. J. Brown: provided a reading and review of the text A. A. Breeveld: provided a reading and review of the text N. P. M Kuin: provided a reading and review of the text S. R. Oates: provided a reading and review of the text M. De Pasquale: provided a reading and review of the text

4. **In which chapter(s) of your thesis can this material be found?** Chapter 3

e-Signatures confirming that the information above is accurate (this form should be co-signed by the supervisor/ senior author unless this is not appropriate, e.g. if the paper was a single-author work)**:**

Candidate: Samuel W. K. Emery

Date:30/09/2023

Supervisor/Senior Author signature (where appropriate): **Mat Page**

Date:30/09/2023

UCL Research Paper Declaration Form: referencing the doctoral candidate's own published work(s)

1. **1. For a research manuscript that has already been published** (if not yet published, please skip to section 2)**:**

    (a) **What is the title of the manuscript?** Swift and NuSTAR observations of GW170817: Detection of a blue kilonova

    (b) **Please include a link to or doi for the work:** https://www.science.org/doi/10.1126/science.aap9580

    (c) **Where was the work published?** Science

    (d) **Who published the work?** American Association for the Advancement of Science

    (e) **When was the work published?** December 2017

    (f) **List the manuscript's authors in the order they appear on the publication:** P. A. Evans and S. B. Cenko and J. A. Kennea and S. W. K. Emery and N. P. M. Kuin and O. Korobkin and R. T. Wollaeger and C. L. Fryer and K. K. Madsen and F. A. Harrison and Y. Xu and E. Nakar and K. Hotokezaka and A. Lien and S. Campana and S. R. Oates and E. Troja and A. A. Breeveld and F. E. Marshall and S. D. Barthelmy and A. P. Beardmore and D. N. Burrows and G. Cusumano and A. D'Aì and P. D'Avanzo and V. D'Elia and M. de Pasquale and W. P. Even and C. J. Fontes and K. Forster and J. Garcia and P. Giommi and B. Grefenstette and C. Gronwall and D. H. Hartmann and M. Heida and A. L. Hungerford and M. M. Kasliwal and H. A. Krimm and A. J. Levan and D. Malesani and A. Melandri and H. Miyasaka and J. A. Nousek and P. T. O'Brien and J. P. Osborne and C. Pagani and K. L. Page and D. M. Palmer and M. Perri and S. Pike and J. L. Racusin and S. Rosswog and M. H. Siegel and T. Sakamoto and B. Sbarufatti and G. Tagliaferri and N. R. Tanvir and A. Tohuvavohu

(g) **Was the work peer reviewd?** Yes

(h) **Have you retained the copyright?** No

(i) **Was an earlier form of the manuscript uploaded to a preprint server (e.g. medRxiv)? If ‘Yes’, please give a link or doi** Yes

If ‘No’, please seek permission from the relevant publisher and check the box next to the below statement:

☒ *I acknowledge permission of the publisher named under 1d to include in this thesis portions of the publication named as included in 1c.*

2. **For a research manuscript prepared for publication but that has not yet been published** (if already published, please skip to section 3)**:**

   (a) **What is the current title of the manuscript?**

   (b) **Has the manuscript been uploaded to a preprint server ’e.g. medRxiv’?**

   If ’Yes’, please please give a link or doi: Yes https://arxiv.org/abs/1710.05437

   (c) **Where is the work intended to be published?**

   (d) **List the manuscript’s authors in the intended authorship order:**

   (e) **Stage of publication:**

3. **For multi-authored work, please give a statement of contribution covering all authors** (if single-author, please skip to section 4)**:** P. A. Evans: Lead-author, wrote most of text and compiled paper, led x-ray analysis S. B. Cenko: SWIFT PI, oversaw team and strategy and commented on manuscript J. A. Kennea: oversaw observing plan and commented on manuscript S. W. K Emery: carried out UV /optical data reduction and analysis, helped guide and advise UVOT observations. Also led search for UV/optical counterpart in 100’s of potential candidates with UVOT. P. M. Kuin and O. Korobkin and R. T. Wollaeger and C. L. Fryer and

K. K. Madsen and F. A. Harrison and Y. Xu and E. Nakar and K. Hotokezaka and A. Lien and S. Campana and S. R. Oates and E. Troja and A. A. Breeveld and F. E. Marshall and S. D. Barthelmy and A. P. Beardmore and D. N. Burrows and G. Cusumano and A. D'Aì and P. D'Avanzo and V. D'Elia and M. de Pasquale and W. P. Even and C. J. Fontes and K. Forster and J. Garcia and P. Giommi and B. Grefenstette and C. Gronwall and D. H. Hartmann and M. Heida and A. L. Hungerford and M. M. Kasliwal and H. A. Krimm and A. J. Levan and D. Malesani and A. Melandri and H. Miyasaka and J. A. Nousek and P. T. O'Brien and J. P. Osborne and C. Pagani and K. L. Page and D. M. Palmer and M. Perri and S. Pike and J. L. Racusin and S. Rosswog and M. H. Siegel and T. Sakamoto and B. Sbarufatti and G. Tagliaferri and N. R. Tanvir and A. Tohuvavohu: all took part in the observing campaign, read and commented on the manuscript.

4. **In which chapter(s) of your thesis can this material be found?** Chapter 5

e-Signatures confirming that the information above is accurate (this form should be co-signed by the supervisor/ senior author unless this is not appropriate, e.g. if the paper was a single-author work)**:**

Candidate: Samuel W. K. Emery
Date:30/09/2023

Supervisor/Senior Author signature (where appropriate): **Mat Page**
Date:30/09/2023

UCL Research Paper Declaration Form: referencing the doctoral candidate's own published work(s)

1. **1. For a research manuscript that has already been published** (if not yet published, please skip to section 2)**:**
   1. (a) **What is the title of the manuscript?** GRB 171205A/SN 2017iuk: A local low-luminosity gamma-ray burst
   2. (b) **Please include a link to or doi for the work:** https://doi.org/10.1051/0004-6361/201833847
   3. (c) **Where was the work published?** Astronomy & Astrophysics
   4. (d) **Who published the work?** EDP Sciences
   5. (e) **When was the work published?** November 2018
   6. (f) **List the manuscript's authors in the order they appear on the publication:** V. D'Elia, S. Campana, A. D'Aì, M. De Pasquale, S. W. K. Emery, D. D. Frederiks, A. Lien, A. Melandri, K. L. Page, R. L. C. Starling, D. N. Burrows, A. A. Breeveld, S. R. Oates, P. T. O'Brien, J. P. Osborne, M. H. Siegel, G. Tagliaferri, P. J. Brown, S. B. Cenko, D. S. Svinkin, A. Tohuvavohu and A. E. Tsvetkova
   7. (g) **Was the work peer reviewd?** Yes
   8. (h) **Have you retained the copyright?** No
   9. (i) **Was an earlier form of the manuscript uploaded to a preprint server (e.g. medRxiv)? If 'Yes', please give a link or doi** Yes https://arxiv.org/abs/1810.03339

      If 'No', please seek permission from the relevant publisher and check the box next to the below statement:

      ☒ *I acknowledge permission of the publisher named under 1d to include in this thesis portions of the publication named as included in 1c.*

2. **For a research manuscript prepared for publication but that has not**

yet been published (if already published, please skip to section 3)**:**

   (a) **What is the current title of the manuscript?**
   (b) **Has the manuscript been uploaded to a preprint server 'e.g. medRxiv'?**
   If 'Yes', please please give a link or doi:
   (c) **Where is the work intended to be published?**
   (d) **List the manuscript's authors in the intended authorship order:**
   (e) **Stage of publication:**

3. **For multi-authored work, please give a statement of contribution covering all authors** (if single-author, please skip to section 4)**:** V. D'Elia: Lead paper compiled paper, wrote whole paper, and discussions S. Campana: helped with discussions, reviewing manuscript A. D'Aì: helped with discussions, reviewing manuscript M. De Pasquale: helped with discussions, reviewing manuscript S. W. K. Emery: performed the UVOT reduction and data analysis for the paper D. D. Frederiks, A. Lien, A. Melandri, K. L. Page, R. L. C. Starling, D. N. Burrows, A. A. Breeveld, S. R. Oates, P. T. O'Brien, J. P. Osborne, M. H. Siegel, G. Tagliaferri, P. J. Brown, S. B. Cenko, D. S. Svinkin, A. Tohuvavohu and A. E. Tsvetkova: all contributed to reviewing the manuscript.
4. **In which chapter(s) of your thesis can this material be found?** Chapter 6

e-Signatures confirming that the information above is accurate (this form should be co-signed by the supervisor/ senior author unless this is not appropriate, e.g. if the paper was a single-author work)**:**

Candidate: Samuel W. K. Emery
Date:30/09/2023

Supervisor/Senior Author signature (where appropriate): **Mat Page**

Date:30/09/2023

Impact Statement

This research delves into the nuanced understanding of thermal components in gamma-ray burst (GRB) afterglows, a field that holds profound implications for our comprehension of some of the universe's most energetic phenomena.

My study contributes significantly to the existing knowledge on GRB afterglows. The emphasis on how we observe GRBs with associated supernovae in the early detection phase has revealed the importance of UV observations in the initial days following a burst. This is especially pivotal for low-luminous, nearby GRBs, where synchrotron emission is expected to be lower. The findings underscore the potential for enhancing observational techniques, possibly impacting UVOT observational modes and driving the case for UV-focused observations during such events.

Furthermore, during my tenure as the burst advocate for the UVOT team on the SWIFT space telescope, I had the privilege of being involved in groundbreaking astronomical events such as GRB171205A, GRB161219B, and notably, GW170817. This last event marked the first correlation between a GRB and a gravitational wave, elucidating that short GRBs originate from neutron star mergers. The expertise and methodologies developed for analysing thermal components in GRBs like 060218 and 100316D were pivotal in decoding these bursts, further enriching our understanding of early thermal components in GRB afterglows.

The broader implications of this research extend to our holistic comprehension of GRB afterglows. By enhancing our grasp on GRB emission mechanisms and their interaction with their surrounding medium, we are better positioned to predict and analyse future events. The work on gravitational waves, particularly, holds massive repercussions; being a part of the data analysis for what was undeniably a blue kilonova, one of the most significant discoveries in astrophysics in recent times, emphasises the magnitude of this research's contribution.

The findings from this research have been presented at various academic conferences and gatherings, fostering dialogue and collaboration within the astrophysical community.

Looking ahead, the next gravitational wave correlated with a GRB will necessitate rapid UV follow-ups. Any GRBs detected alongside a supernova, or those that are proximate with low luminosity, should prioritise early UV observations to further our insights into thermal components in GRBs. Spin-off projects could also explore GRBs not only associated with supernovae but those that are nearby and exhibit low luminosity, offering a broader scope for understanding these cosmic phenomena.

Contents

List of Figures

List of Tables

Chapter 1

Introductory Material

1.1 A Short History

First detected in 1969 by the Vela satellites, specifically Vela 5A, 5B, and 6B (Klebesadel et al., 1973), Gamma-ray bursts (GRBs) are powerful, brief, and intense photon flashes. These bursts exhibit energies in the range of ~ 100 keV to 1 MeV. The discovery of GRBs spurred the launch of numerous satellite detectors and the formulation of various models and theories to decipher the origins of these photon surges. Initially, the prevailing belief was that GRBs emanated from galactic neutron stars. However, this hypothesis was debunked following observations from the Burst and Transient Source Experiment (BATSE) onboard the Compton Gamma Ray Observatory (CGRO).

Until circa 1996, GRB localisations were either delayed and accurate (i.e., localisations provided by the Interplanetary Network (IPN) gave arcmin localisations on the timescale of days); or rapid and not so accurate (i.e., 2 ° error circle localisations on the timescale of just minutes after the GRB trigger provided by BATSE). Given these problems, different strategies were devised and pursued to capture and observe the corresponding optical emission of the GRBs detected. What was required was an instrument that produced more accurate and quicker localisations

BeppoSAX, a satellite for X-ray astronomy, was launched in 1996. The instruments aboard BeppoSAX provided localisation accuracies of $\sim 5\,'$ with notification within a few minutes of the GRB trigger. BeppoSAX also had a slewing time of just a few hours and the ability to re-point its narrow-field X-ray telescope. The first BeppoSAX breakthrough came when the satellite discovered that in the double peaked GRB 970228 (Costa et al., 1997) there was an X-ray counterpart. The burst was detected by the Gamma Ray Burst Monitor (GRBM) and observed with the Wide Field Camera on- board BeppoSAX. From the position determined by BeppoSAX, identification of an afterglow was found in the optical (Van Paradijs et al., 1997). Following GRB 970228, was the rapid localisation of GRB 970508, which enabled the first measurement of the redshift via optical spectroscopy and provided the first measurement of radio afterglow. GRB 970508 was observed in gamma-rays using BATSE (Kouveliotou, 1997) and in X-rays with BeppoSAX (Piro, 1997). This primary emission was subsequently accompanied by X-rays, optical, and radio afterglow signals (Bond, 1997; Frail et al., 1997). Through spectral analysis of the optical transient taken by Keck, a redshift of $z = 0.835$ was determined. This confirmed the origins of GRBs to be extragalactic.

A great step in our understanding of the progenitors of these bursts was the detection of GRB 980425, a burst with a low peak flux compared to typical GRBs. Using the Wide Field Camera on BeppoSAX, a location was determined with an uncertainty of 8 arcminutes. Subsequent ground-based observations from the New Technology Telescope unveiled the occurrence of a type Ic supernova, SN1998bw, coinciding with the timing of the GRB (Galama et al., 1998), Piran (1998). This discovery, stemming from GRB 980425, marked the initial evidence hinting at a potential link between GRBs and supernovae (Pian et al., 1999).

At the turn of the millennium, was the launch of both the High Energy Transient Explorer (HETE-2) in the year 2000, and INTEGRAL (Winkler, 1994) in 2002. Both HETE-2 and INTEGRAL were space satellites designed to detect GRBs quickly and provide a better localisation than the BATSE detectors. However the detection of the prompt emission and the afterglow follow-up observation were delayed by several hours and therefore a new mission was needed to provide observations of the afterglow shortly after the trigger. This issue was solved with the launch of *Swift*. *Swift* is a multi-wavelength satellite observatory, and was launched on November 2004. The *Swift* satellite was equipped with the necessary instruments to detect both the GRB in the gamma-rays and its afterglow in X-ray, optical and UV.

1.2 Observed properties of Gamma-Ray Bursts

1.2.1 Prompt Emission

1.2.1.1 Temporal Structure

Unlike the typical time structures observed in novae or supernovae, GRB light curves exhibit a broad range of disparities. The timing and pulsations of GRBs can vary greatly: some display a singular peak, whereas others manifest multiple distinct peaks of diverse intensities. Certain light curves present a brief, faint pulse preceding more pronounced pulses. Additionally, many GRB light curves seem random, lacking any discernible pattern. Whilst the time profiles of GRBs appear random, some general features appear to be prevalent. For most bursts, more gamma-ray emission occurs at the beginning of the burst. Some bursts that have well-resolved pulse frequency and smooth pulses show a Fast Rise and Exponential Decay (FRED) profile. In cases where the initial pulse that triggered the detector is weak relative to the remaining burst emission, the pulse is known as a precursor event.

The term T_{90} was introduced to express the duration of the prompt gamma-ray emission. T_{90} is defined as the time during which the cumulative counts increase from 5% to 95% above background, thus encompassing 90% of the total GRB counts (Kouveliotou et al., 1993).

A distinctive feature of the data plots of the 2704 GRBs detected by BATSE is the bi-modality in the duration. This bimodal distribution demonstrated that GRBs can be classified in to two groups: short and long GRBs. Short GRBs have an average T_{90} of ~ 0.3 s and long GRBs have an average

T_{90} of ~ 30 s. The bi-modality of GRBs is not only restricted by duration, but also by spectral hardness; the distribution of BATSE detected GRBs can also be grouped by their different average hardness ratios (Kouveliotou et al., 1993).

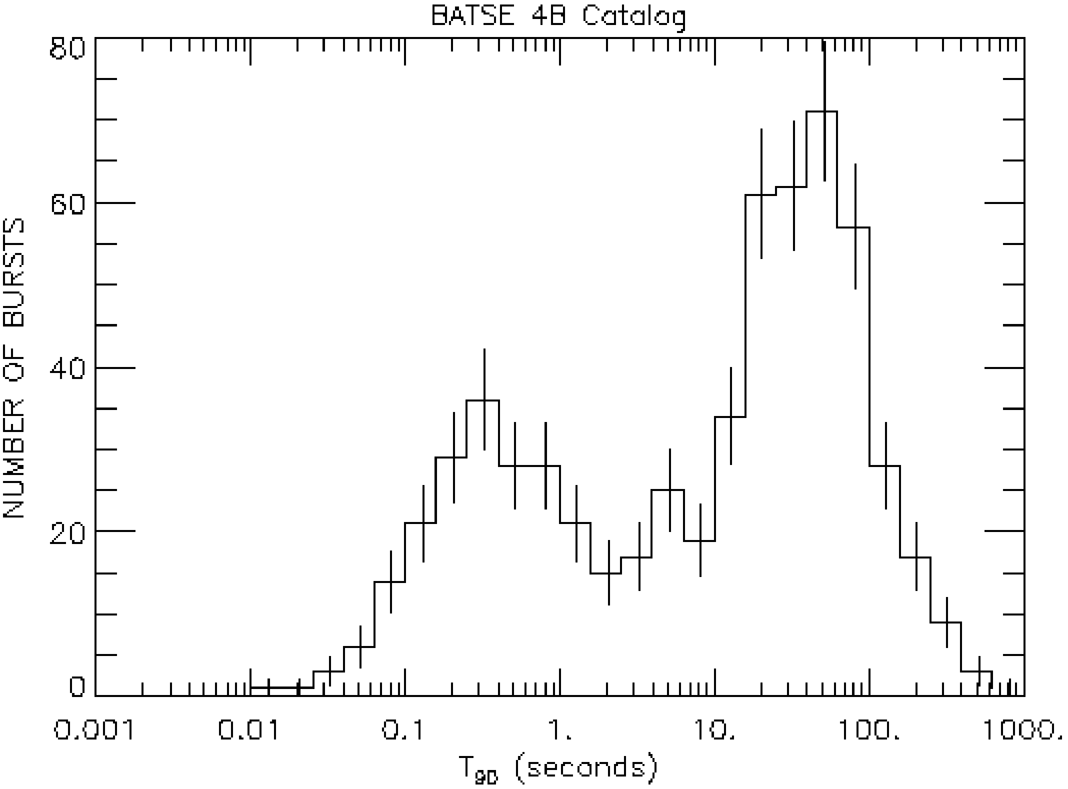

Figure 1.1: T_{90} Distribution from 2704 BATSE GRBs. This image displays the durations of the 4B Catalog Gamma-Ray Bursts [1]

In recent years, a proposal for a new class of GRBs has emerged: ultra long GRBs have a T_{90} exceeding 1000 s. GRB 111209A at redshift z=0.677 is a good example of this: it is the longest GRB ever observed, as it has a rest frame prompt emission duration of $\sim$ 4 hours.

1.2.1.2 Energetics

The energy of a GRB cannot be directly determined from the total energy emitted due to uncertainties in the jet angle. Hence, the isotropic-equivalent energy, E_{iso}, is employed. E_{iso} represents the energy a GRB would radiate if it were to spread out evenly in all directions with the same flux as observed from

---

[1] `http://www.batse.msfc.nasa.gov/batse/grb/duration/`

our vantage point. The ability to measure the fluence of a specific GRB is constrained by the detector's energy range. For a specified observer frame energy range, $[e_1, e_2]$, E_{iso} depends on the fluence recorded within this range, defined as $S_{[e_1,e_2]} = \int_{e_1}^{e_2} ES_0\phi(E)dE$. Here, $\phi(E)$ denotes the GRB's time-integrated spectral shape, $S_{[e_1,e_2]}$ is the fluence measured in that range, and S_0 is the normalisation in terms of photons per unit area per unit energy. E_{iso} is defined as

$$E_{iso} = \frac{4\pi D_l^2}{1+z} S. \tag{1.1}$$

In this context, z represents the redshift and D_l denotes the luminosity distance of the GRB. The isotropic-equivalent radiated energy, E_{iso}, varies widely among GRBs, ranging from the relatively low energy of GRB 980425 at 10^{52} erg, to the exceptionally high energy of GRB 080916C at 8.8×10^{54} erg. To illustrate the magnitude of energy released by GRB 080916C, consider its conversion into mass using $E = mc^2$, where c is the speed of light. This yields a mass equivalence of approximately 9.78×10^{30} kg, or nearly five times the mass of the sun, which is around 1.989×10^{30} kg.

For meaningful comparisons of isotropic energies across different GRBs, E_{iso} must be translated to the rest frame using a standardized rest frame energy range (Bloom et al., 2001). The translation from the observer frame isotropic-equivalent energy to a specified rest frame energy range, $[E_1, E_2]$, involves the application of a k-correction. This k-correction is essentially the ratio of the measured fluence in the rest frame energy range $[E_1/(1+z), E_2/(1+z)]$ to the fluence measured in the observer frame energy range $[e_1, e_2]$. Mathematically, this is expressed as:

$$k = \frac{\int_{E_1/(1+z)}^{E_2/(1+z)} E\phi(E)dE}{\int_{e_1}^{e_2} E\phi(E)dE} \tag{1.2}$$

Upon applying this k-correction, the resultant isotropic-equivalent energy, termed as $E_{iso,k}$, is found by multiplying E_{iso} with k. This relationship is captured by:

$$E_{iso,k} = E_{iso} \times k = \frac{4\pi D_l^2}{1+z} S \times k. \tag{1.3}$$

1.2.1.3 Spectrum

The prompt emission is comprised of soft gamma rays that carry the bulk of the energy of the GRB, and also both higher-energy and lower-energy photons that arrive simultaneously. The spectrum associated with the prompt emission is non-thermal. The best phenomenological fit for the spectrum is by using the Band function first introduced by Band et al. (1993). The flux as function of energy, $F(E)$ is characterised by two power laws joined smoothly at the break energy, $(\alpha$ - $\beta)E_0$:

$$F(E) = A \begin{cases} \left(\frac{E}{100\ \mathrm{keV}}\right)^{\alpha} e^{\left[-\frac{E}{E_0}\right]}, & E \leq (\alpha - \beta)E_0, \\ \left(\frac{E}{100\ \mathrm{keV}}\right)^{\beta} e^{(\beta-\alpha)} \left(\frac{(\alpha-\beta)E_0}{100\ \mathrm{keV}}\right)^{\alpha-\beta}, & E > (\alpha - \beta)E_0, \end{cases} \tag{1.4}$$

Although there is no specific theoretical model that predicts this spectral profile, it provides a good fit for most observed GRB spectra. The value for the peak energy in the νF_ν spectrum is $E_\mathrm{p} = (\alpha + 2)E_0$. Based on samples of GRB spectra by Preece et al. (2000) and Kaneko et al. (2006), the lower- and higher-energy spectral indices are distributed around mean values of $\alpha \approx -1$ and $\beta \approx -2.25$, respectively. Preece et al. (2000) used a sample of bursts with duration 1.66 - 278 s and Kaneko et al. (2006) used the whole BATSE catalogue of 2704, including 17 short, GRBs. The distribution of E_p is larger than the distribution of E_0 and for most bursts the peak energy is within the range 100 - 400 keV, with the mean value of ~200 keV. Kaneko et al. (2006) shows small discrepancies between short and long GRBs with respect to the low and high energy indices and the calculated peak energy.

The discovery of X-ray flashes (XRF)s (Heise et al., 2001), showed the low peak energy cut-off to be false. XRFs have similar time profiles as GRBs, but with lower typical energy and have a softer prompt emission spectrum than GRBs.

1.2.2 Afterglow

Afterglows originate from relativistic blast waves, which provide insights into the Lorentz factors of these waves. The Lorentz factor, denoted as γ, for such a wave can often reach values in the hundreds. Typically, each source produces a single afterglow event. This afterglow is predominantly characterised by synchrotron emission spanning a wide range of wavelengths, from radio to X-rays. Due to the relativistic motion of particles within the blast, when they are accelerated at right angles to a robust local magnetic field, they emit this synchrotron radiation. Electrons are believed to play a pivotal role in this process, given their pronounced radiation properties compared to other particles. As a result, only electrons are considered significant contributors to this synchrotron radiation, while other particles are largely disregarded. Although local magnetic fields are incorporated into this model, overarching intense magnetic fields are perceived to have a minimal impact on the blast waves responsible for the afterglow (van Paradijs et al., 2000).

1.2.2.1 Temporal structure

Afterglows linked with GRBs have been observed to persist for durations ranging from days to even years following the initial prompt emission (De Pasquale et al., 2016). The behaviour of the early-time afterglow is significantly modulated by the range of observed wavelengths. Numerous initial X-ray light curve patterns can be depicted using three or occasionally four power-law segments, with the relation $F_\nu \propto \nu^{-\beta} t^{-\alpha}$ (Nousek et al., 2006). The first power-law segment (referred to as phase I) showcases a bright, steep decay phase with $3 < \alpha_1 < 5$. It seamlessly bridges the prompt emission both in terms of time and spectrum, typically enduring for several hundred seconds. Following this is the plateau phase (phase II), characterised by a comparatively flat decay index with $0.5 \leq \alpha \leq 1.0$. Post the plateau phase, there's a transition around 10^3 to 10^4 seconds into a sharper phase, termed phase III, with $\alpha_3 \approx 1.2$. A potential concluding phase, occurring between 10^4 and 10^5 seconds post prompt emission (designated as phase IV), is recognised as the jet break. This phase is marked by an even steeper decay, with $\alpha_4 \approx 2.2$. Nevertheless, only a subset of bursts observed by *Swift* exhibit signs of the X-ray jet break (Racusin et al., 2009). While flares might overlay any segment of the power-law in the light curve, they are predominantly observed during the earlier phases, making them more prevalent in phases I and II (Willingale et al., 2007).

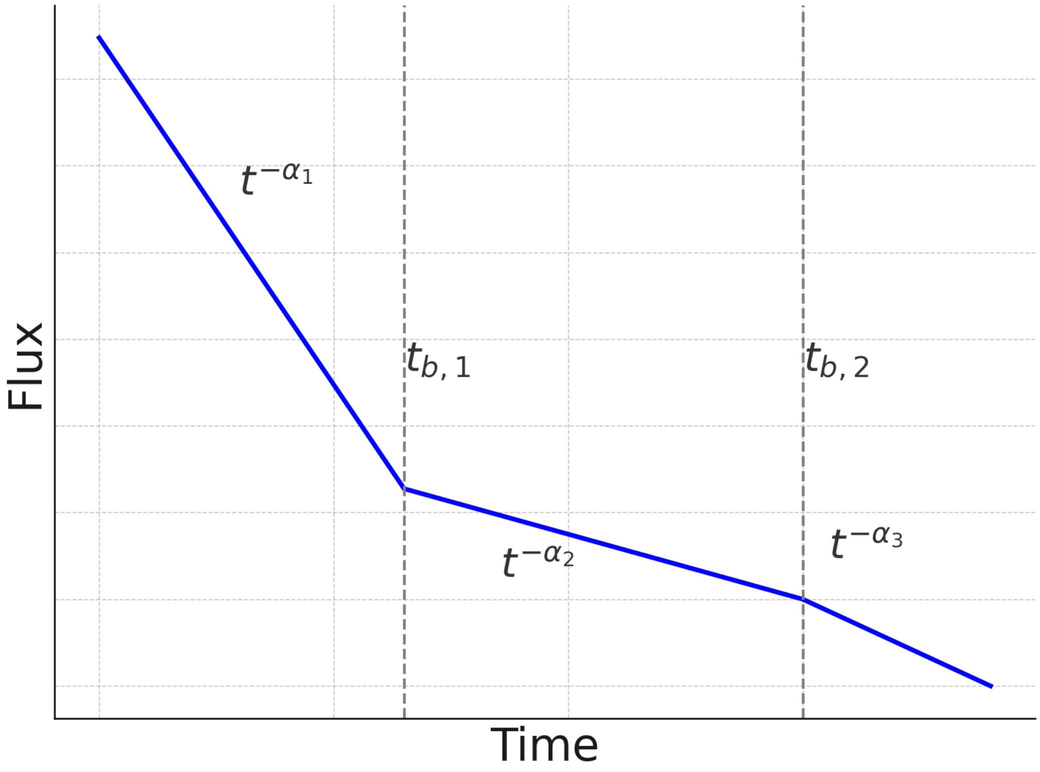

Figure 1.2: A schematic diagram showing the power-law segments and breaking times of the early X-ray afterglow light curve. The temporal index and time period is shown for each phase of the afterglow, each phase represents a separate power law segment. This figure is based on a diagram 3 within Nousek et al. (2006).

In most cases, the optical light curve can be represented by a single power-law. In some cases, the optical afterglow can be best fit with a broken power-law model. Current observations made by *Swift* indicate that at early times (<500 s) the mean temporal index is $\alpha_{opt} \sim 0.5$ (Oates et al., 2009). Whilst, on average, at early times, the optical afterglows decay in flux with time, there is a large variation in α_{opt} at early times. Some light curves have a steep rise before decaying. However, for times >500 s all the light curves used by Oates et al. (2009) decay. Importantly, Oates et al. (2009) looked at the UVOT V band normalised light curves of GRB afterglows and observed a significant trend where the brightest optical afterglows, defined as those with the highest peak magnitudes within the first 500 s, tend to decay the quickest. This faster decay is quantified by the steeper negative values of the temporal decay index α for brighter bursts post 500 s, suggesting a stronger correlation between brightness of the afterglow and decay rate in the observed frame.

1.2.2.2 Energetics

The optical afterglow can be as bright as 5th magnitude (GRB 080319B). GRB 080319B was extremely luminous, and was visible with the naked eye. The brightness of the optical afterglow varies significantly with the extinction of photons from dust in the line of sight to the burst, or the absorption by neutral hydrogen gas at high redshifts. In GRBs observed by *Swift*, most host galaxy extinction curves are similar to that of the Small Magellanic Cloud (SMC) (Schady et al., 2010). The amount of extinction in the lines of sight to observed GRBs ranges from almost no extinction (GRB 050908) to GRBs with detected X-ray afterglow emission and no optical-UV emission, where the extinction is large. X-ray afterglow measurements provide a good measure of the intrinsic energies for GRB afterglows, because the inter-stellar medium (ISM) is almost transparent at energies >2 keV.

1.2.2.3 Spectrum

Like the prompt gamma-ray spectrum, the afterglow spectrum is also non-thermal. The dominating emission process is thought to be synchrotron emission. This is evident by the broad-band spectrum. In some cases inverse Compton scattering can be the dominant emission mechanism in the X-rays (Harrison et al., 2001). Most typical X-ray afterglow spectra can be fit well by an absorbed power law model with a photon index $\beta \sim 1$, with a column density, N_H, ranging between 10^{20} - 10^{22} cm^{-2}.

1.3 Models for gamma-ray burst progenitors

To accurately model GRBs, you need a model that can explain the currently observed features of GRBs. It needs to describe how energies in the range 10^{51-53} erg can be released on a timescale of seconds, with a considerable variability in the light curves.

The only mechanism that can produce this amount of energy is from the accretion of stellar material onto a newly formed black hole. A degree of rotation is required for the accretion disk to form, because when materials fall into it, it is accumulated onto the equator, forming a torus of accreting matter around the BH. A funnel forms along the rotational axis of the torus; gravitational energy is converted to outflowing kinetic energy via neutrino annihilation or Blandford-Znajek mechanism (in the presence of a strong magnetic field), and is released along the rotation axis producing jets (Woosley, 1993a).

Calculations of neutrino annihilation above the torus suggest that neutrino annihilation alone could explain the observed bursts (Fryer and Mészáros, 2003). Neutrinos and antineutrinos annihilate to form electron-positron pairs. Neutrino-annihilation above the disk can input high energy and momentum, and exert pressure against the infalling matter. The annihilation occurs mainly on the rotation axis, in regions with little baryonic loading, as this would dampen the neutrino energy. Once the electron-positron pair radiation pressure exceeds the gravitational energy, the fireball expands and converts its internal energy into kinetic energy, until the expanding shell achieves a maximum velocity. Afterward, the shell grows with constant Lorentz factor ($\Gamma = \frac{1}{\sqrt{1-\frac{v^2}{c^2}}}$) into the external medium, where it sweeps up the material. At this point, the shell is decelerating and converting its kinetic energy into radiation via synchrotron radiation (Woosley, 1993a).

The large variability in the gamma-ray light curves on the scale of $\Delta t \simeq 10\,\mathrm{ms}$ implies that the sources are compact, $R < c\Delta t \simeq 3000\,\mathrm{km}$. The high energy γ-ray photons could interact with lower energy photons and produce electron-positron pairs via $\gamma\gamma \rightarrow e^+e^-$. The corresponding optical depth for this process is larger than unity ($\gg$1). This optical depth is in disagreement with the observed non-thermal GRB spectrum, which indicated that the sources must be optically thin (Goodman, 1986). Considering relativistic effects solves the compactness problem (Krolik and Pier, 1991). If the outflow possesses a bulk Lorentz factor of Γ, photon energies will experience a blue shift by this factor. Consequently, the observed energy of the prompt emission at the source would be reduced by a factor of Γ. This reduction diminishes the fraction of photons that exceed the pair production threshold, thereby decreasing the pair production rate (Krolik and Pier, 1991).

If the outflow is moving with bulk Lorentz factor Γ, the photon energies are blue-shifted by a factor of Γ. The observed prompt emission energy at the source would be a factor of Γ less and will reduce the fraction of photons above the pair production threshold, and this will reduce the pair production rate (Krolik and Pier, 1991). The relativistic motion also increases the physical size of the emission region by a factor of Γ^2; this will decrease the pair production optical depth by a factor of Γ^4. Optical depths < 1 can be achieved in most GRBs with a bulk Lorentz factor of $\Gamma \geq 100$.

Currently, it is thought that short GRBs are formed from the merging of compact objects, such as black holes merging with neutron stars, in regions where star formation rate is relatively small (Blinnikov et al., 1984; Lattimer and Schramm, 1976). Conversely, long GRBs are associated with areas of large star-formation, where the lifetimes of such stars are short; they are also related to the death of massive stars (MacFadyen et al., 2001). Most long GRBs must, therefore, be produced by a NS or BH birth, which means that they are some variety of core-collapse supernova.

1.3.1 The collapsar model

The collapsar model is used to explain the observed features for long GRBs. Woosley (1993a) showed that long GRBs are associated with star-forming regions and since massive stars are short-lived ($\sim 10^7$ years), the death of massive stars. This association is compounded by the evidence that long GRBs are associated with supernovae (SNe).

Observations confirm that long GRBs occur on or near regions with large star formation (Fruchter et al., 1999). Indications of the link between long GRBs and SNe were first seen in the power law decay of the optical afterglow, where there is a brightening in the optical after several days; this is evidence for Type Ib/c supernova occurring simultaneously with some GRBs (e.g. GRB 980425 Kulkarni et al. (1998), GRB 030329 Hjorth et al. (2003), GRB 060218 Campana et al. (2006)).

In the collapsar model, a rapidly rotating massive star, $M > 30M_{\odot}$ with an iron core collapses to a black hole (Woosley, 1993a). This happens either directly or via an accretion phase which follows the core collapse. Sufficient angular momentum is needed to form an accretion disk outside the black hole and for the material not to free fall into the black hole. The progenitor star core must be 10–15 $M_{\odot}$ and have lost its hydrogen envelope before core collapse; this is required so that the relativistic jet can penetrate the progenitor envelope (Woosley, 1993a). These specific requirements shed light on the rate at which the progenitor star sheds its mass during its existence. Stars with high metallicity experience heightened photon pressure in regions abundant with metals, leading them to lose mass at a more accelerated pace compared to stars with lower metallicity (Woosley, 1993a). As a consequence, for the collapsar model to hold true, the progenitor star must possess low metallicity to facilitate the formation of a swiftly rotating accretion disk (Woosley, 1993a).

1.3.2 The binary merger model

Collapsars have long durations, typically $\sim 10\,\mathrm{s}$. This time is constrained by the collapse time of the stellar envelope contributing to the accretion disk. The dynamical timescale for a typical helium star is $\tau \approx 10\,\mathrm{s}$. Larger durations can be accounted for from stars with large mass and longer dynamical time scales, or fall back into the black hole when the neutrino annihilation energy contribution is low. Therefore, the collapsar model cannot produce the short duration GRBs.

Short GRBs are believed to originate from the merging of compact binary systems, specifically neutron star-neutron star (NS-NS) pairs (Paczyński, 1986) or neutron star-black hole (NS-BH) pairs (Eichler et al., 1989). In these scenarios, a black hole is birthed from the coalescence of the binary system.

Empirical evidence, derived from observing short GRBs and their associated host galaxies, indicates that short GRBs, like GRB 051221a (Soderberg et al., 2006a) and GRB 060502b (Bloom et al., 2007), are typically located at significant distances from the centres of galaxies. This spatial distribution can be attributed to the momentum imparted to the binary system from the supernova explosion that resulted in the creation of one of its constituents.

1.4 Emission mechanisms

1.4.1 Prompt emission

As mentioned in Sec. 1.3, the relativistic outflow shell that produces the GRB has a bulk Lorentz factor Γ. Consider the shell with a radius R and width Δ. The jet outflow has an opening angle $\theta > \Gamma^{-1}$. Due to relativistic beaming effects, in the observer's frame, the jet appears narrower with $\theta \sim \Gamma^{-1}$ (Sari et al., 1999). Photons emitted directly towards the observer from the front of the shell will arrive first. However, due to the curvature of the shell and the longer path travelled, photons emitted at an angle $\theta \sim \Gamma^{-1}$ will arrive later, at $t_{\text{ang}} = \frac{R}{2c\Gamma^2}$ (Sari et al., 1999). Differences in the Lorentz factors of the shells γ that contribute to the overall bulk Lorentz factor Γ can arise from relativistic turbulence (Lyutikov and Blandford, 2002). This turbulence means the shell comprises multiple individual emitters with different Lorentz factors $\gamma\prime$. Faster shells can collide with slower ones, leading to gamma-ray production (Lyutikov and Blandford, 2002).

The gamma rays produced from the internal shocks are the prompt emission (Sari et al., 1999). At present it is not clear what the prompt emission mechanism is in GRBs due to large variety in gamma ray light curves. However, some candidates are synchrotron emission (Meszaros et al., 1994) and inverse Compton emission (Meszaros et al., 1994).

1.4.2 Afterglow

As discussed in the previous section, the prompt emission is produced by the internal dissipation of the relativistic outflow. The afterglow is produced by external dissipation, where the shells coalesce into a single shell. At the front of this shell is the external shock which interacts with the interstellar medium at $R = \Gamma ct \approx 10^{16} - 10^{18}\,\mathrm{cm}$.

For a simple afterglow model with an isotropic fireball, constant ISM density n and constant kinetic fireball energy $E_k = nr^3\Gamma^2$ (Zhang and Mészáros, 2004); the Lorentz factor, radius and time are related by:

$$\Gamma \propto r^{-3/2} \propto t^{-3/8}. \tag{1.5}$$

For an ISM-like or wind like circumburst medium the density goes as $\rho = Ar^{-2} = \dot{M}/4\pi r^2 v_w$, where $\dot{M}$ is the rate of mass loss and v_w is the wind velocity (Zhang and Mészáros, 2004). The kinetic energy goes as $E_k = Ar\Gamma^2$ and the Lorentz factor, radius and time are related by:

$$\Gamma \propto r^{-1/2} \propto t^{-1/4}. \tag{1.6}$$

1.4.2.1 Synchrotron emission

Synchrotron emission is produced when a relativistic electron travels in a magnetic field. This mechanism is considered to be the dominating mechanism that produces the afterglow.

The energy of the synchrotron photons and the cooling time of the electrons depend on the Lorentz factor of the relativistic electron γ_e and on the magnetic field B. The material emitted is moving with a bulk Lorentz factor Γ, and therefore the photons are blueshifted (Sari et al., 1996). The photon energy in the observer frame is:

$$(h\nu_{\mathrm{syn}})_{\mathrm{obs}} = \frac{\hbar q_{\mathrm{e}} B}{m_{\mathrm{e}} c} \gamma_{\mathrm{e}}^{2} \Gamma, \tag{1.7}$$

where q_{e} is the electron charge.

The power emitted due to synchrotron radiation, by a single electron, in the local frame is given by:

$$P_{\mathrm{syn}} = \frac{4}{3} \sigma_{\mathrm{T}} c U_{B} \gamma_{\mathrm{e}}^{2}, \tag{1.8}$$

where σ_{T} is the Thomson cross section and $U_B \equiv B^2/8\pi$ is the magnetic energy density (Sari et al., 1998). The cooling time in the fluid frame of the electron follows as $\gamma_{\mathrm{e}} m_{\mathrm{e}} c^2/P$. Therefore the cooling time t_{syn} in the observed frame is (Sari et al., 1996):

$$t_{\mathrm{syn}}(\gamma_{\mathrm{e}}) = \frac{3 m_{\mathrm{e}} c}{4 \sigma_{\mathrm{T}} U_{B} \gamma_{\mathrm{e}} \Gamma}. \tag{1.9}$$

By combining Eq. 1.7 and Eq. 1.9 you obtain the cooling timescale as a function of the observed photon frequency:

$$t_{\mathrm{syn}}(\nu) = \frac{3}{\sigma_{\mathrm{T}}} \sqrt{\frac{2\pi c m_{\mathrm{e}} q_{\mathrm{e}}}{B^{3} \Gamma}} \nu^{-1/2} \tag{1.10}$$

Therefore, t_{syn} at any given observed frequency does not depend on γ_{e}, and is independent of the electron energy distribution in the shock. For an electron emitted due to synchrotron emission, the cooling time scales as $t_{\mathrm{syn}}(\nu) \propto \nu^{-1/2}$. This is not too dissimilar to the observed temporal structure of GRBs, $t \propto \nu^{-0.4}$ (Fenimore et al., 1995). However, the cooling is not thought to determine to temporal profile (Sari et al., 1998).

For a single relativistic electron with initial energy $\gamma_{\mathrm{e}} m_{\mathrm{e}} c^2$, the instantaneous synchrotron spectrum is related to the flux with a simple power law $F_\nu \propto \nu^{1/3}$ until $\nu_{\mathrm{syn}}(\gamma_{\mathrm{e}})$ (Sari et al., 1998). For frequencies that exceed this, the flux decays exponentially. Therefore, the peak synchrotron power occurs at $\nu_{\rm syn}(\gamma_{\rm e})$, where it is given approximately (Sari et al., 1998):

$$P_{\nu,\rm max} \approx \frac{P(\gamma_{\rm e})}{\nu_{\rm syn}(\gamma_{\rm e})} = \frac{m_{\rm e}c^2\sigma_{\rm T}}{3q_{\rm e}}\Gamma B. \tag{1.11}$$

The value of $P_{\nu,\rm max}$ is independent of $\gamma_{\rm e}$, but the position of the peak is not (Sari et al., 1998).

If the electron is energetic, it will cool rapidly until it reaches an energy where it can cool on a hydrodynamic timescale $\gamma_{\rm e,c}$. For an electron cooling rapidly, you have to consider the time- integrated spectrum for $\nu > \nu_{\rm syn}(\gamma_{\rm e,c})$ (Sari et al., 1998).

The overall spectrum is calculated by integrating over the electron Lorentz factor distribution. The electron Lorentz factor follows a power-law distribution with index p, such that $N(\gamma_{\rm e}) \sim \gamma_{\rm e}^{-p}$ for $\gamma_{\rm e} > \gamma_{\rm e,min}$. Where the minimal Lorentz factor $\gamma_{\rm e,min}$ is related to p by (Sari et al., 1998):

$$\gamma_{\rm e,min} = \frac{p-2}{p-1}\frac{e_{\rm e}}{n_{\rm e}m_{\rm e}c^2} = \frac{p-2}{p-1}\langle\gamma_{\rm e}\rangle \tag{1.12}$$

where $n_{\rm e}$ and $e_{\rm e}$ are the electron number density and electron energy density, respectively. It is necessary that $p > 2$ to maintain finite electron energy (Sari et al., 1998).

The minimal Lorentz factor characterises the typical electron Lorentz factor and typical synchrotron spectrum, $\nu_{\rm m} \equiv \nu_{\rm syn}(\gamma_{\rm e,min})$.

The shortest acceleration timescale is given by:

$$t_{\rm acc} \leq \frac{\gamma_{\rm e}cm_{\rm e}}{q_{\rm e}B}. \tag{1.13}$$

The accelerated electrons cool via synchrotron radiation. By comparing the acceleration timescale to the cooling timescale (Eq. 1.9) and further substituting into Eq. 1.10, you obtain the upper limit on the synchrotron frequency, for when the electrons are accelerated in a magnetic field,

$$h\nu_{\rm syn} \leq \frac{6\pi h q_{\rm e}^2}{m_{\rm e} c \sigma_{\rm T}} \approx 50 MeV. \tag{1.14}$$

For the most energetic electrons they will rapidly cool and emit nearly all of their energy at their synchrotron frequency. The number of electrons with Lorentz factors $\sim \gamma_{\rm e}$ and energy $m_{\rm e}c^2\gamma_{\rm e}$ is $\propto \gamma_{\rm e}^{1-p}$ and their energy $\propto \gamma_{\rm e}^{2-p}$. The most energetic electrons cool and deposit nearly all of their energy at $\sim \nu_{\rm syn} \propto \gamma^2$. Therefore for fast cooling electrons the flux is related as $F_\nu \propto \gamma^{-p} \propto \nu^{-p/2}$ and is formally given:

$$F_\nu = N[\gamma(\nu)] m_{\rm e} c^2 \gamma(\nu) d\gamma/d\nu \propto \nu^{-p/2}. \tag{1.15}$$

The spectrum differs between slow cooling if electrons with $\gamma_{\rm e,min}$ do not cool on a hydrodynamic timescale and fast cooling if they do. The Lorentz factor of an electron that cools on a hydrodynamic timescale $\gamma_{\rm e,c}$ determines whether the cooling is fast or slow. From Eq. 1.9, you can obtain $\gamma_{\rm e,c}$ in the observers frame:

$$\gamma_{\rm e,c} = \frac{3 m_{\rm e} c}{4 \sigma_{\rm T} U_B \Gamma t_{\rm hyd}}. \tag{1.16}$$

For fast cooling $\gamma_{\rm e,min} < \gamma_{\rm e,c}$, for slow cooling $\gamma_{\rm e,min} > \gamma_{\rm e,c}$.

During the prompt emission, the process is very efficient and therefore if the prompt emission is produced from synchrotron emission, the electrons are fast cooling. Therefore, $\gamma_{\rm e,c} < \gamma_{\rm e,min}$ and the overall observed flux, F_ν is given (Sari et al., 1998):

$$F_\nu \propto \begin{cases} (\nu/\nu_{\rm c})^{1/3} F_{\nu,\rm max}, & \nu < \nu_{\rm c}, \\ (\nu/\nu_{\rm c})^{-1/2} F_{\nu,\rm max}, & \nu_{\rm c} < \nu < \nu_{\rm m}, \\ (\nu_{\rm m}/\nu_{\rm c})^{-(p-1)/2} F_{\nu,\rm max}, & \nu_{\rm m} < \nu, \end{cases}$$

where $\nu_{\rm m} \equiv \nu_{\rm syn}(\gamma_{\rm e,min})$, and $\nu_{\rm c} \equiv \nu_{\rm syn}(\gamma_{\rm e,c})$. $F_{\nu,\rm max}$ is the observed peak flux at ν_{c} and is given:

$$F_{\nu,\mathrm{max}} = \frac{\sqrt{3}e^3 B N_{\mathrm{e}} \Gamma}{4\pi D^2 m_{\mathrm{e}} c^2} \tag{1.17}$$

where D is the distance to the source (Sari et al., 1998).

During the afterglow phase, relativistic electrons are produced due to external shocks. In this phase, there are two possible scenarios: slow cooling and fast cooling. In the case of slow cooling, where the critical Lorentz factor for electron cooling, $\gamma_{\mathrm{e,c}}$, is greater than the minimum Lorentz factor of the electrons, $\gamma_{\mathrm{e,min}}$, the overall observed flux, denoted as F_ν, is given:

$$F_\nu \propto \begin{cases} (\nu_{\mathrm{a}}/\nu_{\mathrm{m}})^{1/3}(\nu/\nu_{\mathrm{a}})^2 F_{\nu,\mathrm{max}} & \nu < \nu_{\mathrm{a}}, \\ (\nu/\nu_{\mathrm{m}})^{1/3} F_{\nu,\mathrm{max}}, & \nu_{\mathrm{a}} < \nu < \nu_{\mathrm{m}}, \\ (\nu/\nu_{\mathrm{m}})^{-(p-1)/2} F_{\nu,\mathrm{max}}, & \nu_{\mathrm{m}} < \nu < \nu_{\mathrm{c}}, \\ (\nu_{\mathrm{c}}/\nu_{\mathrm{m}})^{-(p-1)/2}(\nu/\nu_{\mathrm{c}})^{-p/2} F_{\nu,\mathrm{max}} & \nu_{\mathrm{c}} < \nu, \end{cases}$$

where ν_{a} is the synchrotron self-absorption frequency (SSA). For $\nu < \nu_{\mathrm{a}}$, radiation is re-absorbed by the same electrons that released the photons (Sari et al., 1998). For fast cooling the overall observed flux is (Sari et al., 1998):

$$F_\nu \propto \begin{cases} (\nu_{\mathrm{a}}/\nu_{\mathrm{c}})^{1/3}(\nu/\nu_{\mathrm{a}})^2 F_{\nu,\mathrm{max}} & \nu < \nu_{\mathrm{a}}, \\ (\nu/\nu_{\mathrm{c}})^{1/3} F_{\nu,\mathrm{max}}, & \nu_{\mathrm{a}} < \nu < \nu_{\mathrm{c}}, \\ (\nu/\nu_{\mathrm{m}})^{-1/2} F_{\nu,\mathrm{max}}, & \nu_{\mathrm{c}} < \nu < \nu_{\mathrm{m}}, \\ (\nu_{\mathrm{m}}/\nu_{\mathrm{c}})^{-1/2}(\nu/\nu_{\mathrm{m}})^{-p/2} F_{\nu,\mathrm{max}} & \nu_{\mathrm{m}} < \nu, \end{cases}$$

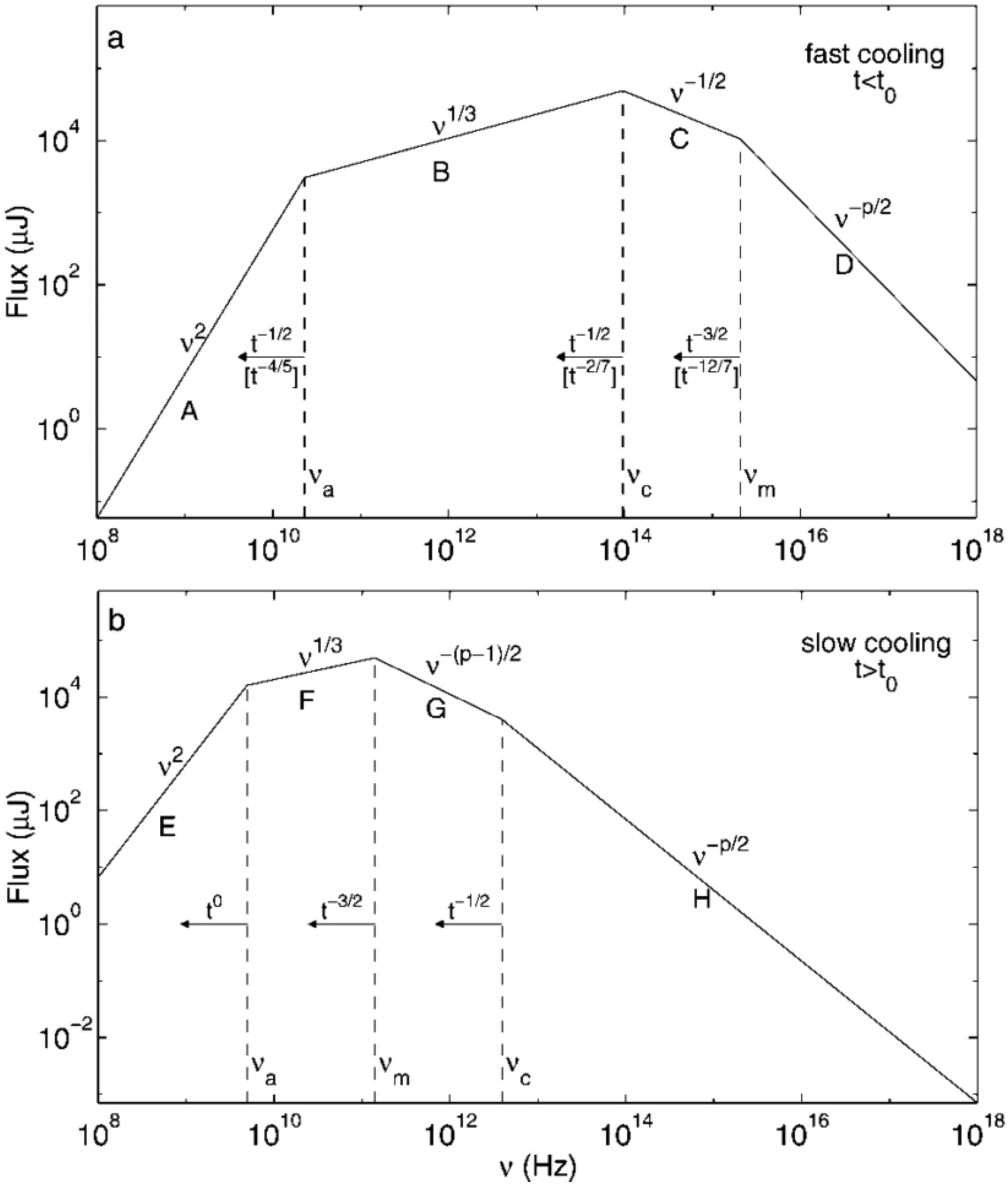

Figure 1.3: Synchrotron spectrum of a relativistic shock that accelerates electrons to a power law electron distribution with index p. Below ν_a the electrons re-absorb the synchrotron emission previously emitted by the same population of electrons. The synchrotron spectrum is segmented with break frequencies ν_a, the cooling frequency ν_c and the minimum frequency ν_m. The top panel shows the case of fast cooling ($\nu_\mathrm{m} > \nu_\mathrm{c}$), and the bottom panel for slow cooling ($\nu_\mathrm{m} < \nu_\mathrm{c}$). The time indices are shown for an ISM and wind density circumburst medium above and below the arrows, respectively. Image is taken from Sari et al. (1998).

1.5 Shock Breakout

Before delving into the intricacies of GRBs, particularly the low-luminosity variants, it's essential to understand a fundamental phenomenon associated with stellar explosions: the shock breakout.

It is predicted that the birth of a supernova (SN) is preceded by the breakout of a shock through the stellar surface; typically this breakout is in the form of a UV or X-ray flash (XRF). Before the instance of breakout, the shock waves become radiation dominated when propagating through the opaque stellar envelope (i.e., the energy density following the shock is radiation dominated) (Nakar and Sari, 2012). The shock accelerates as it travels through the rapidly decreasing density profile of the stellar envelope. The optical depth for photons, τ, in front of the shock to escape the stellar envelope decreases as the shock propagates. When the value of τ approaches a critical value, the shock can no longer be maintained by Compton scattering. At this instance, the photons in the shock transition layer escape ahead of the shock. As τ approaches c/v, where v is the shock velocity and c is the speed of light, the shock breaks out (Nakar and Sari, 2012; Waxman et al., 2007).

1.6 Low Luminosity GRBs (LLGRBs)

Prompt emission isotropic-equivalent luminosities of GRBs range from 10^{46} - 10^{54} erg s^{-1}. At low redshifts are the low-luminosity GRBs (LLGRBs), such as GRB 980425 ($L_{iso} \approx 4.7 \times 10^{46}$ erg s^{-1}). Conversely, at the largest measured L_{iso} is GRB 110918A ($L_{iso} \approx 4.7 \times 10^{54}$ erg s^{-1}). The isotropic-equivalent luminosity L_{iso} corresponds to if the GRB was emitted isotropically with an equal flux to that observed along our line of sight to the GRB. The L_{iso}, isotropic-equivalent luminosity, is used to compare luminosities and is calculated $L_{iso} = 4\pi D_L^2 Fk$. Where D_L is the luminosity distance, k is the k-correction, and F is the flux. This is the same k-correction used to calculate the isotropic equivalent energy, E_{iso}.

What characterises the LLGRBs is their isotropic equivalent luminosities,

10^{46} - 10^{48} erg/s, 4 orders of magnitude less than the average isotropic equivalent luminosities for long GRBs. They are also associated with small values of emitted energy compared to typical GRBs, $E_\gamma \sim 10^{48} - 10^{50}$ erg. While there has only been a small sample of four observed, they have a higher volumetric rate than long GRBs. As they can only be detected from low redshift $z, < 0.1$, the implied event rate is 230^{+490}_{-190} Gpc^{-3} yr^{-1} (Soderberg et al., 2006b). This is 2 - 3 orders of magnitude larger than the rate of long GRBs directed towards earth. For a typical LLGRB, the ejecta are mildly relativistic and the energy of the ejecta is comparable with the energy in the gamma-rays, E_γ. As showcased in Figure 1.4, the distribution of peak isotropic equivalent luminosities observed by *Swift* further highlights the challenge in detecting LLGRBs, especially given their position on the left of the histogram (Virgili et al., 2009).

Presently there are four observed GRBs that have been identified as low-luminosity GRBs (LLGRBs), each with a corresponding spectroscopically confirmed supernova (SN): GRB 980425 (SN1998bw), GRB 031203 (SN200lw), GRB 060218 (SN2006aj), and GRB 100316D (SN2010bh). While being less luminous than the long GRB archetype, LLGRBs exhibit smooth light curves. Unlike typical long GRBs, they show no indication of a high-energy power-law tail. Within this sample of four LLGRBs, two have regular durations (∼20s) and two have ultra-long durations (∼2000s). All detected LLGRBs are nearby (∼40-400 Mpc) as their luminosity is low; unless they are produced close to us, they do not trigger current detectors.

Bromberg et al. (2011) looked at the ratio of the T_{90} duration and the calculated jet breakout time for short, long and low luminosity GRBs. The jet breakout time was calculated using the GRBs isotropic equivalent luminosity and observed opening angle. They concluded that as there was a significant excess of LLGRBs with jet break out times less than the observed durations, the processes that govern the gamma-ray emission of LLGRBs are likely different to those in long GRBs (Bromberg et al., 2011). It was proposed that LLGRBs could originate from failed jets (Campana et al., 2006; Waxman et al., 2007;

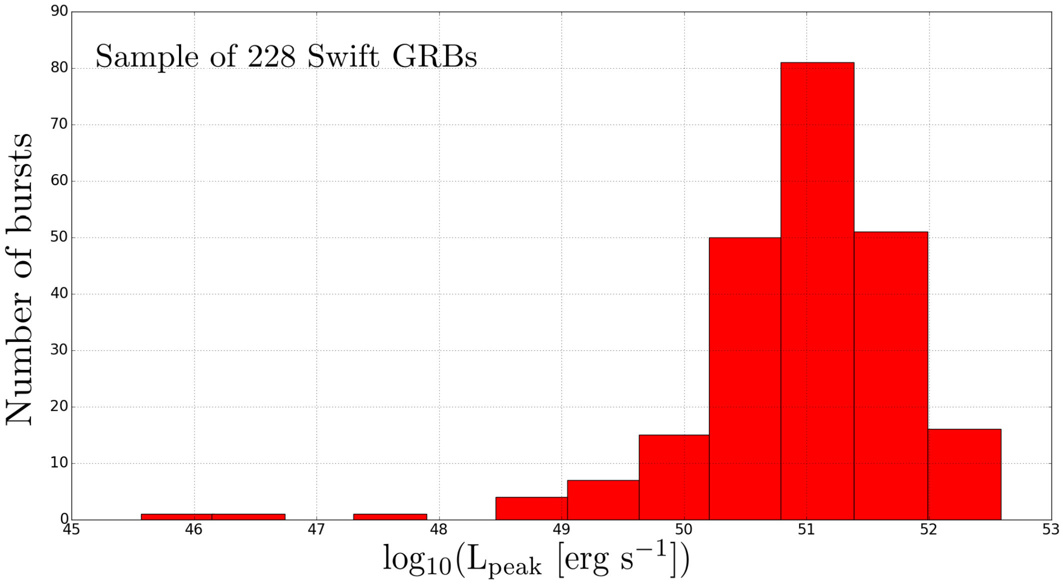

Figure 1.4: A sample of GRBs observed by *Swift* with their associated peak isotropic equivalent luminosities. The low number of GRBs on the left of the histogram is an observational effect because LLGRBs are hard to detect (luminosities used from Virgili et al. (2009)).

Bromberg et al., 2012), jets that cannot successfully break through their progenitor envelope. It was suggested by Bromberg et al. (2011) that failed jets are more frequent than successful ones. Whilst these jets do not break through the envelope they have sufficient driving force to generate shocks which break out of the progenitor envelope.

Chapter 2

The *Swift* Gamma-Ray Burst Mission

Swift is a fast-pointing satellite observatory positioned in a low Earth orbit, specifically designed to study gamma-ray bursts. The mission is equipped with a suite of three main instruments. First, the wide-field gamma-ray (15-500 keV) Burst Alert Telescope (BAT) is capable of detecting bursts and determining their positions with an accuracy of 1-4 $'$. Following this, the narrow-field X-ray Telescope (XRT) offers more precise positioning, achieving arcsecond-level accuracy (3-5 $''$) and provides spectra in the 0.2 -10 keV band. Finally, the UV/Optical Telescope (UVOT) operates in the 170-800 nm band, providing 0.3 $''$ positional accuracy and delivering both optical and UV photometry. For particularly bright afterglows, the UVOT can also obtain UV spectra.

2.1 *Swift* Observing Procedure

Swift is designed to observe not only predefined targets uploaded from the ground but also gamma-ray bursts detected on-board in real time. A Pre-Planned Science Timeline (PPST) is uploaded onto the on-board software every weekday, containing an observing schedule with a list of targets. The BAT utilises a Figure of Merit (FoM) algorithm to assess whether a burst detected by BAT merits slewing the spacecraft for closer observation. FoM scores range from 0 to 100. Each target in the PPST has an associated FoM, and if a detected burst has a higher FoM than the pre-programmed targets, a slew manoeuvre toward the burst is initiated. Similarly, all transients detected by BAT are assigned an FoM, which dictates if a spacecraft slew is necessary. If a transient source is identified as a GRB, it receives the topmost FoM of 100, designating the GRB as the automated target (AT). The spacecraft will then autonomously slew, ensuring the transient source lies within the field of view of both the XRT and UVOT, subsequently initiating an automated observation sequence[1].

Swift can be prevented from continuously viewing by certain pointing constraints. Pointing is constrained when any instrument is within: 46 degrees of the Sun; 23 degrees of the Moon; and due to the low orbit, 28 degrees of the Earth's limb. The UVOT instrument will avoid planets within our solar system and also sufficiently bright stars ($-1.0 - 0\,\mathrm{mag}$). To overcome these constraints, observations are split into observation intervals of between 5 and 30 minutes. Observations cannot exceed 30 minutes due to *Swift*'s observations being occulted by the Earth. Observation segments are made up of multiple observation intervals. The first segment of an observation segment consists of automated observations and following segments are directed from the ground[2].

Following the initial detection, first level data products are swiftly sent to the ground through the Tracking and Data Relay Satellite System (TDRSS). First level data products include raw images and uncalibrated event lists, for example[3]. The TDRSS data are sent to the Mission Operations Center (MOC) and to the Gamma-ray Coordinates Network Notices (GCN Notices) to provide the astrophysics community with preliminary analysis. All high-resolution data sets and housekeeping data from the GRB are downloaded at various Ground Stations when the satellite passes them (typically 9-12 passes per station per day). Data is relayed from the Ground Stations to the MOC also. From the MOC the data are relayed to the Swift Data Center (SDC) in the Goddard

---

[1] `http://swift.gsfc.nasa.gov/proposals/tech_appd/swiftta_v12/node17.html`

[2] `http://swift.gsfc.nasa.gov/proposals/tech_appd/swiftta_v12/node23.html`

[3] `http://swift.gsfc.nasa.gov/proposals/tech_appd/swiftta_v10/node51.html`

Space Flight Center (GSFC) where the reduced data products are produced. The reduced data products are then distributed via the Quick-look Server to the astrophysics community on the web. This final stage is completed within three hours of the SDC receiving the data from the MOC[4].

2.2 Burst Alert Telescope (BAT)

The BAT is an extremely sensitive, coded aperture, hard X-ray/gamma-ray (15-150 keV) imager, but with a non-coded response sensitive up to 500 keV. It has a large, 1.4 steradians, field of view designed to detect and trigger on GRBs with localisations that are accurate to 4 arcminutes (Barthelmy et al., 2005). The instrument specifications are detailed in Table. 2.1.

Table 2.1: BAT instrumentation characteristics[a]

Energy Range:	15-150 keV (up to 500 keV non-coded)
Energy Resolution:	~7 keV
Aperture:	Coded mask, 50% open with a random pattern
Detector Area:	5240 cm^2
Detector Operation:	Photon Counting
Field of View:	1.4 sr (half-coded)
Telescope PSF:	17 arcmin
Source Position Accuracy:	1-4 arcmin

[a] The information in this table was taken from Barthelmy et al. (2005).

The BAT's detector is arranged in an hierarchical structure of multiple detector arrays which affords the benefit to retain burst detection and localisation's despite loss of detector elements (Barthelmy et al., 2005). The BAT is a coded-aperture telescope, and its coded mask comprises approximately 54,000 lead tiles arranged in a D-shaped pattern with a honeycomb structure. Almost all gamma-ray instruments flown post-1990 use coded-aperture techniques as this provides an accurate location of the gamma-ray source in the sky. As the gamma-rays enter the instrument, the gamma-rays pass through the open areas of the mask but are halted where they interact with lead. The calculation

---

[4] `http://swift.gsfc.nasa.gov/proposals/tech_appd/swiftta_v12/node57.html`

of the gamma-ray source in the sky is facilitated by deconvolving this known mask pattern. The area of the BAT coded mask is 2.7 m^2 which provides a FOV (half coded) of 100 ° by 60 ° (Barthelmy et al., 2005).

2.2.1 BAT operation modes

There are two operation modes that BAT runs: Survey Mode and Burst Mode. Survey Mode detects hard X-ray transients and produces all-sky hard X-ray survey data. Burst Mode captures the intensity and sky location of the detected burst (Barthelmy et al., 2005).

2.2.1.1 Burst Mode

There are two key processes involved in BAT's GRB detection. The first process involves analysing the count rate across the detector plane to seek increases. These increases are sought because they represent the detection of a burst at its commencement. The second process involves creating a sky image using the events detected at the onset of the burst (Gehrels et al., 2004).

Burst trigger algorithms look for significant excesses in the detector count rate, which are larger than what is expected from background and constant sources. These algorithms must be versatile, accounting for variations in background count rates and the temporal diversity of GRBs. Due to *Swift* being in a low earth orbit at 600 km, there are fluctuations in the detected background count rates. For instance, in a 90-minute orbit, these rates can differ by a factor of two.

The length of a GRB can range from milliseconds to several minutes and within this, peaks in the gamma-ray emission can vary from one peak to multiple. Consequently, it is necessary that the triggering system be flexible and have the ability to compare the measured detector counts to a background extrapolated over a range of timescales and energy bands. Any detected sources are compared with an on-board catalogue of sources, if the detected source is novel and does not match any catalogued source the burst response procedure is initiated. The classification system used helps differentiate and exclude sources of background such as magnetospheric particle events and galactic sources with variable brightness (Markwardt et al., 2007).

2.3 X-ray telescope (XRT)

The XRT aboard *Swift* is able to measure the fluxes, spectra and light curves of GRBs and their associated afterglows. The XRT is able to improve the localisations provided by the BAT to 5 arcsec accuracies; for a typical GRB this is achieved within 10 second of target acquisition (Burrows et al., 2003).

The XRT has an effective area of ~125 cm^2 at 1.5 keV and a resolution (half-power diameter) of 18 $''$, the half-power diameter refers to the diameter within which half of the focused X-rays enter. The XRT covers a broad energy range (0.2-10 keV, with a 23 $'$ field of view (FOV). Due to the telescope detecting X-rays, it is necessary to use grazing incidence optics. Consequently, the XRT uses a grazing incidence Wolter type I telescope (Burrows et al., 2003). The XRT instrument characteristics are shown in Table. 2.2.

Table 2.2: XRT instrumentation characteristics[a]

Telescope:	Wolter I (3.5 m) focal length
Detector:	e2v CCD-22
Detector format:	600×600 pixels
Pixel size:	40×40 μm
Detector Operation Modes:	Image (IM) Mode Windowed Timing (WT) Mode Photon-Counting (PC) Mode
Pixel scale:	2.36 arcseconds/pixel
Field of view:	23.6×23.6 arcminutes
PSF:	18 arcseconds (half-power diameter) at 1.5 keV 22 arcseconds (half-power diameter) at 8.1 keV
Position accuracy:	3 arcseconds
Energy range:	0.2 - 10 keV
Energy resolution:	140 eV at 5.9 keV
Effective area:	~125 cm^2 at 1.5 keV ~20 cm^2 at 8.1 keV
Sensitivity[a]:	2×10^{-14} erg cm^{-2} s^{-1} in 10^4 s

[a] The information in this table was taken from Burrows et al. (2003).

2.3.1 XRT operation modes

The XRT is operated in three different readout modes to facilitate the coverage of the wide dynamic range in fluxes which arise from, and the rapid variability of, GRB afterglows. The three readout modes are: Imaging (IM) mode, Windowed Timing (WT) mode, and Photon-Counting (PC) mode. There used to be a fourth readout mode on the XRT, Photodiode mode. However, this was disabled in May 2005 due to a micrometeoroid hit. The XRT autonomously alternates between the modes based on the instantaneous count rate in each Charge Coupled Device (CCD) frame (Burrows et al., 2003).

2.3.1.1 IM Mode

IM mode produces both a GRB centroid position and an X-ray flux estimate, however the principal use of IM mode is to acquire the first X-ray position of a detected GRB. IM mode measures the total energy deposited from the target per pixel in the CCD to produce an integrated image. IM mode autonomously selects either a 0.1 or 2.5 second exposure time based on the source flux and is operated with a low gain. IM mode is used to determine the positions of bright source fluxes between $6 \times 10^{-10} - 1 \times 10^{-6}\ \mathrm{erg\,cm^{-2}\,s^{-1}}$ (Burrows et al., 2003).

2.3.1.2 WT Mode

WT mode provides poor position information, however it compensates for this shortcoming with its ability to achieve a high time resolution (1.8 ms) and to perform spectroscopy on bright sources. WT mode data is presented as a single strip of data. This strip's orientation is determined by the spacecraft's roll angle, meaning that depending on the angle, some data strips may appear horizontal, some nearly vertical, and others at various angles in between. This orientation is crucial for understanding and interpreting the data obtained in WT mode. WT mode data is typically the first data obtained for sources as it performs better when observing sources with higher flux than PC mode (Burrows et al., 2003).

2.3.1.3 PC Mode

PC mode provides full imaging and spectroscopic resolution of the source with a time resolution of 2.5 seconds, which is much poorer than that of WT mode. Unlike in WT mode, the data appears as a 2-dimensional image and does not depend on the roll angle of the spacecraft. PC mode is used when the flux falls below the range $10^{-10} - 10^{-11}\,\mathrm{erg\,cm^{-2}\,s^{-1}}$ (Burrows et al., 2003).

2.4 Ultra-Violet/Optical Telescope (UVOT)

UVOT captures the optical/UV photons from the afterglow of GRBs, with the aim of doing so within two minutes of the BAT trigger. UVOT also observes GRB afterglows long-term.

UVOT is a modified Ritchey-Chrétien telescope which is co-aligned with the XRT and has a 30 cm aperture. UVOT operates in the broad optical-UV band 170 - 800 nm (Gehrels et al., 2004), and is host to a range of UV and optical broadband filters and grisms. UVOT carries a filter wheel which consists of: UV and optical grisms; V, B, U filters; UVW1, UVM2,UVW2 filters; and a white light filter. The filter characteristics are shown in Table. 2.3. The filters provide broad-band visible/UV imaging and photometry, and the low-resolution grisms provide grism spectra of bright GRBs. UVOT has a micro-channel plate intensified charged-coupled device (MIC), which is able to detect very low light levels and can function in a photon counting mode (Roming et al., 2005). As photons enter the UVOT detector, they first strike the photocathode. This action discharges electrons, which are accelerated to the micro channel plate (MCP) by a bias voltage. Once the electrons enter the MCP, they are amplified to form an electron cloud. This cloud is then converted to photons using a phosphor screen and directed to the CCD. Notably, the MCP amplifies the original signal to the CCD by a factor of 10^6 (Roming et al., 2005). Photons are detected by reading out the CCD at a high frame rate, and the photon splash position on the CCD is determined by a centroid algorithm (Michel, Fordham, & Kawakami 1997). The centroid algorithm uses

Table 2.3: UVOT instrumentation characteristics[a]

Telescope:	Modified Ritchey-Chrétien
Aperture:	30 cm
f-number:	12.7
Filters:	V, B, U, UVW1, UVM2, UVW2, White
Wavelength Range:	170 - 800 nm
Detector:	MCP Intensified CCD
s Detector Operation:	Photon Counting
Sensitivity:	$m_B = 24.0$ in white light in 1000 s
Field of View:	$17 \times 17\ '^2$
Telescope PSF:	0.9 arcsec FWHM at 350 nm
Pixel scale:	0.5 arcseconds/pixel

[a] The information in this table was taken from Roming et al. (2005).

Table 2.4: UVOT Filter Characteristics[a]

Filter	**λ_c (nm)**	**FWHM (nm)**
V	544	75.00
B	439	98.0
U	345	87.5
UVW1	251	70.0
UVM2	217	51.0
UVW2	188	76.0
White	385	260.0

[a] The information in this table was taken from Roming et al. (2005).

a large image format for the detector which it produces by creating a grid of 8×8 virtual pixels for each of the 256×256 CCD pixels. The use of virtual pixels provides an array of 2048×2048 virtual pixels with a size of 0.5×0.5 arcsec^2 on the sky (Roming et al., 2005). However, a consequence of the use of virtual pixels is that the images obtained from the CCD contain a systematic modulo-8 fixed-pattern noise, as the effective size of the sub-pixels depends on their position within the CCD pixel when processed at ground level (Roming et al., 2005).

UVOT operates in three primary modes. The Image Mode captures two-dimensional images across specified integration duration, typically ranging from 10 to 1000 seconds. This mode predominantly uses the full field of view, yielding a raw image with dimensions of 1024x1024 pixels. In contrast, the Event Mode meticulously logs each photon event, annotating its specific position on the detector alongside the corresponding CCD frame time-stamp. Merging the attributes of both these modes, the Image&Event Mode offers a comprehensive observational data-set (Roming et al., 2005).

Upon detecting a new GRB and successfully generating a finding chart, UVOT initialises an automated exposure sequence. This sequence, tailored to the specific optical decay profile of the GRB and the elapsed time post its detection, employs a strategic combination of onboard filters. Two primary sequences have been established, one targeting luminous GRBs termed the "Bright GRB Sequence", and the other catering to less luminous GRBs, aptly named the "Dim GRB Sequence". The foundation of these sequences was laid based on preliminary observations, but they are inherently flexible. This adaptability ensures they can be updated or expanded upon as our understanding of GRBs deepens (Roming et al., 2005).

Chapter 3

The early optical afterglow and non-thermal components of GRB 060218

3.1 Introduction

It has been known that there is an association between long gamma-ray bursts (GRBs) and supernovae (SNe) since the simultaneous discovery of GRB 980425 and SN 1998bw. This connection strengthened the notion that long duration GRBs were caused by the core collapse of massive stars (Woosley et al., 2002). In the preferred model for long GRBs, the collapsar model, the core collapse of a massive star into a black hole or a neutron star with an accretion disk drives a highly relativistic jet, which penetrates the outer stellar envelope, producing a GRB (Woosley, 1993b). The relativistic jet begins to decelerate when it interacts with the external medium; this leads to the external shock afterglow, which radiates a significant fraction of the initial total energy (Mészáros and Rees, 1997). A number of SNe have been identified spectroscopically following a number of GRBs; see Cano et al. (2016) for a recent list.

Some GRBs are observed at much lower luminosities ($10^{46} - 10^{48}\,\mathrm{erg\,s^{-1}}$) than typical GRBs ($10^{50} - 10^{52}\,\mathrm{erg\,s^{-1}}$); these bursts are classified as low-luminosity GRBs (LLGRBs). So far, six LLGRBs have been identified, four of which have corresponding spectroscopically confirmed SNe: GRB 980425 (SN 1998bw), GRB 031203 (SN 2003lw), GRB 060218 (SN 2006aj), and GRB 100316D (SN 2010bh). GRB 111005A, was identified as a LLGRB with a redshift of $z = 0.0133$; however, an associated SN was not found (MichałowskI et al., 2018). GRB 170817A was a short GRB that produced gravitational waves, GW 170817, detected by LIGO, and was associated with a blue kilonova at a redshift of $z = 0.009$ (Abbott et al., 2017). Within this sample of four LLGRBs associated with SNe, two have regular long GRB durations ($\sim 20\,\mathrm{s}$), and two have ultra-long durations ($\sim 2000\,\mathrm{s}$); all four have smooth gamma-ray light curves. Soderberg et al. (2006b) estimated the volumetric rate to be a factor of 100 times greater than that of typical long GRBs. All detected LLGRBs occurred nearby ($\sim 40-400\,\mathrm{Mpc}$); it is a consequence of their luminosities being low, which implies that unless they occur close to us, they do not trigger current detectors.

One such LLGRB and associated SN is GRB 060218 (Campana et al., 2006) and SN 2006aj (Cusumano et al., 2006). GRB 060218, like other LLGRBs, is shown to be faint and soft with a smooth gamma-ray light curve. However, I can study GRB 060218 in great detail, due to the extensive coverage of the observations in the UV/optical bands, days before the Ni^{56}-decay-powered emission from SN 2006aj was observed. This coverage allows us to examine the emission before the optical SN emission, and enables us to investigate the link between the outflow components of both GRB 060218 and SN 2006aj.

GRB 060218 was first detected by the Burst Alert Telescope (BAT) (Barthelmy et al., 2005) on-board *The Neil Gehrels Swift Observatory* (Gehrels et al., 2004). A very long T_{90} (the duration containing 90% of the gamma-ray flux) (Kouveliotou et al., 1993) was measured from the BAT gamma-ray light curve, of $2100 \pm 100\,\mathrm{s}$ and GRB 060218 is therefore considered to be an ultra-long GRB ($\mathrm{T}_{90} > 1000\,\mathrm{s}$) (Virgili et al., 2013). GRB 060218 had a redshift of $z = 0.0331$ (Sollerman et al., 2006), making it the fourth nearest GRB with a determined redshift, after GRB 111005A (MichałowskI et al., 2018), GRB 170817A (Abbott et al., 2017), and GRB 980425 (Galama et al., 1998). The gamma-ray spectrum of GRB 060218 is atypically soft for a long GRB, with an average peak energy $E_{\text{peak}} = 4.9^{+0.4}_{-0.3}$ keV (Campana et al., 2006). The isotropic equivalent emitted energy was calculated as $E_{\text{iso}} = (6.2 \pm 0.3) \times 10^{49}$ ergs, extrapolated to the $1-10000$ keV rest frame energy band (Campana et al., 2006).

Whilst GRB 060218 exhibits a low E_{peak} and an E_{iso} that is four orders of magnitude smaller than the value for typical long GRBs (Campana et al., 2006; Sazonov et al., 2004), GRB 060218 adheres to the Amati correlation (Campana et al., 2006), linking E_{peak} and E_{iso} (Amati et al., 2002). Furthermore, Liang et al. (2006) showed that GRB 060218 conforms to the luminosity-lag relation, a relationship seen in many long GRBs (Norris et al., 2000; Ukwatta et al., 2012). This is a correlation between the GRB isotropic peak luminosity and spectral lag, where the lag is defined as the difference in time of arrivals of high and low energy photons. The luminosity-lag relation observed in GRB 060218, coupled with its compliance with the Amati correlation, indicates that GRB 060218 has similar radiation physics to long GRBs (Liang et al., 2006), despite being a low luminosity, ultra-long GRB. However, it has been argued that the prompt X-ray emission in GRB 060218 is produced by shock break-out emission (Waxman et al., 2007; Nakar, 2015). Furthermore, Nakar (2015) suggested that all high-energy emission of LLGRBs are entirely due to shock break-out emission (Nakar, 2015).

The Ultraviolet Optical Telescope (UVOT) (Roming et al., 2005) on-board *Swift* observed strong UV/optical emission, both during the prompt gamma-ray emission and for days following the trigger, with good coverage. *Swift* also provided simultaneous observations from the X-ray Telescope (XRT) (Burrows et al., 2003). The observed X-ray flux rose to a peak luminosity of $\sim 3 \times 10^{46}\,\text{erg}\,\text{s}^{-1}$ $(0.3-10\,\text{keV})$. The peak in the X-ray flux was followed by a fast decay, and at $\sim 10^{4}$ s the flux began to decrease at a steady rate as a power-law ($F_{\nu} \propto t^{-1.1}$); this decreasing phase lasted for several days. During the initial 10 ks there is a thermal blackbody component in the X-ray spectra, which ranges in kT from 0.05 to 0.12 keV. The UV/optical light curve shows a continuously rising UV and optical profile until it peaks in luminosity at ~30 ks, after which the source fades, and then the Ni^{56}-decay-powered emission from SN 2006aj is observed rising in the V-band at ~200 ks. During the initial 3000 s, GRB 060218 was observed with good time coverage in the UV/optical bands with UVOT. The coverage enables the UV/optical spectra to be examined systematically, and the search for an UV/optical afterglow can be performed with an in-depth analysis of the early UV/optical emission, something that is lacking in previous studies of GRB 060218. Due to the detection of both GRB 060218 and SN 2006aj, and the presence of a thermal component in the UV/optical and X-ray emission, a variety of models have been put forward to explain the observations. Campana et al. (2006) and Waxman et al. (2007) modelled the thermal emission as being produced from the breakout of a shock driven by a mildly relativistic shell, where the radiation generated by the shock travels through a dense wind surrounding the Wolf-Rayet (WR) progenitor star of the SN.

In this model, the shock reaches a region where the optical depth of the stellar envelope is low enough that the photons from the shock escape, producing a bright flash in the UV and X-ray (Waxman et al., 2007). Waxman et al. (2007) suggested that this takes place at a breakout radius, $R = 7.8 \times 10^{12}$ cm. Assuming spherical symmetry, the time it takes for the photons to escape the shock (the breakout duration) is the breakout radius divided by the speed of light. For a breakout radius of $R = 7.8 \times 10^{12}$ cm this corresponds to a duration of 260 s (Waxman et al., 2007). This duration is a lot shorter than the time it takes for the X-ray to peak in luminosity at 1000 s. Waxman et al. (2007) argued that an anisotropic shock will change the timescale, as the timescale would not be represented by R/c, but rather a timescale influenced by an angular velocity profile in an anisotropic shell (Waxman et al., 2007). Waxman et al. (2007), suggested that an optically thick wind would increase the breakout radius and therefore argued that the shock break out occurred in the wind around the envelope. Ghisellini et al. (2007a) argued that fine tuning is required to achieve a longer breakout duration. Li (2007) presented a model which computed the characteristic quantities for the transient emission from the shock breakout in a Type Ibc SN which follows the core collapse of a WR star in a dense wind region. When the model described by Li (2007) is applied to GRB 060218, the energy predicted for the shock breakout in the underlying SN is much lower than the measured energy of the thermal components, which was $\gtrsim 10^{49}$ erg.

In keeping with the shock breakout model, Campana et al. (2006) and Waxman et al. (2007) suggested that the early UV/optical emission ($t <$10 ks) could be produced from the Rayleigh-Jeans tail of the thermal X-ray emission produced by a shock propagated into the wind surrounding the envelope. The UV/optical light curve would then be governed by the expansion of the wind and the decreasing temperature. Within this model, the emission in UV/optical at 120 ks is produced from the envelope of the star, which is initially hidden by the wind (Campana et al., 2006).

Ghisellini et al. (2007a) and Ghisellini et al. (2007b) propose that if the UV/optical radiation is a result of the Rayleigh-Jeans section of the blackbody spectrum, the implied blackbody luminosities are too high, particularly in the early times ($t <$3000 s). Therefore, Ghisellini et al. (2007a) argued that the emission mechanism that governs the observed UV/optical radiation is unclear at early times. Furthermore, Ghisellini et al. (2007a) argued that the spectrum across the UV/optical and X-ray can be produced from self-absorbed synchrotron emission, where the flux, $F \propto \nu^{2.5}$. But they find that the model does not account for the thermal component in the X-rays. Therefore, Ghisellini et al. (2007a) proposed an alternative explanation for the origin of the thermal emission, in which the emission is produced at the transparency radius of a GRB jet. Such an optically thick component from the jet photosphere has been observed in the prompt gamma-ray emission from GRB 100724B (Guiriec et al., 2011) and also GRB 110205A (Guiriec et al., 2016). However, this component is distinctly different to the shock heated expanding envelope proposed by Waxman et al. (2007), which they argue describes the thermal component in the UV/optical emission at 120 ks.

By investigating the radio observations of GRB 060218, Soderberg et al. (2006b) conclude that the radio emission is dominated by synchrotron self-absorbed emission, and the emission is from a mildly relativistic outflow ($\Gamma = 2.3$). Soderberg et al. (2006b) also show that due to the lack of jet-break in the radio up until 22 days, the opening angle of the outflow can be constrained to $\theta_0 > 1.4$ rad. Furthermore, based on the same observations, Soderberg et al. (2006b) rule out an off-axis jet, where the angle from the line of sight to the jet axis is double the opening angle, $\theta_{obs} = 2\theta_j$.

Toma et al. (2007) argued that the radio afterglow was produced by a non-relativistic phase of an initially collimated jet within the external shock synchrotron model, and showed that it is possible for a jet with an opening angle $\theta_0 \simeq 0.3$ rad and an initial Lorentz factor $\Gamma_0 \simeq 5$, to penetrate the stellar envelope.

In this chapter, I present a detailed breakdown of the observations of GRB 060218, with a particular focus on the UV/optical and X-ray emission. My goal is to determine what the mechanisms are that produce the emission from GRB 060218 and SN 2006aj. I pay particular attention to the early spectral evolution in the UV/optical emission, and study the thermal component across the optical to X-ray energy range. In Sec. 3.2 I provide a summary of the data reduction methods and describe the models and fitting techniques. The results of my analysis are given in Sec. 3.3. The implications of this analysis are discussed in Sec. 3.4.

I will use the convention for power laws: $F_\nu \propto t^{-\alpha}\nu^{-\beta}$ where F_ν is the flux density, t and ν are time and frequency, α and β are the temporal and spectral indices respectively (Sari et al., 1998). I use a subscript to denote the waveband of interest, so the spectral index for X-ray spectra is β_X and that for

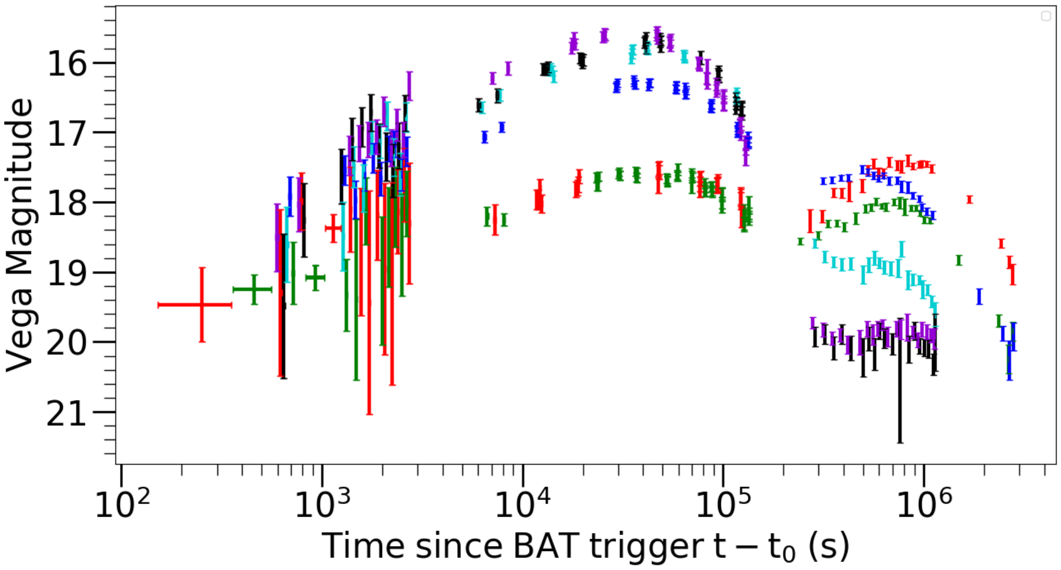

Figure 3.1: The UV/optical light curves of GRB 060218 in six UVOT filters. The colours represent the different UVOT filters: V as red points, B as green, U as blue, $UVW1$ as turquoise, $UVM2$ as black, and $UVW2$ as violet. The light curve is not binned before 150 ks and has been binned at late times (>150 ks) to increase the signal-to-noise ratio (S/N>2).

UV/optical spectra is β_{UV}. Throughout this chapter I use the values measured in Adam et al. (2016) for the Hubble parameter $H_0 = 67.8\,\mathrm{km\,s^{-1}\,Mpc^{-1}}$ and density parameters $\Omega_\Lambda = 0.69$ and $\Omega_m = 0.31$. Uncertainties are quoted at $1\,\sigma$ unless otherwise stated.

3.2 Data reduction and analysis

3.2.1 Observations

GRB 060218 was detected with the Burst Alert Telescope (BAT) on-board *Swift* and *Swift* slewed autonomously to the burst. GRB 060218 was simultaneously observed with the XRT and UVOT after the trigger, and observations continued until both GRB 060218 and SN 2006aj were no longer detectable. Due to the rising UV/optical flux in the initial 60 ks and the identification of SN 2006aj at 10 days past the trigger, GRB 060218 and SN 2006aj were observed with excellent coverage in both UVOT and XRT.

3.2.2 UVOT data

I started with the sky images which had been produced by the pipeline- processing . These images are mod-8 corrected, and aspect corrected to ensure the correct sky coordinates.

Count rates were obtained using the standard UVOT FTOOLS: UVOTMAGHIST software from HEASOFT (version 6.7). When the source was brighter than 1 count per second, the standard aperture for UVOT photometry of radius 5 arcsec was implemented. When the source was fainter than 1 count per second a source aperture of radius 3 arcsec was selected to maintain a good signal-to-noise ratio and aperture corrected to 5” (Breeveld et al., 2010; Poole et al., 2008). Background was measured from a large region offset from the source position. The background area was chosen to be free of any contaminating sources, and large enough that weak contaminating sources did not contribute to the mean count rate significantly. Magnitudes were calculated using the observed count rates and the UVOT zero points from Breeveld et al. (2011). The count rates were not host galaxy subtracted, because the host galaxy was not detected in any UVOT bands in my source aperture.

Fig. 3.1 shows the UV/optical light curves. At 138 s after the trigger time, the UVOT started taking data. The V and B finding charts were taken with 200 s long exposures each after the 9 s settling exposure in the V filter. I do not include the settling exposure in my analysis, because its duration is too short to be of much value.

In the initial 50 ks I have created eight spectral energy distributions (SEDs) covering the UVOT energies. The time intervals for the SEDs are given in Table. 3.1. The first SED was created after the finding charts were taken, at which point a 20 s image was taken in each filter. After the initial 1000 s, 20 s exposure images were taken in each filter every 200 s until $\sim$3000 s; therefore, five SEDs can be obtained during this time. After 3000 s the exposure time for each filter increased to 200 s. There were no observations between 2700 s and 5950 s due to GRB 060218 being occulted by the Earth during these times. Two SEDs can be obtained between 6000 s and 8000 s, as GRB 060218 was observed in each filter twice during this interval.

When creating the SEDs, even though the exposures were taken close together in time, the magnitudes in different filters must be adjusted to common epochs. Therefore a model of the light curve is required to determine the adjustments. For this purpose, a second order polynomial curve was fitted to the UV/optical light curve (as magnitude against log time) in the interval $5-60$ ks. Adjustments made before 5 ks were performed assuming a power-law with a temporal index of $\alpha = -0.7$. For the adjustments made after 60 ks I used a power-law decay with slopes determined individually for each filter.

3.2.3 XRT data

For the X-ray contribution to the SED, the X-ray event data were first cleaned using FTOOLS: XRTPIPELINE. Event data were selected in grades 0 to 12 for Photon Counting (PC) mode data and grades 0 to 2 for Windowed Timing (WT) mode data (Capalbi et al., 2005). The auxiliary response files were produced by FTOOLS: XRTMKARF. These response files contain the product of telescope area, filter efficiency and quantum efficiency as a function of energy. The X-ray spectra were extracted using XSELECT (version 2.4c) and the energy range used to analyse the X-ray data was $0.3-10$ keV.

The WT mode spectra were extracted from the event data with a circular region of radius 11 arcsec around the 1D image strip (rotated by the instrument roll angle). The background was removed using the same size region, shifted away from the source along the image strip. The PC mode spectra were extracted in the same way but from a 2D image. XRT spectra were grouped to a minimum of 20 counts in each bin, which allows the use of χ^2 statistics.

Where possible, the X-ray spectra were extracted over the same time intervals as the UV/optical spectra were taken. However, after 6000 s, larger durations were required to achieve adequate quality for the X-ray spectra. For all SEDs, the mid-point of the X-ray exposures were chosen to be equal to the mid-points of the corresponding UVOT time intervals, and the X-ray spectra

Table 3.1: Times used for creating the UV/optical-X-ray SEDs. The SED central time, is the central time from both the UV/optical and X-ray SED time ranges.

SED central time (s)	UVOT SED range (s)	X-ray SED range (s)
650	$550-750$	$550-750$
1250	$1150-1350$	$1150-1350$
1625	$1400-1850$	$1400-1850$
2125	$1900-2350$	$1900-2350$
2550	$2400-2700$	$2400-2700$
6500	$6410-6590$	$6000-7000$
7500	$7410-7590$	$7000-8000$
120000	$117500-122500$	$10000-130000$

were scaled to the corresponding count rate at the mid-point time. The time intervals used for the SEDs are shown in Table. 3.1.

3.2.4 Analysis and modelling

The SEDs were analysed using XSPEC (version 12.9.0) and were modelled with a combination of power-law and spherically outflowing blackbody components, together with photoelectric absorption and dust extinction from our Galaxy and the host galaxy of the GRB. The Galactic reddening was fixed at $E(B-V)=0.14$, based on the extinction maps in Schlegel et al. (1998). The determination of the host galaxy reddening is discussed in detail in Sec. 3.3. The X-ray absorption in our galaxy is accounted for by fixing the hydrogen column density, N_H, in our galaxy for GRB 060218 to $N_H = 1.0\times10^{21}\,\mathrm{cm}^{-2}$ (Kalberla et al., 2005); the host galaxy absorption is a free parameter in the SED fitting.

3.2.4.1 Spherically outflowing blackbody components

The blackbody emission from GRB 060218 is thought to arise in material flowing out from the stellar explosion at tens of thousands of $\mathrm{km\,s^{-1}}$ (Campana et al., 2006). To model the blackbody emission, I assume a spherically symmetric blackbody model.

However, the outflow of the blackbody component has not been included in the model fitted to the data for GRB 060218 before this study. To correctly describe the relativistic blackbody emission from a spherical outflow, relativistic beaming and Doppler shift must be taken into consideration. Due to relativistic effects, I observe the apparent flux which is related to that in the blackbody rest frame through the Lorentz factor, Γ, the Doppler factor, δ, and the angle of the outflow with respect to the line of sight from the observer, θ. The Lorentz factor, Γ, is related to the intrinsic velocity of the outflow, v, by

$$\Gamma = (1 - (\tfrac{v}{c})^2)^{-1/2}, \tag{3.1}$$

and the Doppler factor, δ, is defined as

$$\delta = \Gamma^{-1}(1 - \tfrac{v}{c}\cos\theta)^{-1}. \tag{3.2}$$

The observed blackbody temperature, T, in relation to the temperature in the outflow frame, T_o, is given by

$$T = \delta T_o, \tag{3.3}$$

and the observed blackbody flux from a surface element, F_ν, is given by

$$F_\nu = \frac{2\pi h\nu^3\delta^3}{c^2}\frac{1}{e^{\frac{h\nu}{k\delta T_o}} - 1}\frac{A}{D^2}, \tag{3.4}$$

where A is the projected area of the emitter, and D is the distance between the emitter and the observer.

My spherical outflowing blackbody model is composed by splitting the emitting surface in to ten components according to the angle, θ, with a corresponding line of sight velocity, $v = v_0\cos\theta$, where v_0 is the outflow velocity. In the simple single blackbody model, the outflow is observed with a projected area of $A = \pi R^2$, with radius R. In the spherical outflow model, this area is divided into ten ring components.

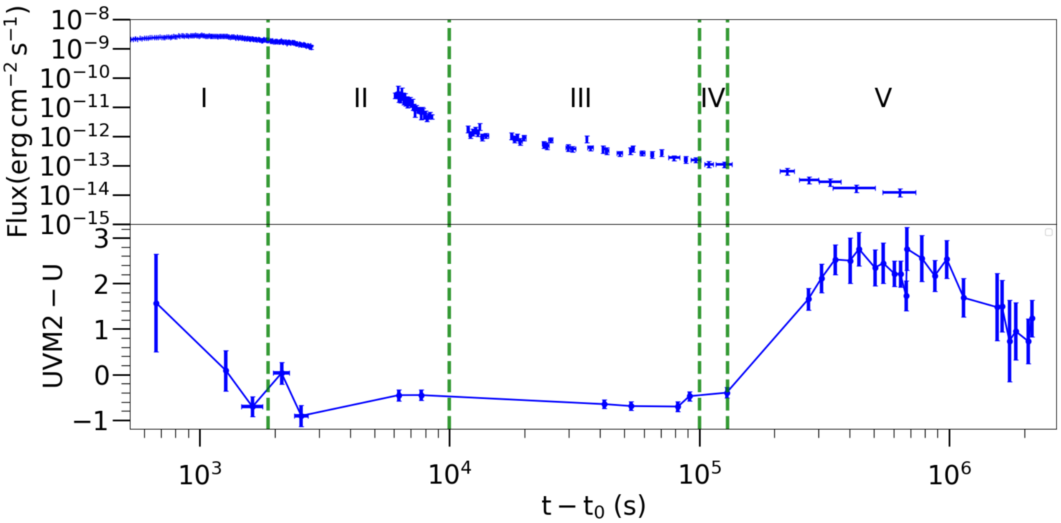

Figure 3.2: The figure shows in the top panel the X-ray light curve of GRB 060218 and in the bottom panel, the colour $UVM2-U$ of GRB 060218 from 650 s to 2000 ks. The plot is separated by four times to form five phases.

3.3 Results

Using the observations of GRB 060218 and SN 2006aj taken in the first few days, I can use the colour $(UVM2-U)$ and the X-ray light curve to help separate the observations into five different phases of evolution. Splitting the light curve into phases is useful because the spectral shape across the UV/optical and X-ray energy range changes substantially from the time of the GRB trigger until the Ni^{56}-decay-powered emission becomes the dominant source of emission in the optical energy range. The colour $(UVM2-U)$ is used because it provides a good indication of the balance of UV vs. optical radiation, which changes considerably over the course of the observations.

The X-ray light curve and colour $(UVM2-U)$ are shown in Fig. 3.2. Phase I represents the period between the start of the UVOT and XRT observations at 159 s and the time when the UV/optical power-law component is no longer detected at 1350 s. The spectral change that characterises Phase I is also clear in the spectral index calculations, β_{UV}, shown in Table. 3.4 and Fig. 3.5. Phase II is the time when the colour $(UVM2-U)$ is consistent with a constant value $(UVM2-U)\sim-0.5$ and the thermal blackbody emission is visible at UV/optical and X-ray energies. The constant $(UVM2-U)$ colour is

Table 3.2: Summary of emission components used to model the SEDs in each phase. In phase III, the temperature and radius of the outflowing blackbody cannot be determined because it peaks between the UV/optical and X-ray energies. Therefore I have used simply a power law of $\beta_{UV} = -2$ to represent the Rayleigh-Jeans tail in the UV/optical. In phase IV, the outflowing blackbody has no contribution in the X-ray spectra. No fits were done in phase V.

Phase	Time (s)	Emission components
I	$159-1350$	power law (UV/optical only) power law (X-ray only) outflowing blackbody
II	$1350-10000$	power law (X-ray only) outflowing blackbody
III	$10000-100000$	power law (X-ray only) Rayleigh-Jeans tail (UV/optical only)
IV	$100000-130000$	power law (X-ray only) outflowing blackbody

expected when the UV/optical emission is dominated by the Rayleigh-Jeans tail of a blackbody.

The line at 10 ks, shown in Fig. 3.2, marks the end of the X-ray blackbody emission, and so the end of this phase. During phase III the X-ray emission has a power-law spectrum without any observed contribution from a thermal component. During phase IV the $(UVM2-U)$ colour changes as the blackbody cools sufficiently to peak in the UV. During Phase V the Ni^{56}-decay-powered emission from SN 2006aj becomes dominant at optical wavebands leading to a much redder colour in $(UVM2-U)$. The red colour is because of line blanketing from iron-peak elements in the UV spectra, as seen for example in the HST UV spectra of SN 1994I in Millard et al. (1999).

Table. 3.2 summarises the components which I used to model the SEDs for each phase.

3.3.1 Determination of the host galaxy reddening

Before I examine the evolution of the SED, it is useful to determine the optical reddening due to dust in the host galaxy of the GRB. Previous works have argued that the UV/optical emission for times < 50 ks is dominated by the

Rayleigh-Jeans tail of the blackbody-like emission component (Campana et al., 2006; Waxman et al., 2007; Ghisellini et al., 2007a). During this period I can determine the reddening rather precisely because the underlying spectrum has a well understood spectral shape: a power law with spectral index, $\beta_{UV} = -2$.

In the interval $5-60$ ks I fitted second order polynomials simultaneously to the light curves in the different UVOT filters. The polynomials were constrained to have the same shape (first and second order coefficient) but different offsets in the different bands, which allowed us to get the differences in magnitudes for each filter precisely while the colour was constant. The best fit set of parabolae is shown in Fig. 3.3. I created a SED at 40 ks, using the fitted magnitudes from my simultaneous fitting.

When modelling the SED the best extinction curve $k(\lambda)$ can be determined, and reddening values $E(B-V)R_v$ from fitting, by fixing the known spectral index at $\beta_{UV} = -2$, because I assume that the UV/optical spectra have a Rayleigh-Jeans shape. I found that the Small Magellanic Cloud (SMC) and Large Magellanic Cloud (LMC) extinction curves produced acceptable fits with χ^2/dof= 3.9/4 and χ^2/dof= 6.9/4, respectively. However, the Milky Way (MW) extinction curve can be excluded based on the χ^2, where I found χ^2/dof= 42.2/4 corresponding to a null-hypothesis probability $p = 1.6 \times 10^{-8}$. The SMC extinction curve provided the best fit and for this curve I obtained $E(B-V) = 0.179 \pm 0.007$ mag. The details of the fits for each extinction curve are given in Table. 3.3. Based on the result that minimises the χ^2, I use an SMC extinction curve and $E(B-V) = 0.179$ to fit the host-galaxy extinction for all of my SEDs.

3.3.2 The early time UV/optical emission

The evolution of the $(UVM2-U)$ colour, evident in Fig. 3.2, at early times, suggests that the spectral slope in the UV/optical changes during phase I. This spectral change is confirmed by fitting an absorbed power-law model across the UV/optical energies in my SEDs. The parameters of the fits are shown in Table. 3.4 together with the χ^2/dof values for the fits and the associated

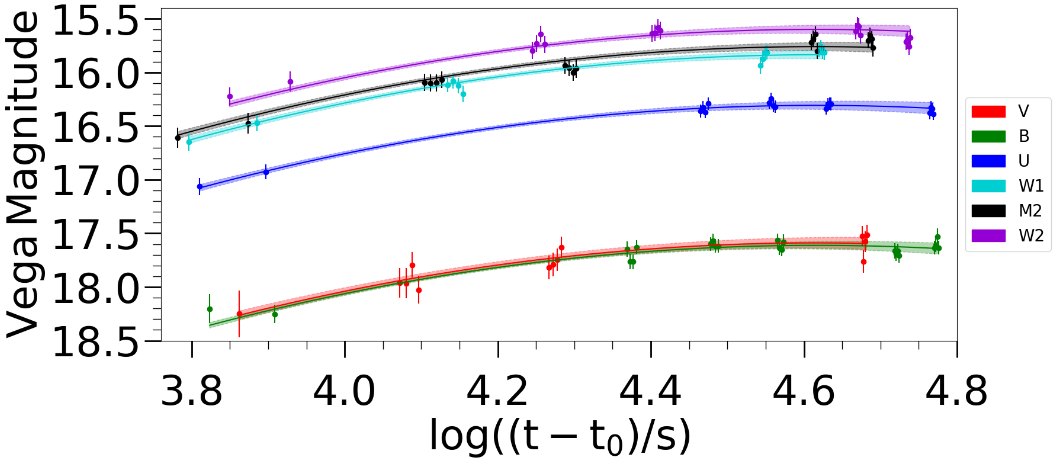

Figure 3.3: Light curves for GRB 060218 in the time range 5 − 60 ks. The six different colours represent the different UVOT filters. The best-fit parabolic model light curves for each filter are shown as coloured lines, with associated 1 σ errors in the shaded regions.

Table 3.3: Host galaxy extinction curve comparison. R_V is the extinction A_V divided by the colour excess $E(B-V)$. χ^2/dof is the best fit chi-square/degrees of freedom and p is the corresponding null hypothesis probability.

Extinction curve shape	R_v	$E(B-V)$ (mag)	χ^2/ν	p
SMC	2.93	0.179 ± 0.007	3.9/4	0.41
LMC	3.16	0.197 ± 0.008	6.9/4	0.14
MW	3.08	0.215 ± 0.009	42.2/4	1.6×10^{-8}

p values. All of the p values are above 0.01, and hence I consider all of the fits to be acceptable. Fig. 3.4 shows how the spectral shape changes between 650 s and 1625 s across the UV/optical energy range. Superimposed on the SEDs in Fig. 3.4 are the best fit power-law models for each epoch, shown in red. Additionally, the model with a fixed Rayleigh-Jeans power-law index, $\beta_{UV} = -2$, is shown in blue. At 650 s the data are best modelled with fitted spectral index $\beta_{UV} = 0.20^{+0.58}_{-0.63}$ and this value for the spectral index is consistent with the typical GRB afterglow spectral index, $\langle\beta_{UV}\rangle = 0.66 \pm 0.04$, (Kann et al., 2010; Schady et al., 2012). The UV/optical spectral shape evolves after 650 s and by 1625 s the UV/optical SED is consistent with a Rayleigh-Jeans slope.

Fig. 3.5 shows the fitted spectral index β_{UV} as a function of time. I have

Table 3.4: Summary of the UVOT time-resolved SED fits for GRB 060218. Here I show the best fit chi-square, χ^2, when comparing the fit of the spectral index, β_{UV} (4 dof), to the fixed Rayleigh-jeans spectral shape, $\beta_{UV} = -2$ (5 dof). p is the corresponding null hypothesis probability.

Time	β_{UV} fitted			β_{UV} fixed at -2	
(s)	β_{UV}	χ^2	p	χ^2	p
650	0.2 ± 0.6	2.37	0.67	15.3	9.3e-3
1250	-0.5 ± 0.3	11.60	0.02	25.7	1.0e-4
1625	-1.8 ± 0.3	4.37	0.36	4.6	0.47
2125	-1.4 ± 0.3	2.92	0.57	7.2	0.21
2550	-1.8 ± 0.3	4.11	0.39	4.5	0.48
6500	-2.0 ± 0.1	7.75	0.10	7.8	0.17
7500	-2.0 ± 0.1	8.21	0.08	8.2	0.14

explicitly tested whether a single value of β_{UV} could fit all of the UV/optical SEDs by fitting a constant value to the power-law spectral indices. This fit results in a large chi-squared, $\chi^2 = 38.7$ for 6 degrees of freedom with an associated null hypothesis probability, $p = 8.2e-7$. Therefore I can reject the hypothesis that the UV/optical emission can be characterised by a constant power-law spectral index.

I have also tested the consistency of each UV/optical SED with a Rayleigh-Jeans shape, which is equivalent to a power law with β_{UV} fixed at -2, by fitting such a model to each UV/optical SED. Table 3.4 includes χ^2 and associated null hypothesis probabilities for these fits. This model does not fit well ($p < 0.01$) for times < 1350 s, but is an acceptable fit at later times. Therefore a second component, in addition to the Rayleigh-Jeans emission is needed to describe the UV/optical emission before 1350 s.

3.3.3 Fitting the full optical to X-ray SED

When analysing the X-ray and UV/optical emission, I fitted my SEDs with different models depending on the SED epoch. I took this approach because the UV/optical power-law component is not detected after phase I and also, the thermal emission component only contributes to the total X-ray radiation in the initial 10 ks. The combination of components I used in my models for the different SED epochs are shown in Table. 3.2.

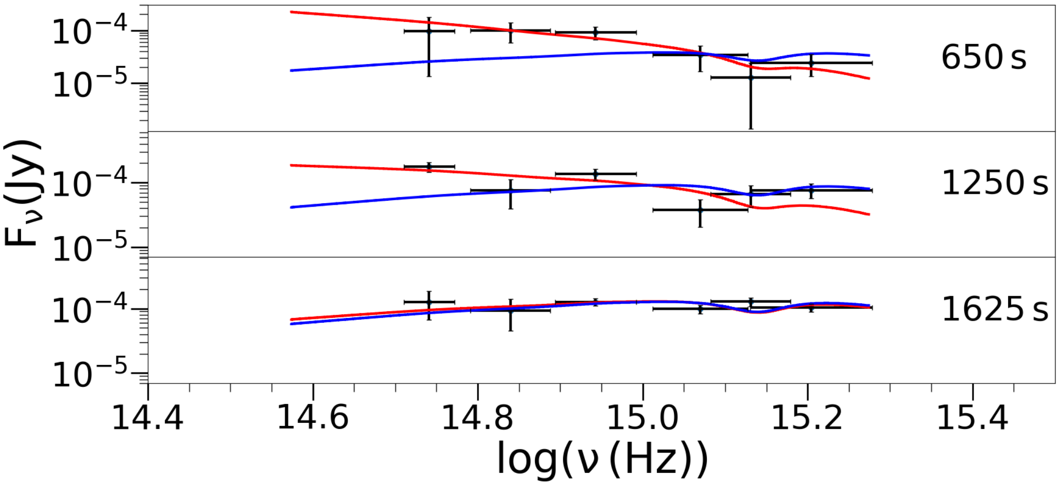

Figure 3.4: The SEDs of GRB 060218 at 650 s, 1250 s and 1625 s. Each SED is fitted with a power-law model, with Galactic reddening $E(B-V) = 0.14$ and host galaxy reddening $E(B-V) = 0.179$. The red line represents the fitted power-law whose results are shown in Table. 3.2.2, and the blue line is the Rayleigh-Jeans power-law model with β_{UV} fixed at -2.

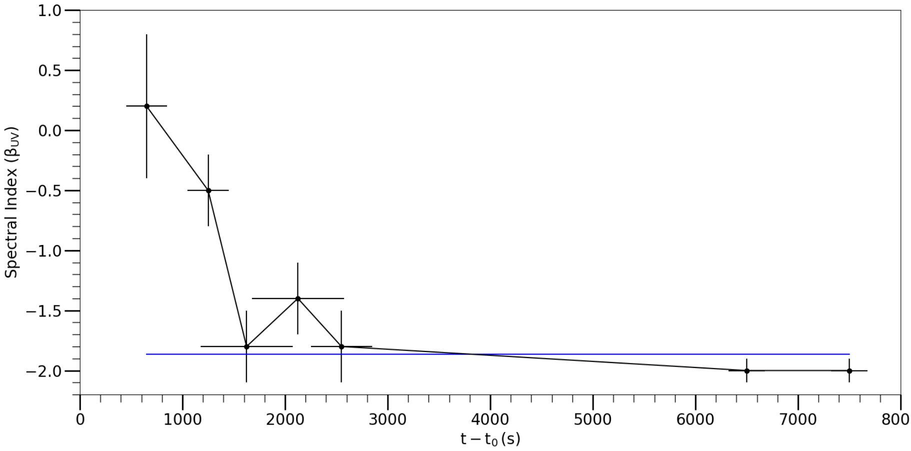

Figure 3.5: The best-fitting spectral indices, β_{UV}, to the UV/optical SEDs, from Table. 3.4. The blue horizontal line shows an attempt to fit the values of β_{UV} with a constant (see Section 3.3.2).

For the phases which include the outflowing blackbody emission, I employ a spherically outflowing blackbody model as detailed in Sec. 3.2.4.1. The model is initially fitted with the velocity of the outflow set to zero to simplify the baseline estimation of the blackbody emission radius over time. This setting serves as the foundation for subsequent iterative refinements. Unlike typical freely adjustable parameters, the outflow velocity is derived from the rate of change in the radius, calculated by fitting a functional form to the radius-time data. This derived velocity is then used to adjust the model parameters iteratively. The refinement process involves recalculating the velocity and refitting the model until the changes in the chi-squared values of successive fits fall below a statistically significant threshold, indicating that the model fitting has stabilised. Both the initial model with zero velocity and the iteratively refined model are depicted in Fig. 3.6.

For all SED fitting the host-galaxy UV/optical reddening was fixed to the value discussed earlier, $E(B-V) = 0.179$. However, the host-galaxy X-ray absorption was left as a free parameter, because I have no prior knowledge of this.

When modelling the spherically outflowing blackbody model during phase I to my SEDs, I included a power-law component across the UV/optical energies, because there is a substantial power-law component during this time, as seen in Fig. 3.4. At 650 s and 1250 s I measured the flux of the power-law component in the UV/optical as $\nu F_\nu(10^{15}\,\mathrm{Hz}) = (6 \pm 2)$ and $(7 \pm 2) \times 10^{-13}\,\mathrm{erg\,cm^{-2}\,s^{-1}}$, contributing 99.5% and 82% to the total flux respectively.

Fitting my SEDs with my spherically outflowing blackbody model allows us to see the evolution of the blackbody (photospheric) radius over time. When modelling the radius, neither a linear model nor a power-law model provided acceptable fits to the measurements, and so a power-law plus constant model was used; this model is represented by the black line in Fig. 3.6. The best-fit parameters from my model are shown in Eq. 3.5,

$$R_{BB} = \Big((233 \pm 6) + (1.0 \pm 0.1)(t - t_0)^{0.68 \pm 0.01}\Big) \times 10^{11}\,\mathrm{cm} \qquad (3.5)$$

where the radius can be expressed as $R_{BB} = R_0 + A(t - t_0)^B$. which gives the inferred blackbody radius in terms of the initial radius, R_0, and the time since the event was triggered, $t - t_0$. In this equation, A and B are free parameters determined in fitting. The value that I calculate, $R_0 = (2.33 \pm 0.06) \times 10^{13}$ cm, represents the radius at which the blackbody radiation is first released.

The power-law plus constant model was not fitted to the data at 650 s and 1250 s because there is a large contribution to the X-ray flux from the prompt emission and a large contribution to the UV/optical flux from the afterglow component. As a consequence, I do not consider the constraints on the radius to be very reliable at these times. Furthermore, during the initial 800 s light travel time affects the observed blackbody emission. At 650 s I observe 85 percent of the blackbody surface area emitted at an initial radius $R_0 = (2.33 \pm 0.06) \times 10^{13}$ cm. The effect would be more pronounced if the expansion is non-spherical. This could be the case in the early evolution of the outflow if a jet along the line-of-sight induces an aspherical outflow.

The results from the model fits to the SEDs are shown in Table. 3.5. The measurements and model of the outflowing blackbody radius against time are displayed in Fig. 3.6. The full SEDs with the best-fitting models and the data/model ratios are shown in 3.7.

3.4 Discussion

In this paper, I have given detailed analysis of the early UV/optical and X-ray emission from GRB 060218. There is a substantial change in the spectral shape of the early UV/optical emission, with the spectral index of the fitted power-law changing by $\Delta\beta_{UV} = 2.2 \pm 0.6$. At 650 s after the GRB trigger, the spectral index across the UV/optical energies, β_{UV}, calculated from the SED power-law fit is $\beta_{UV} = 0.20^{+0.58}_{-0.62}$. The spectral index calculated from the UVOT SED

Table 3.5: Summary of results for SED fits of GRB 060218 modelled with a spherical outflowing blackbody component. N_H denotes the hydrogen column density. In the context of the fitted blackbody component, kT represents the product of the Boltzmann constant and the temperature, while R corresponds to its radius. β_X is the spectral index from the power-law component from the fitted model across the X-ray energy range, and β_{UV} is the spectral index from the power-law component from the fitted model across the UV/optical energy range. v/c is the converged value of the velocity/c for the spherically outflowing blackbody. χ^2/dof is the best fit chi-square/degrees of freedom. For the SED at 120 ks the fitted model included a blackbody component over the UV/optical energies.

Time (s)	N_H $(10^{-22}\,\mathrm{cm}^{-2})$	kT (eV)	Blackbody radius R $(10^{13}\,\mathrm{cm})$	β_X	β_{UV}	(v/c)	χ^2/dof
650	0.58 ± 0.04	117 ± 14	0.16 ± 0.07	0.42 ± 0.03	0.21 ± 0.63	0.292	311.3/327
1250	0.94 ± 0.04	84.7 ± 6.0	1.40 ± 0.50	1.00 ± 0.03	-0.17 ± 0.43	0.237	381.4/326
1625	1.09 ± 0.01	73.9 ± 0.6	3.94 ± 0.12	1.38 ± 0.01	–	0.218	637.4/529
2125	1.08 ± 0.01	74.4 ± 0.3	4.20 ± 0.13	1.67 ± 0.02	–	0.199	500.3/456
2550	1.09 ± 0.01	74.2 ± 0.5	4.39 ± 0.17	1.86 ± 0.03	–	0.189	431.9/323
6500	1.28 ± 0.02	56.2 ± 0.8	6.34 ± 0.01	2.61 ± 0.19	–	0.140	32.7/25
7500	1.55 ± 0.03	52.4 ± 1.0	7.25 ± 0.09	2.70 ± 0.25	–	0.134	19.2/17
120000	0.52 ± 0.07	3.9 ± 0.4	31.5 ± 3.7	3.33 ± 0.35	–	0.056	42.6/26

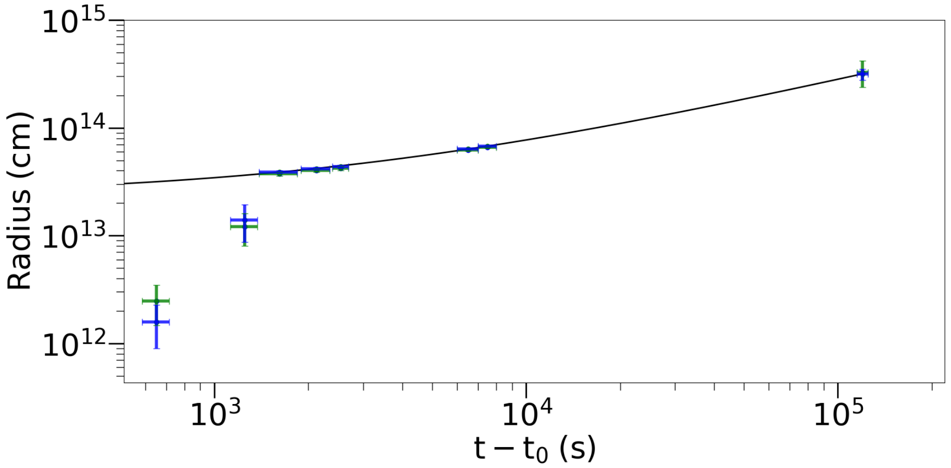

Figure 3.6: The radius against time, determined from fitting UV/optical/X-ray SEDs with a spherically outflowing blackbody component plus power-law model. The photospheric radii are shown with one sigma errors in blue. The fitted photospheric radii using a stationary blackbody model are shown in green. The power-law plus constant model fit to the photospheric radii (Eq. 3.5) is shown as a black line.

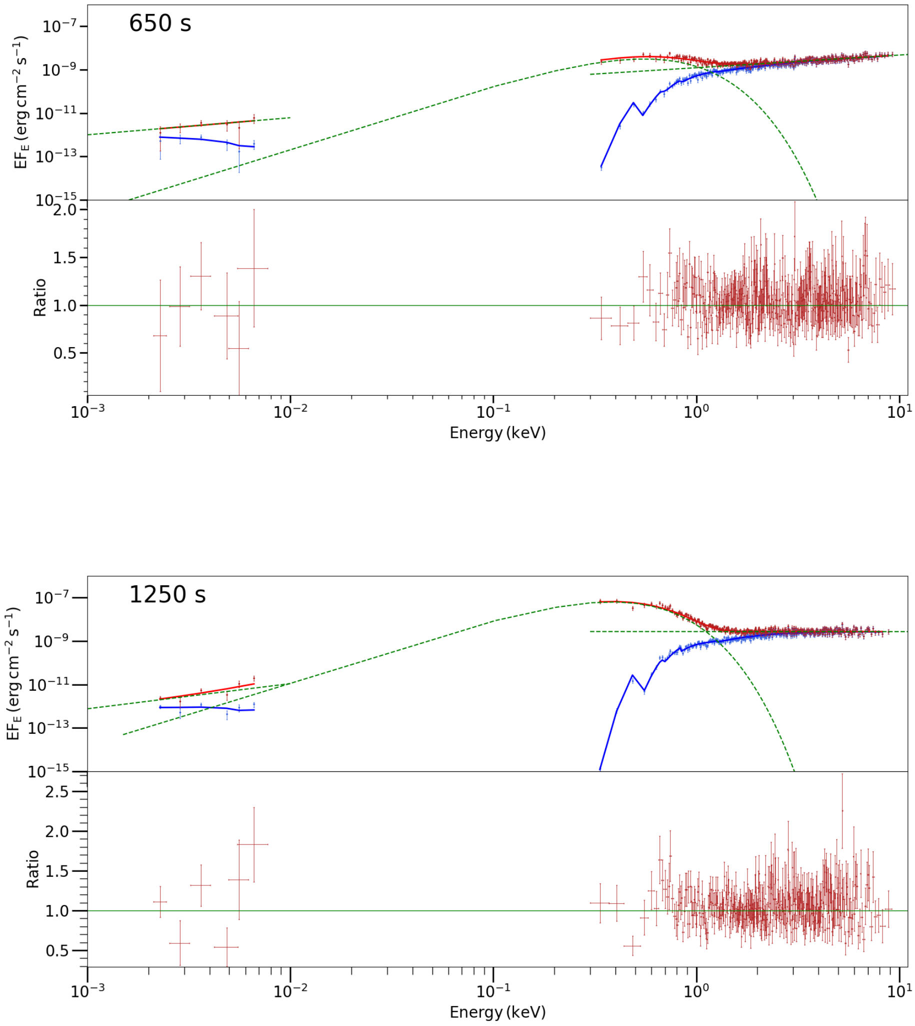

Figure 3.7: The SEDs of GRB 060218 for all of the times shown in Table. 3.1. The SEDs are shown across the UV/optical and X-ray energies (0.0015–10 keV). The models used in the fitting are listed in Table. 3.2. The flux is displayed as EF_E. The red data points represent the dereddened UV/optical and unabsorbed X-ray flux. The blue data points represent the UV/optical and X-ray flux including absorption as measured by UVOT and XRT. The dashed lines represent the model components. The bottom panel of the figure shows the ratio of the data to overall model.

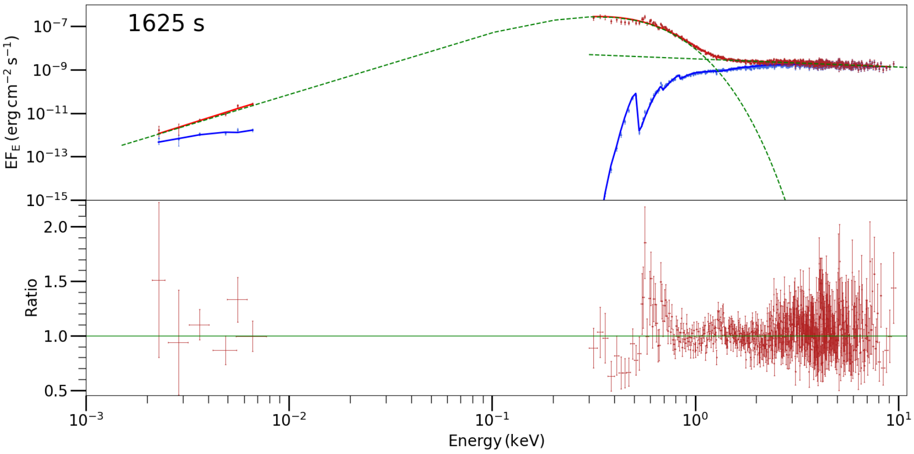

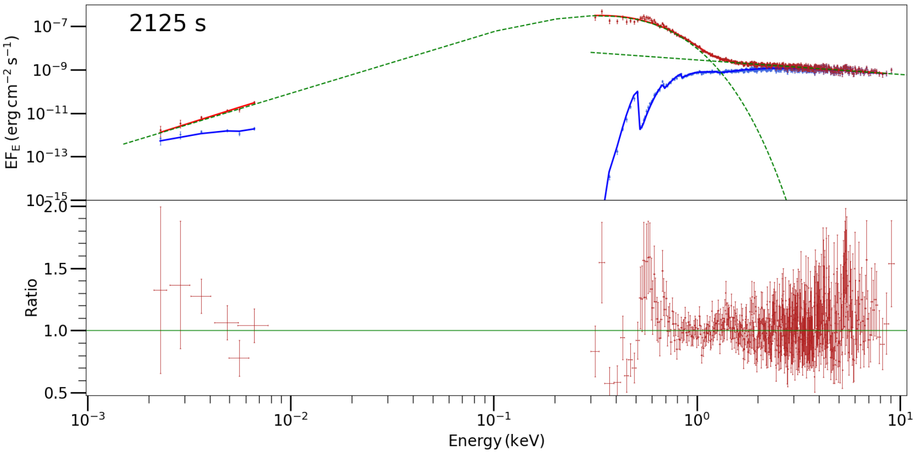

Figure 3.7: caption (continued)

power-law fit measured for different times shows an evolution in the spectral index, which quickly converges to a constant value of β_{UV}.

The UV/optical and X-ray emission can be characterised by a spherically outflowing blackbody plus power-law model for the times 1350–10000 s. During this period the power-law model is fit only over the X-ray energy range in my SEDs.

In the initial 1350 s the UV/optical power-law component has a higher contribution to the overall flux in the UV/optical than the blackbody component. For times after 1350 s, the thermal component in the UV/optical and

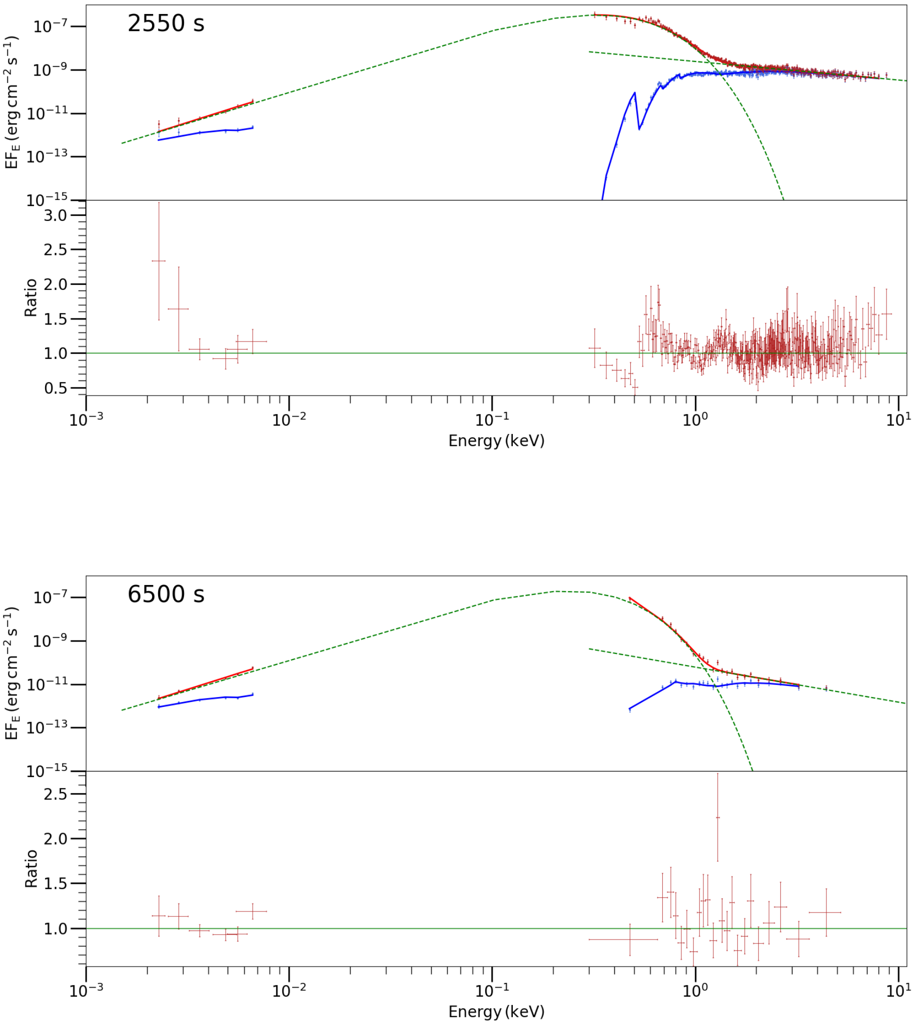

Figure 3.7: caption (continued)

X-ray spectra is the dominant source of the observed luminosity. After 10 ks there is no longer an observed thermal component in the X-ray spectrum.

At 120 ks, the blackbody cools sufficiently to peak in the UV, and I measure the UV blackbody temperature. After 130 ks the UV/optical flux is predominantly produced by the Ni^{56}-decay-powered emission, and the X-ray spectrum is still characterised by a soft power-law.

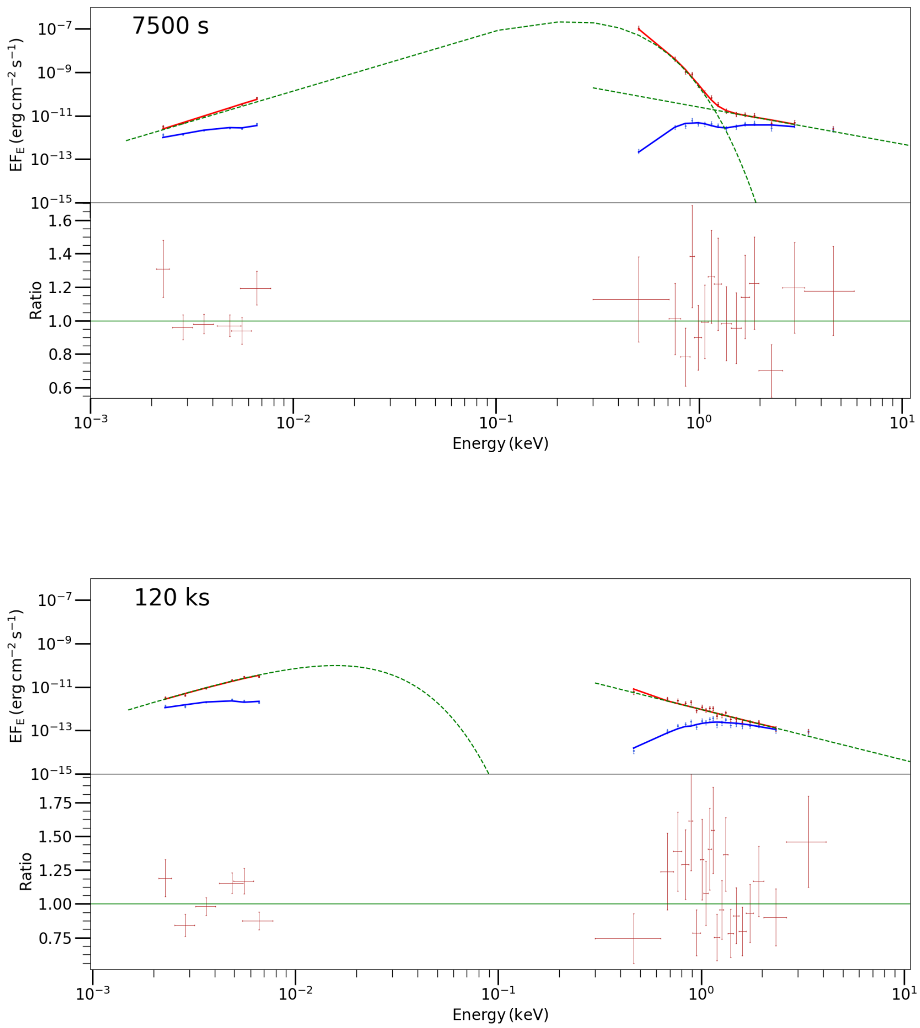

Figure 3.7: caption (continued)

3.4.1 Origin of UV/optical emission before the SN peak

I measured the UV/optical spectral index at 650 s as $\beta_{UV} = 0.20^{+0.58}_{-0.62}$. Within one sigma, this spectral index is consistent with the mean value of GRB afterglow spectral indices as calculated by Kann et al. (2010); Schady et al. (2012), $\langle\beta_{UV}\rangle = 0.66 \pm 0.04$. Similar to typical GRB afterglows, the emission mechanism that produces the spectral slope at 650 s is likely to be synchrotron emission. Typically the synchrotron spectrum extends from the UV/optical to X-ray. However, this cannot be tested in GRB 060218 because the prompt emission still dominates the X-ray at early times (Toma et al., 2007). If the power-law model, which best fits the UV/optical data at 650s, is extrapolated to the X-ray band, it represents only one fifth of the observed X-ray flux. Therefore the early UV/optical spectra are consistent with the UV/optical emission being the afterglow, where the emission is produced by the interaction of a jet with the circumburst medium. At the date of writing, this is the first observation of an UV/optical afterglow in a low-luminosity GRB.

The observations at times $1350 - 60000$ s suggest that the UV/optical emission is dominated by emission from the Rayleigh-Jeans part of a blackbody spectrum. At 120 ks the peak of the blackbody emission has moved into the UV/optical, with $kT = 3.9 \pm 0.5$ eV at an inferred blackbody radius, $R = (3.2 \pm 0.4) \times 10^{14}$ cm. The observations of the blackbody peaking in the UV/optical are in agreement with the expanding shock-heated wind model proposed in Waxman et al. (2007); Nakar (2015); Irwin and Chevalier (2016). However, the expanding shock-heated wind model cannot explain the spectral shape before 1350 s. Therefore there is two contributions to the total observed UV/optical flux: the synchrotron component, and the blackbody component; both components are observed simultaneously. It is for this reason that I argue that the non-thermal UV/optical emission is observed outside the optically thick expanding shock-heated wind. The characteristics of the non-thermal UV/optical emission are comparable to typical GRB afterglows; therefore, I propose that the non-thermal UV/optical emission is generated from the external shocks as the jet is slowed by the surrounding ISM.

Ghisellini et al. (2007a) interpret the UV/optical emission for times $<$ 100 ks, as being produced through self-absorbed synchrotron emission. For this model, Ghisellini et al. (2007a) require the UV/optical spectrum to be $\propto \nu^{2.5}$. They can accommodate this value by using a value of the reddening, $E(B-V) = 0.3$ mag, 0.12 greater than the value I derived from the techniques discussed in Sec. 3.3, where I argue that the UV/optical is on the Rayleigh-jeans tail of the blackbody that is peaking in X-ray energies. However, the model used in Ghisellini et al. (2007a) only addresses the UV/optical emission during the initial 100 ks and does not account for the UV/optical spectral shape changing to resemble a blackbody that peaks in the UV/optical energy range at 120 ks. Additionally, the model used in Ghisellini et al. (2007a) does not account naturally for the blackbody component in the X-ray emission, and they argue that this requires an additional component to explain the thermal X-ray emission. However, I have shown that the thermal X-ray emission can be emitted simultaneously from the same radius as the UV/optical blackbody emission. Therefore, my model addresses areas that Ghisellini et al. (2007a) did not, providing a more holistic explanation of the non-thermal and thermal components of the UV/optical emission.

3.4.2 Existence of a jet?

As described in Section 3.4.1, the observations of the non-thermal UV/optical emission in the initial 1350 s suggest that the early UV/optical emission is synchrotron radiation. The synchrotron emission is likely due to the interaction of the GRB outflow with the circumburst region, which is predicted in the external shock model (Mészáros and Rees, 1997). Furthermore, Toma et al. (2007) analysed the X-ray -Gamma-ray SED from BAT and XRT and showed that the non-thermal emission in the prompt phase of the GRB can be modelled well with a band function (Band et al., 1993). The low and high energy indices, from this model, are consistent with typical values of typical GRBs (Toma et al., 2007) where the emission is thought to be from a jet outflow. Therefore both the prompt emission spectral characteristics and the presence of non-thermal emission in the UV/optical at early times point towards a scenario in which the jet has penetrated the optically thick envelope.

There are predominantly two models that attempt to reconcile the radio observations of GRB 060218. The first is put forward by Soderberg et al. (2006b), who argue that the observed radio afterglow requires a mildly relativistic ($\Gamma \gtrsim 2$) outflow interacting with the surrounding medium. Soderberg et al. (2006b) and Fan et al. (2006) suggest that this could be an effectively spherical, wide outflow with $\theta_j \gtrsim 1$ rad, due to the lack of jet break in the radio observations up to 22 days. In order to model the radio light curves, Soderberg et al. (2006b) require an isotropic kinetic energy, $E_{k,iso} \sim 10^{48}$ erg, circumburst density, $n \sim 10^{2}\text{cm}^{-3}$, and the ratios of the electron and magnetic field energy density to the total thermal energy, $\varepsilon_e \sim 10^{-1}$ and $\varepsilon_B \sim 10^{-1}$, respectively. However the gamma-ray efficiency is too high, $\eta_\gamma = \frac{E_{iso,\gamma}}{E_{iso,\gamma}+E_{k,iso}} =\sim 98\%$.

An alternative model that helps resolve the gamma-ray efficiency problem was offered by Toma et al. (2007), where the radio emission is produced by the external shock synchrotron model, which requires a jet with an initial Lorentz factor, $\Gamma_0 = 5$, where Γ_0 is the initial Lorentz factor of the jet just as it exits the star (Toma et al., 2007). In this model, the radio emission is produced in the non-relativistic phase of the outflow and requires an opening angle of $\theta_0 = 0.3\,\text{rad}$ (Toma et al., 2007), which is smaller than the opening angle required in the models proposed by Soderberg et al. (2006b) and Fan et al. (2006). The opening angle was required by Toma et al. (2007) to obtain a reasonable γ-ray efficiency and also to satisfy a condition that was needed for the jet to penetrate the stellar envelope. Toma et al. (2007) remark that the jet could initially be collimated, to penetrate the progenitor envelope, like in the standard collapsar model (Woosley, 1993b; MacFadyen and Woosley, 1999a). They explain that the radio emission is observed at a period where the initially collimated jet moves towards a spherical geometry.

At 650 s and 1250 s the UV/optical fluxes of the power-law component are measured to be $\nu F_\nu(10^{15}\,\text{Hz}) = (6 \pm 2)$ and $(7 \pm 2) \times 10^{-13}\,\text{erg}\,\text{cm}^{-2}\,\text{s}^{-1}$, respectively. These are comparable to the predicted synchrotron flux in the jet model of Toma et al. (2007); see Fig. 3 in Toma et al. (2007). The values calculated in Toma et al. (2007) for the UV/optical flux are $\nu F_\nu(10^{15}\,\text{Hz}) \approx 3$ and $\approx 7 \times 10^{-13}\,\text{erg}\,\text{cm}^{-2}\,\text{s}^{-1}$ for 650 s and 1250 s, respectively. Therefore my observations of the UV/optical emission in the first 1350 s agree well with the jet model discussed in Toma et al. (2007) and this further strengthens the reasoning for a jet model to explain the observations from GRB 060218.

The presence of a jet, required to explain the UV/optical synchrotron emission, could induce some asphericity into the envelope. This reasoning for asphericity has been argued for both GRB/SN 1998bw (Maeda et al., 2002) and SN 2003jd (Mazzali et al., 2005). Aspherical expansion of the SN is favoured by Gorosabel et al. (2006), from the detection of linear polarisation in SN 2006aj. Linear polarisation in SNe has previously been linked with the non-spherical expansion of Type Ic SNe (Hoflich, 1991). Furthermore, the detection of the linear polarisation supports the jet model. Although I have shown that the observations do not disagree with a spherical model, a link between asphericity and SNe connected with GRBs has been seen in some studies (Maeda et al., 2002; Mazzali et al., 2001).

Conversely to a jet model to explain the observed emission from GRB 060218, Nakar (2015) argue that GRB 060218 and all other LLGRBs are produced from the shock breakout of a low-mass extended envelope that has choked the jet. Therefore within their model, no emission from the jet or the interaction of the jet outside the extended envelope can be observed. However, this choked jet scenario is incompatible with my data, because it does not explain the synchrotron component seen in the UV/optical spectra before 1350 s. Also, the scenario does not address the blackbody component in the X-ray spectra at early times, before the breakout timescale argued by Nakar (2015), $t_{BO} \sim 1000\,\mathrm{s}$.

3.4.3 Host galaxy reddening

The best estimate of the host-galaxy reddening, an SMC extinction law and $E(B-V) = 0.179 \pm 0.007$ mag, was obtained by assuming that the underlying UV/optical continuum has a Rayleigh-Jeans shape at all times between 5 ks and 60 ks after the GRB trigger. The reddening estimates used by Campana et al. (2006) and Waxman et al. (2007) were also based on the assumption of an underlying Rayleigh-Jeans shape, though with a less developed fitting procedure, and using the UV/optical SED from only one epoch (32 ks). They obtained $E(B-V) = 0.20 \pm 0.03$ mag for an SMC extinction law, consistent with, but less precise than, the value I have obtained. The SMC extinction curve, which is favoured by my fits to GRB 060218, is usually found to be the best fit in GRB host galaxies (Schady et al., 2010). As with the majority of GRB host galaxies, the host galaxy of GRB 060218 also has a low metallicity, in this specific case $12+\log(\mathrm{O/H}) \sim 0.07\,\mathrm{Z}_\odot$ (Wiersema et al., 2007).

Two alternative approaches to estimating the host-galaxy reddening towards GRB060218, which do not require any assumption about the underlying continuum shape, can be found in the literature: the equivalent width (EW) of the interstellar NaI D (5895.9 Å) absorption line and the linear polarisation. A measurement of the NaI D absorption lines is reported in Guenther et al. (2006), and is translated to an estimate of $E(B-V) = 0.04$ mag using the empirical relation between NaI D EW and $E(B-V)$ derived by Munari and Zwitter (1997) from observations of hot stars in the Milky Way. This reddening estimate is adopted in the works of Sollerman et al. (2006) and Pian et al. (2006). Munari and Zwitter (1997) suggest an uncertainty of 0.05 magnitudes for $E(B-V)$ derived in this way, suggesting a host-galaxy reddening somewhat lower than my measurement, but it is not known whether the relation found by Munari and Zwitter (1997) is applicable for the lower-metallicity, perhaps higher-ionisation interstellar medium (ISM) of the dwarf-galaxy host of GRB 060218. Gorosabel et al. (2006) observed a stable linear polarisation of 1.4 ± 0.1 per cent in SN 2006aj at 13 and 19 days after GRB 060218, and suggested that the host galaxy ISM may be responsible for the polarisation. Gorosabel et al. (2006) used this measurement together with the empirical relation obtained by Serkowski et al. (1975) relating polarisation to reddening in the Milky Way, $P \leq 9E(B-V)$. The implied host galaxy reddening is $E(B-V) \geq 0.15$ mag. This value is somewhat higher than the estimate based on NaI D, and is consistent with my measurement of the host galaxy reddening. However, I note a similar caveat as for the NaI D measurement: it is not known to what degree the relation found by Serkowski et al. (1975) is applicable for the dust species in the lower-metallicity ISM of the dwarf-galaxy host of GRB 060218. Given their inherent uncertainties, I consider that the NaI D and polarisation-based estimates of the host reddening are compatible with my measurement of $E(B-V) = 0.179 \pm 0.007$ mag.

3.4.4 The blackbody emission component(s) and the geometry of the emission

I have shown that an outflowing blackbody component contributes to the SED at optical, UV and X-ray energies. The outflowing blackbody emission peaking at X-ray energies before 10 ks. The concurrent observation of the Rayleigh-Jeans spectral shape in the UV/optical suggests that the same blackbody component is present in both energy ranges. In contrast, to explain the thermal emission observed in the X-ray and UV/optical, Waxman et al. (2007) require that the thermal component in the UV/optical arises from a separate region to that of the thermal component in the X-ray. In their model, the thermal X-ray emission is produced from a compressed wind shell, while the thermal UV/optical emission is produced at a lower temperature in the outer shells of the progenitor star. Thus in the model of Waxman et al. (2007) the X-ray emission originates further from the progenitor star than the UV/optical emission. However, for a blackbody of lower temperature to dominate the emission of a higher temperature blackbody, it must have a larger surface area, and therefore one would expect it to arise at a greater, rather than smaller radius around the progenitor star. I cannot envisage a geometrical configuration in which a region of lower temperature, and at a significantly smaller distance from the progenitor star, than that giving rise to the blackbody emission observed in the X-ray, could produce emission that would dominate in the UV/optical. Therefore I consider my spectral model, in which the UV/optical and thermal X-ray emission are produced by the same blackbody component, to be more compelling than the two-component description advocated by Waxman et al. (2007).

Ghisellini et al. (2007b) investigated the possibility that the UV/optical and X-ray radiation belonged to a single blackbody. They used the photospheric radius model in Waxman et al. (2007) to get a temporal relation for the radius.

$$R = R_0 + 3.6 \times 10^{10}(t - t_0)^{0.80}\,\mathrm{cm}. \tag{3.6}$$

They assumed that the UV/optical emission before 120 ks corresponds to the Rayleigh-jeans part of the blackbody spectrum and used the observed UV/optical fluxes to determine the blackbody luminosity. They then estimated the associated energy emitted by the blackbody at each step of their UV/optical lightcurve using $L\Delta t$, where Δt was the time period for the UV/optical flux measurement. Ghisellini et al. (2007b) argued that the energy emitted by the blackbody was too large ($E_{BB} \sim 10^{51}$ ergs) to be viable when compared to the total kinetic energy of the SN explosion, $E_{SN,K} \sim 2 \times 10^{51}$ ergs (Mazzali et al., 2006).

I find that the blackbody energy is smaller at early times (< 1350 s) than Ghisellini et al. (2007b), because I have found that the UV/optical emission is dominated by a synchrotron component at these times. I have made my own estimate of the energy emitted by the blackbody by integrating the luminosity of the blackbody model component with respect to time. I find that during the initial 650–2700 s the integrated luminosity of the blackbody is $E = 1.1 \times 10^{51}$ ergs. Thus my spectral modelling leads to a similar energetic requirement to that raised by Ghisellini et al. (2007b). The large amount of energy radiated by the blackbody would suggest a more energetic supernova than that inferred by Mazzali et al. (2006), for example $E_{SN,K} = 10^{52}$ ergs as found by Cano (2013), which is more consistent with the supernovae usually associated with GRBs.

From, Eq. 3.5, it can be seen that my calculated breakout radius, $R_0 = 2.3 \times 10^{13}$ cm far exceeds the typical radius of a WR star ($\sim 10^{11}$ cm), which is the preferred candidate for the progenitor (Campana et al., 2006). Waxman et al. (2007) propose two possibilities for explaining the large breakout radius. The first is that the star is surrounded by an optically thick shell, formed by a large mass-loss event from the progenitor star which occurred before the SN explosion. The second is that a dense stellar wind can be optically thick to a large radius. Nakar and Piro (2014) advocate the former, whereas Li (2007) discusses the latter. My value for R_0, exceeds considerably even the breakout radius of 7.8×10^{12} cm derived by Waxman et al. (2007), in their model of a wind from a WR star. A progenitor star which is larger than a WR star (e.g. 100 $R_\odot$) with a WR-like wind (Li, 2007), or a significant pre-explosion mass-loss event, could account for the R_0 which I derive.

From my observations, I calculated the velocities from the spherical outflow model using the derivative of the blackbody radius against time. The inferred velocities from the spherically outflowing blackbody range from 65400 km s^{-1} at 1615 s, to 16800 km s^{-1} at 120 ks. Extrapolating Eq. 3.5, to 2.89 days gives a velocity of $v = (15000 \pm 4000)$ km s^{-1}, which is inconsistent with the velocity calculated in Pian et al. (2006) from the spectroscopic analysis of SN 2006aj at 2.89 days, $v = 26000$ km s^{-1}. However, if I fit a power-law plus constant model to the velocity data for GRB 060218 from Pian et al. (2006), I find, $v \propto t^{-0.3}$ and this is in good agreement with my prediction for the velocity of $v \propto t^{-0.32 \pm 0.01}$. The inconsistency with the velocity measurement by Pian et al. (2006) at 2.89 days, could be because the velocities calculated in Pian et al. (2006) are measured from the Doppler shift in the absorption lines from the velocity in the line of sight to the observer. The velocities are measured in the transverse direction. A non-spherical expansion which is faster in the line of sight direction would produce such a discrepancy between the line of sight and transverse velocities, and hence could account for the difference between the velocities I have derived and those derived by Pian et al. (2006).

3.5 Conclusions

The work in this paper analyses the early UV/optical emission and the thermal components observed in both the UV/optical and X-ray, in GRB 060218.

I have shown that the observed UV/optical spectral index at early times indicates that before thermal emission dominates the UV/optical, the UV/optical emission is the GRB afterglow. I have proposed that the UV/optical afterglow is likely to be produced from external shock synchrotron emission from a jet; additionally, the same mechanism can be used to explain the radio emission at later times ($\gtrsim 2$ days), as explained by Toma et al. (2007). Conversely, after the initial observations of the UV/optical synchrotron component, the UV/optical spectrum resembles a Rayleigh-Jeans spectral shape $F_\nu \propto \nu^2$ at $t > 1350$ s, until the blackbody peak is measured in the UV/optical bands at 120 ks.

I have proposed a basic model that accounts for most of the observed features in GRB 060218. This model includes a jet that penetrates the envelope surrounding the progenitor core. The extended envelope is optically thick and emits UV/optical and thermal X-ray emission from the same expanding region. Within the time interval of $1400 - 8000$ s, the UV/optical emission corresponds to the same blackbody spectrum as the X-ray emission. The photosphere continues to expand, and at 120 ks, the thermal UV/optical emission is observed when the blackbody is peaking at UV energies. My basic model improves upon previous models, because I have shown the evidence for a jet which is needed to produce the UV/optical emission during $t \leq$1350 s and this UV/optical jet signature has not been recognised in previous studies of GRB 060218. The synchrotron component observed in the UV/optical agrees with the late observations of a synchrotron component in the radio emission. Furthermore, I have shown that the UV/optical and X-ray blackbody emission can be produced in the same region and can be produced in a spherical outflow.

I have demonstrated that the UV/optical emission during $5 - 60$ ks could be characterised by Rayleigh-Jeans emission. I have shown that the UV/optical spectral shape does not change during this time, and this provided us with an accurate value of the UV/optical reddening, and moreover allowed us to rule out a Milky Way extinction curve for the host galaxy.

Finally, it is important to note that GRB 060218 is one of only four LLGRBs observed, providing a rare opportunity to analyse the early UV/optical emission in the very early stages of a SN. If my interpretation is correct, GRB 060218 represents the first LLGRB with a clear observed UV/optical afterglow, which is valuable in understanding what is happening to produce this emission. It is proposed that this is the product of a jet penetrating the progenitor envelope and interacting with the surrounding medium. My proposed model has implications on future observations of LLGRBs and also highlights the importance of UV/optical observations during the prompt emission of LLGRBs, as this is the only time where the observation of the UV/optical afterglow is possible before the dominant emission from a thermal photospheric component.

Chapter 4

A multi-wavelength analysis of GRB 100316D, evidence for thermal emission analogous to GRB 060218?

4.1 Introduction

As mentioned in previous chapters, GRBs can be classified into two groups by their burst duration: short GRBs and long GRBs. Short GRBs are produced by the NS-NS / NS-BH mergers, confirmed at least in one case by the detection of a gravitational wave followed 2 seconds later by a GRB, and later a kilonova explosion (Abbott et al., 2017). Long GRBs are produced from the core collapse of massive stars (Woosley, 1993b; MacFadyen and Woosley, 1999b). This model is supported by the association of broad-lined type Ic SNe observed for a number of GRBs both spectroscopically and photometrically. Typically these SNe show similar properties to SN1998bw; however, their GRBs counterparts show diverse properties, both in duration (anywhere from 2–10000 s) and isotropic equivalent luminosity ($10^{46} - 10^{52}$ $\mathrm{erg\,s^{-1}}$). The photometric confirmation of these SNe comes from an optically-bright bump in the GRB afterglow light curve, which typically occurs 10 days after the gamma-ray emission triggers detectors. This "red bump" in the light curve is dominantly powered by the radioactive decay of Ni^{56} in the SN ejecta. Additionally, the early UV/optical afterglow light curves of GRBs associated with SNe do not always follow the typical synchrotron model, where the flux is expected to decay as a power-law. Also, the GRB light curves can have early breaks, that are not achromatic, signifying spectral evolution, and therefore can not be described by a single synchrotron emitting component.

GRB 060218/SN 2006aj was a GRB that was extensively observed by *Swift* in the initial 10 days, and also during its decaying SN emission. This allowed a deep analysis of the UV/optical/X-ray emission. This emission was found to be composed of a non-thermal synchrotron emission and a thermal component. It can be seen in Chapter 3 that this thermal component extends from X-ray to optical bands and described the cooling ejecta that had been heated by the shocks of SN2006aj. There is a component in the optical emission due to emission from a shock wave as the outer shell of an initially collimated jet interacts with its surrounding medium. GRB 100316D/SN 2010bh was similar to GRB 060218 in many ways. Both were low redshift ($z = 0.0591$ and $z = 0.033$, respectively) GRBs with a spectroscopically confirmed SN, and had a thermal component in the X-ray emission during the first 1000 s (Starling et al., 2011). However, GRB 100316D did not have as good a coverage in the UV/optical bands as GRB 060218. So unlike GRB 060218, I do not see a clear bright UV bump in the UV/optical light curve for GRB 100316D, but there was evidence of this in the form of a brightening in the $UVW1$ emission at 33ks (Olivares E. et al., 2012; Cano et al., 2011a). Therefore, it is possible that during this time, the observed emission mechanism is the same as that which governed GRB 060218: the Rayleigh-Jeans tail of a bright thermal component in the emission.

Therefore analysing the UV/optical emission at 33ks is vital in helping to understand what emission mechanisms are producing the pre-SN GRB light curve in GRB 100316D. Alongside the UVOT observations in $UVW1$, there are also observations in g, r, i, and z with the ground-based telescopes GROND and Gemini-S (Olivares E. et al., 2012; Starling et al., 2011; Cano et al., 2011a).

However, when comparing the observations from GROND and Gemini-S in works by Olivares E. et al. (2012) and Cano et al. (2011a) there is a clear discrepancy in the AB magnitudes. For example, with GROND the i and z emission at 42.5 ks was measured at $i = 20.87 \pm 0.05$, $z = 20.77 \pm 0.07$; with Gemini-S the i and z emission at 41 ks was measured at $i = 20.42 \pm 0.04$ mag, $z = 20.24 \pm 0.11$. Furthermore there are inconsistencies with the magnitudes shown in Table 2 and Fig. 4 in Cano et al. (2011a). Therefore, in order to model the UV/optical emission and resolve the pre-SN GRB emission component(s), it is required to know if the optical flux values given in these previous works are valid.

Starling et al. (2011) discovered similarities between GRB 100316D and GRB 060218, namely the X-ray lightcurve and spectral hardness resembled that of GRB 060218. Furthermore, Starling et al. (2011) found that X-ray emission (144-737 s) was best modelled with a synchrotron plus blackbody model. The temperature of the blackbody was constant at $kT = 0.14$ keV and $R = 8 \times 10^{11}$ cm. They argued that the UV/optical thermal component was not observed in GRB 100316D (as it was for GRB 060218) offering that if the extinction was similar to that of GRB 060218, then the emission from a shock breakout similar to GRB 060218 would be fainter by a factor of two or more and therefore they posited that the host galaxy would be dominating the UV/optical shock breakout emission. Olivares E. et al. (2012); Cano et al. (2011a) modelled the UV/optical SED during the time before the SN emission started to rise. Olivares E. et al. (2012) argued that the UV/optical and X-ray emission at 42 ks can be best modelled with a blackbody plus a power-law, and their best fit model had a blackbody component with, $kT = 0.079 \pm 0.003$ keV and $R = (3.9 \pm 0.4) \times 10^{13}$ cm. However their model required a hydrogen column density $N_H = 4.4 \times 10^{22}$ cm^{-2}, four times larger than that required by the model used in Starling et al. (2011). Cano et al. (2011a) modelled the UV/optical SED at 52 ks with a power-law model and no blackbody component. They estimated the spectral power-law index $\beta = 0.94 \pm 0.05$ from the spectral fit and argued that because this power-law is harder than you would typically expect for synchrotron emission, that this emission likely contains a component from the shock-heated, expanding stellar envelope.

The aim of this study is to determine if GRB 100316D is analogous to GRB 060218; in the sense of its pre-SN UV/optical emission. Therefore the light curve and the UV/optical spectra must be analysed in order to test this hypothesis. However, it is unclear which photometry to use, due to the differences between the GROND and Gemini-S photometry (Olivares E. et al., 2012; Cano et al., 2011a). The Gemini-S data is inconsistent and therefore I aim to reprocess the Gemini-S data during the interval 30-50 ks. Due to the different interpretations of the pre-SN UV/optical emission from Starling et al. (2011); Olivares E. et al. (2012); Cano et al. (2011a), reprocessing the images and doing the photometry will allow us to resolve the issues between the previous works and enable us to probe the nature of the UV/optical emission. I will take a similar approach as I have with GRB 060218 and see if the UV/optical spectral shape can be consistent with the the Rayleigh-Jeans tail of a blackbody.

4.1.1 Observations

GRB 100316D was observed by a multitude of ground observatories and space telescopes. The initial observations of GRB 100316D were performed using all seven filters of UVOT for 3 ks. However, the host galaxy subtraction could not be performed during the initial observation, because the optical/UV afterglow count rates were consistent with that of the host galaxy. The source was observed later at 33 ks in the *uvw*1 and *u* filter, where the flux of the afterglow emission was distinguishable from the host galaxy emission. The imagery of GRB 100316D and it's surrounding field were also taken by Gemini-South (-S). The Gemini-S images were taken with the Gemini Multi-Object Spectrograph (GMOS) (Crampton et al., 2000) 40 ks after the GRB trigger. The multichannel imager GROND (Greiner et al., 2007, 2008), started observations of GRB 100316D 42 ks after the GRB trigger and observed the source simultane-

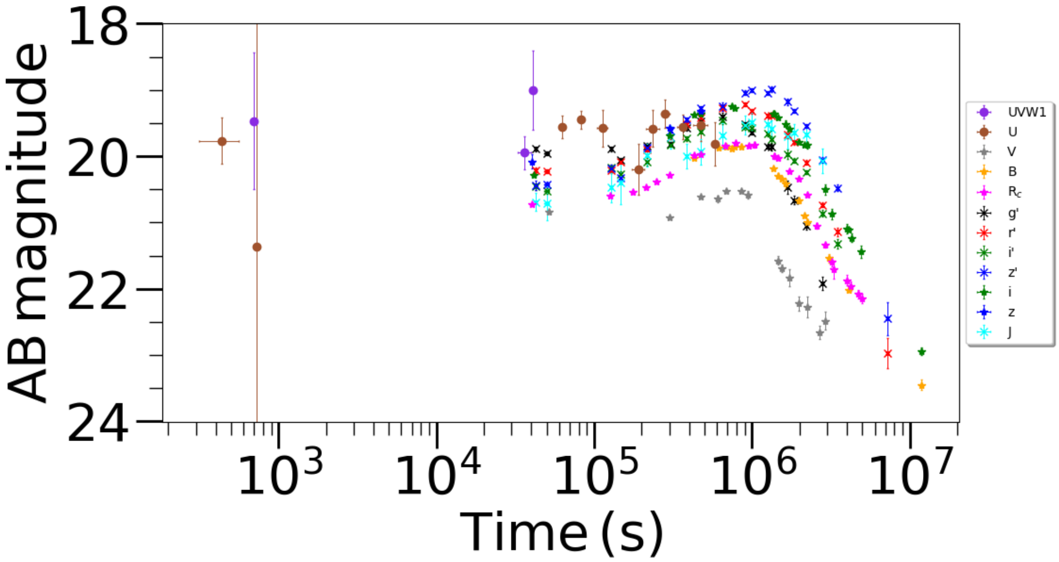

Figure 4.1: Lightcurves of GRB 100316D. Shown in the lightcurves are the observations from GROND (g',r',i',z',J), Gemini-S (B,V,R_c,i,z) and UVOT (U,$UVW1$). All magnitudes are given in AB and have been corrected for host galaxy contamination, they have also been corrected for foreground and host galaxy extinction of $E(B-V) = 0.18$, the extinction used in Cano et al. (2011a). The GROND data is extracted from Olivares E. et al. (2012) and Gemini-S is extracted from Cano et al. (2011a).

ously in g, r, i, z, J, H and K. UVOT, GROND and Gemini-S observed GRB 100316D and SN2010bh from 100 ks after the GRB trigger until the emission faded to the host galaxy level.

4.1.2 Gemini-S data

As previously explained, the UVOT $UVW1$ emission at 33 ks shows evidence of rebrightening. Therefore in order to probe whether this emission is consistent with the shock-breakout type of behaviour seen in GRB 060218, additional observations at 33ks are required to construct an SED. GROND and Gemini-S have observations in the g, r, i and z filters at 40 ks and 42 ks respectively. It can be seen in Fig. 4.1 that the i',r' AB magnitudes given in Olivares E. et al. (2012) and i,r AB magnitudes given in Cano et al. (2011a) are significantly different. In Fig. 4.1 the magnitudes have been corrected for the same foreground plus host extinction and therefore should be reasonably consistent. It is expected that they are not exactly the same due to slight difference of the responses for the i, z filters of Gemini-S and GROND; however, the differences are as large as 0.5 mag between the i magnitudes of the GROND (Olivares E. et al., 2012) and Gemini-S data (Cano et al., 2011a). Furthermore, as a check on the Gemini-S data for ~ 0.5 days from Table 2. in Cano et al. (2011a), the magnitudes in each filter were converted into flux densities, correcting for Galactic plus host extinction, which was estimated by Cano et al. (2011a) as $E(B-V) = 0.18$. the foreground and host galaxy corrected flux densities were compared to the values in Fig. 4 of Cano et al. (2011a) in which they display the SED at ~ 0.5 days. Inconsistencies were found with the magnitudes in Table 2 in Cano et al. (2011a) and the flux densities in Fig. 4 of Cano et al. (2011a). Therefore I decided that in order to examine the UV-NIR SED, the raw Gemini-S data in each filter needed to reprocessed and the photometry reperformed and be found independantly from those in Cano et al. (2011a). I chose to reprocess the Gemini-S data over the GROND data because the V and i band observations from Gemini-S are consistent with HST observations of V and i (Cano et al., 2011a).

4.1.2.1 Gemini-S image reduction

Image reduction was performed on the raw Gemini-S images taken of GRB 100316D. Images were taken from the Gemini-S archive [1] and processed using an array of tools in Image Reduction and Analysis Facility (IRAF). Specifically, this was performed using the IRAF tools: GBIAS, GIFLAT, GIREDUCE, GIFRINGE, GIRMFRINGE, GMOSAIC, AND IMCOADD [2].

The first step in the image reduction was to subtract the bias from the images. The bias is an offset added to the CCD before the start of an exposure. To get the bias frame, the zero second exposure images taken at the beginning and end of the observations were combined together (Massey, 1997). Furthermore, when clocking out the CCD, there is a small residual charge that is not moved from one pixel to the next during readout. This builds across

---

[1] https://archive.gemini.edu/searchform

[2] http://www.gemini.edu/sciops/data/IRAFdoc/gmosinfoimag.html

the width of the CCD and gets displaced into the first columns of the overscan (Massey, 1997). Therefore, this overscan buildup needs to be removed in the bias subtraction. The bias image was produced using GBIAS. In addition to the bias subtraction, flat field correction must also be performed. This action is to correct for imperfection of the optical surface of Gemini-S, sensitivity variances between pixels on the CCD, and illumination variances such as vignetting (Lucey, 2016). The flat field image is processed from twilight flat field images using GIFLAT. GIFLAT normalises the flat field images, subtracts both the bias and overscan image and combines them to one master flat image (Carrasco, 2011). To perform corrections from the bias and master flat GIREDUCE was used. The final step in processing the images is to correct for fringing in the images. Fringing occurs due to the slight variations of the thickness of the CCD (Snodgrass and Benoît, 2013). Fringing is caused by multiple reflection inside the CCD and at long wavelengths, where the CCD may become transparent, light can be reflected from the rear surface. The ripple-like pattern is caused by constructive and deconstructive interference (Snodgrass and Benoît, 2013). The fringe frames are produced by combining the images that make up the observation for that filter and then bias subtracting and flat fielding the image. This is performed using GIFRINGE. The fringe pattern is obtained by averaging this combined image with rejection of the highest values for each pixel (ESO, 2013). The fringing can then be corrected for by subtracting the scaled fringe frame from an image using GIRMFRINGE. The fringing correction has the most significant impact for the i' and z' images (ESO, 2013). The processed images for each observation and filter were then combined using GMOSAIC and IMCOADD.

4.1.2.2 Star catalogues for calibration

The filters used in the Gemini-S and GROND observed were: g, r, i and z. In order to calibrate the Gemini-S images my strategy was to use unsaturated stars in the Gemini-S images and calibrate the magnitudes using the known, catalogued magnitudes of those stars. The magnitudes of the Gemini-

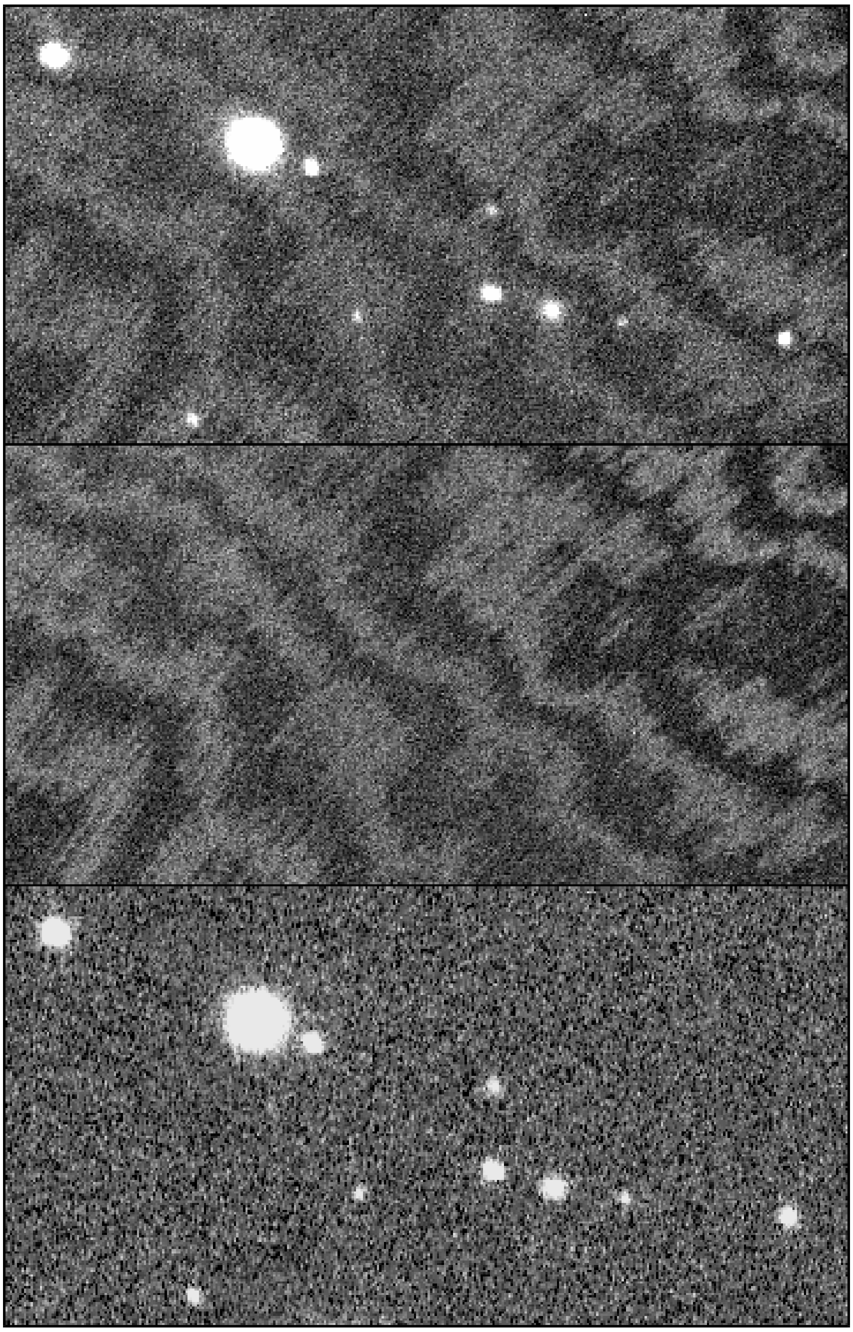

Figure 4.2: Three images showing the effect of fringing on the images on the Gemini-S i-band image of GRB 100316D. Top: raw image with fringing, middle: fringe frame image for subtraction, bottom: final fringing subtracted image.

S stars can be calculated using an arbitrary zero-point and using the IRAF task PHOT. The photometry for calibration can be performed for any stars which are contained in the star catalogue. The differences between the two magnitudes can then be used to calibrate for all stars, including the object of interest - GRB 100316D. There were three options to calibrate the images to: the AAVSO Photometric All-Sky Survey (APASS) catalogue; field stars observed by GROND; the SkyMapper Southern Sky Survey DR1 catalogue. APASS observed stars in the filters: Johnson B and V and Sloan g, r and i. The stars in the catalogue range from 7th to 17th magnitude and there were 19 stars in the same region as the Gemini-S image of GRB 100316D (2.5 arcmin region). However there were no observations in the z-band in this catalogue. The field stars observed with GROND (Olivares E. et al., 2012) consisted of 7 ∼16th magnitude stars located around the position of GRB 100316D within 0.5 arcmin. The GROND field stars were observed in g, r, i, z. Whilst it is an advantage to have the z band calibration, which I can't do using the APASS catalogue, there are only 7 field stars observed by GROND, and therefore the calibration errors would be much larger than with APASS. Additionally, the GROND field stars were calibrated using Sloan Digital Sky Survey (SDSS) catalogue in another region, during photometric conditions relative to their photometry. Therefore there was a degree of difference in magnitudes between the APASS catalogue and the GROND field stars. One other catalogue that offered the benefits of both the APASS catalogue and the GROND field stars was the SkyMapper Southern Sky Survey DR1 catalogue. The SkyMapper catalogue offers g, r, i, and z magnitudes of more than 100 stars in the same region as the Gemini-S observations of GRB 100316D.

I performed the magnitude calibration using all three catalogues, because whilst skymapper offers the largest amount of catalogued stars in the region of GRB 100316D, the spread of the magnitude difference, mag (Gemini-S) - mag (catalogued stars), could be larger. The spread of magnitudes differences will be fit with a constant for each catalogue and this will provide the calibration correction.

4.1.2.3 Matching stars from Gemini-S with catalogue stars

In order to perform the photometry for the calibration I first need to find the stars that match the coordinates in the selected catalogue. The IRAF task STARFIND was used to detect stellar objects in the Gemini-S images. For this task, the maximum threshold ellipticity of the region file was selected at $\varepsilon = 0.5$, where $\varepsilon = 1 - b/a$ and the parameters a and b represent the semi-major and -minor axes, respectively. The full width half maximum (FWHM) of the point spread function (PSF) was chosen as 4 pixels. STARFIND finds stars in the image above a threshold of 100 ADU above the background. The background mean of the pixel distribution was determined using IMSTAT. The stars produced from STARFIND were compared in image coordinates to those in the selected catalogue and stars within 10 pixels in y- and x-axes were considered a match. This matching was also inspected visually using the image viewing software DS9 (Joye and Mandel, 2003), which allows the region files to be overlaid on the image for closer examination. Therefore it was possible to remove any stars that were saturated in the image, by checking if the star core had a flat top from the star profile along its axis.

4.1.2.4 Performing magnitude calibration

To perform the photometry on the Gemini-S images and calculate the magnitude brightness of GRB 100316D, it was required to first determine which catalogue provided a precise consistent calibration. To calculate the magnitudes from the subtracted images, the zero-point of the afterglow image was first calculated and then the magnitude of the subtracted image was measured. This zero-point was used to obtain the true magnitude of the afterglow, without host galaxy contamination. To find the zero-point of the afterglow image the magnitudes of the stars that were in both the image and the the selected catalogue (APASS, Skymapper, and GROND field stars) were calculated using an arbitrary zero-point of 25. The difference between those calculated magnitudes and the ones in the catalogue were determined and a constant was fit to the differences, in order to obtain the zero-point of the image. The Photometry on all images were performed using the iraf task PHOT. The best aperture for photometry was selected such that the $\frac{F_i - F_{i-1}}{Fi-1} < 0.01$, where F is the flux and i represents the first index of an array of aperture sizes. The background was calculated from the image with all stars removed; this was done by creating a mask from stars found with the software package SEXTRACTOR.

4.1.2.5 Subtracting and aligning images

Due to the large contamination of flux from the host galaxy to the afterglow of GRB 100316D, the images needed to be subtracted so that this contamination was removed and I was only measuring the afterglow emission. Each image was aligned with the host-galaxy image in that filter and then subtracted, ready for photometry. The subtracted images in the Gemini-S g-band, r-band, i-band, and z-band are shown in Figures 4.3, 4.4, 4.5, and 4.6 respectively. A region file of star positions was used to calculate the shifts for each image; the shifts were applied to align the images. To subtract the images, the Python package HOTPANTS was utilized. HOTPANTS is a Python implementation of the image subtraction algorithm by (Alard and Lupton, 1998). Due to differences in seeing between the two images, their respective PSFs differ. For the observations of GRB 100316D, the seeing in the afterglow images was worse than in the host galaxy image. Therefore, the PSF on the host galaxy images was converted to match the PSF of the afterglow images using a PSF convolution kernel. The convolution kernel is created using a linear combination of three Gaussian functions: one half the size of the seeing, one the size of the seeing, and another twice the size of the seeing. After image subtraction, the flux of the subtracted image is normalized to the afterglow image.

4.1.3 UVOT data

GRB 100316D was initially observed in all UVOT filters. Observations were taken in image mode. Source counts were extracted with heasarc tool UVOTSOURCE, using a circular aperture of 3” radius centered on the position of GRB

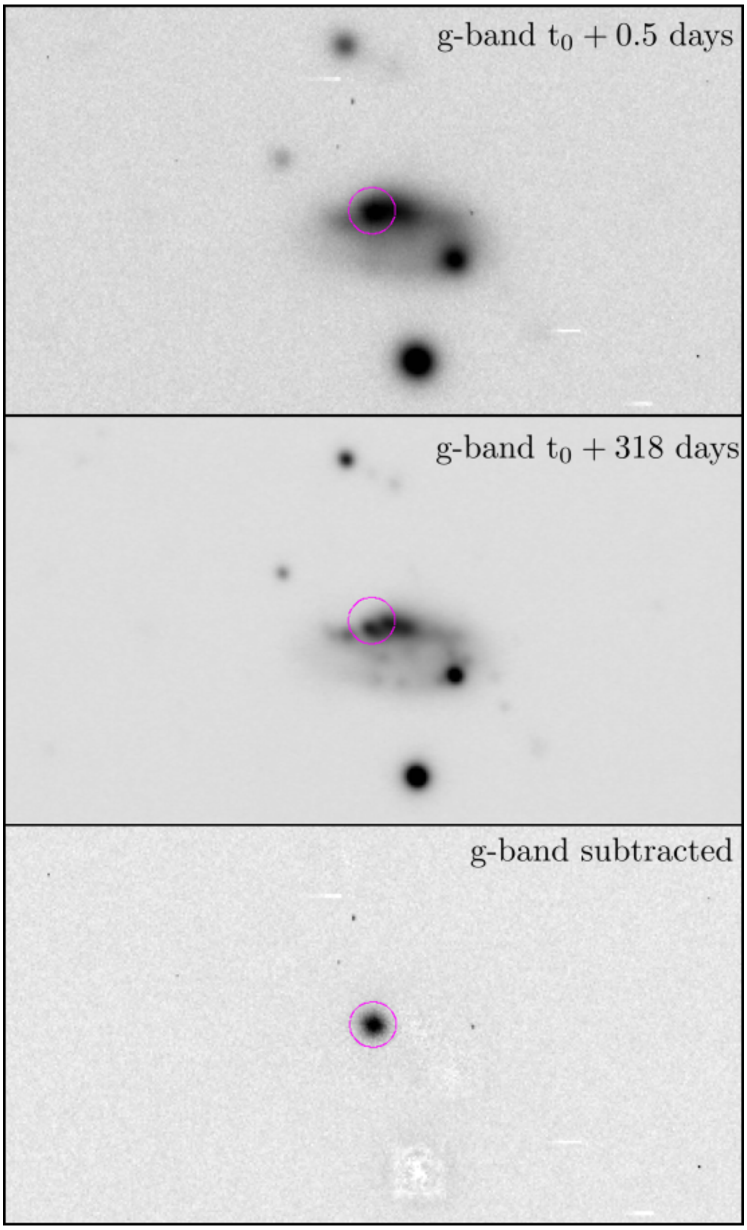

Figure 4.3: Top panel: Gemini-S g-band image of GRB 100316D 0.5 days after the GRB trigger. Middle panel: Gemini-S g-band image of GRB 100316D 318 days after the GRB trigger. This image provides the host galaxy contribution. Lower panel: subtracted g-band image, of afterglow image at 0.5 days subtracting the host galaxy image at 318 day, using the techniques described in Sec. 4.1.2.5.

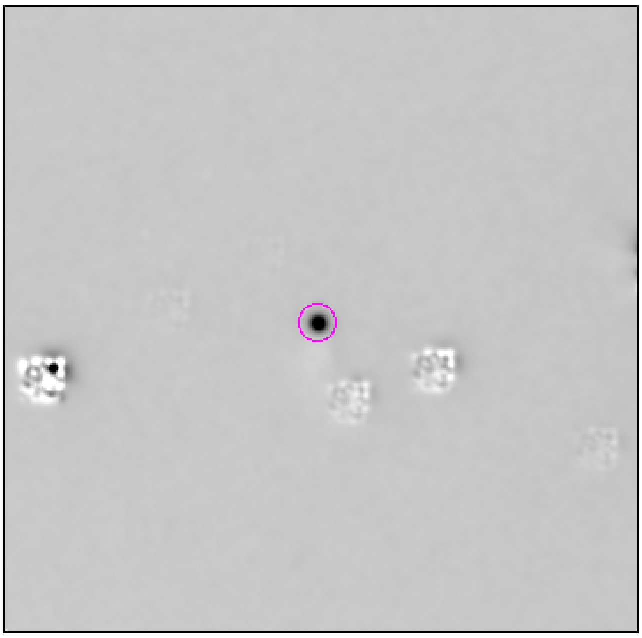

Figure 4.4: Host subtracted Gemini-S r-band image of GRB 100316D.

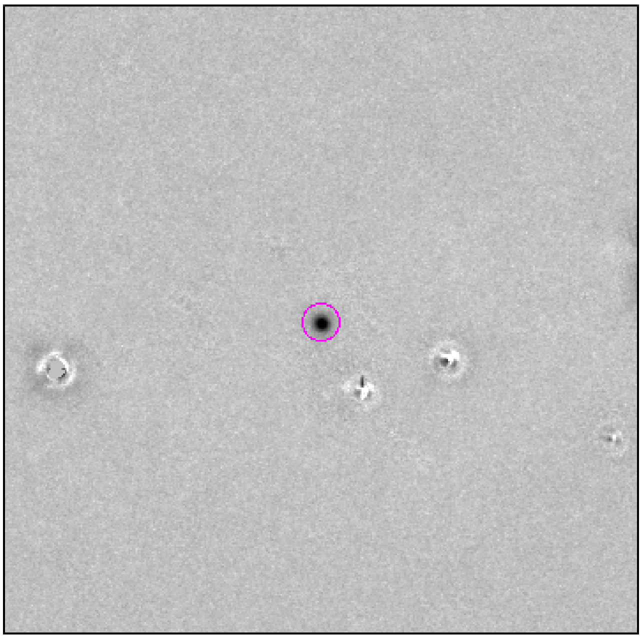

Figure 4.5: Host subtracted Gemini-S i-band image of GRB 100316D.

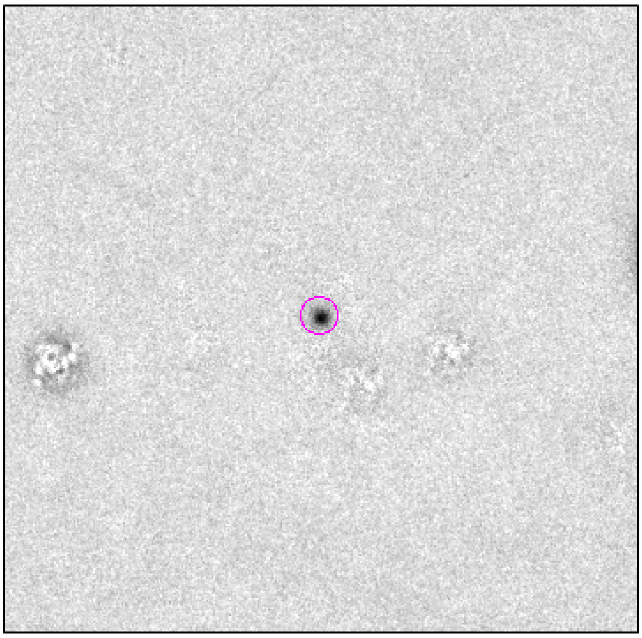

Figure 4.6: Host subtracted Gemini-S z-band image of GRB 100316D.

100316D. This aperture was preferred to the standard aperture for UVOT photometry of radius 5" both to reduce contamination from the presumed host galaxy and because the smaller aperture is more accurate when the count rate is low (Poole et al., 2008). These count rates were then corrected to the standard aperture using the curve of growth contained in the calibration files for accurate absolute photometry. Background counts were extracted from a region located outside of the host galaxy. To determine the host galaxy contribution to the source, the count-rate in the source region was measured in the interval 331–337 days after the GRB trigger, by which time the source had faded and was no longer contributing significant counts to the region. This count-rate was then subtracted from the earlier measurements of the source. Observations of the host galaxy were only observed with the U and $UVW1$ filters at 331–337 days, therefore I created light curves for the U and $UVW1$ emission of GRB 100316D and SN 2010bh. The UVOT data is included in the light curves figure shown in Fig. 4.1. The light curves count rates were converted to AB magnitudes using the UVOT photometric zero points (Breeveld et al., 2011). Each light curve was grouped using a bin size of $\Delta t/t = 0.2$ to ensure the best S/N for the afterglow light curves. For the purpose of comparing the emission in Fig. 4.1 the UVOT light curves were corrected for foreground and host galaxy extinction, $E(B-V) = 0.18$ (taken from Cano et al. (2011a)). However, the UVOT measurements included in my SED at 33ks will not be corrected for Galactic and host galaxy extinction. The host galaxy extinction and extinction curve will be determined in SED fitting.

4.2 Results

4.2.1 Gemini-S photometry

In order to construct the UV/optical SED, the Gemini-S observations of GRB 100316D at 40-42 ks were reprocessed and the photometry was performed to get the host subtracted g, r, i, z band emission. This required that the processed Gemini-S images were host subtracted and calibrated. I calibrated the images with the APASS catalogue, GROND field stars, and the Skymapper catalogue. The photometry was performed using PHOT with a zero-point of 25. This photometry was compared with each catalogue and the differences were plotted. The magnitude differences were fit with a constant and this provided the new zero-point for the Gemini-S images. Based on the fitting of the magnitude differences and the number of my samples, Skymapper was the best catalogue to use to calibrate the Gemini-S images. The zero-points, determined using the Skymapper catalogue, and the photometry results from the Gemini-S images are presented in Table 4.1.

Table 4.1: The Skymapper calibrated AB magnitudes from the Gemini-S observations of GRB 100316D at 40-42 ks. The zero-point is determined in calibration and used to calibrate the photometry of the host subtracted images.

Filter	zero-point	AB magnitude
g	27.759 ± 0.058	20.634 ± 0.062
r	28.237 ± 0.056	20.845 ± 0.058
i	27.575 ± 0.051	20.770 ± 0.053
z	26.634 ± 0.038	20.784 ± 0.041

4.2.2 GRB 100316D light curves

In the first 1000 s of observation of GRB 100316D with UVOT the afterglow emission was not detected in any filters. The host galaxy contribution in the U and $UVW1$ were obtained from the UVOT observations taken 331–337 days past the GRB trigger that I processed. I measured the host galaxy contribution to be UVW1$_{vega} = 18.82 \pm 0.06$ mag and U$_{vega} = 18.65 \pm 0.08$ mag. The magnitudes for the host galaxy were determined using the same 3" radius, aperture corrected to 5" as the photometry at 33 ks. After determining the host galaxy contribution, I analysed the GRB afterglow emission in the U and $UVW1$ bands. The U band emission from the GRB remained consistent, within error margins, until observations ended at 600 ks. However, the $UVW1$ band emission from the GRB faded and was no longer detectable by 100 ks. A comparison of the light curves from UVOT, GROND and Gemini-S are shown in Fig. 4.1. Apart from the UVOT observations the data in this light curve are taken from literature (Cano et al., 2011a; Olivares E. et al., 2012).

Fig. 4.7 shows the comparison of the U and $UVW1$ light curves of GRB 100316D and GRB 060218 (Emery at al. 2019). The light curves are shown with normalised magnitude to see the comparison of peak emission.

4.2.3 SED results

You can see that from Fig. 4.7 that the period of brightening in the GRB 100316D coincides with the peak UVW1 emission in GRB 060218. However, it is hard to distinguish any UVW1 emission from GRB 100316D outside of the observations at 33ks, due to the bright host galaxy. To investigate the source of the UVW1 emission in GRB 100316D I constructed an SED using the g, r, i, and z band Gemini-S photometry given in Sec. 4.2.1. The SED also included the $UVW1$ emission from 33 ks. Due to the presence of a blackbody in the X-ray spectra, previously reported by (Starling et al., 2011) between 144–737 s, it is expected that the optical-UV is the tail of this blackbody emission, and therefore follows a Rayleigh-Jeans power-law shape, where $F \propto \nu^2$. Starling et al. (2011) also found that the X-ray emission at 33–505 ks was in-

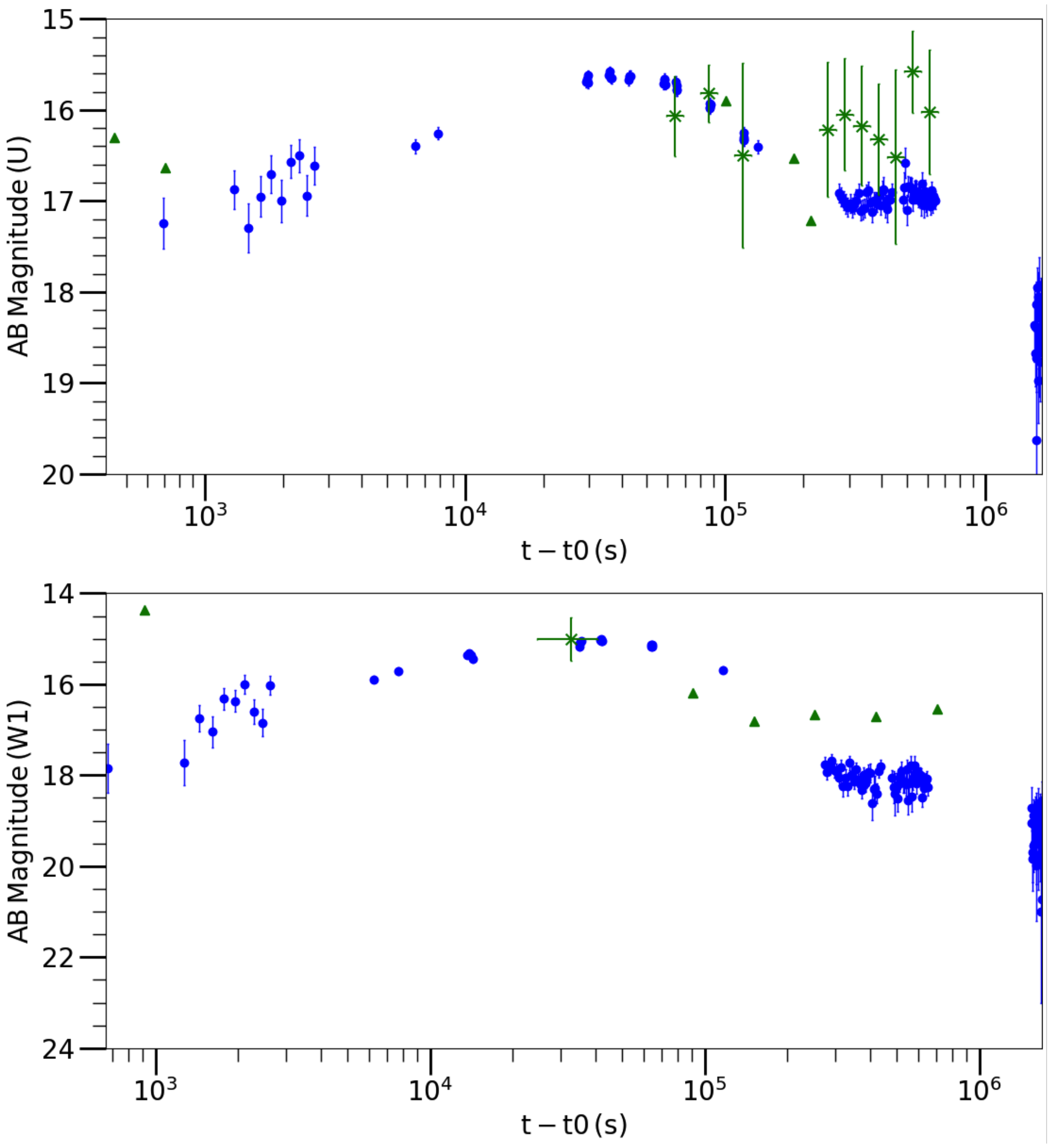

Figure 4.7: Top: U band light curves for GRB 060218 and GRB 100316D, shown in blue and green, respectively. Bottom: $UVW1$ band light curves for GRB 060218 and GRB 100316D. The upper limits, shown as triangles, were taken when the $S/N < 1$, the upper limits are given as the (count rate + 3× count rate error) converted into AB magnitudes.

consistent with being produced by a thermal component with a power-law, and found the best fit model was a power-law with $\beta = 3.5$. This is consistent with the X-ray emission of GRB 060218: similarly to GRB 100316D the thermal component in the X-ray emission of GRB 060218 had gone. Therefore in my analysis of the UV/optical SED I did not include X-ray data. This is because the power-law component in the X-ray emission likely does not correspond to synchrotron emission; Waxman et al. (2007) explained that such a soft spectral component could be explained with inverse Compton scattering. This inverse Compton scattered emission would not extend to UV/optical energies. I fit the UV/optical SED with a blackbody plus powerlaw model and I fixed Galactic reddening as $E(B-V) = 0.12$ (Schlafly and Finkbeiner, 2011). The host extinction was left as a free parameter. I performed each SED fit with a different extinction curve (MW, LMC, SMC) to determine which best represented the dust properties of the host galaxy. To test whether the UV/optical emission could be produced by the Rayleigh-Jeans tail of a blackbody component, therefore I fixed the blackbody temperature to a value between the UV and X-ray emission ($kT = 0.01$ keV) and fitted for the normalisation - because I assume it is no longer detected in the X-ray emission. The power-law component was a free parameter.

The results from the SED fitting are shown in Table. 4.2. MW, LMC, and SMC extinction all produce acceptable fits to the data, but the best fit is using the MW extinction. Therefore, I used this to derive the thermal and power-law component properties.

4.3 Discussion

The focus of this study was to reprocess the Gemini-S photometry for GRB 100316D and use this in combination with the $UVW1$ observations from UVOT, enabling us to investigate the properties of the pre-SN emission from GRB 100316D. Therefore, the Gemini-S was redone since it was first reported in Cano et al. (2011a). In Cano et al. (2011a) they report that at 41 ks, $i = 20.42$

Table 4.2: The results from the UV/optical SED fitting. The SED was modelled with MW, LMC and SMC extinction curves. The radius is the inferred blackbody radius from the normalisation of the blackbody model. Γ is the photon index from the power-law component. χ^2/dof is the chi-squared fit statistic against the degrees of freedom.

Extinction curve	E(B-V)$_{host}$ (mag)	R$_{BB}$ ($\times 10^{14}$ cm)	Γ	χ^2/dof
SMC	0.292 ± 0.633	1.128 ± 0.167	2.523 ± 1.338	4.92/2
LMC	0.299 ± 0.622	1.200 ± 0.181	2.616 ± 1.510	4.74/2
MW	0.309 ± 0.066	1.181 ± 0.185	2.501 ± 1.421	4.29/2

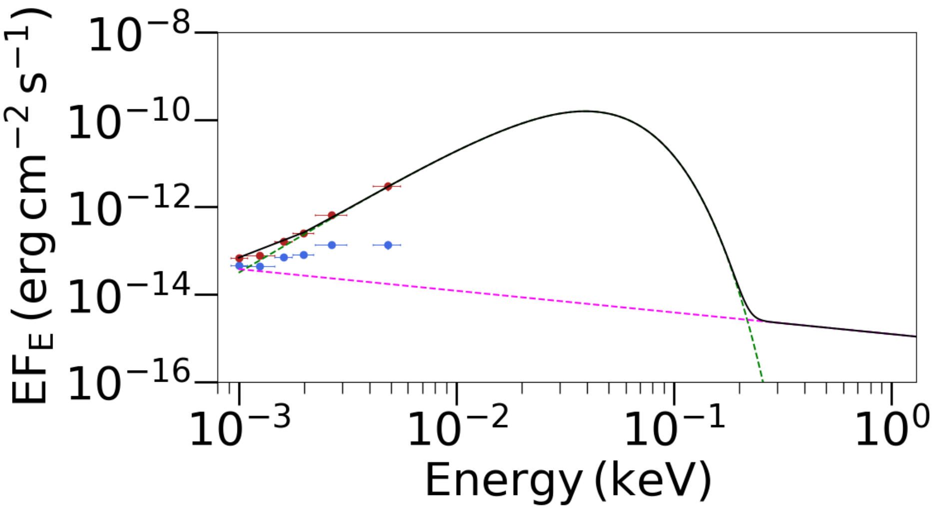

Figure 4.8: The SED of GRB 100316D at the time (33000–52000) s. The SED shown is fitted with a power-law plus blackbody model, shown by the pink and green dashed lines, respectively. The combined model is displayed with a black line. The parameters for this fit are shown in Table 4.2, where I have used a MW extinction curve to describe the dust. Data points are shown in blue and red, for the absorbed and unabsorbed observed flux.

mag, $z = 20.24$ (uncorrected for foreground and host extinction E(B-V)=0.18), this is largely different to that reported by GROND in Olivares E. et al. (2012), who find at 42.5 ks, $i = 20.87$ mag, $z = 20.77$. It can be seen from Table. 4.1 that my photometry of GRB 100316D is consistent with that reported by GROND (Olivares E. et al., 2012).

As mentioned in the previous sections, the combination of a thermal component that peaks at X-ray energies observed by Starling et al. (2011) and brightening of the UV emission before the Ni^{56}-powered optical emission indicated that GRB 100316D is comparable to GRB 060218. These properties are not typical for long GRBs. The afterglow of long GRBs have non-thermal, synchrotron emission, and the UV/optical lightcurves generally decay after 500s as a power-law (Oates et al., 2009), which I associate with the synchrotron emission from the external forward shock model. The similarities between the UV emission can be seen in Fig. 4.7, the $UVW1$ emission is only visible at 33 ks. This time coincides with the peak in the $UVW1$ light curve of GRB 060218. Therefore, it is possible that a similar light curve shape to GRB 060218 is being observed, but the contribution of the host galaxy to the total emission of GRB 100316D is so pronounced that the emission outside the peak emission remains unobserved. This behaviour is unlike synchrotron emission because if it was synchrotron emission, the emission peak would have seen far earlier than 33 ks and therefore observed the emission earlier. Therefore the $UVW1$ emission is more consistent with the emission being produced from an expanding shock heated envelope, which can produce a strong UV brightening, as can be seen in GRB 060218 (Chapter 3).

Due to there being no evidence for thermal emission in the X-ray emission after 10 ks (Starling et al., 2011), I fixed a blackbody component at 0.01 keV and modelled the normalisation, such that the UV/optical is modelled on the Rayleigh-Jeans part of the blackbody model. This best fit model is shown in Fig. 4.8.

In my investigation of the UV/optical emission of the SED at 33ks, I first attempted to fit the spectra with a single component model, hypothesising the emission to be on the Rayleigh-Jeans tail. The fit parameters for this single component model revealed a χ^2 value of 71.71 (for 6 bins), indicating a poor fit to the data. Given the inadequacy of the single Rayleigh-Jean tail component in describing the data, I then employed a two-component model: the Rayleigh-Jean tail combined with an additional power-law component. This approach yielded a significantly improved χ^2 value of 5.71 (for 6 bins). From my analysis, it is evident that solely relying on the Rayleigh-Jean tail does not provide a satisfactory representation of the UV/optical emission. A composite model, encompassing both the Rayleigh-Jeans tail and an additional power-law component, is necessary for an accurate depiction of the data.

This is different to the model suggested by Olivares E. et al. (2012) where they fit the UV/optical and X-ray emission to a single blackbody and require a very large absorption to fit a blackbody to the X-ray emission, $N_H = 4.4 \times 10^{22}$ cm, which is more than double that found by Starling et al. (2011) when they fit the thermal component to the XRT/BAT SED during 144-737 s. Therefore I think it is not appropriate to model the X-ray with a thermal component after 10 ks. Instead in my model I have fitted the blackbody with fixed temperature, such that it does not contribute to the X-ray emission.

By modelling the normalisation of the blackbody component I can see if such a blackbody component would be realistic taking into consideration the energy budget of SN2010 bh. The best fit normalisation at kT=0.01 keV provides $R = (1.181 \pm 0.185) \times 10^{14}$ cm, and $L = (1.862 \pm 0.561) \times 10^{45}$ $\mathrm{erg\,s^{-1}}$. Whilst this luminosity is smaller than reported by Starling et al. (2011) ($L = (3-4) \times 10^{46}$ $\mathrm{erg\,s^{-1}}$), it does not exceed the kinetic energy of SN 2010bh considering the SED time bin of 3000 s, reported as high as $E_k = (2.4 \pm 0.7) \times 10^{52}$ erg by Cano et al. (2011a).

I determined from my SED fitting that a MW extinction curve with a host galaxy extinction $E(B-V) = 0.309 \pm 0.066$ mag provided the best fit. Cano et al. (2011a) argued a lower value for total extinction (foreground + host galaxy) than ours. Cano et al. (2011a) estimated $E(B-V) = 0.18 \pm 0.08$ mag by assuming that the $(V-R)$ colour at 10 days after maximum are the same for all Type Ibc SNe. This is based on a relationship argued in Drout et al. (2011), therefore the difference in $(V-R)$ after maximum with those of other Type Ibc SNe provided them with an estimate of the total extinction. Whilst my value for the host galaxy reddening differs from Cano et al. (2011a), the $(V-R)$ colour relation is only empirical and it is not clear if this would be true for all Type Ibc SNe. Starling et al. (2011) used the U -band $3-\sigma$ upper limit at 324 s with the XRT/BAT spectrum, to estimate a value of $E(B-V) = 0.9$ mag for the host extinction. This is much larger than I predicted, but the value estimated in Starling et al. (2011) is under the assumption that there is no contribution of the thermal component in the UV/optical emission and assumes that the power-law fitted to the XRT/BAT spectrum extends to the UV/optical spectrum. Furthermore Starling et al. (2011) used much brighter host-galaxy values for U and $UVW1$, because they measured the contribution at 500 ks, when there was still contribution from SN 2010bh.

I measured the power-law component in my SED fits as $\beta = 2.501 \pm 1.421$. In GRB 060218 the X-ray spectral index softened over time, from $\beta = 0.4 - 3.3$ (Chapter 3). A similar behaviour was measured by Starling et al. (2011), who observe the X-ray power-law soften from $\beta = 0.5 - 2.5$. This was explained in GRB 060218 as possibly being caused by inverse compton emission (Waxman et al., 2007).The UV/optical power law could be a synchrotron component from a jet, analogous to the optical synchrotron component that was observed in GRB 060218 at early times.

The behaviour of the UV emission of GRB 100316D at 33 ks is very similar to that seen in GRB 060218. Both brighten to a peak in the $UVW1$ emission at 33 ks. At 33 ks the magnitudes can be compared as: $UVW1_{\rm vega} = 17.755 \pm 0.054$ mag for GRB 100316D and $UVW1_{\rm vega} = 15.469 \pm 0.08$ for GRB 060218, respectively, both corrected for their total extinction. The brightening in GRB 100316D is not as substantial as that seen in GRB 060218. Importantly, it's essential to note that GRB 100316D is at almost twice the distance as GRB 060218. Due to the inverse square law, the flux from GRB 100316D should naturally be almost a factor of 4 fainter just based on this distance difference. This flux discrepancy cannot be attributed solely to afterglow emission from the jet, given the considerable time lapse since the GRB trigger. An explanation for this emission is that it is due to the adiabatic cooling of shock heated ejecta from SN 2010bh, which in the case of GRB 060218, was seen during the period 6-60 ks as a UV bright bump in the optical light curves. This observation aligns with the thermal component observed in the X-ray emission in the initial 1000 s (Starling et al., 2011). However, the UVW1 flux is an order of magnitude lower at 33ks than that of GRB 060218. This could be explained by a weaker cooling emission of the SN shock heated envelope of the progenitor star, in comparison to GRB 060218. This weaker cooling emission could be due to a faster cooling by 33 ks compared to in GRB 060218.

4.4 Conclusions

In my analysis of the UV/optical/X-ray emission from GRB 100316D before the Ni-56-powered emission in SN 2010bh, I examined the multi-wavelength emission and its potential origins. My reprocessed Gemini-S photometry aligns with the GROND observations, addressing inconsistencies in the datasets presented by Cano et al. (2011a).

The Spectral Energy Distribution (SED) between 33-52 ks is best modelled by a combination of a blackbody and a power-law. This model is consistent with the blackbody component observed at 330s in Starling et al. (2011), suggesting an expanding and cooling mechanism similar to the thermal emission in GRB 060218.

My findings indicate that the thermal component in the UV/optical/X-ray emission from 33-52 ks originates from the cooling envelope emission after the shock breakout. The spectral index from the power-law component, $\beta = 1.507 \pm 1.402$, although not easily constrained with only UV/optical data, is necessary alongside the blackbody component for an accurate fit to the SED.

Overall, this study contributes to our understanding of GRB 100316D and offers a basis for future investigations into similar phenomena.

Chapter 5

GW170817 study

5.1 Introductory Material

Long GRBs have been linked to star-forming regions and massive stars' death, as shown by the observational connection between long GRBs and SNe. On the other hand, short GRBs should not be taken to the same conclusions since they are not associated with star-forming regions and, therefore, with the death of massive stars.

While long GRBs are typically associated with intense star-forming regions in their host galaxies, short GRBs are in diverse star-forming and non-star-forming regions. This relationship supports the theory that the progenitors of short gamma-ray bursts have a wide range of time delays between stellar birth and death and result from compact binaries' merging, in particular the merger of two neutron stars or a neutron star with a black hole.

Moreover, many short GRBs have a large offset compared to the centre of their host galaxy (Troja et al., 2008; Church et al., 2011; Fong and Berger, 2013), implying that the sources' progenitors have travelled from their birth sites to their final explosion sites. The offset distribution and short GRB positions relative to their hosts' stellar light suggest systemic kicks.

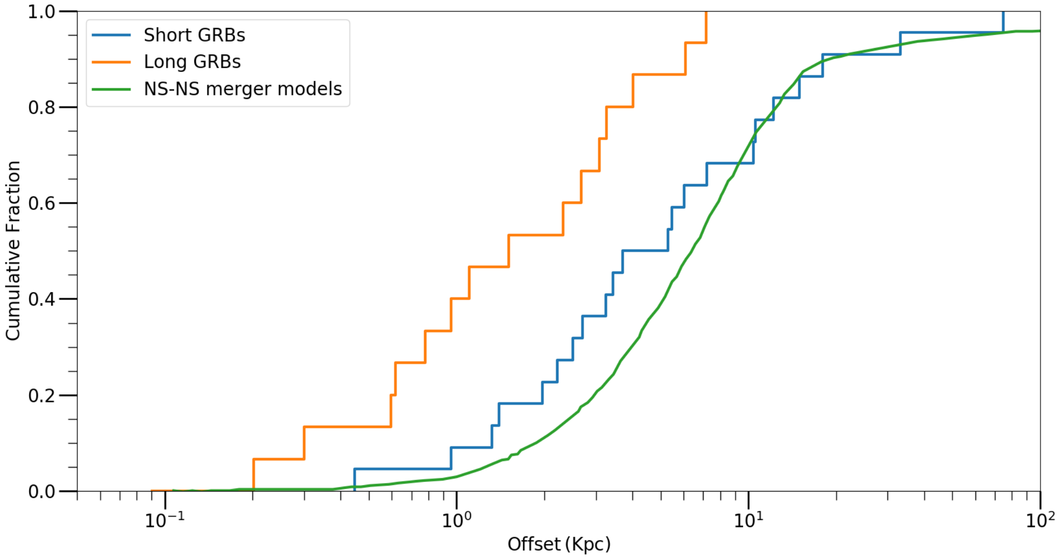

Figure 5.1: Cumulative distribution of the projected spatial offsets for short GRBs (blue) (Fong et al., 2009; Berger, 2010; Fong et al., 2012) and long GRBs (orange) Bloom et al. (2002)). The projected offset distributions for NS-NS binary mergers in Milky Way-type galaxies based on population synthesis models in (Belczynski et al., 2006) are also shown for comparison (green).

Such SN kicks are anticipated from SN explosions that result in neutron stars' development due to asymmetries that arise during the collapse, either due to neutrino emission or an anisotropic explosion (Kusenko and Segrè, 1996; Janka et al., 2007; Janka, 2013).

Hulse and Taylor identified the first binary neutron star, labeled PSR B1913+16. Observations of PSR B1913+16 (Hulse and Taylor, 1975) indicated a decrease in its orbital energy, offering the preliminary indirect proof for gravitational waves, consistent with the predictions of general relativity (Taylor and Weisberg, 1982). As a binary neutron star (BNS) system's orbit contracts, the luminosity from gravitational waves increases, hastening the inspiral process. In the moments leading up to the stellar collision, this mechanism is anticipated to produce a detectable gravitational-wave signal, capturable by terrestrial detectors (Drever, 1983; Hawking and Israel, 1989). Subsequent to the discovery of PSR B1913+16, radio pulsar surveys have identified numerous additional BNS formations within our Galaxy (Manchester et al., 2005).

Presently, the network of gravitational wave detectors comprises three

Fabry-Perot-Michelson interferometers that measure space-time strain caused by traversing gravitational waves as a changing phase variation between laser light travelling in perpendicular arms: the two Advanced LIGO detectors (Aasi et al., 2015) and the Advanced Virgo detector (Acernese et al., 2014). These detectors running at design sensitivity are predicted to see (10–200) BNS mergers every year (Abadie et al., 2010; Abbott et al., 2017, 2020).

As well as a GRB and its associated afterglow, NS–NS and BH–NS binaries mergers are also expected to be accompanied by a more isotropic counterpart, a 'kilonova' (Metzger et al., 2010). Kilonovae are thermal transients that are about 1000 times brighter than a typical nova but less luminous than a supernova. Their emission typically lasts from days to weeks. This thermal emission arises from the radioactive decay of heavy r-process nuclei, which are synthesized in the ejecta that expands following a merger event (Li and Paczyński, 1998). While the gravitational wave (GW) chirp signal arises during the merger process, the subsequent kilonova serves as a prominent electromagnetic (EM) counterpart to this event. It's predicted that such EM counterparts will accompany a limited percentage of black hole-neutron star (BH-NS) mergers but will be present in almost all neutron star-neutron star (NS-NS) mergers. Moreover, kilonovae can serve as a direct probe into uncovering the origin of the heaviest elements that exist (Metzger et al., 2010).The emission from a kilonova is a combination of its blue (lanthanide-free ejecta) and red (lanthanide-rich ejecta) components. This is because, based on the viewing angles, both high and low electron fraction (Y_e) ejecta components can be simultaneously visible. The electron fraction, Y_e, is defined as $Y_e = \frac{n_p}{n_n+n_p}$, where n_p and n_n are the number density of protons and neutrons, respectively. Typically, a value of Y_e less than 0.1 indicates neutron-rich material. In some cases, the blue emission component can be blocked by the high-opacity lanthanide-rich ejecta (Kasen et al., 2015).

The observation of gravitational waves from a short GRB will be a huge scientific breakthrough with far-reaching implications for merger mechanics, progenitor types, and NS equations of state.

Throughout this chapter I will discuss the UV/optical counterpart to GW170817, with a thorough analysis of the data reduction and modelling of the emission. The data that will be discussed is published in Evans et al. (2017), however the analysis in this chapter will focus more on the thermal component, using a spherically outflowing blackbody model as opposed to a kilonova wind model using in Evans et al. (2017). There is a breakdown of the observation that led to the precise location of EM counterpart to GW170817 in Sec. 5.2, with the data reduction in Sec. 5.3 and 5.3.2. The modelling of the SEDs are explained in Sec. 5.3.3, with the results given in Sec. 5.4. Finally I discuss the implications of these results in Sec. 5.5 and draw my conclusions in Sec. 5.6.

5.2 Observations

At 12:41:04.45 UTC on 2017 August 17, the Laser Interferometric Gravitational-Wave Observatory (LIGO) detected a gravitational wave (GW) signal (LVC trigger G298048; Essick (2017)) and named GW170817 (Abbott et al., 2017). Two seconds after the GW trigger time, the Gamma-Ray Burst Monitor (GBM) on the Fermi satellite triggered on a short GRB with a localisation consistent with GW170817 (Goldstein et al., 2017). The gravitational strain signal indicated a neutron star merger with a combined mass of 2.73–3.29 $M_{\odot}$.

Swift searched for the GRB afterglow counterpart at 0.039d past the GW trigger. The search was initially performed with a $\sim 1.1^{\circ}$ region centred on the Fermi-GBM localisation (90% of containment region of 1626 deg^2). The search was refined with a more precise localisation from LIGO and Virgo detectors with a 90% containment region of 33.6 deg^2. In addition, Swift took a series of 120 s exposures centred on known galaxies located within the GW localisation. No significant X-ray or UV/optical sources were detected in any Swift UVOT and XRT observations.

An optical source was detected in the galaxy NGC 4993 (d~ 40 Mpc) at 0.5 days past the GW trigger - Swope Supernova Survey 17a (SSS17a) (Coulter et al., 2017). This source was later confirmed to be the counterpart to GW170817, making it the closest detected GRB. For the purposes of this discussion, the source SSS17a in NGC 4993 will henceforth be referred to as EM170817.

Swift started UVOT observations of EM170817 (RA, Dec (J2000) = $13^h09^h47.65^s, -23^{\circ}23^{'}01.6^{''}$) at 03:37 on August 18, 2017 (t = 0.6 d), initially using only the UVW2, UVM2, UVW1, and U filters. Using a pointing offset, observations with the complete 6-filter complement (including the V and B bands) started at t = 2.5 d. The offset was required to avoid a nearby bright star that would have exceed the UVOT's brightness limit in V and B. UVOT detected the source in all UV filters; however, the B and V bands show only partial detections or upper limits, owing to the significant galaxy background. In the initial exposures, UVOT detected a bright, fading UV source, $U_{AB} = 18.19^{+0.09}_{-0.08}$ mag. Subsequent UVOT exposures indicated fast fading UV emission, unlike the optical/NIR, which stayed flat for longer.

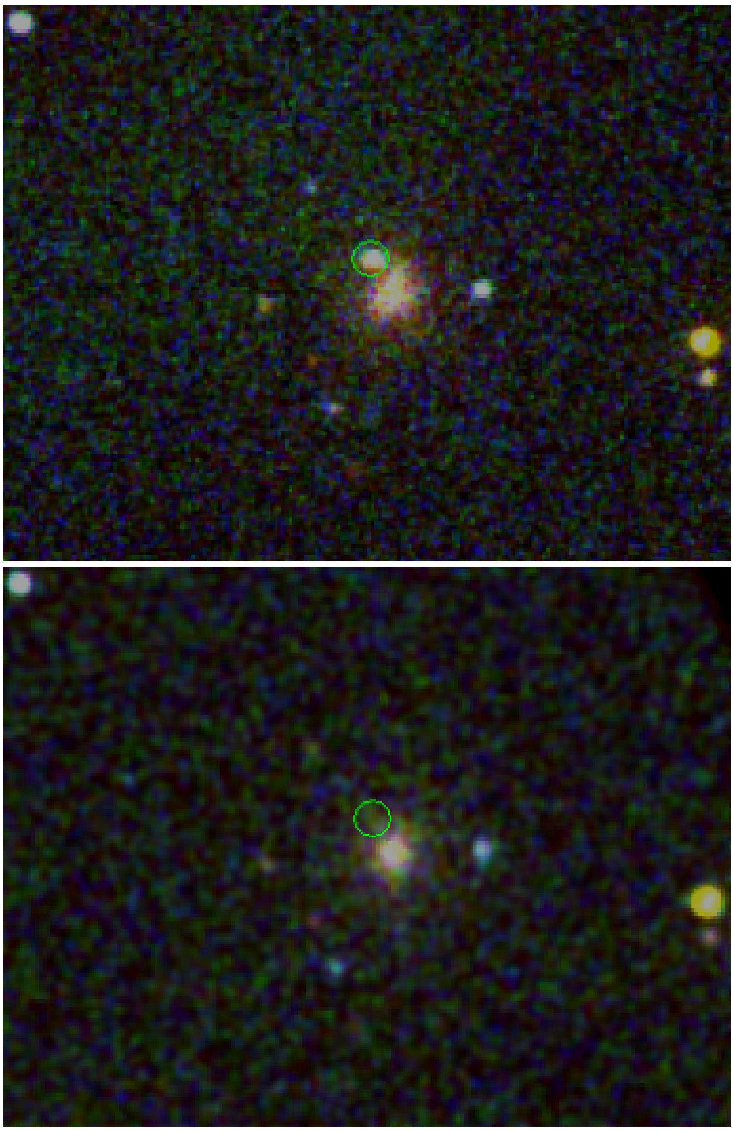

Figure 5.2: UVOT images of EM170817 shown in false colour. The images are produced using U, UVW1, and UVM2 bands as red, blue, and green channels. The image in the top and bottom panels are the sources at 0.6 and 4.9 days past the GW trigger time.

5.3 Data reduction

5.3.1 Photometry

Absolute photometry was obtained by extracting photon counts with a 3" radius circular aperture centered on EM170817, with a 5" aperture correction to the calibration standard. The narrower aperture minimised contamination from NGC4993 while increasing the signal-to-noise ratio (Poole et al., 2008).

The background counts were obtained from a region well outside the host galaxy. The UVOT analysis was conducted with HEASOFT v6.21 (Irby, 2017) and UVOT CALDB version 20170130 (Corcoran, 2017). UVOTSOURCE, a HEASOFT tool, was used to calculate count rates (including coincidence loss correction). I calculated the background-subtracted count rate in the source region in the interval t = 9.5–16 d, when the source had faded below detectability in all filters, to assess the host galaxy's contribution to the source. Some images were removed because of the unstable spacecraft attitude of Swift. The host galaxy count rate was then subtracted from the earlier EM170817 measurements; this was conducted separately for each filter and exposure. The host galaxy subtracted count rates were converted to AB magnitudes using the zero points in Breeveld et al. (2011).

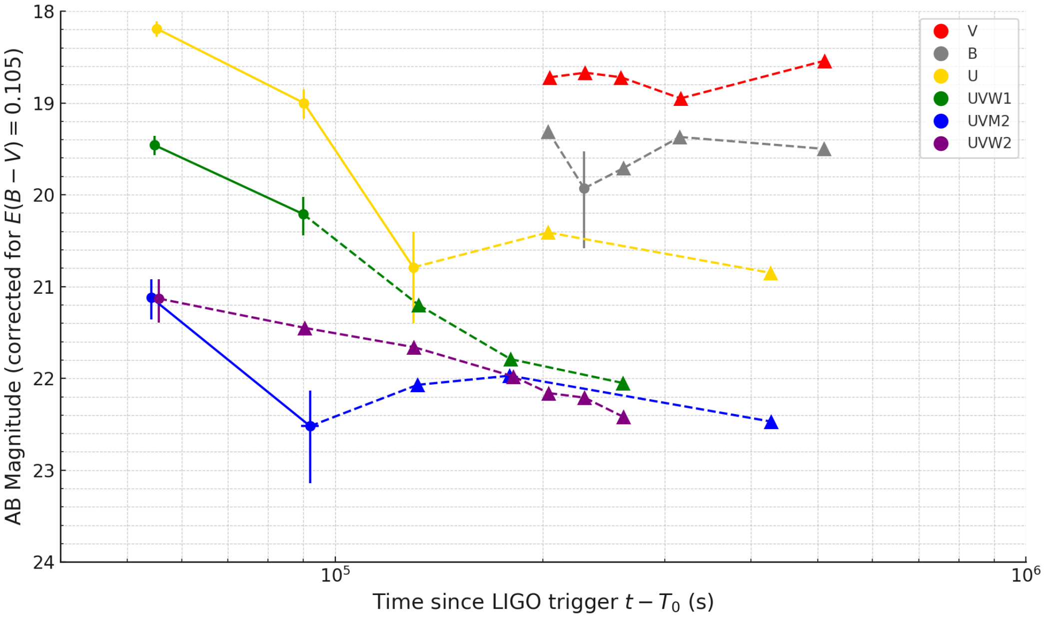

Figure 5.3: UV/optical light curve for UVOT observations of EM170817. The data shown match those in Table 5.1. Upper limits at the 3σ level are shown as triangles.

5.3.2 Spectral energy distribution

UVOT only detected the UV emission for GW170817 until t = 1 day; therefore, early-time SEDs were used to analyse the electromagnetic counterpart to the gravitational wave, EM170817. The optical data i, z, y were obtained from the

Table 5.1: UVOT photometry of EM 170817. All AB magnitudes are corrected for host contamination, but not Galactic extinction. Upper limits are given at the 3σ mark.

Filter	t (d)	Δt (d)	Count Rate (s^{-1})	AB Magnitude
UVW2	0.6431	0.0029	0.151 ± 0.032	$21.13^{+0.26}_{-0.21}$
UVW2	1.0469	0.0029	0.041 ± 0.024	> 21.45
UVW2	1.5067	0.003	0.026 ± 0.022	> 21.66
UVW2	2.0992	0.0646	0.027 ± 0.014	> 21.98
UVW2	2.3612	0.0702	0.021 ± 0.013	> 22.16
UVW2	2.6601	0.0376	0.013 ± 0.014	> 22.21
UVW2	3.0286	0.196	0.0195 ± 0.0088	> 22.42
UVM2	0.6272	0.0043	0.092 ± 0.018	$21.12^{+0.24}_{-0.20}$
UVM2	1.0652	0.0308	0.026 ± 0.011	$22.52^{+0.62}_{-0.39}$
UVM2	1.5237	0.0378	0.0122 ± 0.0087	> 22.07
UVM2	2.0723	0.0336	0.012 ± 0.010	> 21.97
UVM2	4.9533	0.4697	0.0062 ± 0.0068	> 22.47
UVW1	0.6344	0.0029	0.641 ± 0.064	$19.46^{+0.11}_{-0.10}$
UVW1	1.0407	0.0016	0.321 ± 0.062	$20.21^{+0.23}_{-0.19}$
UVW1	1.5293	0.0345	0.042 ± 0.029	> 21.20
UVW1	2.0777	0.0350	0.004 ± 0.023	> 21.79
UVW1	3.0211	0.1960	0.004 ± 0.018	> 22.05
U	0.6387	0.0014	2.93 ± 0.22	$18.19^{+0.09}_{-0.08}$
U	1.0431	0.0008	1.39 ± 0.20	$19.00^{+0.17}_{-0.15}$
U	1.5021	0.0015	0.27 ± 0.11	$20.79^{+0.61}_{-0.39}$
U	2.3546	0.0674	0.098 ± 0.094	> 20.41
U	4.9461	0.4673	0.038 ± 0.072	> 20.85
B	2.3565	0.0674	0.27 ± 0.16	> 19.31
B	2.6554	0.0348	0.42 ± 0.19	$19.93^{+0.65}_{-0.40}$
B	3.0258	0.1951	0.15 ± 0.12	> 19.71
B	3.6517	0.1006	0.26 ± 0.15	> 19.37
B	5.9098	0.1654	0.22 ± 0.14	> 19.50
V	2.3668	0.0683	0.11 ± 0.12	> 18.72
V	2.6657	0.0357	0.12 ± 0.12	> 18.67
V	3.0029	0.1628	0.172 ± 0.097	> 18.72
V	3.6620	0.1016	0.07 ± 0.10	> 18.95
V	5.9161	0.1641	0.19 ± 0.12	> 18.54

counterpart's Pan-STARRS observations to model the emission correctly. Like my prepared UVOT data, the Pan-STARRS data is also host-subtracted, and the transient field was calibrated in these filters prior. Due to minor time differences in observations between UVOT and Pan-STARRs, the Pan-STARRS data were linearly interpolated to match the observations time overlapped with UVOT at t = (0.6 and 1 day). Pan-STARRS detected i, z, y emission until $t > 2.676$ days. There were further observations from Pan-STARRs at 3.671 days, but by this time the i and y band observations were given as upper limits and the z band measurement had a more significant error associated with the measurement ($z = 18.1 \pm 0.3$) (Smartt et al., 2017). Therefore, when constructing SEDs at epochs >1 day, the GROND g, r, i, z, J, H, K_s observations were used in conjunction with remaining UVOT optical detections. The same methods of interpolation were used for the GROND data to match UVOT observation epochs. The SEDs were created from the host-subtracted Vega magnitudes from UVOT, Pan-STARRS, and GROND, where needed magnitudes were converted to Vega from AB. Spectral and response files were created for each measured magnitude using the instrument responsivity and the Vega spectrum for a given magnitude and error. This process was repeated for the instrument. UVOT responsivities were taken from CALDB version 20170817.

5.3.3 Analysis and modelling

The SEDs were analysed using XSPEC (version 12.10.1) and were modelled with spherically outflowing blackbody components, together with dust extinction from our Galaxy and the host galaxy of the GRB. The Galactic reddening was fixed at $E(B-V) = 0.106$ (Schlafly and Finkbeiner, 2011).

For SED fitting, spherically outflowing blackbody components were used to model the UV/optical emission; this is the same technique used for GRB 060218 in Emery et al. (2019). I adopted this methodology because, similar to GRB 060218, a single power-law cannot adequately model the early UV/optical emission. The wellness of fit provided by a blackbody model strongly implies the presence of a thermal component. By simply fitting a stationary blackbody, one can estimate the expansion velocity with $v = R/t$, where R is the stationary blackbody radius, and t is the time since the LIGO trigger. The calculated velocity suggests, analogous to GRB 060218, that the expansion velocity of the outflow is a considerable fraction of the speed of light, $v \sim 0.1 - 0.3c$. Therefore, to accurately model the blackbody component, it is essential to account for any Doppler-boosted thermal emission.

Due to relativistic effects, the observed flux is related to that in the blackbody rest frame through the Lorentz factor, Γ, the Doppler factor, δ, and the angle of the outflow with respect to the line of sight from the observer, θ. The formulae for Γ and δ, as well as their impact on the observed blackbody temperature, T, and the observed blackbody flux, F_ν, are detailed in Section 3.2.4.1. Briefly, the observed blackbody temperature relative to the temperature in the outflow frame, T_o, is given by $T = \delta T_o$, and the observed blackbody flux from a surface element, F_ν, is described by Equation 3.4.

My spherical outflowing blackbody model divides the emitting surface into ten components based on the angle, θ, with the corresponding line of sight velocity, $v = v_0 \cos\theta$, where v_0 is the outflow velocity.

5.4 Results

When analysing the UV/optical emission of EM170817, I fit the spherically outflowing blackbody model (Eq. 3.4) for all SED epochs. This approach was adopted because the fit is poor when fitting the SEDs with a power-law model. Each SED was checked to see if the spectra were compatible with a power-law model, and the results are given in Table 5.2. A comparison of the power-law and spherically outflowing blackbody model for the SED fit at 0.6431 days is shown in Fig. 5.4

Table 5.2: Summary of results for UV/optical SED fits of GW170827 modelled with a power-law model. β is the spectral index. χ^2/dof is the best fit chi-square/degrees of freedom.

Time (d)	β	χ^2/dof
0.6431	1.75 ± 0.07	149.72/5
1.0469	2.35 ± 0.10	87.95/4
2.4	1.03 ± 0.05	181.03/5
3.4	1.57 ± 0.03	604.08/4
4.4	1.96 ± 0.05	163.66/5

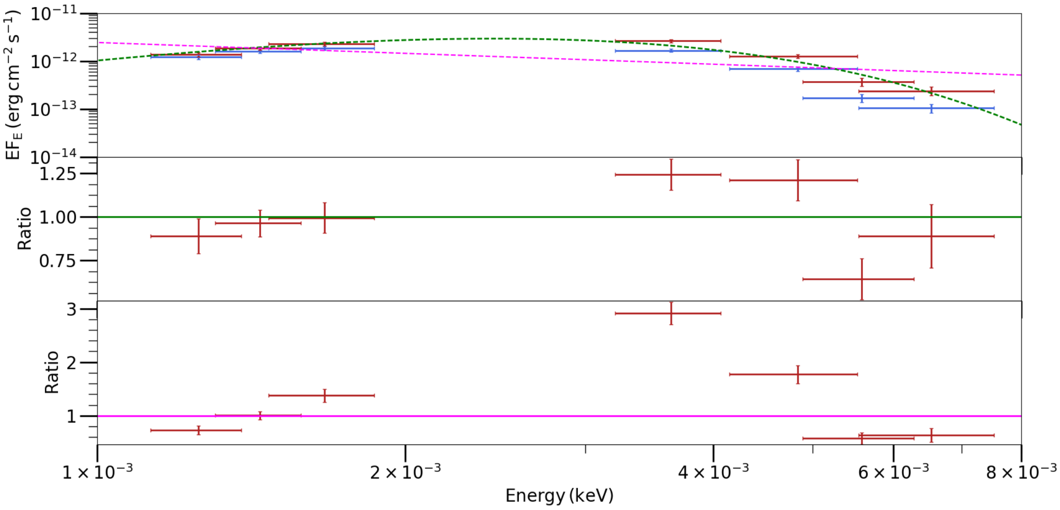

Figure 5.4: Top Panel: The SED of EM170817 at 0.6421 days past the GW trigger. The SED is shown across the UV/optical (1–8 eV). The models shown for comparison (dashed lines) are the spherically outflowing blackbody model (green) and a power-law model (magenta). I display the flux as EF_E. The red data points represent the de-reddened UV/optical. The blue data points represent the UV/optical flux, including absorption measured by UVOT. Middle panel: ratio of data to model for the outflowing blackbody model. Lower panel: ratio of data to model for the power-law model.

The outflow velocity parameter in the blackbody model was initially set to zero. I determined the velocity using the differential of a function fitted to the radius against time fit, then iterated this new velocity until the function's parameters converged. In Fig. 5.5, the fitted model and the model with zero velocity are displayed.

The development of the blackbody (photospheric) radius over time can be examined by fitting my SEDs with my spherically outflowing blackbody model. When modeling the radius, a power-law model with constant provided the best fit, compared with power-law and linear. The power-law model is represented by the magenta line in Fig. 5.5. The best-fit parameters from my model are shown in Eq. 5.1,

$$R_{BB} = (3.4 \pm 2.6) \times 10^{14} + ((3.6 \pm 1.8) \times 10^{10})(t - t_0)^{0.82 \pm 0.37}\,\mathrm{cm} \tag{5.1}$$

where the radius can be expressed as $R_{BB} = R_0 + At^B$. which gives the inferred blackbody radius in terms of the initial radius, R_0, and the time since the event was triggered, $t - t_0$. In this equation, A and B are free parameters determined in fitting. The value that I calculate, $R_0 = (3.4 \pm 2.6) \times 10^{14}$ cm, represents the radius at which the blackbody radiation is first released.

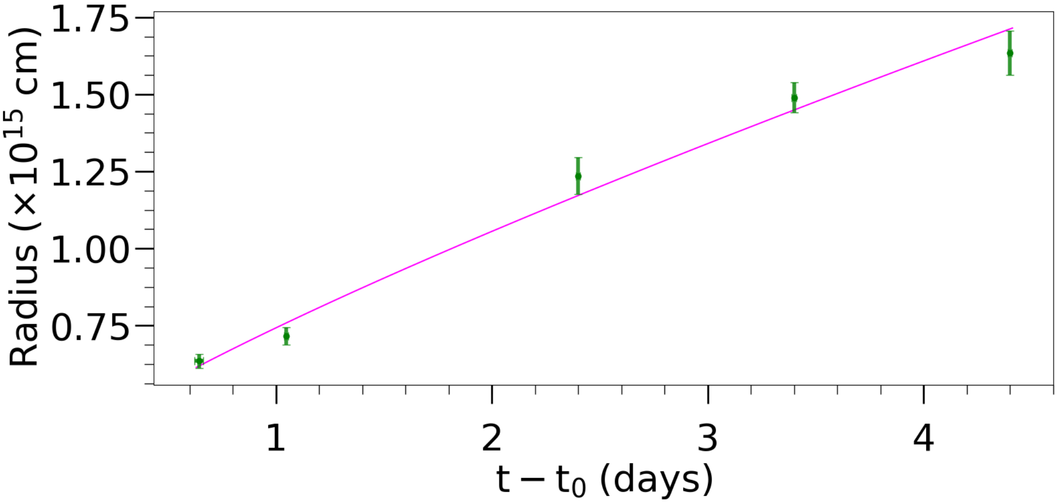

Figure 5.5: The radius against time, determined from fitting UV/optical SEDs with a spherically outflowing blackbody model. The fitted photospheric radii using a stationary blackbody model are shown in green. The linear plus constant model fit to the photospheric radii (Eq. 5.1) is shown as a magenta line.

Table. 5.3 shows the results of the model fits to the SEDs. In Fig. 5.5, the data and model of the outflowing blackbody radius against time are shown. Figure 5.6 contains the complete SEDs with the best-fitting models and data/model ratios.

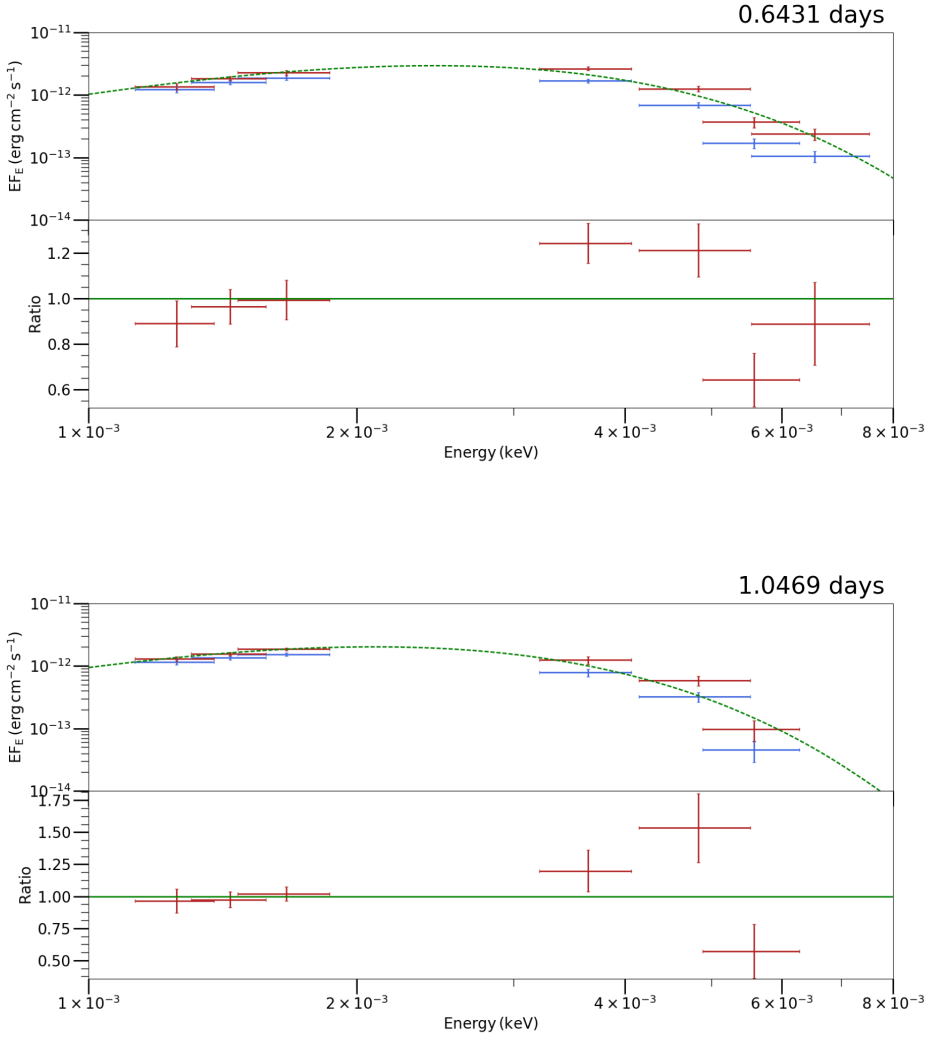

Figure 5.6: The SEDs of GW170817 for all of the times given in Table. 5.3.The SEDs are shown across the UV/optical (1–8 eV). The green dashed line represents the outflowing blackbody model. The flux is displayed as EF_E. The red data points represent the de-reddened UV/optical. The blue data points represent the UV/optical and X-ray flux, including absorption measured by UVOT. The bottom panel of the figure shows the ratio of the data to the model.

Table 5.3: Summary of results for SED fits of GW170827 modelled with a spherical outflowing blackbody component. kT and R represent the energy and radius of the fitted blackbody component, respectively. v/c is the converged value of the velocity/c for the spherically outflowing blackbody. ΔE is the energy range of the SED. χ^2/dof is the best fit chi-square/degrees of freedom. Also shown are the associated p-values for model fits at different times. A p-value greater than 0.05 suggests that the model provides a good fit to the data, while a p-value less than 0.05 suggests a poor fit.

Time (d)	kT (eV)	Blackbody radius R (10^{14} cm)	(v/c)	χ^2/dof	p-value
0.6431	0.57 ± 0.09	6.35 ± 0.22	0.191	21.85/6	1.29e-3
1.0469	0.49 ± 0.11	7.16 ± 0.28	0.152	9.99/5	7.55e-2
2.4	0.30 ± 0.06	12.36 ± 0.59	0.103	21.46/6	1.52e-3
3.4	0.26 ± 0.03	14.89 ± 0.49	0.087	8.76/5	1.19e-1
4.4	0.24 ± 0.03	16.35 ± 0.71	0.077	21.62/6	1.42e-3

5.5 Discussion

In the standard model for GRBs (Meszaros and Rees, 1993; Piran, 2004), the prompt γ-ray emission is produced by a series of internal processes within a highly collimated, ultra-relativistic jet. Electrons accelerate and emit synchrotron afterglow emission as the ejecta expands and shocks the circumburst medium. When fitting the early UV/optical emission at 0.6431 days, I fit both a power-law model and a spherically outflowing blackbody model. The results are shown in 5.2, and I can see that the power-law fit can be rejected based on the poorness of the fit. A power-law would be expected if the emission from EM170817 was produced by synchrotron afterglow radiation; the spectral fit rules this model out as an option and indicate the UV/optical emission at these times is not produced by an on-axis GRB afterglow.

While my UV/optical observations rule out an afterglow origin, the effective blackbody radius, R_{BB}, shown in Table 5.3 shows that the ejecta velocity is a large fraction of the speed of light, c. Using an average outflow velocity of $v = R_{BB}/(t - t_0)$, where $t - t_0$ is the time since the GRB trigger, this velocity is calculated at v(0.06days)= 0.3c, v(1.0days) = 0.2c. These velocities far exceed some of the fastest supernova explosions, e.g., GRB 100316D with a SN expansion velocity of 0.16c, measured from broad spectral features (Bufano

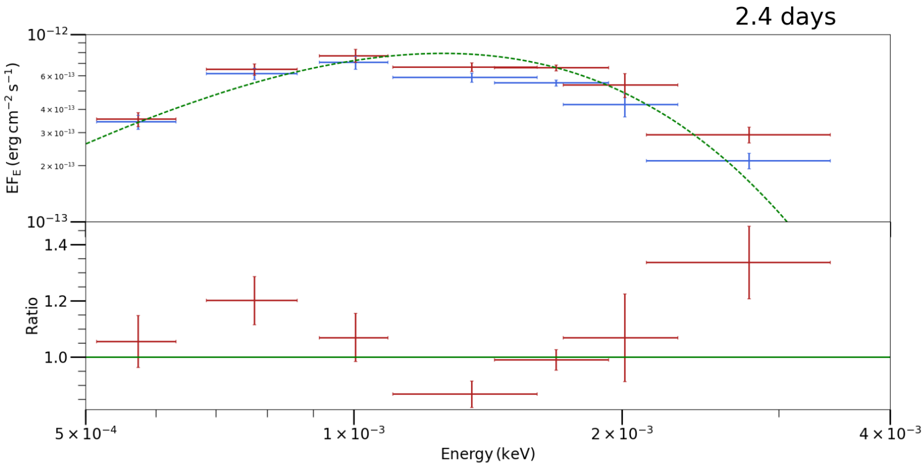

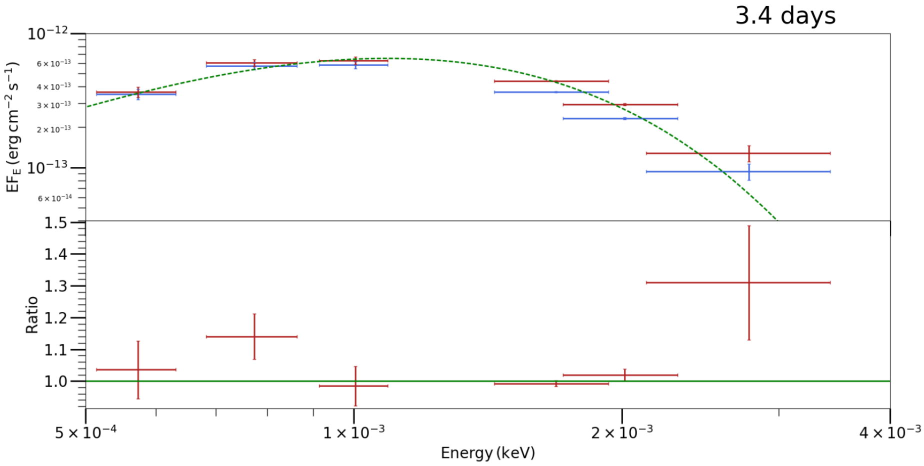

Figure 5.6: caption (continued)

et al., 2012). With the additional feature of the radiation rapidly cooling from UV(0.06 days) to red (1 day), both the velocity and the rate of cooling are consistent with the theoretical predictions of Kilonovae.

When evaluating the fit of the expanding blackbody model, it's essential to also consider alternative models for a comprehensive analysis. I have already ruled out a power-law model, thus excluding a synchrotron afterglow model to explain the UV/optical emission from 0.6-4.4 days. A less physically precise model is a stationary blackbody model, which does not consider the Lorentz boosting factor on the emission energies; these fits are statistically comparable

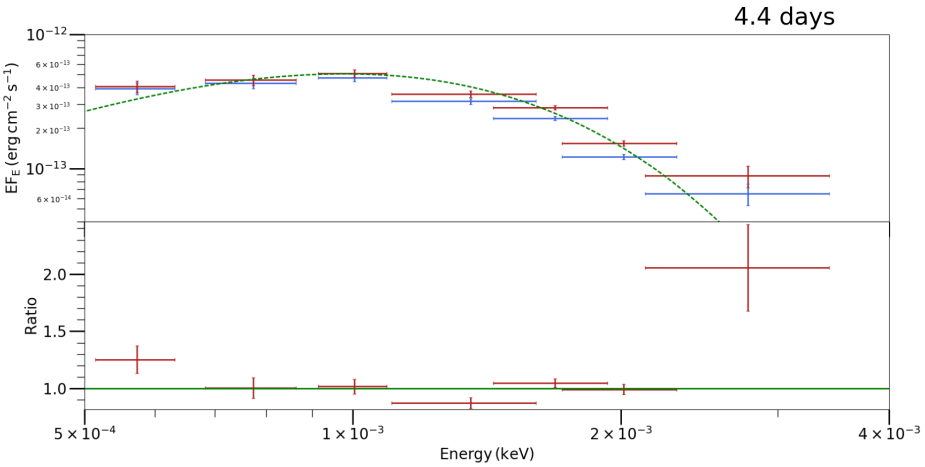

Figure 5.6: caption (continued)

to the expanding blackbody equation Eq. 3.4, but a stationary blackbody is only an approximation of the expanding model, and therefore the parameters from the radius equation would be inaccurate. Further alternative models are variations of the kilonova model explored in Evans et al. (2017), that deal with kilonova wind and dynamical ejecta parameters and viewing angle.

When evaluating the model fits for the SED epochs, I observed that the optical-UV emission generally aligns well with the blackbody peak. However, upon closer examination of the statistical fit quality, I found discrepancies. Specifically, the epochs at 0.6431, 2.4, and 4.4 days yielded p-values less than 0.05, suggesting that these models may not provide an optimal fit to the data. These findings emphasise the significance of the UV residuals at these epochs, especially for UVW1 at 0.6431 days which deviates by 2σ. Although the kilonova characteristics explored in Fig. S4 of Evans et al. (2017) provide some insights, they do not fully account for the observed UV emission discrepancies. Their Fig. 3, for instance, reveals a slight misalignment between their kilonova model and the Pan-STARRS optical/near-infrared data at 0.6 days, while my spherically outflowing blackbody model seems to align more seamlessly, as showcased in Figure 5.6. This comparison underscores the potential of my model in capturing the intricate dynamics of UV and optical/near-IR emissions. Further models or additional parameters may need to be considered to better explain the UV/optical emission during these epochs.

I measured a radius at the origin of the blackbody emission as $R_0 = (3.4 \pm 2.6) \times 10^{14}$ cm. Such a large radius, when compared to that of a $1.4M_\odot$ neutron star, $R_{1.4M_\odot} = 11.0^{+0.9}_{-0.6}$ km, suggests that the observed emission at this epoch originates from a more extended, possibly less lanthanide-rich region of the ejecta. Given the complex nature of the ejecta (with potentially multiple components, different compositions, and a range of velocities), it's quite plausible for the early-time emission to come from such extended regions.

In the framework of the kilonova theory, even during its initial phases, a range of atomic transitions from lanthanide elements results in a pronounced opacity, which in turn hampers the UV emission (Kasen et al., 2013). Notably, the ejecta, which is formed due to tidal forces and the hydrodynamic processes during the instant of the merger (termed as dynamical ejecta), is predominantly neutron-rich, characterised by an electron fraction ($Y_e \leq 0.2$). This composition leads to the generation of a considerable number of heavy nuclei (around 126 neutrons) via the r-process (Burbidge et al., 1957). In comparison, the outflows stemming from the hyper-massive neutron star and the surrounding accretion disk (often termed as the wind) exhibit a composition that's less neutron-rich and has a heightened electron fraction, Y_e. This fraction is postulated to be $Y_e = 0.2$ for rapidly rotating black holes and $Y_e = 0.3$ for outflows from hyper-massive neutron stars (Fernández et al., 2014). Given a raised Y_e, it's predicted that the nucleosynthesis won't proceed beyond atomic nuclei with 50 to 82 neutrons. This composition leads to a diminished opacity, which conversely affects its potential to suppress UV emission. The interplay of merger dynamics, coupled with the subsequent nucleosynthesis, can result in the formation of extensive regions in the ejecta with high opacity. Observational data, such as the early blue emission and the deduced expansive R_0, among other indicators, collectively suggest the existence of such an opaque component in the GW170817 kilonova.

5.6 Conclusions

The joint detection of a short-gamma ray burst and a gravitational wave from a binary neutron star merger has ushered in a groundbreaking era in astrophysics, reaffirming the role of neutron star mergers as progenitors of short gamma-ray bursts and fortifying the foundations of multi-messenger astronomy.

Central to my analysis is the identification of distinct thermal components in the UV/optical emissions, particularly evident from the emission patterns at epochs 0.6431, 1.0469, and 3.4. The prompt UV emission observed at epoch 0.6431 stands out, not only due to its statistical significance but also because of its deviation from canonical kilonova models, highlighting the rapidly fading and intense nature of this UV emission.

A cornerstone of my study is the spherically outflowing blackbody model, which has effectively captured the intricate dynamics of the UV and optical/near-IR emissions. When compared with the findings of Evans et al. (2017), my model exhibits a more seamless alignment, especially evident in the early blue emission at epoch 0.6431. This nuanced agreement underscores the potential of my modelling approach in deciphering the complexities of post-merger emissions.

My observations also indicate a significant opaque wind surrounding the merger, as suggested by the large effective blackbody radius, R_{BB}. Such an extensive radius, particularly when compared to a typical neutron star, implies that the observed emissions at these epochs originate from extended regions, potentially less enriched with lanthanides. This aligns with the kilonova models where atomic transitions of lanthanide elements in the early stages introduce substantial opacity, suppressing the UV emission. The presence of this UV emission, combined with my measurements of the UV residuals at epoch 0.6431, hints at the dynamic interplay of early tidal stripping, merger hydrodynamics, and post-merger nucleosynthesis.

In conclusion, my findings, rooted in the spherically outflowing blackbody model, provide compelling insights into the r-process post-merger dynamics of neutron stars, emphasising the need for a deeper understanding of early UV emissions and their implications in kilonova models.

Chapter 6

GRB-SN sample study

6.1 Introduction

Gamma-Ray Bursts (GRBs) stand as some of the universe's most enigmatic and powerful events. The connection between long-duration GRBs and supernovae (SNe) has garnered substantial attention in astrophysical circles, yet ambiguities persist concerning their emission processes, especially in the X-ray and UV/optical bands. While earlier chapters of this thesis delved into specific GRBs and their unique emission characteristics, this chapter embarks on a comprehensive exploration, analysing a curated sample of GRBs to unravel the nuances of their X-ray and UV/optical emissions.

My systematic approach aims to discern patterns, anomalies, and shared characteristics in the emission processes across different GRBs. By examining both the X-ray and UV/optical realms, I aspire to provide a comprehensive view of GRB emissions, potentially revealing intricacies that may remain obscured in single-wavelength studies.

Section 6.2 delves deep into the reduction and analysis methodology, detailing my GRB-SN sample selection, data reduction procedures, and the intricacies of light curve and SED fitting. In Section 6.3, I furnish detailed results of my comprehensive analysis for each GRB, elucidating their emission profiles and associated supernova signatures. The overarching discussion in Section 6.4 extrapolates the broader implications of my findings, categorising GRBs based on emission traits and probing into the potential influence of redshift and other burst attributes. The chapter culminates with Section 6.5, where I encapsulate my findings, drawing conclusions about their broader significance in high-energy astrophysics.

As I traverse this chapter, I aim to illuminate the multifaceted nature of GRB emissions and contribute meaningfully to the ongoing discourse on the intricate GRB-SN connection.

6.2 Reduction and analysis

6.2.1 GRB-SN sample

I have utilised the grading system constructed by Hjorth and Bloom (2012) to create my sample of GRBs associated with SN. My aim is to gauge the significance of the relationship between GRBs and their associated SNe. ***A*** denotes a SN with strong spectroscopic evidence. ***B*** is a clear and obvious bump in the optical light curve with weak spectroscopic evidence. ***C*** is a clear bump in the optical light curve that is consistent with other GRB-SNe at the spectroscopic redshift of the GRB. ***D*** is a bump in the optical light curve but the inferred SN properties do not fully agree with other GRB-SNe, or the bump is poorly sampled, or there is no spectroscopic redshift of the GRB. ***E*** is a low significance bump in the optical light curve or inconsistent with other GRB-SNe.

Only GRBs that are associated with an SN and have UV/optical measurements taken within 100 ks after the GRB trigger are included in my sample. This condition is required because I aim to probe the pre-SN emission and look for evidence of shock-heated cooling emission, which peaks in the UV bands. Additionally, I require that there is a spectroscopic redshift of the GRB. Furthermore, only GRBs that were observed at redshift $z < 0.6$ are included. Applying these selection criteria gives a sample of 11 GRBs that have an associated SN detection, provided in Table 6.1.

It's worth noting that while GRB060218 and GRB100316D are included in Table 6.1, detailed analyses of these bursts are not presented in sections 6.3 or 6.4. This is because comprehensive studies for these two bursts are already provided in Chapters 3 and 4, respectively. However, they will be considered when examining the ensemble properties of the sample in Section 4.4.

Table 6.1: GRB sample. The GRBs are shown with their corresponding supernova, confirmed redshift to the GRB

GRB	SN	redshift	SN grade	Ref.
060218	2006aj	0.03342	A	
090618	–	0.54	C	
091127	2009nz	0.49044	B	
100316D	2010bh	0.0592	A	
101219B	2010ma	0.55185	A/B	
120422	2012bz	0.28253	A	
130427A	2013cq	0.3399	B	
130831A	2013fu	0.479	A/B	
161219B	2016jca	0.1475	A	
171205	2017pie	0.037	A	
180728	2018fip	0.117	A	

6.2.2 UVOT data reduction and host galaxy correction

I applied the same UVOT data reduction techniques to each GRB in Table 6.1 to produce count rate light curves. Source counts were extracted using a circular aperture of 3 or 5 arcsec radius centred on the position of the GRB. The choice of aperture size was based on the signal-to-noise ratio (S/N). For faint sources, an aperture of 3 arcsec was used when the S/N dropped below 2. If a 3 arcsec aperture was used, the count rates were then corrected to the standard aperture using the curve of growth contained in the calibration files for accurate absolute photometry. Background counts were extracted from a region located outside of the host galaxy. Count rates were obtained using the HEASARC tool UVOTSOURCE and were converted to magnitudes using the UVOT photometric zero points (Breeveld et al., 2011).

The regions of GRB 161219B and GRB 171205 were contaminated by their host galaxy light. For these GRBs, observations were taken by UVOT once the flux had stabilised, allowing us to observe the light from the host galaxy. For

GRB 100316D, the host contribution was addressed in the dedicated chapter for GRB 100316D and hence is not repeated here.

To subtract the host galaxy contamination for GRB 161219B and GRB 171205, I used the same technique on each GRB. A 5 arcsec source aperture was used to measure the count rate in a summed image centred on the times shown in Table 6.2, by which time the GRB had faded beyond detection. This count rate is then subtracted from the count rate measured for the GRB. The host galaxy correction was performed on the measured count rates in each filter available. After subtracting the host contribution, I binned the light curves to achieve a S/N greater than 2. The AB magnitudes of the host galaxy for each GRB are shown in Table 6.2.

Table 6.2: Host galaxy AB magnitudes

GRB 161219B		
t (ks)	mag	filter
9388	19.92 ± 0.09	V
3940	19.00 ± 0.04	B
8771	20.82 ± 0.13	U
8771	21.08 ± 0.17	UVW1
8771	22.15 ± 0.15	UVM2
10329	22.79 ± 0.13	UVW2
GRB 171205		
6759	18.57 ± 0.11	V
6759	19.11 ± 0.08	B
6759	20.28 ± 0.11	U
6759	20.94 ± 0.09	UVW1
6759	21.07 ± 0.07	UVM2
6759	21.26 ± 0.08	UVW2

6.2.3 UV/optical colour

For each GRB, I produced a set of 6 light curves in the UVOT filters: V, B, U, $UVW1$, $UVM2$, $UVW2$. To probe the characteristics of the GRB, I calculated the colour change between the filters. I developed an algorithm to locate filter observations that were close in time to each other and interpolate those filter count rates to a common time.

The algorithm selected measurements based on a range of predefined time differences, X. For my analysis, I utilised values of X set to 50, 100, 500, 1000, and 2000 seconds. The specific value chosen depended on the number of points I had in each filter: more data points allowed for a smaller time difference. These numbers were chosen arbitrarily, ensuring they weren't too large, as a significant change in colour introduces a bias.

Measurements within these time differences were grouped together into an array, $A[...]$. Iterating over this array, the algorithm rejected points that deviated by more than a specified number of standard deviations from the mean count rate of the array. The mean of the final array was denoted as t_{μ}. The count rates in $A[...]$ were then interpolated to t_{μ} to obtain the final count rates for the colour plots. This process was repeated for each iteration, with these data points being removed from the light curve, producing a new light curve with common interpolated count rates for each filter. Data points separated by more than 5000 s were not interpolated. If the light curves showed no evidence for colour change and their flux could be modelled as a power-law in time, the count rate was estimated from the extrapolated power-law for a given time. The count rate light curves were then converted into AB magnitude light curves.

With the new light curves in place, I generated colour plots for $UVM2-V$, $UVM2-B$, and $UVM2-U$. $UVW1$ and $UVW2$ were excluded due to a small red leak in these filters (Brown et al., 2010). Colour changes were identified in the colour plots by a 2σ deviation from a fitted constant across the plot.

Analysing the UVOT colour helps us understand the variations in the spectral shape of the UV/optical emission. Previously, it was observed that the colour $UVM2-U$ shows an excess of optical emission compared to UV at times < 2000 s and at > 10 days, shown in 3. This excess is due to the dominance of synchrotron emission in the UV/optical emission until 2000 s, after which the Rayleigh-Jeans tail of the thermal component dominates. The increase in optical emission after 10 days is due to radioactive Ni^{56} decay from SN 2006aj. Similar methods were used to distinguish the synchrotron component from the contribution of SNe, as seen in GRB 030329 / SN 2003dh (Šimon et al., 2004).

6.2.4 SED creation

The Spectral Energy Distributions (SEDs) were derived from the Vega magnitude light curves, as described in Section 5.3.2. For each measured magnitude on the light curves, a spectral file and a response file were created using the instrument's responsivity and the Vega spectrum for the given magnitude and error. This was repeated for each light curve. The responsivities of the UVOT filters were taken from CALDB version 20170817.

6.2.5 Light curve fitting

The light curves of the GRB afterglows show a variety of behaviours. Modelling these curves enables us to reveal the characteristics of the afterglow emission. The synchrotron model is the most favoured model when describing the UV/optical and X-ray afterglow emission of a GRB. This emission mechanism occurs when the collimated ejecta interact with the external medium, producing synchrotron emission. The observed flux of the synchrotron emission is dependent on the emission frequency relative to the synchrotron self-absorption frequency ν_a, the synchrotron cooling frequency ν_c, and the synchrotron peak frequency ν_m. The microphysical parameters also impact the emission, such as the kinetic energy of the ejecta E_k, the fraction of energy given to the electron and magnetic field, ε_e and ε_m respectively and the properties of the external medium as well as the electron energy index p. It has been shown in previous works that GRBs typically interact in media of constant density medium (Rykoff et al. (2009); Schulze et al. (2011)), and therefore I consider this the case with my sample of GRBs. However, the external shock synchrotron afterglow emission is not always seen. Additional components have been observed that change the light curve shape from the typical power-law decay, synonymous with the external shock model. Some GRBs associated with SNe exhibit atypical afterglow, with thermal components in their spectra; these additional components are produced from the SN shock heated cooling envelope around the progenitor star. GRB 060218 and GRB 100316D are examples of two GRBs that fit this category and that show divergence from the external shock synchrotron model. There is evidence in both cases of brightening in the UV emission at 10-60 ks after the GRB trigger, shown in chapter 3. Therefore, a parabolic component is superimposed on the typical power-law decay. Therefore, it is important to look at all observed GRBs that share similar properties to GRB 060218 and GRB 100316D, and see if their light curves are consistent with the typical external shock model or if there is an additional emission component.

In my light curve fitting, I attempted to fit the afterglow light curves with a variety of power-law models, including one or more power-law components. I removed optical flares that occur in the early emission simultaneous with X-ray observations from the model fitting. The models used are shown in Eq. 6.1, 6.2, 6.3 and 6.4 and are taken from Li et al. (2012).

Eq. 6.1 shows the simple power-law model and Eq. 6.2 gives the smooth broken power-law model. α, α_1, α_2 are the temporal indices, t_b is the power-law break time, and ω provides how sharp the break is.

$$F_1 = F_{01} t^{-\alpha} \tag{6.1}$$

$$F_2 = F_{02} \left[\left(\frac{t}{t_{b,1}} \right)^{\alpha_1 \omega} + \left(\frac{t}{t_{b,1}} \right)^{\alpha_2 \omega} \right]^{-1/\omega}, \tag{6.2}$$

In my light curve fitting, I also included a smooth triple power-law model 6.3. I include this additional model because the afterglow light curve can involve a shallow segment similar to the plateau phase in the X-ray afterglow light curves. This shallow decay phase can be produced by: 1) a refreshed shock, where the leading edge of the external shock decelerates, producing the afterglow, and interacts with slower ejecta arriving later (Rees and Mészáros, 1998; Sari and Mészáros, 2000). 2) The second possibility is due to prolonged central-engine activity, for up to a day (Woosley and Heger, 2006). Following the shallow decay is a possible jet break. The jet break occurs because the relativistic jet decelerates due to its interaction with the circumburst medium. As a result of this deceleration, the relativistic beaming angle, $\theta_j = 1/\Gamma$, increases with time. When $1/\Gamma > \theta_j$, the jet break is observed in the afterglow light curve, and it is seen as a steepening in the decay at all wavelengths.

$$F_3 = (F_2^{-\omega_2} + F_j^{-\omega_2})^{-1/\omega_2} \tag{6.3}$$

where ω_2 represents the sharpness of the jet break time, $t_{b,2}$, and

$$F_j = F_2(t_{b,2}) \left(\frac{t}{t_{b,2}} \right)^{-\alpha_3}. \tag{6.4}$$

Typically jet breaks are observed at 90 ks after the GRB trigger, and opening angle $\theta_j = (2.5 \pm 1.0)^\circ$; however, the observed break times can range from $t_b = (0.4 - 1024)$ ks (Wang et al., 2018), with the typical jet break time of $t_b = 90 \pm 84$ ks.

6.2.5.1 Simultaneous polynomial fitting

In the event where the UV/optical light curve is dominated by the thermal emission attributed to the shock breakout, I use the same modelling techniques as in chapter 3. The polynomials are of the form $At^2 + Bt + C$, where A, B are coefficients, C is a constant, and t is time. The simultaneous fitting models all 6 light curves where they share the same A, B and have six separate constants, so there are 8 fitting parameters. I adopted this modelling approach because there is no colour change when the UV/optical emission is on the Rayleigh-Jeans tail of a blackbody. Therefore the A, B should not change, only the constants, which represent the differences in magnitudes for each filter. From the best-fit polynomial curves, I can create the SED at the mean time of the polynomials.

The SED can be used to determine the extinction curve and host galaxy extinction, $E(B-V)$. I achieve this by assuming that the UV/optical emission is on the Rayleigh-Jeans tail and fitting the SED with the spectral index fixed at $\beta = -2$, leaving only the reddening component as a free parameter in the fit. However, this only applies to GRBs where the afterglow contribution (synchrotron component) is negligible compared to the thermal component.

6.2.6 XRT data

To determine the origin of the UV/optical emission, it is worthwhile to use the X-ray spectra and test if a model can be fitted across optical–X-ray energies. For instance, if the synchrotron afterglow emission from the forward shock is the dominant contributor to the UV/optical emission, then the optical–X-ray SED can be modelled with either a power-law or a broken power-law. The main approach in my SED fitting is checking if the UV/optical SED can be fitted with a Rayleigh-Jeans power-law. However, the spectra can be contaminated with the forward shock synchrotron component. This component can be determined by fitting an additional power-law component to the UV–X-ray SED. Furthermore, the X-ray SED can be used to determine if there is evidence for a thermal component, previously seen in GRB 060218 (chapter 3) and GRB 100316D (Chapter 4). Additionally, I expect that any thermal component in the X-ray emission would have faded sufficiently that it would not be observed at $t > 10$ ks. Therefore, I use this as a cutoff point in my modelling to indicate whether I use a blackbody or a power-law model at X-ray energies.

The XRT data reduction follows the process outlined in Section 3.2.3, with the X-ray spectra extracted at the same times as the UV/optical spectra.

6.2.7 SED fitting

The SED fitting for each GRB is approached in a consistent manner. Following the methods outlined in Section 3.2.2, SEDs are created when observations across the six UVOT filters fall within a specified interval. Where feasible, X-ray SEDs are also generated concurrently with the UV/optical SEDs. These

SEDs are fitted using various combinations of power-law/broken power-law and a blackbody model, as specified by Eq. 6.5, Eq. 6.6, and Eq. 6.7.

$$A_E = K_P E^{-\Gamma} \tag{6.5}$$

$$A_E = \begin{cases} K_P E^{-\Gamma_1}, & \text{if } E \leq E_b. \\ K_P E_b^{\Gamma_2-\Gamma_1}(E/1\ \text{keV})^{-\Gamma_2}), & \text{if } E > E_b. \end{cases} \tag{6.6}$$

$$A_E = \frac{K_{BB} 1.0344 \times 10^{-3} E^2 dE}{e^{E/kT} - 1} \tag{6.7}$$

In these equations, AE represents the photon flux (photon cm^{-2} s^{-1}), K_P and K_{BB} denote the normalisations. The term K_{BB} signifies R^2_{km}/D^2_{10}, where D_{10} is the luminosity distance in units of 10kpc. E is the energy in keV, and kT is the temperature in keV.

Galactic extinction is fixed based on the dust maps detailed by Schlegel et al. (1998). The Galactic absorption column is derived from Willingale et al. (2007) using the Wilms et al. (2000) abundances. Host galaxy absorption and reddening are treated as free parameters during the SED fitting, although host galaxy absorption is set to a fixed value if it can be determined from a late time SED, under the assumption that the X-ray emission follows a single power-law model.

Both the UV/optical SED and the joint UV/optical–X-ray SEDs are modeled as described in Table 6.3. From the spectral fitting, the model with the minimised χ^2/dof is selected as the final model. Consideration is also given to whether the model parameters are physically plausible and an F-test is utilised to determine if certain models fit significantly better than others. All SED fitting procedures are performed using XSPEC V.12.10.1 (Arnaud, 1996).

Table 6.3: List of SED models used in my analysis. Models marked with an asterisk (*) are used only for $t < 10$ ks.

UV/optical	UV/optical–X-ray
power-law	power-law
blackbody	broken power-law
	power-law + blackbody*
	broken power-law +blackbody*

6.3 Results

6.3.1 GRB 090618, z=0.54, SN grade C

6.3.1.1 Light curve modelling

The light curves were modelled with a power-law and a broken power-law (Eq. 6.1, Eq. 6.2). Table 6.4 shows the best-fitted model and parameters for GRB 090618. For all light curves, the broken power-law model provided the best fit. Table 6.4 shows the best-fitted model and parameters for GRB 090618. The optical light curves were well modelled by the broken power-law except for the $UVM2$ and $UVW2$, which did not fit well using either the power-law or broken power-law. The break in the light curve is not achromatic - there is a significant difference in the best-fitted break location in the light curve. By comparing the second power-law index, α_2, the index is consistent between the V, B and $UVW1$, $UVM2$. This consistency, alongside the constant colour, indicates that the supernova is not observed in the UVOT data.

6.3.1.2 Colour analysis

The colour plots for GRB 090618 are shown in Fig. 6.2. The colour plots show some variation at the beginning of the afterglow emission, but the colours remain constant within error thereafter. There is no sign of the supernova optical emission in the UVOT observations. However, the supernova was detected in the R_c and i light curves at t > 10 days (Cano et al., 2011b).

6.3.1.3 UV/optical-X-ray SED fitting

I constructed the UVOT SEDs at 1100, 1400, 25000, 42000, and 74000 s. XRT SEDs were constructed at the same times as the 1100, 1400, 25000 s UVOT

Table 6.4: Results from the light curve fitting of GRB090618. α_1 and α_2 correspond to the power-law indices before and after the break in the light curve, respectively. Moreover, the break time t_b, normalisation N and the chi-squared divided by the degrees of freedom, χ^2/dof.

filter	α_1	α_2	t_b (s)	N ($\times 10^{-15}$)	χ^2/dof
V	0.161 ± 0.180	1.24 ± 0.078	$(3.73 \pm 1.80) \times 10^3$	1.44 ± 0.5	14/14
B	0.568 ± 0.050	1.49 ± 0.095	$(2.29 \pm 0.86) \times 10^4$	0.39 ± 0.15	9/14
U	0.704 ± 0.014	1.85 ± 0.086	$(4.45 \pm 0.53) \times 10^4$	0.21 ± 0.03	35/22
$UVW1$	0.339 ± 0.075	1.46 ± 0.056	$(7.43 \pm 1.90) \times 10^3$	1.54 ± 0.37	16/19
$UVM2$	0.546 ± 0.130	1.52 ± 0.105	$(1.33 \pm 0.94) \times 10^4$	0.8 ± 0.58	39/20
$UVW2$	0.747 ± 0.032	2.45 ± 0.260	$(5.53 \pm 0.90) \times 10^4$	0.16 ± 0.036	34/16

Table 6.5: Results from the SED fitting of GRB090618, across UVOT ($V, B, U, UVW1, UVM2$ and $UVW2$) and XRT (0.3–10) keV. Shown in the table are the results from a blackbody + broken power-law model (BB+BPL). All models are fitted across UVOT and XRT energies. The time at which the SED is taken (data interpolated to this time) are given in the time column. The temperature of the blackbody kT and radius R, power-law indexes β_1 and β_2, the energy at which the power-law breaks E_{break}, absorption in the X-rays was fixed at $N_H = 0.22 \times 10^{22}$ and the UV-optical reddening are fitted for ($E(B-V)$). The chi-squared divided by the degrees of freedom, χ^2/dof is provided for each fit. Additionally, the last column presents the p-value from the F-test comparing the BB+BPL model to a BPL only model.

model	time (s)	kT keV	R (cm)	β_1	β_2	E_{break} keV	NH ($\times 10^{22}$) cm^{-2}	$E(B-V)$ mag	χ^2/dof	F-test p-value
BPL	1100	–	–	0.42 ± 0.04	0.92 ± 0.05	0.13 ± 0.05	0.22	0.03 ± 0.08	171.13/142.0	-
BB+BPL	1100	0.032 ± 0.036	$(2.05 \pm 5.64) \times 10^{15}$	0.47 ± 0.02	0.97 ± 0.02	0.57 ± 0.13	0.22	0.00 ± 0.04	136.02/140.0	1.1×10^{-7}
BPL	1400	–	–	-0.55 ± 0.04	-0.05 ± 0.04	0.29 ± 0.10	0.22	0.00 ± 0.02	157.34/93.0	-
BPL+BB	1400	0.225 ± 0.028	$(3.79 \pm 0.10) \times 10^{12}$	-0.39 ± 0.04	0.11 ± 0.04	2.5 ± 0.6	0.22	0.01 ± 0.02	159/90	1.0
BPL	25000	–	–	-0.68 ± 0.03	-0.18 ± 0.03	0.009 ± 0.004	0.22	0.00 ± 0.05	169/84	-
BPL+BB	25000	0.030 ± 0.066	$(4.84 \pm 25.8) \times 10^{14}$	-0.66 ± 0.04	-0.16 ± 0.04	0.02 ± 0.01	0.22	0.00 ± 0.05	142/82	8.0×10^{-4}
BPL	42000	–	–	-0.7 ± 0.02	-0.2 ± 0.02	0.010 ± 0.005	0.22	0.00 ± 0.02	137/84	-
BPL+BB	42000	0.001 ± 0.043	$(6.27 \pm 65.1) \times 10^{14}$	-0.74 ± 0.04	-0.24 ± 0.04	0.010 ± 0.007	0.22	0.00 ± 0.02	125/82	2.3×10^{-2}
BPL	74000	–	–	-0.55 ± 0.04	-0.06 ± 0.04	0.01 ± 0.18	0.22	0.00 ± 0.01	150/84	-
BPL+BB	74000	0.001 ± 0.163	$(2.22 \pm 91.2) \times 10^{15}$	-0.64 ± 0.04	-0.14 ± 0.04	0.59 ± 0.17	0.22	0.14 ± 0.65	143/82	0.14

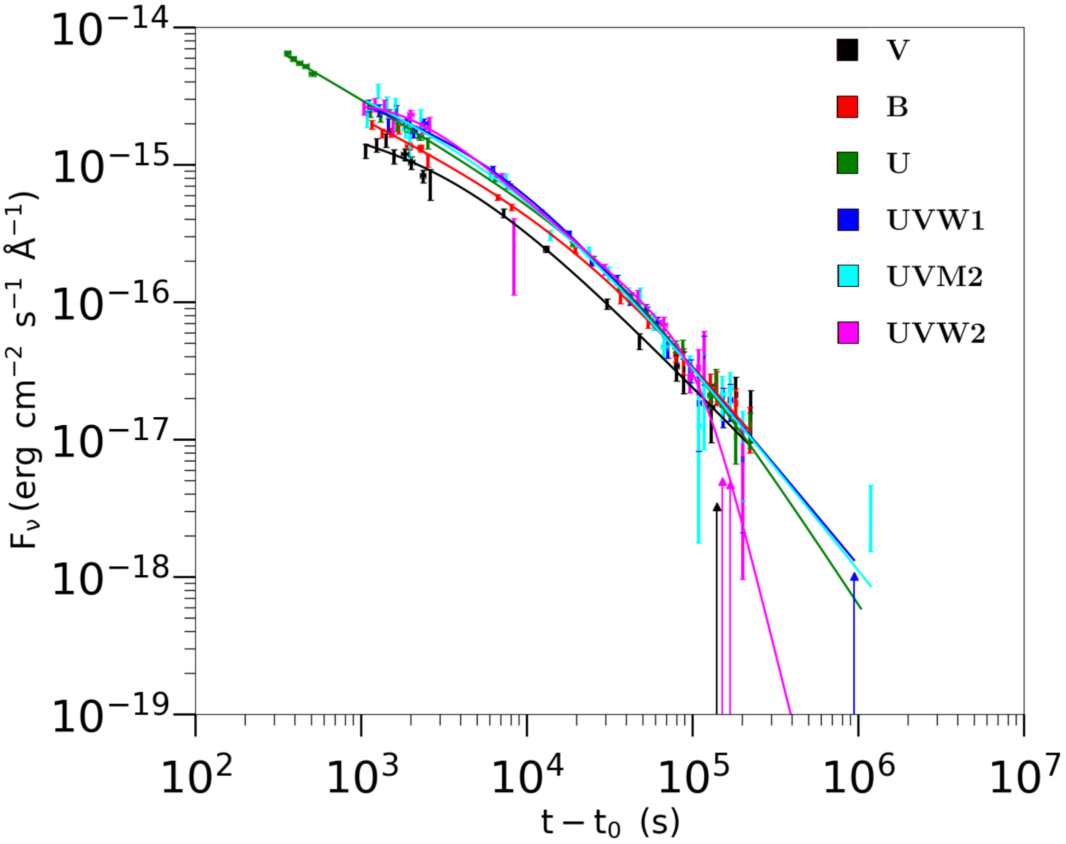

Figure 6.1: GRB 090618 light curve of the optical afterglow. UVOT filters are shown in the key. Up arrows represent 3σ upper limits.

SEDs. The X-ray SED at 25000 s was scaled to the later epochs (42 and 74 ks) based on the light curve following a power-law model. I used the late-time X-ray SED to model the host galaxy absorption at $N_H = 0.22 \times 10^{22}\mathrm{cm}^{-2}$. In my SED fitting, I used a combination of models presented in Table 6.3. Galactic reddening was fixed at $E(B-V) = 0.09$ (Schlegel et al., 1998) and Galactic absorption was fixed to $N_H = 7.59 \times 10^{20}\mathrm{cm}^{-2}$ (Willingale et al., 2007).

I considered the addition of a blackbody component to be a significant improvement over either a power-law or broken-power law model if the F-test probability was $p < 0.05$. For all SEDs, the inclusion of the blackbody component significantly improved the fit compared to the power-law model alone. Additionally, I conducted fits using a combination of blackbody and broken power-law model, yielding a further reduction in chi-squared compared to the blackbody + power-law model. It was also observed that the blackbody

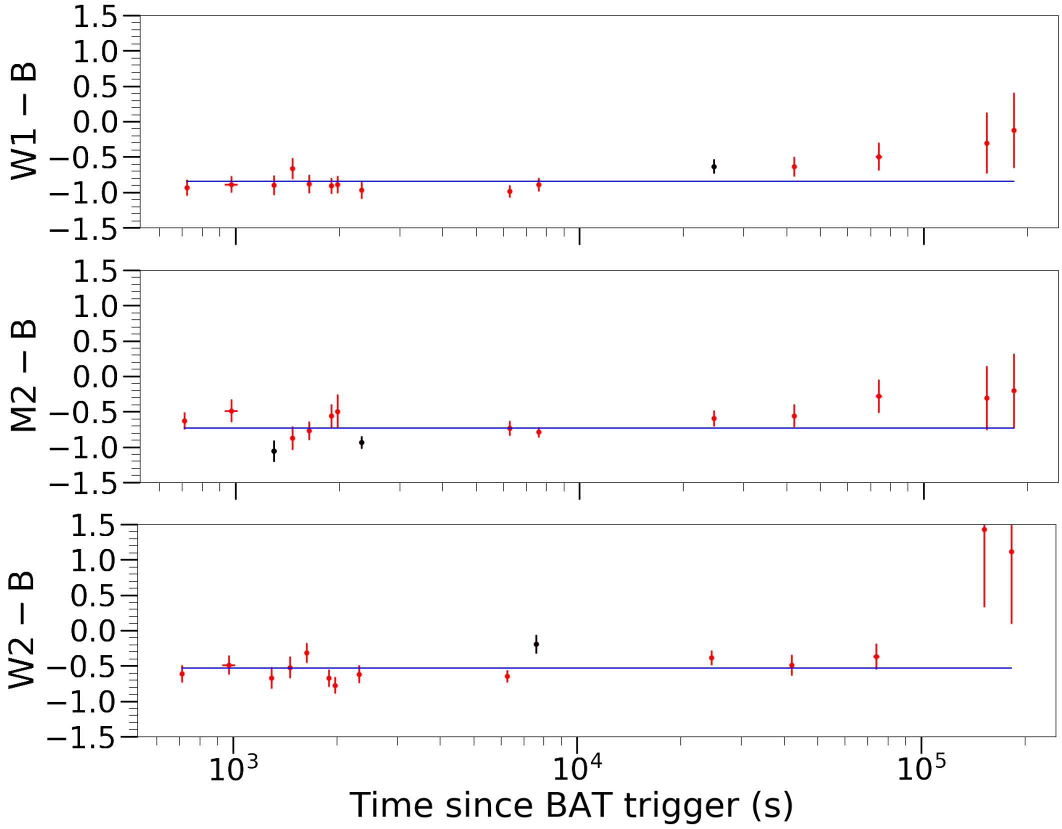

Figure 6.2: Colour indices of the afterglow of GRB090618 (UVOT data). Comparisons are made between *UV* filters (*UVW*1, *UVW*2 and *UVM*2) and the *B* filter. Data points are represented in red. The blue line represents the mean value of the colour index over the duration shown in the figure. Data points are coloured black to denote a colour index $> 3\sigma$ away from the mean value.

+ broken power-law model provided a more adequate fit in certain instances. The F-test p-values affirming these additional improvements can be found in the aforementioned table. The broken power-law was fitted such that the $\beta_2 = \beta_1 + 0.5$, which would be expected if the UV/optical and X-ray were separated by the synchrotron cooling break frequency,ν_c. It must be noted that the UV emission was poorly modelled for all models. This can be seen in my SED figures Fig. 6.3.

Instances were noted where the blackbody + broken power-law model provided a more adequate fit as indicated by the F-statistic. However, the parameters derived from this model exhibited larger error bars, implying a higher degree of uncertainty in these fits. Despite the lower chi-squared value indicating a better statistical fit, the larger uncertainties suggest caution in interpreting these results. Therefore, while the blackbody + broken power-law model may provide a better fit in certain instances, the validity of its predictions may be compromised by the higher uncertainties associated with its parameters.

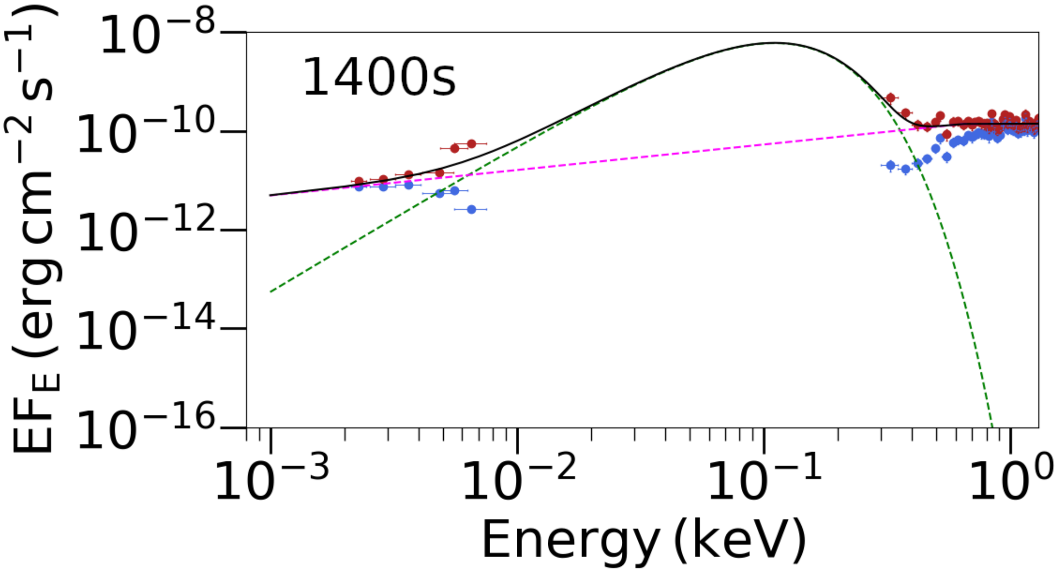

Figure 6.3: The SED of GRB090618 at 1400 s past the GRB trigger. The SED is shown across the UV/optical and X-ray energies (0.0015–10 keV). The models used in the fitting are listed in Table 6.3. The flux is displayed as EF_E. The red data points represent the dereddened UV/optical and unabsorbed X-ray flux. The blue data points represent the UV/optical and X-ray flux including Galactic and host-galaxy reddening and absorption as measured by UVOT and XRT. The dashed lines represent the model components.

6.3.2 GRB 091127, z=0.49, SN grade B

6.3.2.1 Light curve modelling

GRB 091127 was primarily observed with the V,U, and $UVW1$ UVOT filters. There were late-time observations with the $UVW1$,$UVM2$, and $UVW2$ filters (>41 days past the GRB trigger) and one observation with $UVM2$ at 3000 s. Figure 6.4 displays the light curve and best fit models for V,U, and $UVW1$. I fitted the power-law models to the light curves up to 500 ks because the light curves are contaminated by SN 2009nz after this time. The V and U light curves were comparable in break time, with slightly different power-law slopes before and after the break time. This discrepancy might be due to some optical emission contribution in the *V* filter due to the supernova's radioactive decay emission.

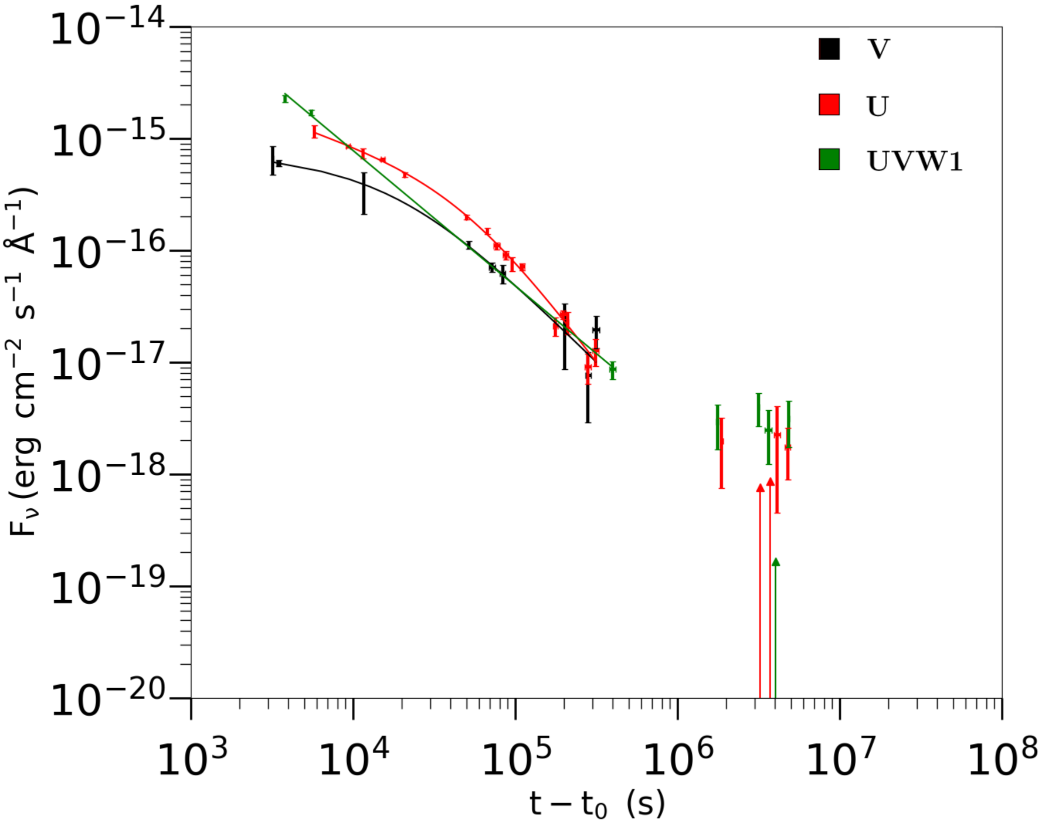

Figure 6.4: GRB 091127 light curve of the optical afterglow. UVOT filters are shown in the key. Up arrows represent 3σ upper limits.

6.3.2.2 Colour analysis

There were insufficient UVOT observations to create a meaningful colour diagram. Therefore, I used the GROND observations from Filgas et al. (2011) to calculate the $U - i$ colour, shown in Figure 6.5. The colour is constant until ~ 200 ks, at which point the supernova emission is shown to contribute to the *i*-band emission.

Table 6.6: Results from the light curve fitting of GRB091127. α_1 and α_2 correspond to the power-law indices before and after the break in the light curve, respectively. Moreover, the break time t_b, normalisation N and the chi-squared divided by the degrees of freedom, χ^2/dof.

filter	α_1	α_2	t_b (s)	N ($\times 10^{-15}$)	χ^2/dof
V	0.11 ± 0.29	1.40 ± 0.16	$(2.03 \pm 1.40) \times 10^4$	0.54 ± 0.35	3/5
U	0.49 ± 0.07	2.00 ± 0.09	$(5.00 \pm 0.87) \times 10^4$	4.10 ± 0.86	15/12
$UVW1$	1.20 ± 0.04	–	–	54000 ± 17000	3/1

Table 6.7: Results from the SED fitting of GRB091127, across UVOT (V,B,U,$UVW1$,$UVM2$ and $UVW2$) and XRT (0.3–10) keV. Shown in the table are the results from both a single power-law (PL) and also a blackbody + power-law (BB+PL). All models are fitted across UVOT and XRT energies. The time at which the SED is taken (data interpolated to this time) are given in the time column. The temperature of the blackbody kT and radius R, power-law index β_1, absorption in the X-rays was fixed at $N_H = 0.1 \times 10^{22}$ and the UV-optical reddening are fitted for ($E(B-V)$). The chi-squared divided by the degrees of freedom, χ^2/dof is provided for each fit. The last column presents the p-value from the F-test comparing the BB+PL model to a PL only model for XRT data, and BB+BPL model to a BPL only model for XRT+UV/opt data

obs:model	time (s)	kT keV	R (cm)	β_1	β_2	E_{break} keV	N_H ($\times 10^{22}$) cm^{-2}	$E(B-V)$ mag	χ^2/dof	F-test p-value
XRT: PL	3300	–	–	0.81 ± 0.02	–	–	0.1	–	158/172	-
XRT: BB+PL	3300	0.060 ± 0.019	$(9.03 \pm 9.96) \times 10^{13}$	0.78 ± 0.03	–	–	0.1	–	148/170	3.9×10^{-3}
XRT+UV/opt:PL	3300	–	–	0.562 ± 0.002	–	–	0.1	0.00 ± 0.01	624/176	-
XRT+UV/opt:BB+PL	3300	0.0348 ± 0.0006	$(2.74 \pm 0.18) \times 10^{15}$	0.571 ± 0.003	–	–	0.1	0.14 ± 0.01	253/174	-
XRT+UV/opt:BPL	3300	–	–	0.20 ± 0.02	0.70 ± 0.03	0.013 ± 0.003	0.1	0.01 ± 0.03	212/175	3×10^{-2}
XRT+UV/opt:BB+BPL	3300	0.0430 ± 0.0023	$(5.32 \pm 1.13) \times 10^{14}$	0.29 ± 0.04	0.79 ± 0.03	0.026 ± 0.008	0.1	0	154/172	6.4×10^{-12}
XRT: PL	15000	–	–	0.72 ± 0.07	–	–	0.10 ± 0.04	–	47/48	-

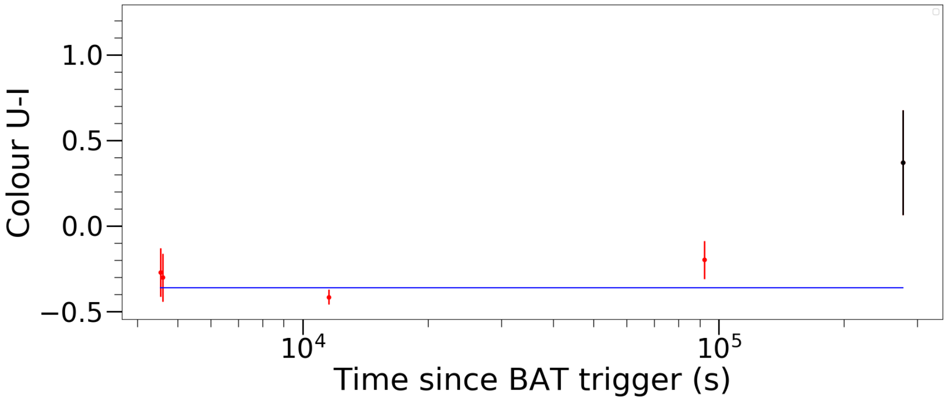

Figure 6.5: Colour indices of the afterglow of GRB091127. Comparisons are made between U filters and the I filter. Data points are represented in red. The blue line represents the mean value of the colour index over the duration shown in the figure. Data points are coloured black to denote a colour index $> 3\sigma$ away from the mean value.

6.3.2.3 UV/optical-X-ray SED fitting

GRB 091127 was observed with both GROND and UVOT. The UVOT U-band provides good coverage of the GRB afterglow emission before the Ni^{56}-powered-emission from SN 2009nz. To test for evidence of a thermal component in the afterglow emission, I created SEDs with the g, r, i, U -band data to use in conjunction with the X-ray data observed during the same times. Due to the scarcity of X-ray data after 4 ks, when it is observed in a lower time resolution PC mode, I selected the g, r, i, U -band data contemporaneous with the X-ray data. I selected X-ray data from 8–20 ks, with this large time range needed to obtain enough data for χ^2 fitting. The results from my SED fitting for GRB 091127 are shown in Table 6.7.

The X-ray SED at 15000 s enabled us to measure the host absorption, $N_H = 0.1 \times 10^{22}$ cm^{-2}. I fixed this value for the absorption in all of my SED fits. At 3300 s, I modelled the X-ray SED with a BB+BPL and found a significant improvement in the χ^2, where F-stat $p = 0.004$. I also modelled the $UVW1$, $UVM2$, g, r, i + X-ray SED with a BB+PL model and found a significant improvement compared to a power-law model, F-stat $p = 6 \times 10^{-12}$. Although the BB+PL model was an improvement over the PL model, there was an excess at >1 keV in the X-ray. I compared a BPL fit with a BPL+BB fit and found the BB+BPL model best fit the SED out of all my models. The thermal component was measured at $kT = 0.043$ keV, $R = (5.32 \pm 1.13) \times 10^{14}$ cm. While the inclusion of a BB model significantly improves the fit, the best-fit blackbody properties are not realistic. The radius, $R = (5.32 \pm 1.13) \times 10^{14}$ cm, implies an expansion speed exceeding c. Therefore, with a p-value of 0.03, the BPL model best fits the data with $\beta_1 = 0.20 \pm 0.02$, $\beta_2 = 0.70 \pm 0.03$ $E_{break} = 0.013 \pm 0.003$ keV, and no host galaxy reddening. It cannot be determined if there is the presence of a thermal component for GRB 091127.

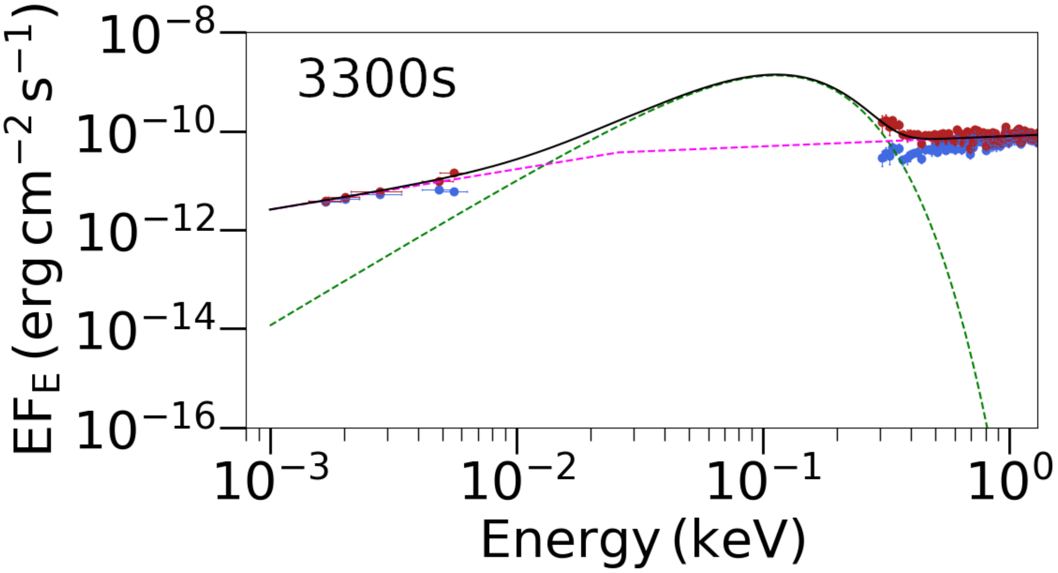

Figure 6.6: The SED of GRB091127 at 3300 s past the GRB trigger. The SED is shown across the UV/optical and X-ray energies (0.0015–10 keV). The models used in the fitting are listed in Table 6.3. The flux is displayed as EF_E. The red data points represent the dereddened UV/optical and unabsorbed X-ray flux. The blue data points represent the UV/optical and X-ray flux including Galactic and host-galaxy reddening and absorption as measured by UVOT and XRT. The dashed lines represent the model components.

6.3.3 GRB 101219B, z=0.552, SN grade A/B

6.3.3.1 Light curve modelling

Figure 6.7 displays the UVOT light curves. The models were fit until 140 ks, which I identified using the colour as the time when the emission from SN 2010bh begins to dominate the afterglow emission. Clear breaks are visible in all UV/optical bands except for $UVW2$. The breaks in the light curve range from 1–100 ks. Differences in the best fit parameters for the power-law model could be due to the lack of $UVW1$ and $UVW2$ observations before 9 ks. The afterglow synchrotron emission produced from the external shocks should decay at a constant rate $F \propto t^{-\beta}$, but in this case, there appears to be an additional emission component. This additional component could be produced by a cooling, expanding, optically thick shell emitting blackbody radiation.

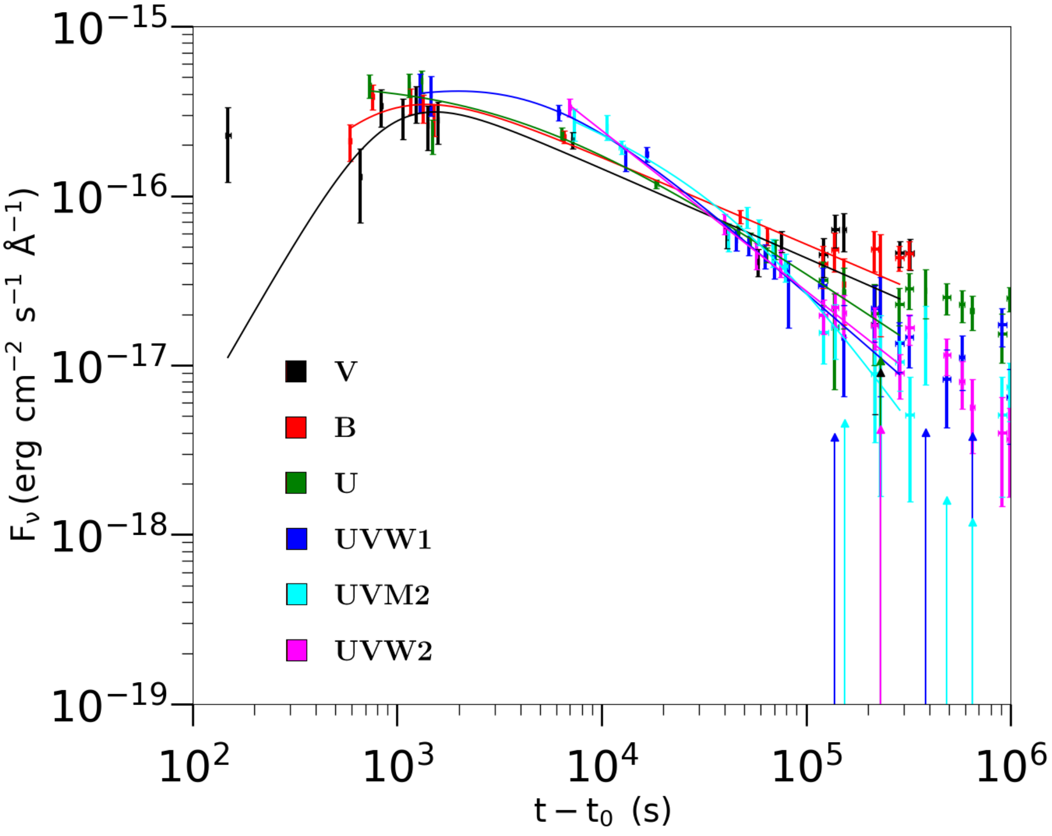

Figure 6.7: GRB 101219B light curve of the optical afterglow. UVOT filters are shown in the key. Up arrows represent 3σ upper limits.

6.3.3.2 Colour analysis

The colour diagram clearly demonstrates the contribution from the radioactive decay of nickel in SN 2010bh starting at 140 ks. There is no noticeable colour change before the appearance of the supernova.

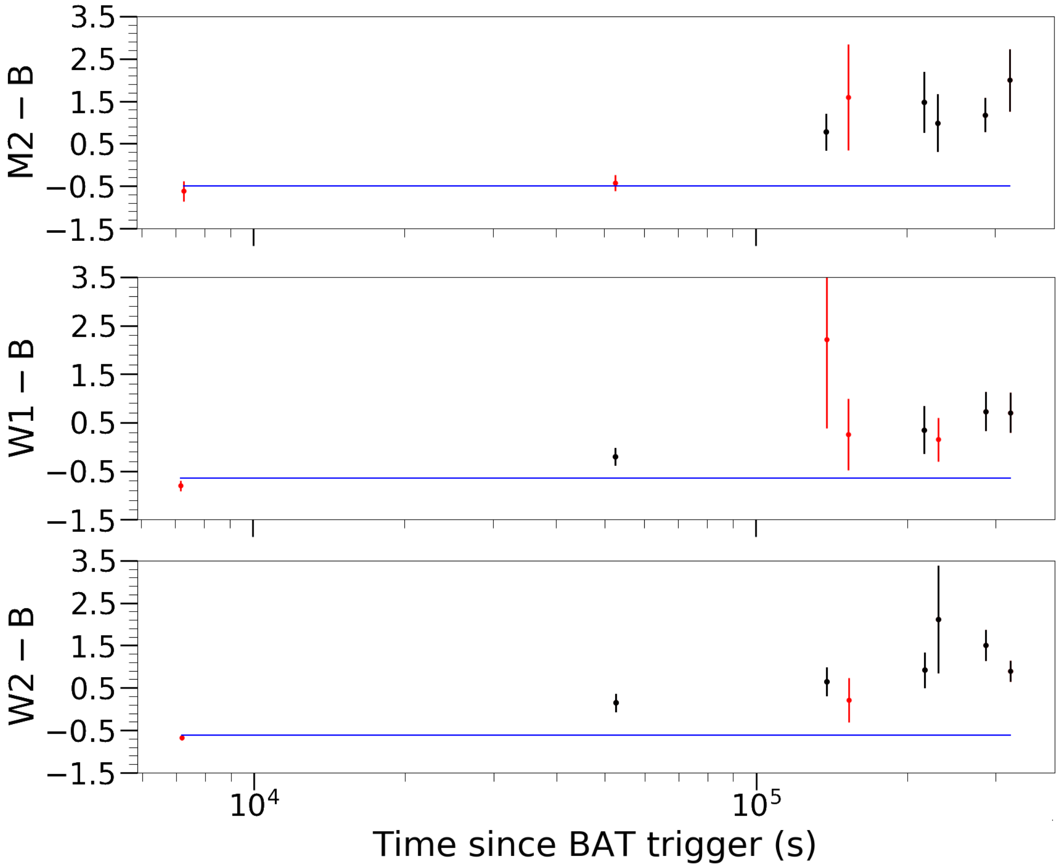

Figure 6.8: Colour indices of the afterglow of GRB 101219B (UVOT data). Comparisons are made between *UV* filters (*UVW*1, *UVW*2 and *UVM*2) and the *B* filter. Data points are represented in red. The blue line represents the mean value of the colour index over the duration shown in the figure. Data points are coloured black to denote a colour index $> 3\sigma$ away from the mean value.

6.3.3.3 UV/optical-X-ray SED fitting

I found that the SED at 53 ks did not constrain the host galaxy absorption. Therefore, in my fitting, I left the absorption as a free parameter. I measured a thermal component in the X-ray spectrum at 400 and 1300 s past the GRB trigger. I checked whether the same blackbody could be significantly contributing to the UV/optical emission and found that when a blackbody

Table 6.8: Results from the light curve fitting of GRB 101219B. α_1 and α_2 correspond to the power-law indices before and after the break in the light curve, respectively. Moreover, the break time t_b, normalisation N and the chi-squared divided by the degrees of freedom, χ^2/dof.

filter	α_1	α_2	t_b (s)	N ($\times 10^{-15}$)	χ^2/dof
V	-2.10 ± 1.01	0.53 ± 0.05	910 ± 180	5.1 ± 0.61	35/17
B	-1.51 ± 0.43	0.52 ± 0.03	820 ± 110	6.1 ± 0.32	11/14
U	-0.06 ± 0.24	0.82 ± 0.10	3400 ± 3100	5.8 ± 2.2	15/16
$UVW1$	-0.35 ± 0.25	1.10 ± 0.08	4400 ± 1700	0.73 ± 0.14	13/16
$UVM2$	0.46 ± 0.40	1.71 ± 0.48	51420 ± 64442	1.2 ± 1.7	13/14
$UVW2$	0.95 ± 0.02	–	–	15154 ± 270	4/10

Table 6.9: Results from the SED fitting of GRB 101219B, across UVOT (V,B,U,$UVW1$, and $UVM2$) and XRT (0.3–10) keV. Shown in the table are the results from both a single power-law (PL) and also a blackbody + power-law (BB+PL). All models are fitted across UVOT and XRT energies. The time at which the SED is taken (data interpolated to this time) are given in the time column. The temperature of the blackbody kT and radius R, power-law index β_1, absorption in the X-rays was left as a free parameter and the UV-optical reddening are fitted for ($E(B-V)$). The chi-squared divided by the degrees of freedom, χ^2/dof is provided for each fit.The last column presents the p-value from the F-test comparing the PL+BB model to a PL only model for XRT data, and PL+BB model to a PL only model for XRT+UV/opt data.

obs:model	time (s)	kT keV	R (cm)	β_1	N_H ($\times 10^{22}$) cm^{-2}	$E(B-V)$ mag	χ^2/dof	F-test p-value
XRT: PL	400	–	–	1.13 ± 0.05	0	–	87/49	-
XRT: PL+BB	400	0.204 ± 0.027	$(7.23 \pm 2.28) \times 10^{12}$	0.42 ± 0.13	0.02 ± 0.082	–	40/47	1.2×10^{-8}
XRT: PL	1300	–	–	0.56 ± 0.09	0	–	28/14	-
XRT: PL+BB	1300	0.114 ± 0.027	$(5.96 \pm 3.23) \times 10^{12}$	0.29 ± 0.13	0	–	10/12	2.1×10^{-3}
XRT+UV/opt: PL	1300	–	–	0.81 ± 0.05	0	0.044 ± 0.043	35/17	-
XRT+UV/opt: PL+BB	1300	0.070 ± 0.010	$(1.48 \pm 1.20) \times 10^{14}$	0.76 ± 0.02	0.52 ± 0.19	0	20/15	1.5×10^{-2}
XRT: PL	53000	–	–	1.15 ± 0.19	0.12 ± 0.09	–	4/9	-
XRT+UV/opt: PL	53000	–	–	1.07 ± 0.01	0.07 ± 0.08	0.01 ± 0.06	20/14	-
XRT+UV/opt: PL+BB	53000	0.0009 ± 0.0002	$(1.45 \pm 0.76) \times 10^{16}$	0.98 ± 0.11	0.012 ± 0.047	0	14/12	0.12

is fit across optical–X-ray energies, the resulting radius is too large. For the UV/optical–X-ray SEDs I fit at 1300 s and 53 ks, the measured thermal components have radii of $R = 1.48 \times 10^{14}$ cm and $R = 1.45 \times 10^{16}$ cm, respectively. The results are presented in Table 6.9, and the fit at 1300s is illustrated in Figure 6.9. This suggests an expansion speed $v > c$, which is not physically plausible. Therefore, I reject this model. The blackbody component is not observable by 53000 s, and the optical–X-ray SED can be fit by a power-law with $\beta = 1.07 \pm 0.01$. This is softer than the power-law measured with the blackbody at 400 s, $\beta = 0.42 \pm 0.13$.

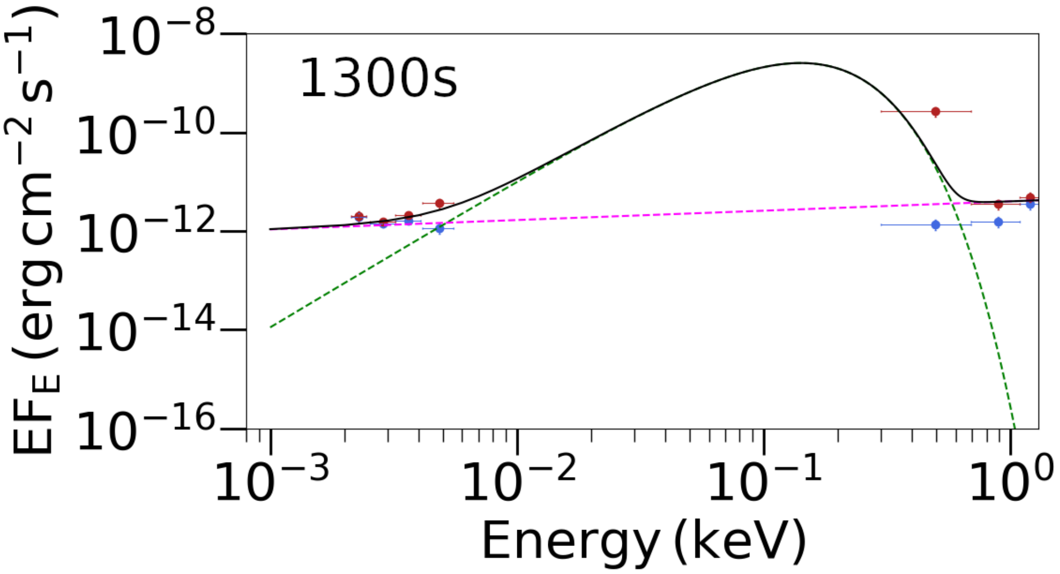

Figure 6.9: The SED of GRB 101219B at 1300 s past the GRB trigger. The SED is shown across the UV/optical and X-ray energies (0.0015–10 keV). The models used in the fitting are listed in Table 6.3. The flux is displayed as EF_E. The red data points represent the dereddened UV/optical and unabsorbed X-ray flux. The blue data points represent the UV/optical and X-ray flux including Galactic and host-galaxy reddening and absorption as measured by UVOT and XRT. The dashed lines represent the model components.

6.3.4 GRB 120422, z=0.283, SN grade A

6.3.4.1 Light curve modelling

All light curves were fit with a broken power-law. The first observations with UVOT only detected UV emission, with the optical emission brightening at around 10 ks. The breaks in the light curves seem to shift with increase in the energy of the emission, possibly suggesting a thermal component that is peaking around UV/optical energies. The light curves were only fitted until 200 ks, which is when the supernova radioactive nickel decay begins to dominate the afterglow emission.

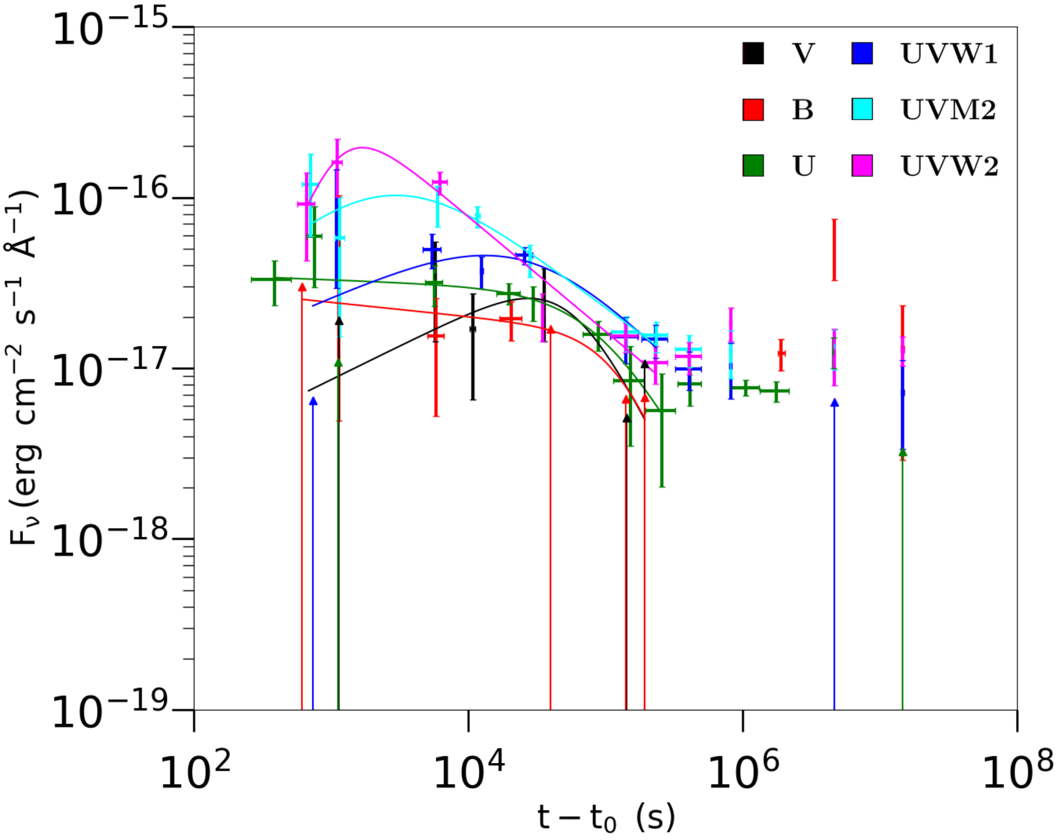

Figure 6.10: GRB 120422 light curve of the optical afterglow. UVOT filters are shown in the key. Up arrows represent 3σ upper limits.

6.3.4.2 Colour analysis

The $M2$–optical colour plots, shown in Figure 6.11, are limited to data before 200 ks due to UV emission fading and no longer being detectable by UVOT, but no significant colour changed are observed. However, the increase in the optical emission from the light curve in Figure 6.10 gives us a rough idea of when the supernova is having a large contribution to the optical emission.

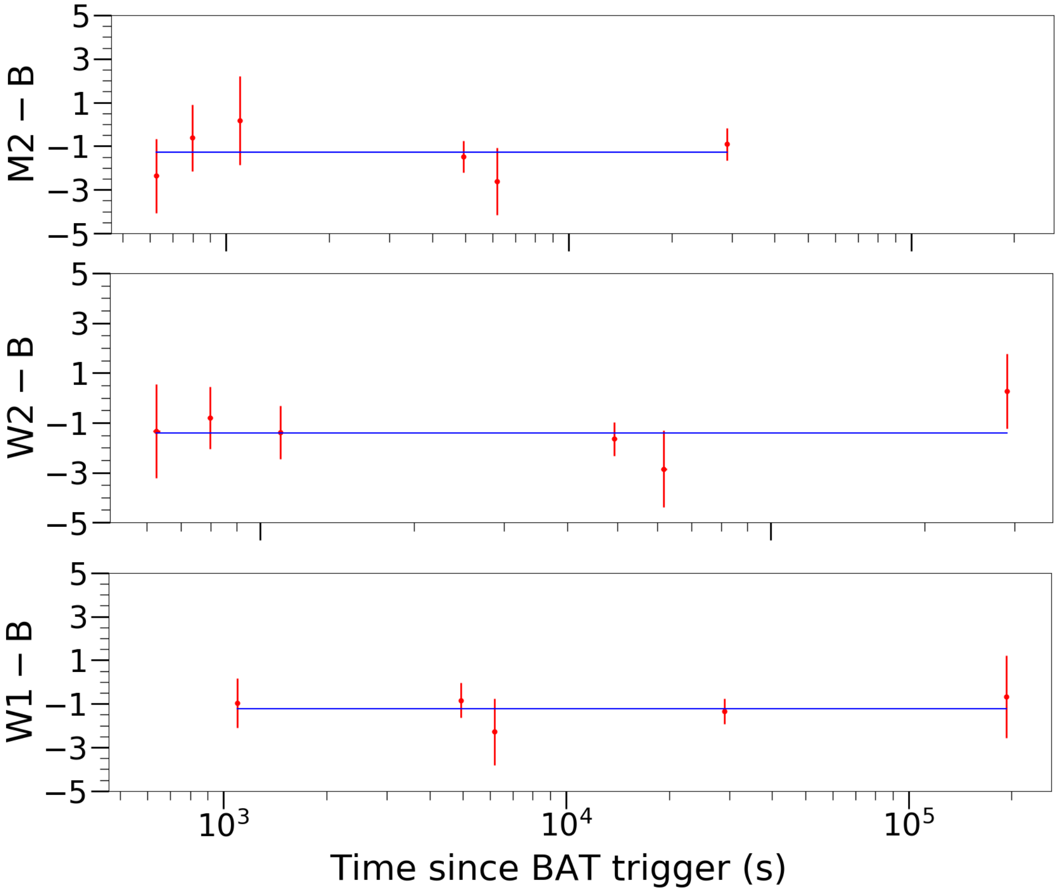

Figure 6.11: Colour indices of the afterglow of GRB 120422 (UVOT data). Comparisons are made between *UV* filters (*UVW*1, *UVW*2 and *UVM*2) and the *B* filter. Data points are represented in red. The blue line represents the mean value of the colour index over the duration shown in the figure.

6.3.4.3 UV/optical-X-ray SED fitting

SEDs were obtained at times that coincided with UVOT observations in all filters, and the X-ray SED was obtained for the XRT observations from 2-100 ks, assuming that the spectral shape of the X-ray emission is not changing during this time. A thermal component was identified that shifts from $kT = 26 \pm 0.4$ eV to $kT = 2.9 \pm 0.6$ eV (28–141 ks) and expands from $R = (1.05 \pm 0.43) \times 10^{14}$ cm to $R = (5.75 \pm 2.38) \times 10^{14}$ cm. This translates to an average expansion velocity of approximately 0.139c, relative to the speed of light, during the observed period. However, it should be noted that a fit incorporating a broken power-law model plus a blackbody could not be performed due to an insuffi-

Table 6.10: Results from the light curve fitting of GRB 120422. α_1 and α_2 correspond to the power-law indices before and after the break in the light curve, respectively. Moreover, the break time t_b, normalisation N and the chi-squared divided by the degrees of freedom, χ^2/dof.

filter	α_1	α_2	t_b (ks)	N ($\times 10^{-15}$)	χ^2/dof
V	-0.40 ± 0.56	1.60 ± 1.51	55 ± 76	0.42 ± 0.26	1.9/7
B	0.083 ± 0.087	2.2 ± 2.4	140 ± 55	0.16 ± 0.05	0.8/7
U	0.031 ± 0.34	1.5 ± 0.28	98 ± 20	0.29 ± 0.04	1.5/9
$UVW1$	-0.36 ± 0.34	0.82 ± 0.35	27 ± 35	0.84 ± 0.24	4.4/7
$UVM2$	-0.68 ± 0.5	0.61 ± 0.08	2.7 ± 1.9	2.1 ± 0.27	2.2/7
$UVW2$	-2.2 ± 1.7	0.67 ± 0.066	1.1 ± 0.32	3.4 ± 0.61	5.5/6

Table 6.11: Results from the SED fitting of GRB 120422, across UVOT ($V, B, U, UVW1, UVW2$ and $UVM2$) and XRT (0.3–10) keV. Shown in the table are the results from both a single power-law (PL) and also a blackbody + power-law (BB+PL). All models are fitted across UVOT and XRT energies. The time at which the SED is taken (data interpolated to this time) are given in the time column. The temperature of the blackbody kT and radius R, power-law index β_1, absorption in the X-rays was left as a free parameter and the UV-optical reddening are fitted for ($E(B-V)$). The chi-squared divided by the degrees of freedom, χ^2/dof is provided for each fit. The last column presents the p-value from the F-test comparing the PL+BB model to a PL only model.

obs:model	time (s)	kT keV	R (cm)	β_1	N_H ($\times 10^{22}$) cm^{-2}	$E(B-V)$ mag	χ^2/dof	F-test p-value
XRT+UVOT: PL	1100.0	–	–	0.998 ± 0.054	0.00 ± 0.01	0.000 ± 0.006	12/9	-
XRT+UVOT: PL+BB	1100.0	0.024 ± 0.032	$(6.55 \pm 22.3) \times 10^{13}$	0.927 ± 0.108	0.000 ± 0.001	0.00 ± 0.03	11/7	0.74
XRT+UVOT: PL	5900.0	–	–	1.254 ± 0.068	0.043 ± 0.051	0.23 ± 0.07	28/9	-
XRT+UVOT: PL+BB	5900.0	0.088 ± 0.021	$(2.46 \pm 2.23) \times 10^{12}$	1.202 ± 0.075	0.64 ± 0.332	0.19 ± 0.08	24/7	0.58
XRT+UVOT: PL	28000.0	–	–	1.065 ± 0.024	0.00 ± 0.01	0.01 ± 0.02	71/9	-
XRT+UVOT: PL+BB	28000.0	0.026 ± 0.004	$(1.05 \pm 0.43) \times 10^{14}$	0.806 ± 0.117	0.00 ± 0.03	0.00 ± 0.01	24/7	2.2×10^{-2}
UVOT: PL	141000.0	–	–	-1.72 ± 0.28	–	0.00 ± 0.54	4/5	-
UVOT: BB	141000.0	0.0029 ± 0.0006	$(5.75 \pm 2.38) \times 10^{14}$	–	–	0.00 ± 0.01	5/3	1.0

cient number of data points.

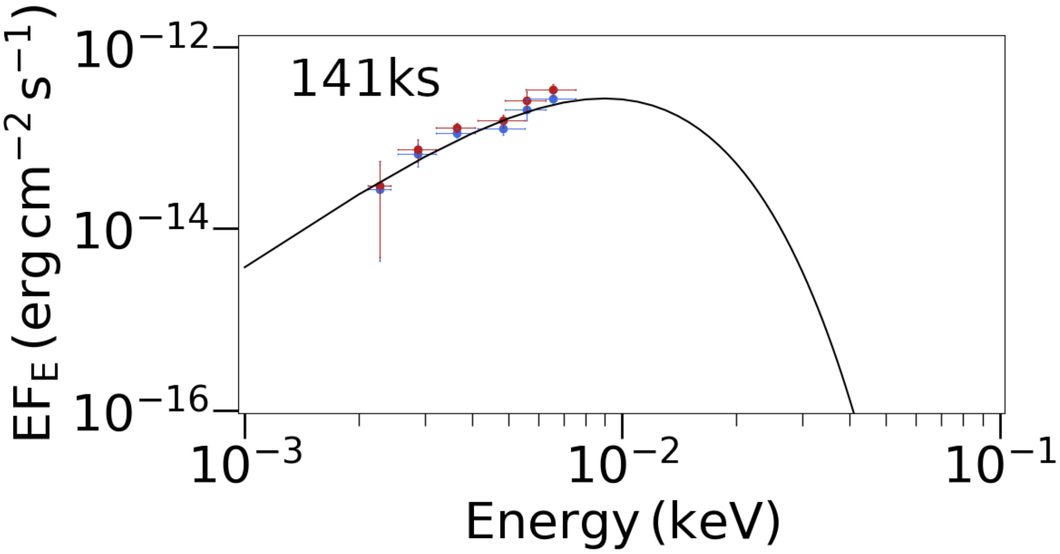

Figure 6.12: The SED of GRB 120422 at 141 ks past the GRB trigger. The XRT did not sufficiently cover this time period, therefore I fit and display only UVOT data. The SED is shown across the UV/optical range and the Wien tail of the blackbody model (0.001-0.1 keV). The models used in the fitting are listed in Table 6.3. The flux is displayed as EF_E. The red data points represent the dereddened UV/optical. The blue data points represent the UV/optical flux including Galactic and host-galaxy reddening as measured by UVOT. The dashed lines represent the model components.

6.3.5 GRB 130427A, z=0.34, SN grade B

6.3.5.1 Light curve modelling

The light curve can be modelled with a broken power-law for V and B, and a power-law model. The break in the light curve occurs at the same time in the $U, UVW1, UVM2$ and $UVW2$ light curves at $t_b = 200-340$ ks. The light curve fitting was cut at 300 ks due to the presence of the radioactive nickel decay from SN 2013cq.

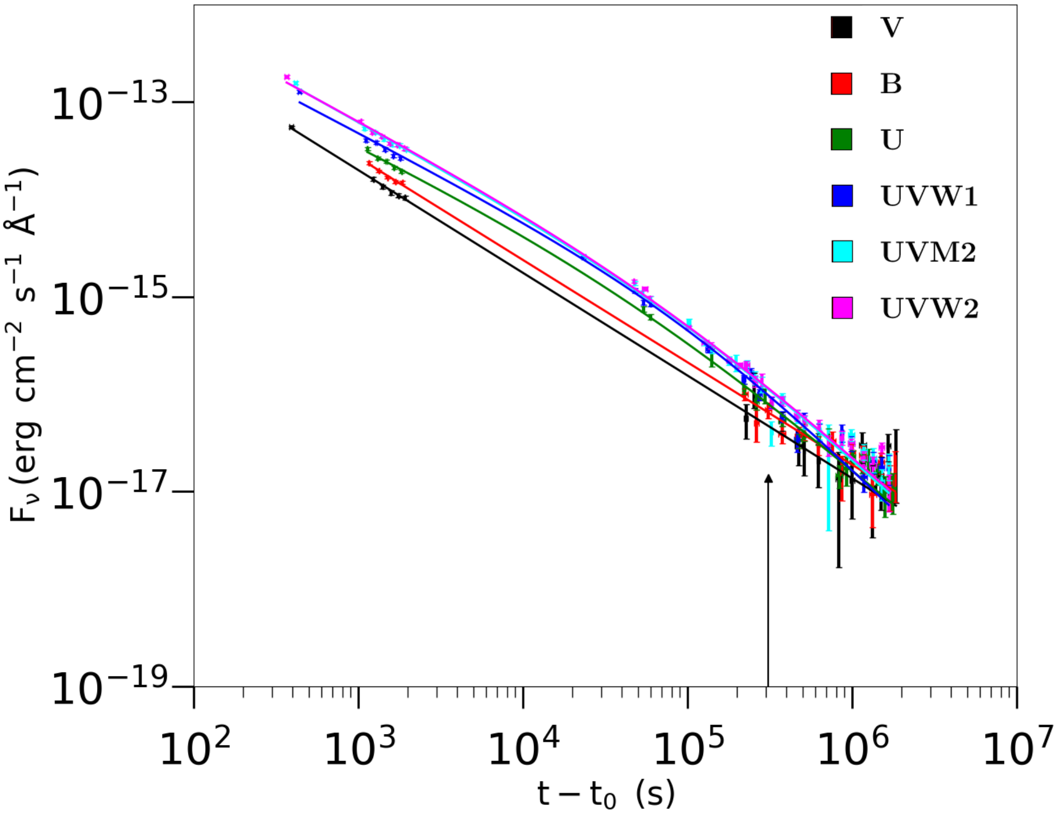

Figure 6.13: GRB 130427A light curve of the optical afterglow. UVOT filters are shown in the key. Up arrows represent 3σ upper limits.

6.3.5.2 Colour analysis

The colour was constant until the contribution from SN 2013cq at around ~ 250 s.

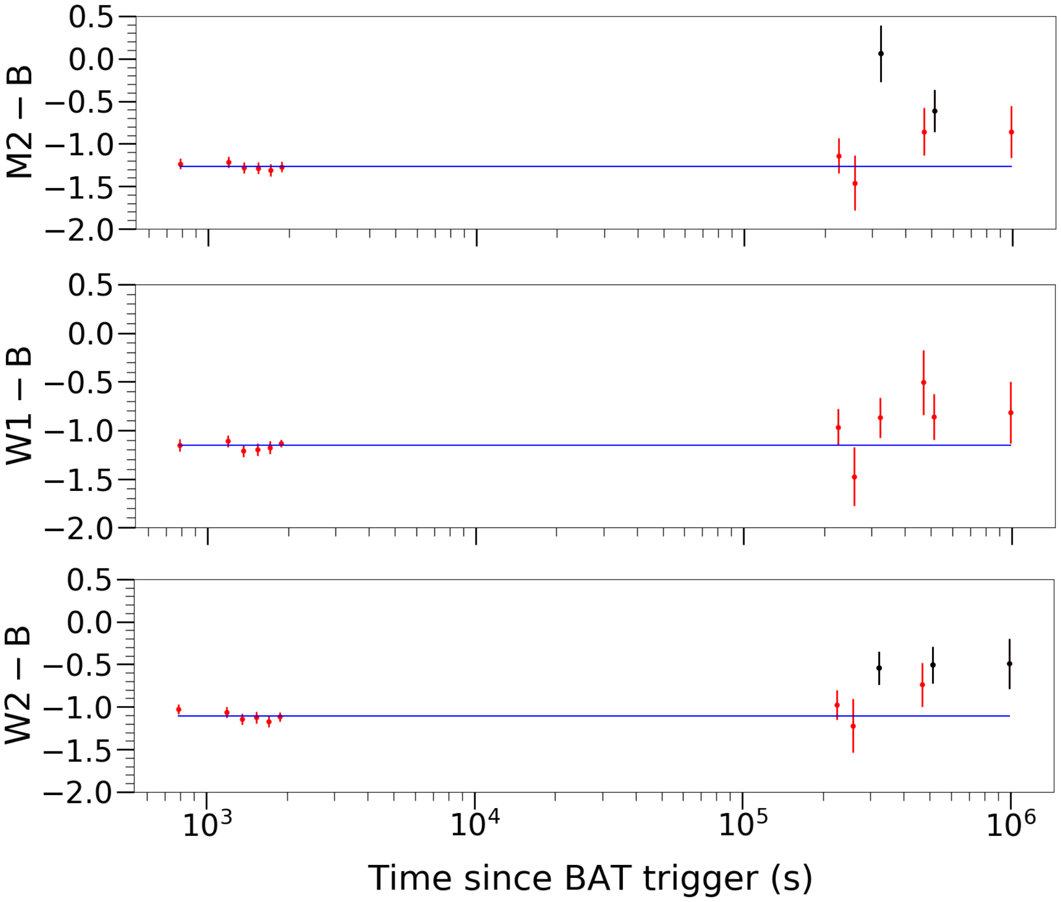

Figure 6.14: Colour indices of the afterglow of GRB 130427A (UVOT data). Comparisons are made between UV filters ($UVW1$, $UVW2$ and $UVM2$) and the B filter. Data points are represented in red. The blue line represents the mean value of the colour index over the duration shown in the figure. Data points are coloured black to denote a colour index $> 3\sigma$ away from the mean value.

6.3.5.3 UV/optical-X-ray SED fitting

The host galaxy absorption was calculated from the X-ray SED at 59 ks as $(N_H = 0.108 \pm 0.024) \times 10^{22}$ cm^{-2}. The absorption was fixed at this value for all of the model fits. The optical–X-ray SED was best modelled with an additional blackbody component, because a single power-law resulted in a poor fit. However, the thermal component is too large. Therefore, an additional component is needed to explain the UV/optical–X-ray emission during this time.

Table 6.12: Results from the light curve fitting of GRB 130427A. α_1 and α_2 correspond to the power-law indices before and after the break in the light curve, respectively. Moreover, the break time t_b, normalisation N and the chi-squared divided by the degrees of freedom, χ^2/dof.

filter	α_1	α_2	t_b (ks)	N ($\times 10^{-16}$)	χ^2/dof
V	1.11 ± 0.013	–	–	37000 ± 3300	9/10
B	1.13 ± 0.015	–	–	51000 ± 5600	12/9
U	0.99 ± 0.015	3.20 ± 1.5	340 ± 53	1.08 ± 0.17	17/13
$UVW1$	0.95 ± 0.02	2.30 ± 0.38	210 ± 37	3.22 ± 0.86	63/16
$UVM2$	0.99 ± 0.016	2.33 ± 0.3	270 ± 34	2.54 ± 0.51	28/20
$UVW2$	0.96 ± 0.022	2.09 ± 0.22	200 ± 38	3.87 ± 1.2	53/20

Table 6.13: Results from the SED fitting of GRB 130427A, across UVOT ($V,B,U,UVW1,UVW2$ and $UVM2$) and XRT (0.3–10) keV. Shown in the table are the results from both a single power-law (PL) and also a blackbody + power-law (BB+PL). All models are fitted across UVOT and XRT energies. The time at which the SED is taken (data interpolated to this time) are given in the time column. The temperature of the blackbody kT and radius R, power-law index β_1, absorption in the X-rays was fixed at $N_H = 0.1 \times 10^{22}$ and the UV-optical reddening are fitted for ($E(B-V)$). The chi-squared divided by the degrees of freedom, χ^2/dof is provided for each fit. The last column presents the p-value from the F-test comparing the PL+BB model to a PL only model.

obs:model	time (s)	kT keV	R (cm)	β_1	N_H ($\times 10^{22}$) cm^{-2}	$E(B-V)$ mag	χ^2/dof	F-test p-value	
XRT: PL	787	–	–	0.599 ± 0.016	0.1	–	373/306	-	
XRT: PL+BB	787	0.090 ± 0.023	$(4.59 \pm 2.82) \times 10^{13}$	0.557 ± 0.021	0.1	–	357/304	1.2×10^{-3}	
XRT+UVOT: PL	787	–	–	0.648 ± 0.003	0.1	0.00 ± 0.01	1146/301	-	
XRT+UVOT: PL+BB	787	0.033 ± 0.002	$(7.69 \pm 0.97) \times 10^{15}$	0.567 ± 0.006	0.1	0.00 ± 0.03	332/299	1.1×10^{-16}	
XRT: PL	1878	–	–	0.663 ± 0.018	0.1	–	312/258	-	
XRT: PL+BB	1878	0.012 ± 0.037	$(1.92 \pm 78.6) \times 10^{20}$	0.656 ± 0.019	0.1	–	307/256	0.13	
XRT+UVOT: PL	1878	–	–	0.686 ± 0.003	0.1	0.00 ± 0.02	1022/263	-	
XRT+UVOT: PL+BB	1878	0.024 ± 0.005	$(4.59 \pm 0.10) \times 10^{15}$	0.594 ± 0.006	0.1	–	383/261	2.6×10^{-56}	
XRT: PL	59000	–	–	0.697 ± 0.048	0.108 ± 0.024	–	79/95	-	
XRT+UVOT: PL	59000	–	–	0.852 ± 0.007	0.093 ± 0.009	0.000 ± 0.004		154/98	-

6.3.6 GRB 130831A, z=0.479, SN grade A/B

6.3.6.1 Light curve modelling

The light curves were best fit with a single power-law. A Flare, that was present in the X-ray light curve, was not included in the power-law fit. Nor was the contribution from the supernova at $t > 200$ ks. The average temporal index was $\alpha \sim 0.88$, which was the observed shape for all of the filters.

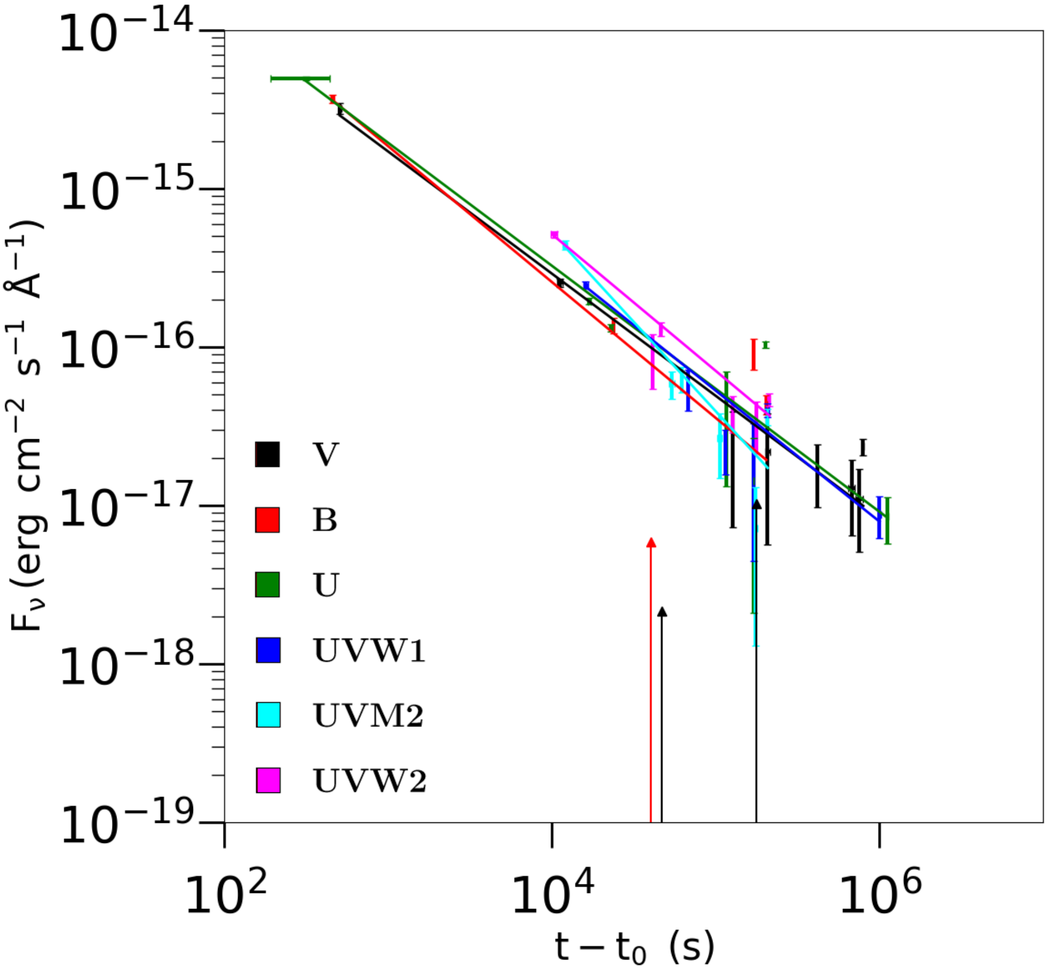

Figure 6.15: GRB 130831A light curve of the optical afterglow. UVOT filters are shown in the key. Up arrows represent 3σ upper limits.

6.3.6.2 Colour analysis

There were not enough UVOT observations to observe the colour for GRB 130831A.

Table 6.14: Results from the light curve fitting of GRB 130831A. α_1 corresponds to the power-law index. Moreover, the normalisation is represented by N and the chi-squared divided by the degrees of freedom, χ^2/dof.

filter	α_1	N ($\times 10^{-13}$)	χ^2/dof
V	0.84 ± 0.020	6.1 ± 1.0	7/6
B	0.86 ± 0.055	6.9 ± 2.9	55/5
U	0.78 ± 0.04	4.2 ± 1.3	306/6
$UVW1$	0.84 ± 0.066	7.9 ± 5.4	22/5
$UVM2$	1.10 ± 0.075	170 ± 130	29/6
$UVW2$	0.86 ± 0.032	15 ± 4.6	14/6

Table 6.15: Results from the SED fitting of GRB 130831A, across UVOT ($V, B, U, UVW1, UVW2$ and $UVM2$) and XRT (0.3–10) keV. Shown in the table are the results from both a single power-law (PL) and also a blackbody + power-law (BB+PL). All models are fitted across UVOT and XRT energies. The time at which the SED is taken (data interpolated to this time) are given in the time column. The temperature of the blackbody kT and radius R, power-law index β_1, absorption in the X-rays was left as a free parameter and the UV-optical reddening are fitted for ($E(B-V)$). The chi-squared divided by the degrees of freedom, χ^2/dof is provided for each fit. The last column presents the p-value from the F-test comparing the PL+BB model to a PL only model.

obs:model	time (s)	kT keV	R (cm)	β_1	N_H ($\times 10^{22}$) cm^{-2}	$E(B-V)$ mag	χ^2/dof	F-test p-value
XRT: PL	707	–	–	0.665 ± 0.111	0.0 ± 0.01	–	10.68/10	-
XRT: PL+BB	707	1.28 ± 0.16	$(1.05 \pm 0.27) \times 10^{11}$	3.28 ± 1.20	0.29 ± 0.192	–	12.1/8	1.0
XRT+UVOT: PL	707	–	–	1.055 ± 0.011	0.0 ± 0.011	0.0 ± 0.1	37/14	-
XRT+UVOT: PL+BB	707	0.0020 ± 0.0006	$(2.10 \pm 1.29) \times 10^{16}$	1.018 ± 0.027	0.0 ± 0.1	0.00 ± 0.04	26.22/12	0.12
XRT: PL	15000	–	–	0.675 ± 0.105	0.055 ± 0.064	–	31.09/23.0	-
XRT: PL+BB	15000	0.079 ± 0.014	$(3.96 \pm 4.54) \times 10^{13}$	0.947 ± 0.171	0.716 ± 0.331	–	27.3/21.0	0.26
XRT+UVOT: PL	15000	–	–	0.934 ± 0.010	0.00 ± 0.01	0.0 ± 0.1	53.22/25.0	-
XRT+UVOT: PL+BB	15000	1.16 ± 0.13	$(2.26 \pm 0.55) \times 10^{10}$	0.997 ± 0.022	0.008 ± 0.009	0.0 ± 0.3	32.35/23.0	3.3×10^{-3}

6.3.6.3 UV/optical-X-ray SED fitting

The best fit model was a power-law model at all of the epochs I looked at. A blackbody model plus power-law improves the fit but it is not a significant improvement for any of the times. There was also no consistency with the blackbody parameters in my fits. This indicates there is no clear evidence for a blackbody component in the UV/optical emission.

6.3.7 GRB 161219B, z=0.148, SN grade A

6.3.7.1 Light curve modelling

The light curves exhibited substantial variability in their fitted parameters, with a broken power-law model providing the best fit across the board. There was no common break time across the light curves. The B-band data were excluded due to the inability to perform host subtraction, with the latest B-band data still contaminated by the supernova radioactive decay emission.

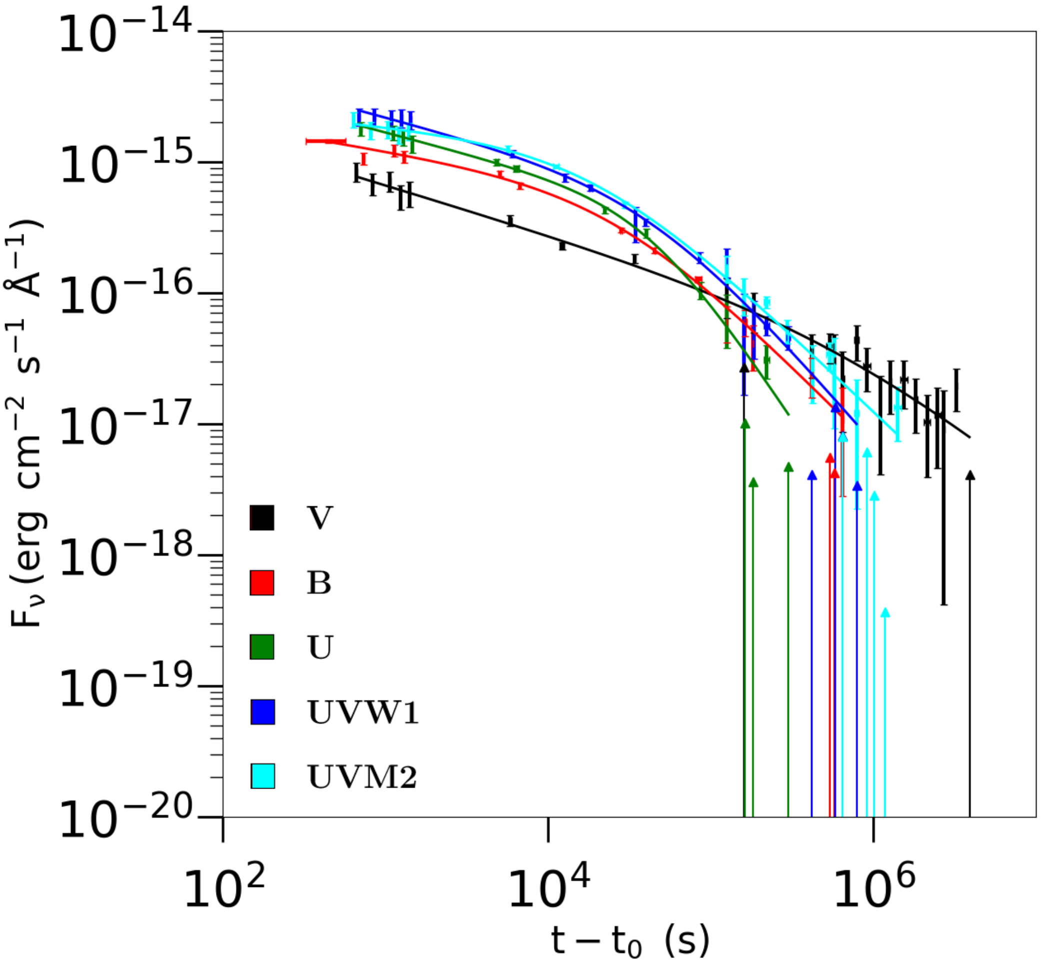

Figure 6.16: GRB 161219B light curve of the optical afterglow. UVOT filters are shown in the key. Up arrows represent 3σ upper limits.

6.3.7.2 Colour analysis

The V band flux density is shallower than the UV band flux density, as evident from the colour at ~ 20 ks (Fig. 6.17) and the light curve (Fig. 6.16).

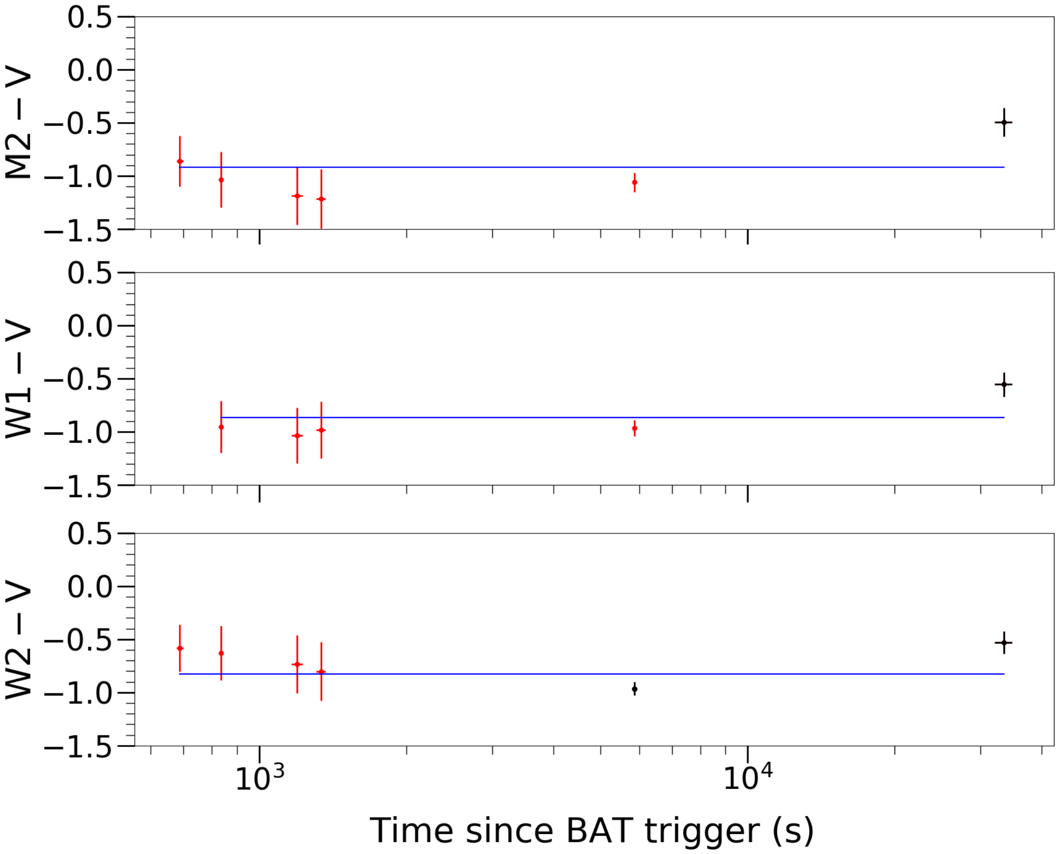

Figure 6.17: Colour indices of the afterglow of GRB 161219B (UVOT data). Comparisons are made between *UV* filters (*UVW*1, *UVW*2 and *UVM*2) and the *V* filter. Data points are represented in red. The blue line represents the mean value of the colour index over the duration shown in the figure. Data points are coloured black to denote a colour index $> 3\sigma$ away from the mean value.

Table 6.16: Results from the light curve fitting of GRB 161219B. α_1 and α_2 correspond to the power-law indices before and after the break in the light curve, respectively. Moreover, the break time t_b, normalisation N and the chi-squared divided by the degrees of freedom, χ^2/dof.

filter	α_1	α_2	t_b (ks)	N ($\times 10^{-16}$)	χ^2/dof
V	0.36 ± 0.04	1.02 ± 0.19	0.7 ± 0.5	0.65 ± 0.34	15/20
B	0.45 ± 0.01	4.92 ± 0.44	44.7 ± 0.8	1.69 ± 0.06	0.3/2
U	0.20 ± 0.02	1.25 ± 0.05	27 ± 3.8	6.38 ± 0.62	10/11
*UVW*1	0.35 ± 0.03	1.97 ± 0.13	48.7 ± 6.1	4.48 ± 0.57	8/9
*UVM*2	0.39 ± 0.03	1.56 ± 0.09	65.9 ± 12	4.63 ± 0.75	8/14
*UVW*2	0.11 ± 0.05	1.18 ± 0.05	18.5 ± 4.3	13.8 ± 2.0	15/15

Table 6.17: Results from the SED fitting of GRB 161219B, across UVOT ($V, B, U, UVW1, UVW2$ and $UVM2$) and XRT (0.3–10) keV. Shown in the table are the results from both a power-law (PL) and also a blackbody + power-law (BB+PL) and a broken power-law (BPL) and also a blackbody + broken power-law (BB+BPL). All models are fitted across UVOT and XRT energies. The time at which the SED is taken (data interpolated to this time) are given in the time column. The temperature of the blackbody kT and radius R, power-law index β_1, absorption in the X-rays was fixed at $N_H = 0.219 \times 10^{22}$ and the UV-optical reddening are fitted for ($E(B-V)$). The chi-squared divided by the degrees of freedom, χ^2/dof is provided for each fit. The last column presents the p-value from the F-test comparing the PL+BB model to a PL only model and BPL+BB model to a BPL only model.

obs:model	time (s)	kT keV	R (cm)	β_1	β_2	E_{break} keV	N_H ($\times 10^{22}$) cm^{-2}	$E(B-V)$ mag	χ^2/dof	F-test p-value
XRT: PL	400.0	-	-	1.249 ± 0.034	–	–	0.219	0.00 ± 0.02	149.74/120	-
XRT: PL+BB	400.0	0.127 ± 0.0104	$(2.90 \pm 0.53) \times 10^{12}$	0.986 ± 0.057	–	–	0.219	0.0 ± 0.2	107.97/118	4.2×10^{-9}
XRT+UVOT: PL	850	–	–	0.641 ± 0.011	–	–	0.219	0	49/28	-
XRT+UVOT: PL+BB	850	0.294 ± 0.051	$(1.61 \pm 0.59) \times 10^{11}$	0.667 ± 0.015	–	–	0.219	0	32/26	3.9×10^{-3}
XRT+UVOT: BPL	850	–	–	0.47 ± 0.07	0.97 ± 0.06	0.06 ± 0.02	0.219	0	23/27	-
XRT+UVOT: BPL+BB	850	0.114 ± 0.039	$(1.26 \pm 0.97) \times 10^{12}$	0.62 ± 0.02	1.12 ± 0.03	0.027 ± 0.002	0.219	0	22/25	0.57
XRT+UVOT: PL	1300	–	–	0.621 ± 0.008	–	–	0.219	0.0 ± 0.2	94/37	-
XRT+UVOT: PL+BB	1300	0.144 ± 0.015	$(1.10 \pm 0.26) \times 10^{12}$	0.635 ± 0.009	–	–	0.219	0	55/35	8.4×10^{-5}
XRT+UVOT: BPL	1300	–	–	0.49 ± 0.06	0.99 ± 0.06	0.43 ± 0.35	0.219	0	51/36	-
XRT+UVOT: BPL+BB	1300	0.109 ± 0.052	$(1.13 \pm 1.20) \times 10^{12}$	0.35 ± 0.09	0.85 ± 0.09	0.06 ± 0.06	0.219	0	40/34	1.6×10^{-2}
XRT+UVOT: PL	5850	–	–	0.663 ± 0.006	–	–	0.219	0	101/51	-
XRT+UVOT: PL+BB	5850	0.028 ± 0.003	$(2.62 \pm 0.95) \times 10^{14}$	0.672 ± 0.011	–	–	0.219	0.1 ± 0.1	50/49	3.3×10^{-8}
XRT+UVOT: BPL	5850	–	–	0.30 ± 0.04	0.80 ± 0.04	0.02 ± 0.01	0.219	0	43/50	-
XRT+UVOT: BPL+BB	5850	0.170 ± 0.078	$(1.96 \pm 1.98) \times 10^{11}$	0.26 ± 0.05	0.76 ± 0.04	0.012 ± 0.007	0.219	0	42/48	0.57
XRT+UVOT: PL	33000	–	–	0.716 ± 0.008	–	–	0.219	0	33/37	-
XRT+UVOT: PL+BB	33000	0.024 ± 0.036	$(1.25 \pm 4.42) \times 10^{14}$	0.758 ± 0.057	–	–	0.219	0.1 ± 0.2	28/35	5.6×10^{-2}
XRT+UVOT: BPL	33000	–	–	0.34 ± 0.06	0.84 ± 0.06	0.010 ± 0.008	0.219	0.05 ± 0.02	34/36	-
XRT+UVOT: BPL+BB	33000	0.399 ± 0.143	$(3.50 \pm 1.42) \times 10^{10}$	0.72 ± 0.10	1.22 ± 0.12	0.01 ± 0.46	0.219	0 ± 0.6	28/34	3.7×10^{-2}
XRT: PL	120000	–	–	0.76 ± 0.07	–	–	0.219 ± 0.021	0.08 ± 0.04	60/59	-

6.3.7.3 UV/optical-X-ray SED fitting

The X-ray SED at 120000 s provided a measure of the host galaxy absorption as $N_H = (0.219 \pm 0.021) \times 10^{22}$ cm^{-2}. At 400 s, the X-ray SED fit significantly improved with the inclusion of a blackbody component, evidenced by F-stat $p = 4.17e-09$. The blackbody component was measured with $kT = 0.127 \pm 0.010$ keV and $R = (2.90 \pm 0.53) \times 10^{12}$ cm. I examined epochs of 850, 1300, 5850, and 33000 s, finding that a broken power-law plus blackbody model provided the best fit for each. The broken power-law was modelled such that $\beta_2 = \beta_1 + 0.5$, as expected if the cooling frequency lies between the two segments. Little to no extinction was caused by the host galaxy. The blackbody component was measured at every epoch. However, it's worth noting that the radius and temperature of the blackbody component showed fluctuations, increasing and decreasing across different epochs. This is somewhat unexpected for an expanding blackbody, which would typically show a consistent trend of increasing radius and decreasing temperature. Additionally, the large errors associated with these measurements, despite the improved fits, suggest that there may be significant uncertainty about the reality of the blackbody component at later times.

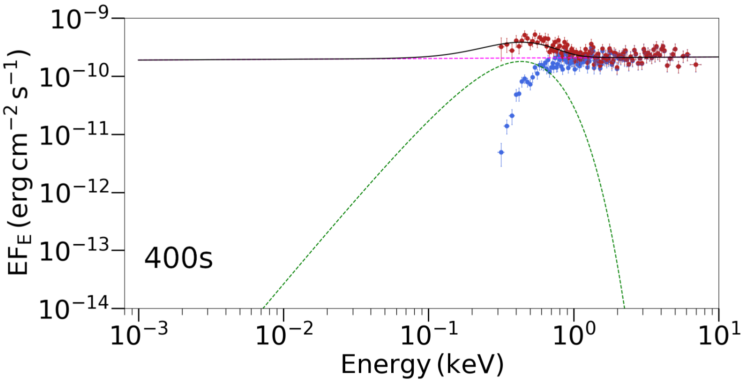

Figure 6.18: The SED of GRB 161219B at (in descending order of figures) 400 s, 1300 s and 5866 s past the GRB trigger. The SEDs are shown across the UV/optical and X-ray energies (0.0015–10 keV). The models used in the fitting are listed in Table 6.3. The flux is displayed as EF_E. The red data points represent the dereddened UV/optical and unabsorbed X-ray flux. The blue data points represent the UV/optical and X-ray flux including Galactic and host-galaxy reddening and absorption as measured by UVOT and XRT. The dashed lines represent the model components.

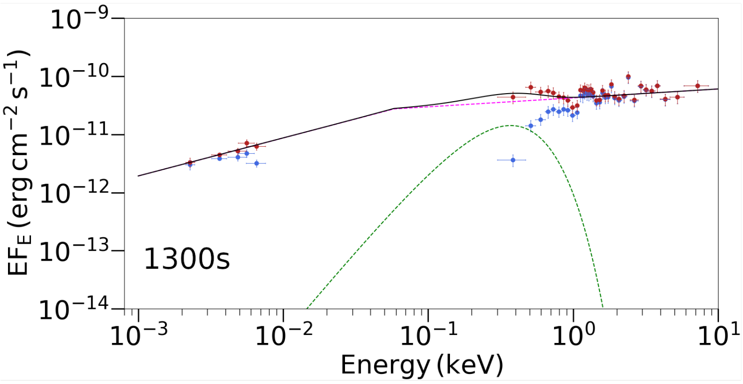

Figure 6.18: caption (continued)

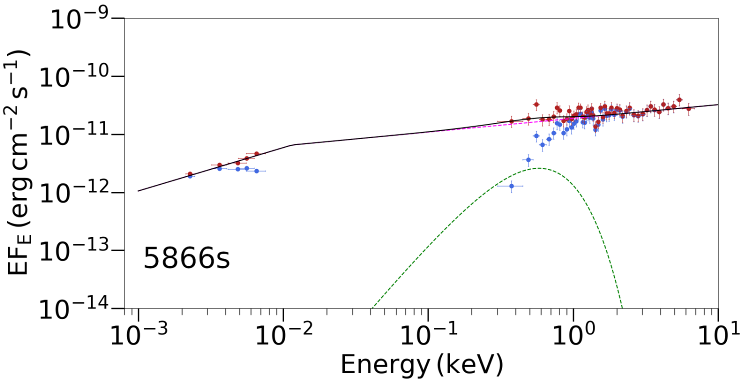

Figure 6.18: caption (continued)

6.3.8 GRB 171205A, z=0.037, SN grade A

6.3.8.1 Light curve modelling

The optical light curves were flat until around 100 ks, after which they faded. The UV light curves showed some brightening around 10 ks in the $UVM2$ band, along with a significant colour change during the initial 100 ks. A broken power-law model fitted best for all light curves, except for the V band light curve that was fitted best with a power-law. Given the inconsistency in the fits, an additional component is likely present in the UV/optical emission.

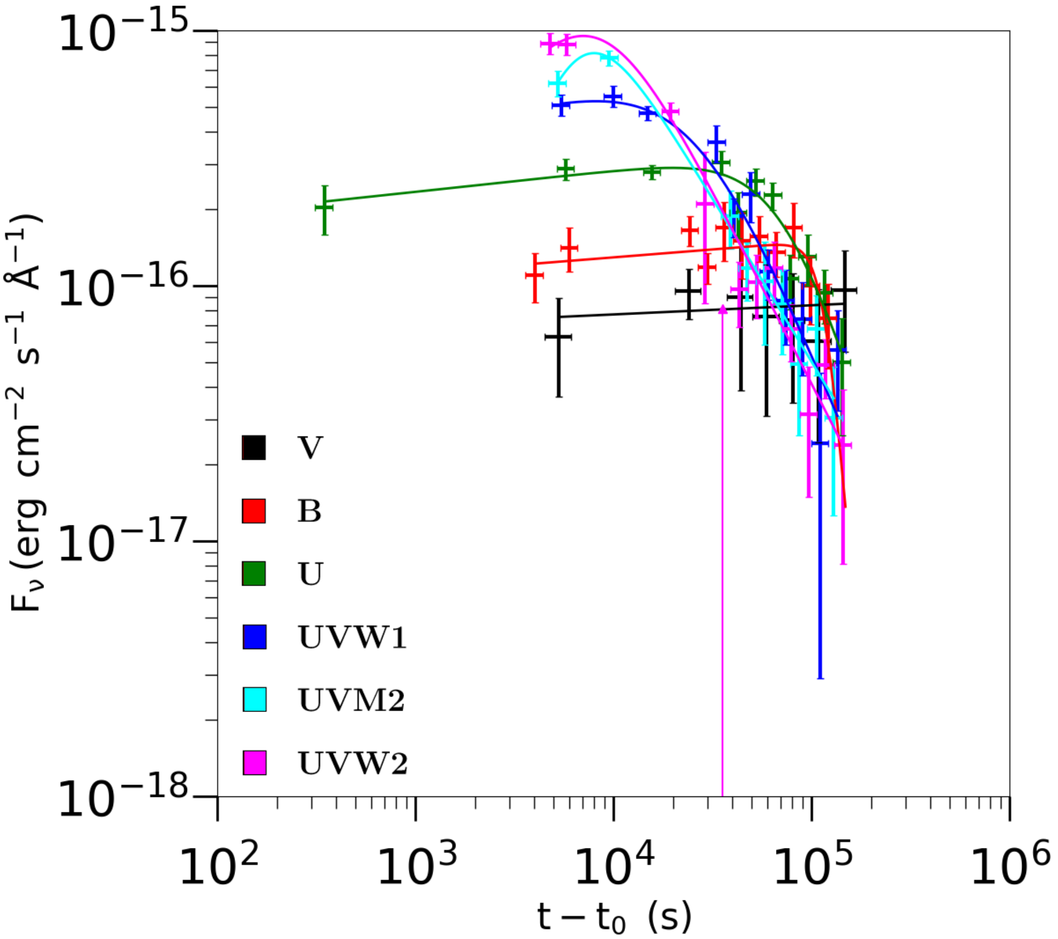

Figure 6.19: GRB 171205 light curve of the optical afterglow. UVOT filters are shown in the key. Up arrows represent 3σ upper limits.

6.3.8.2 Colour analysis

The colour revealed a significant UV excess before 10 ks and an optical excess after 10 ks. The increase after 100 ks could be attributed to the optical emission from the radioactive decay of Nickel in SN 2017iuk.

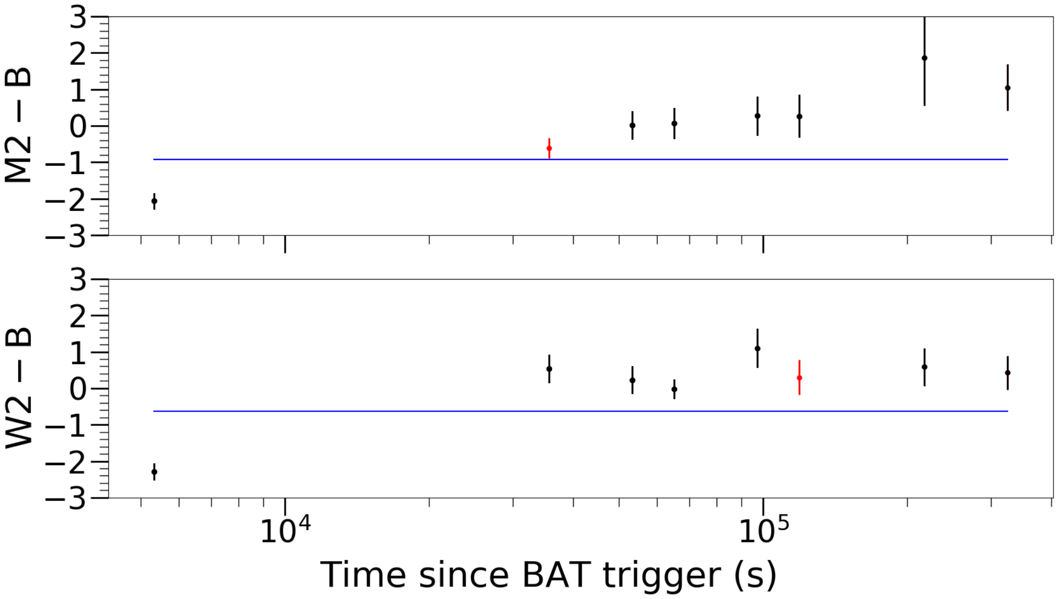

Figure 6.20: Colour indices of the afterglow of GRB 171205 (UVOT data). Comparisons are made between *UV* filters (*UVW*2 and *UVM*2) and the *B* filter. Data points are represented in red. The blue line represents the mean value of the colour index over the duration shown in the figure. Data points are coloured black to denote a colour index $> 3\sigma$ away from the mean value.

6.3.8.3 UV/optical-X-ray SED fitting

The host galaxy absorption, calculated from the late time X-ray SED, was $N_H = 0.014$. I created several UV/optical SEDs in the initial 100 ks past the GRB trigger and selected X-ray SEDs that coincided with the epochs of the UV/optical SEDs. The X-ray SED at 234 s significantly improved with the inclusion of a blackbody component, as demonstrated by F-stat=32, $p = 5.63 \times 10^{-8}$. I modelled the full SED at 35, 55, 65, and 97 ks, finding that a blackbody plus power-law model fit the optical–X-ray SED best at each time. The spectral index was modelled as $\beta = 0.60 \pm 0.03$, consistent across all SEDs. From 234s to 97000s, the velocity of the blackbody, as a fraction of the speed of light, is approximately $v = 0.362c \pm 0.100c$.

My SED fitting procedure enables the detailed examination of the photospheric radius as it evolves over time. For this specific dataset, neither a linear

Table 6.18: Results from the light curve fitting of GRB 171205. α_1 and α_2 correspond to the power-law indices before and after the break in the light curve, respectively. The break time t_b, normalisation N and the chi-squared divided by the degrees of freedom, χ^2/dof.

filter	α_1	α_2	t_b (ks)	N ($\times 10^{-16}$)	χ^2/dof
V	-0.04 ± 0.04	–	–	0.56 ± 0.21	1/5
B	-0.06 ± 0.04	9.2 ± 3.1	116 ± 4.2	1.5 ± 0.09	7/8
U	-0.08 ± 0.03	2.51 ± 0.35	73.9 ± 6.1	3.34 ± 0.25	10/7
$UVW1$	-0.17 ± 0.13	1.88 ± 0.25	26.3 ± 5.9	7.03 ± 1.2	7/7
$UVM2$	-2.23 ± 0.87	1.28 ± 0.10	6.83 ± 1.1	15.7 ± 0.42	2/5
$UVW2$	-1.02 ± 0.58	1.53 ± 0.10	8.25 ± 1.6	18.6 ± 2.5	9/8

Table 6.19: Results from the SED fitting of GRB 171205, across UVOT ($V, B, U, UVW1, UVW2$ and $UVM2$) and XRT (0.3–10) keV. Shown in the table are the results from both a single power-law (PL) and also a blackbody + power-law (BB+PL). All models are fitted across UVOT and XRT energies. The time at which the SED is taken (data interpolated to this time) are given in the time column. The temperature of the blackbody kT and radius R, power-law index β_1, absorption in the X-rays was fixed at $N_H = 0.014 \times 10^{22}$ and the UV-optical reddening are fitted for ($E(B-V)$). The chi-squared divided by the degrees of freedom, χ^2/dof is provided for each fit. The last column presents the p-value from the F-test comparing the PL+BB model to a PL only model

obs:model	time (s)	kT keV	R (cm)	β_1	N_H ($\times 10^{22}$) cm^{-2}	$E(B-V)$ mag	χ^2/dof	F-test p-value
XRT: PL	234	–	–	0.751 ± 0.020	0.014	–	312.87/235	
XRT: PL+BB	234	0.086 ± 0.004	$(1.91 \pm 0.01) \times 10^{13}$	0.701 ± 0.031	0.014	-	262.83/233	1.52×10^{-9}
XRT+UVOT: PL	35000	–	–	1.24 ± 0.02	0.014	0	45.80/9	
XRT+UVOT: PL+BB	35000	0.00110 ± 0.00006	$(5.66 \pm 0.71) \times 10^{14}$	0.533 ± 0.145	0.014	0	10/7	4.9×10^{-3}
XRT+UVOT: PL	55000	–	–	1.28 ± 0.04	0.014	0.13 ± 0.02	46.85/10	
XRT+UVOT: PL+BB	55000	0.00081 ± 0.00005	$(9.06 \pm 1.12) \times 10^{14}$	0.585 ± 0.128	0.014	0	9/7	6.7×10^{-3}
XRT+UVOT: PL	65000	–	–	1.24 ± 0.00	0.014	0.11 ± 0.02	19.82/8	
XRT+UVOT: PL+BB	65000	0.00080 ± 0.00008	$(8.11 \pm 1.74) \times 10^{14}$	0.801 ± 0.175	0.014	0	11/7	5.0×10^{-2}
XRT+UVOT: PL	97000	–	–	1.281 ± 0.061	0.014	0	11.00/6	
XRT+UVOT: PL+BB	97000	0.00066 ± 0.00008	$(1.07 \pm 0.29) \times 10^{15}$	0.554 ± 0.358	0.014	0	5/4	0.21
XRT: PL	70000	–	–	0.646 ± 0.120	0.014 ± 0.036	–	15/21	

nor a power-law model adequately described the observed radius dynamics. Consequently, a power-law augmented with a constant term was employed, best visualised by the magenta line in Fig. 6.21. The best-fit parameters for this model are summarised in Eq. 6.8:

$$R_{BB} = \Big((101 \pm 290) + (112 \pm 147)(t - t_0)^{0.68 \pm 0.259}\Big) \times 10^{11}\,\mathrm{cm} \tag{6.8}$$

This equation represents the photospheric radius R_{BB} in terms of an initial radius R_0 and the time elapsed since the GRB event, $t - t_0$. Here, A and B are the coefficients determined from my fitting, with $R_0 = (1.01 \pm 2.90) \times 10^{13}\,\mathrm{cm}$ depicting the initial radius where the blackbody emission commences. The considerable uncertainties in my parameters can be attributed to the strong correlations present in the covariance matrix, making the fit sensitive to small perturbations in the data.

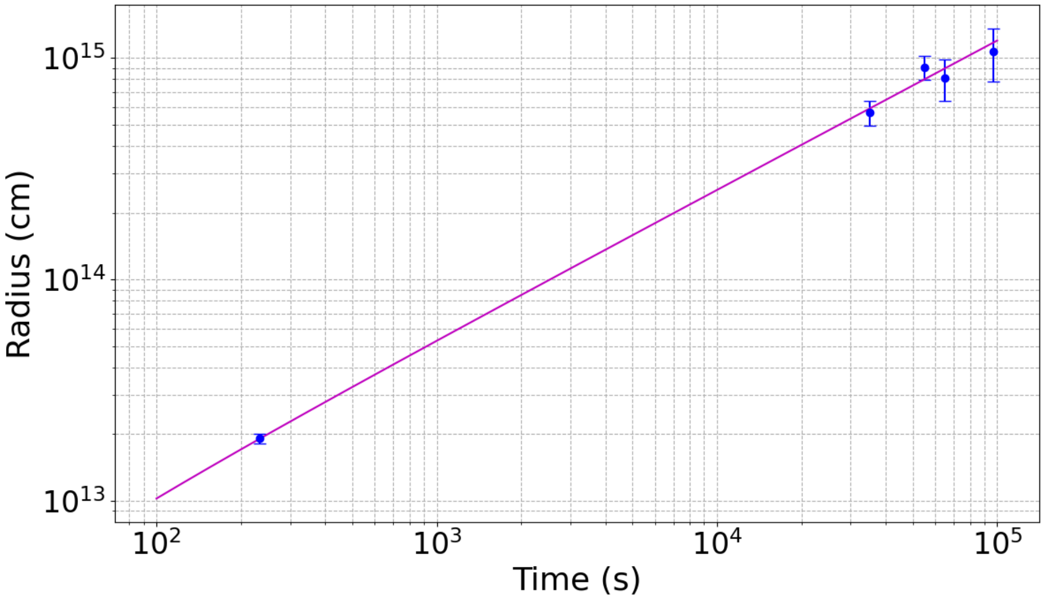

Figure 6.21: Radius versus time for GRB 171205, determined from fitting UV/optical/X-ray SEDs using a thermal blackbody model. The photospheric radii are displayed with one-sigma errors in blue. The best-fit model to the photospheric radii, given by $R = A + Bt^C$, is depicted as a magenta line.

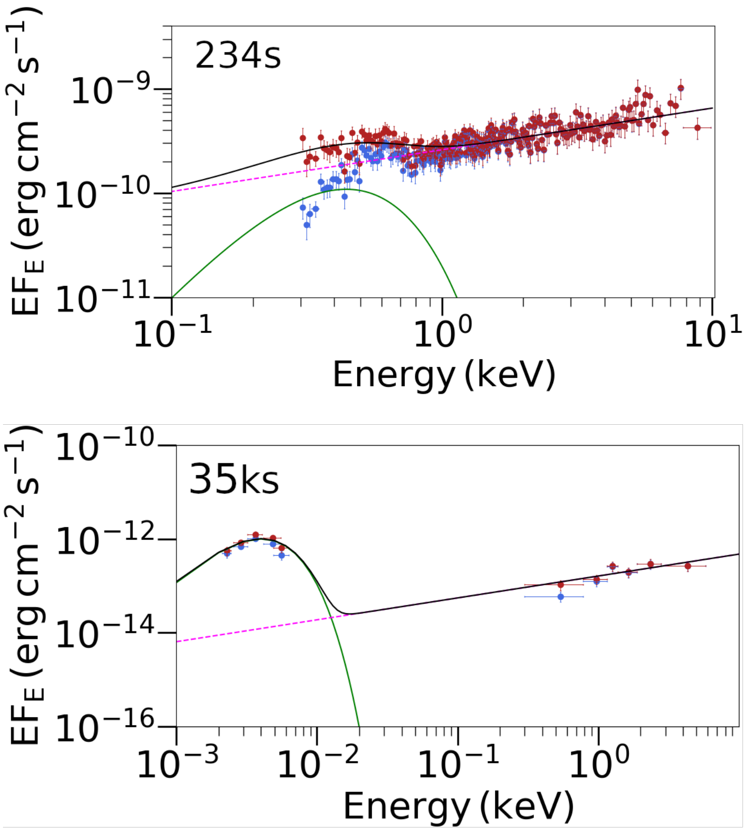

Figure 6.22: The SED of GRB 171205 at (in descending order of figures) 234 s, 35000 s, 55000 s, 65000 s and 97000 s past the GRB trigger. The SEDs are shown across the UV/optical and X-ray energies (0.0015–10 keV). The models used in the fitting are listed in Table 6.3. The flux is displayed as EF_E. The red data points represent the dereddened UV/optical and unabsorbed X-ray flux. The blue data points represent the UV/optical and X-ray flux including Galactic and host-galaxy reddening and absorption as measured by UVOT and XRT. The dashed lines represent the model components.

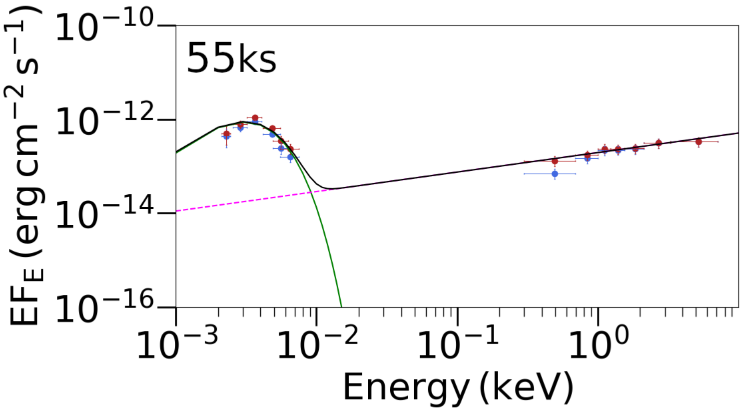

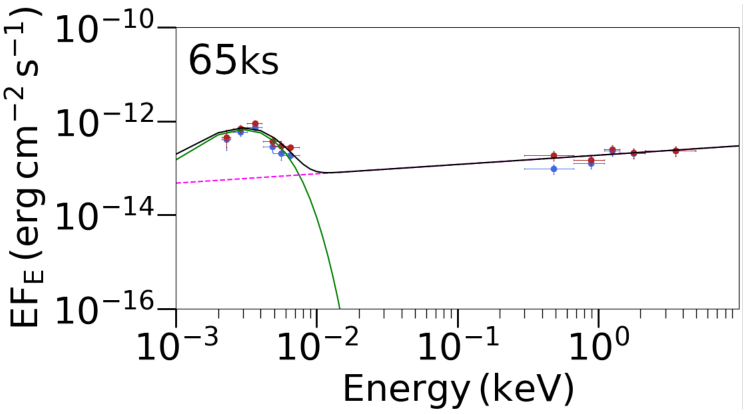

Figure 6.22: caption (continued)

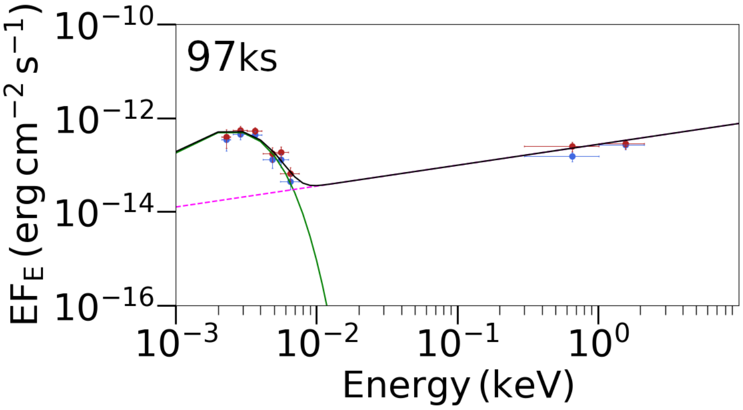

Figure 6.22: caption (continued)

6.3.9 GRB 180728, z=0.117, SN grade A

6.3.9.1 Light curve modelling

There was a plateau at the beginning of the observed UV/optical flux density that lasted until around 3 ks, after which the UV/optical light curves decayed with the same power-law slope of ~ 1. All breaks in the light curve occurred before 10 ks.

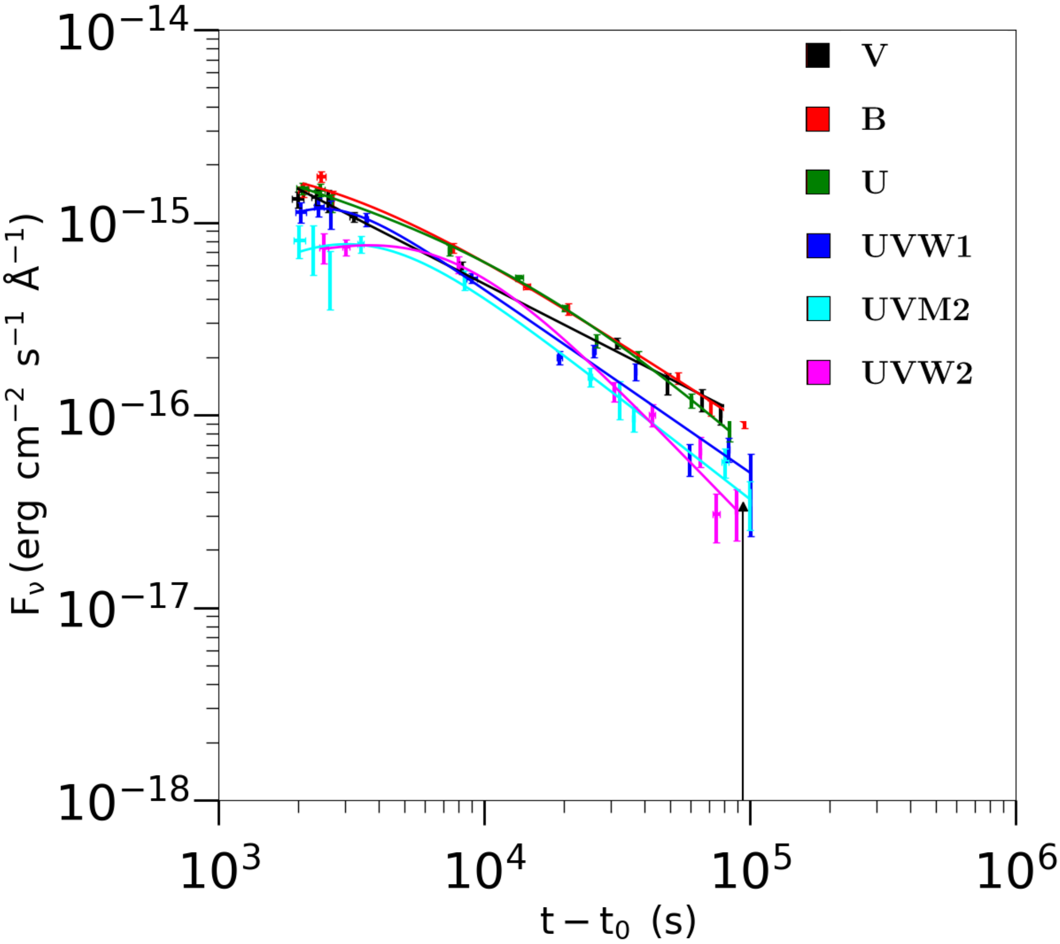

Figure 6.23: GRB 180728 light curve of the optical afterglow. UVOT filters are shown in the key. Up arrows represent 3σ upper limits.

6.3.9.2 Colour analysis

In the time range covered, the colour was constant, exhibiting a slight excess in the optical emission compared to UVM2 and UVW2. No significant change was observed in the optical emission due to the supernova.

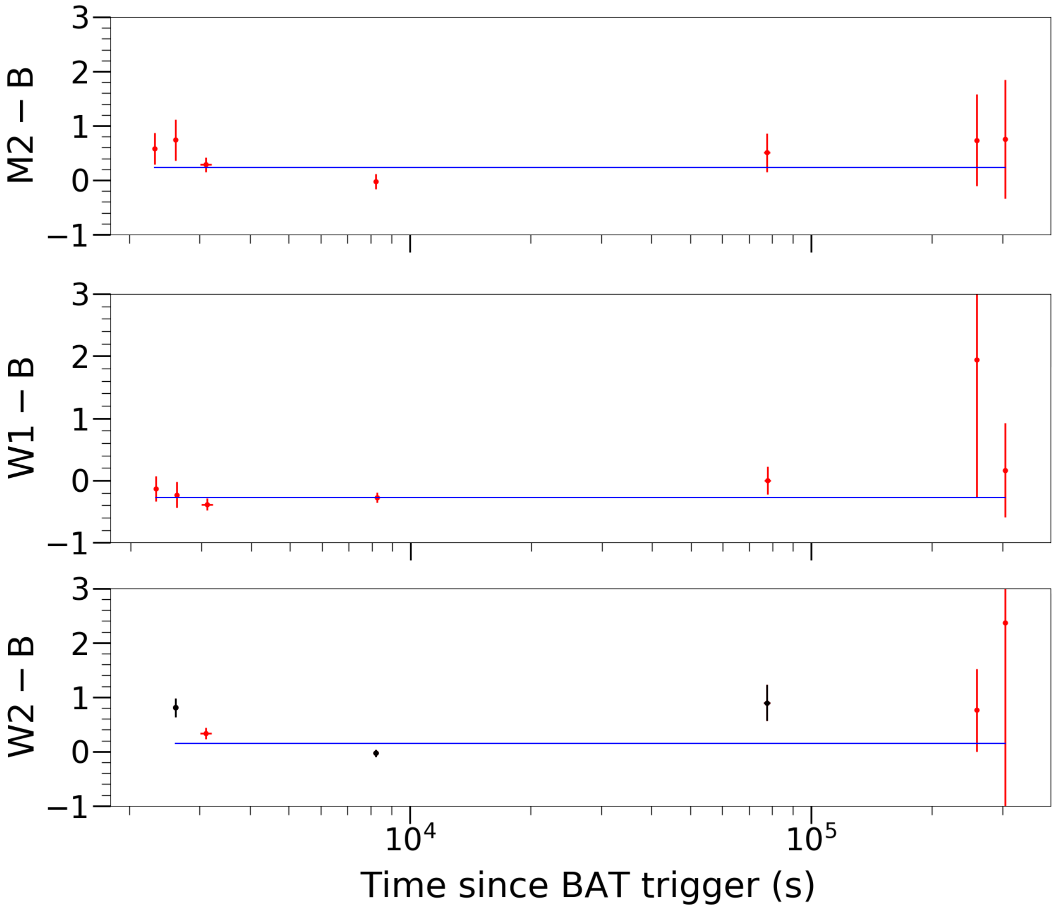

Figure 6.24: Colour indices of the afterglow of GRB 180728 (UVOT data). Comparisons are made between UV filters ($UVW1$, $UVW2$ and $UVM2$) and the B filter. Data points are represented in red. The blue line represents the mean value of the colour index over the duration shown in the figure. Data points are coloured black to denote a colour index $> 3\sigma$ away from the mean value.

6.3.9.3 UV/optical-X-ray SED fitting

I excluded the early <7000 s XRT data in WT mode due to potential contamination from trailing charge, which could increase the background level at low energies <1 keV and underestimate the column density when modelling. Consequently, I focused on the PC mode data when I had contemporaneous UVOT observations. I was thus only able to examine a single epoch at 8000 s for the optical–X-ray SED. The late X-ray SED centred at 150 ks allowed us to calculate the host galaxy absorption as $N_H = (0.067 \pm 0.025) \times 10^{22}$ cm. I found a significant improvement in the fit with a blackbody plus power-law

Table 6.20: Results from the light curve fitting of GRB 180728. α_1 and α_2 correspond to the power-law indices before and after the break in the light curve, respectively. Moreover, the break time t_b, normalisation N and the chi-squared divided by the degrees of freedom, χ^2/dof.

filter	α_1	α_2	t_b (ks)	N ($\times 10^{-15}$)	χ^2/dof
V	0.71 ± 0.01	–	–	310 ± 27	12/14
B	-2.1 ± 1.2	0.84 ± 0.02	1.7 ± 0.15	2.8 ± 0.3	10/12
U	0.24 ± 0.12	1.2 ± 0.08	9.8 ± 4.9	1.3 ± 0.5	9/14
$UVW1$	-1.8 ± 1.1	0.98 ± 0.04	2.1 ± 0.2	2.2 ± 0.2	27/14
$UVM2$	-1.2 ± 0.4	1.03 ± 0.04	2.9 ± 0.3	1.51 ± 0.05	6/13
$UVW2$	-0.7 ± 0.4	1.3 ± 0.1	5.3 ± 0.2	1.5 ± 0.2	6/10

Table 6.21: Results from the SED fitting of GRB 180728, across UVOT (V,B,U,$UVW1$,$UVW2$ and $UVM2$) and XRT (0.3–10) keV. Shown in the table are the results from both a single power-law (PL) and also a blackbody + power-law (BB+PL). All models are fitted across UVOT and XRT energies. The time at which the SED is taken (data interpolated to this time) are given in the time column. The temperature of the blackbody kT and radius R, power-law index β_1, absorption in the X-rays was fixed at $N_H = 0.067 \times 10^{22}$ and the UV-optical reddening are fitted for ($E(B-V)$). The chi-squared divided by the degrees of freedom, χ^2/dof is provided for each fit. The last column presents the p-value from the F-test comparing the PL+BB model to a PL only model

obs:model	time (s)	kT keV	R (cm)	β_1	N_H ($\times 10^{22}$) cm^{-2}	$E(B-V)$ mag	χ^2/dof	F-test p-value
XRT: PL	8000	–	–	0.771 ± 0.055	0.067	–	43/49	
XRT: PL+BB	8000	0.043 ± 0.052	$(6.04 \pm 32.8) \times 10^{13}$	0.751 ± 0.059	0.067	–	40/47	0.18
XRT+UVOT: PL	8000	–	–	0.661 ± 0.006	0.067	0	74/54	
XRT+UVOT: PL+BB	8000	0.037 ± 0.007	$(1.52 \pm 1.45) \times 10^{14}$	0.671 ± 0.041	0.067	0.05 ± 0.12	53/52	1.7×10^{-4}
XRT: PL	150000	–	–	0.612 ± 0.034	0.067 ± 0.025	–	287/239	

model, with F-stat=10.3, $p = 0.000017$, over a power-law fit. Broken power-law models did not improve the fit statistics and indicated a single power-law segment. The parameters from the SED fits are shown in Table. 6.21 and the best fit model is shown in Fig. 6.25.

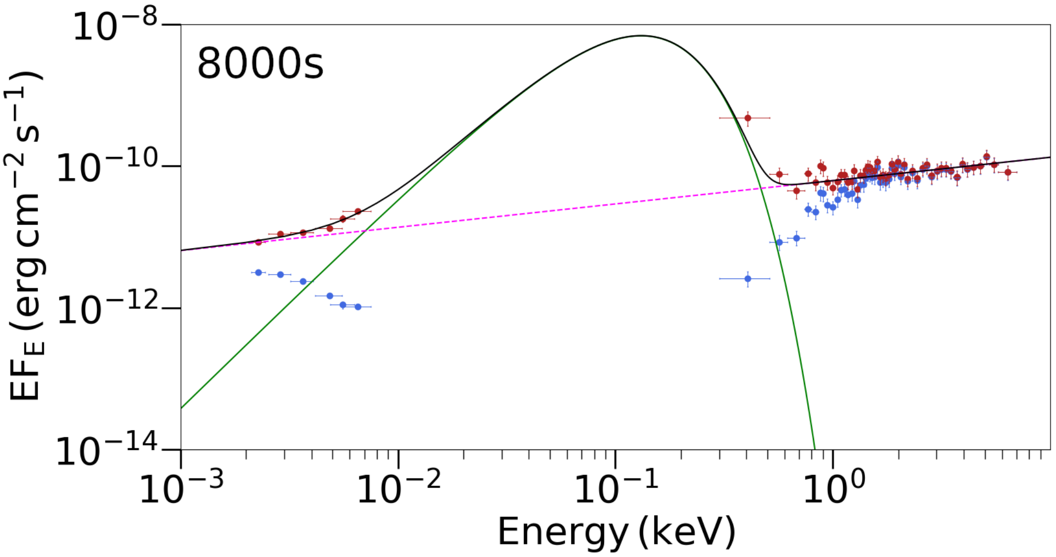

Figure 6.25: The SED of GRB 180728 at 8000 s past the GRB trigger. The SED is shown across the UV/optical and X-ray energies (0.0015–10 keV). The models used in the fitting are listed in Table 6.3. The flux is displayed as EF_E. The red data points represent the dereddened UV/optical and unabsorbed X-ray flux. The blue data points represent the UV/optical and X-ray flux including Galactic and host-galaxy reddening and absorption as measured by UVOT and XRT. The dashed lines represent the model components.

6.4 Discussion

6.4.1 GRBs with no detectable thermal component

In my sample of GRBs, there were four bursts that had no detectable thermal component in either the X-ray or UV/optical spectra: GRB 091127, GRB 130427A, GRB 130831A, GRB 180728.

6.4.1.1 GRB 130427A

The light curve for GRB 130427A was well modelled by a broken power-law, and a power-law for the light curves with less data. All power-law segments were consistent with $\alpha_1 = 1$ and $\alpha_2 = 2.3$, with a break in all UVOT bands at ∼250 ks. The light curves were fitted until 300 ks because this is where I detected a significant increase in the optical flux, which I attributed to the Ni^{56} radioactive decay from SN 2013cq. If the UV/optical emission is caused by a synchrotron component below the cooling frequency, the best fit temporal power-law indices imply $p = (4/3) + 1 = 2.3$ for $t^{-3(p-1)/4}$ before the break, and $p = 2.3$ after the break for t^{-p}, assuming the break corresponds to the jet-break. These values of p are reasonable for a typical GRB afterglow. I did not detect any significant improvement when adding a blackbody component to the SED fits. My inability to detect a blackbody component could well be due to the strong synchrotron component detected in GRB 130427A.

6.4.1.2 GRB 130831A

I removed the flare that was in the UV/optical light curve from my light curve fitting. I found a power-law model fit all the light curves best, with $\alpha \sim 0.86$. There wasn't much coverage in the UV/optical when excluding the flare and the late-time SN emission, so the B and U light curves were fit poorly. The addition of a blackbody component in my SED fitting did not significantly improve the fit. I left the X-ray absorption as a free parameter in fitting and I found that a power-law fit the optical–X-ray SED best, with $\beta = 1.9$.

6.4.1.3 GRB 091127

The early coverage of GRB 091127 was mainly observed in the V, U, and $UVW1$ bands. The V and U light curves were consistent with a broken power-law model, but there were not enough observations in the $UVW1$ band to fit this model. I found that the break times for the V and U bands were significantly different, with times of 20 ± 14 ks and 50 ± 9 ks, respectively. The V light curve had a shallower slope than the U light curve, with $\alpha_1 = 0.11 \pm 0.29$ and $\alpha_2 = 1.4 \pm 0.16$ compared to $\alpha_1 = 0.49 \pm 0.07$ and $\alpha_2 = 2.0 \pm 0.1$ for the U band. I fitted the light curve until 500 ks to ensure enough data for my fit. The discrepancies between the U and V bands could be due to a larger contribution from SN 2009nz in the V band. Notably, the $U - i$ colour and GROND data reveal a significant excess of optical emission at 280 ks, likely due to SN 2009nz.

I created an SED at 3300 s using observations of the g, r, and i bands from GROND and the $UVW1$ and $UVM2$ bands from UVOT. A broken power-law plus blackbody model provided the best fit to the SED, significantly improving over a broken power-law alone; the model fitted well with $\chi^2/\text{dof} = 154/172$. I measured the thermal component at $kT = 0.043 \pm 0.023$ keV and $R = (5.32 \pm 1.13) \times 10^{14}$ cm. Starling et al. (2012) investigated the possibility of a thermal component but concluded that the late XRT observations (after 3 ks) might be too late to detect it, as they were only modelling the X-ray emission. They fitted their X-ray SED with $N_H = 0.11 \times 10^{22}$ cm^{-2} and found a poorly constrained blackbody at $kT = 0.06$ keV, which did not significantly improve the fit compared to a power-law model. However, by including UVOT and GROND data in my analysis, I was able to measure the thermal component.

The power-law exhibits a break at 26 eV, where the post-break power-law is given by $\beta = 1.79 \pm 0.03$. This value aligns with the power-law observed in the X-ray SED at 15000 s, which is $\beta = 1.72 \pm 0.07$. This suggests that there is no significant evolution in the behavior between these observations. However, this pattern contrasts with GRB 060218, which exhibited a softening at late times in the X-ray emission. The power-law component parameters I measured align with those found in Troja et al. (2012), who reported $\beta_1 = 0.30 \pm 0.01$, $\beta_2 = 0.80 \pm 0.01$, and a decreasing break energy from 150 eV at 6 ks to 6 eV at 55 ks. My break energy is smaller, likely due to the addition of a blackbody component. However, while the inclusion of a blackbody model significantly improves the fit, the best-fit blackbody properties imply unrealistically high expansion speeds, approaching and even exceeding the speed of light. Therefore, with a p-value of 0.03, the broken power-law model is the best fit to the data, and I cannot determine whether a thermal component is present in GRB 091127.

6.4.1.4 GRB 180728

All light curves were shallower than expected if they were only produced by synchrotron radiation. The mean power-law slope after the break in the light curve was $\beta_2 = 1.01$, which is much lower than the expected, $\beta = p$, assuming that this is the jet-break. However the broken power law indices vary significantly across the UVOT bands, suggesting some additional emission contributing the the differences in the UV and optical β_1 and β_2. I detected a significant thermal component at 8000 s in the optical–X-ray SED, with $kT = 0.037$ keV and $R = (1.52 \pm 1.45) \times 10^{14}$ cm, however this radius is poorly constrained and would imply expansion speeds of 0.6c. This could help explain the shallow light curves. But due to the limited observations I was only able to analyse the spectrum at 8000 s. There was a small amount of reddening required for the model to fit, but that was poorly constrained at $E(B-V) = 0.05 \pm 0.12$ mag.

6.4.2 GRBs with significant thermal component in the UV/optical emission

6.4.2.1 GRB 120422

The light curves of 120422 were all best fitted with a broken power-law model. There was no consistency between the parameters of the light-curve fits and the break time appeared earlier for the UV than the optical. This could represent a thermal component cooling. As time progresses in the light curve, the blackbody shifts to lower energies. I fit the optical–X-ray SED at 1100, 5900, 28000 and 141000 s, for 28000 s. It can be seen from the work conducted in Starling et al. (2012) that there is a thermal component in the X-ray SED at 128–192 s, with $kT = 0.204$ keV and $R = 3 \times 10^{12}$ cm. Comparing this to my results, at 1100 s the blackbody parameters could not be estimated due to the limited number of data points in the X-ray. However, this radius, $R = 3 \times 10^{12}$ cm, is comparable to the radius I measure at 5900 s, $R = (2.46 \pm 2.23) \times 10^{12}$ cm, even though my errors are large. I also measure the thermal component at

28 ks as, $R = (1.05 \pm 0.43) \times 10^{14}$ cm and at 141 ks as, $R = (5.75 \pm 2.38) \times 10^{14}$ cm. The component at 141 ks was measured from only the UV/optical SED with just a blackbody model, similarly to the blackbody component in GRB 060218 at 120 ks. Due to the limited number of measurements I cannot model how the radius evolves. However if the expansion is linear, this implied an expansion speed of 0.141 c or 42400 kms^{-1} (5900–141000 s). Schulze et al. (2014) measured a thermal component in the optical–X-ray SED at 5000 s, however their component is cooler and larger than my measurement, they estimated $kT = 16$ eV and $R = 7 \times 10^{13}$ cm. Whilst it is larger than I found, at 5900 s the blackbody plus power-law model was measured with a higher absorption, so this could possibly account for the differences. Regardless, the thermal component measured from the UV/optical SED at 141 ks is independent of the absorption. Therefore I agree with Schulze et al. (2014) that this is the shock heated cooling ejecta emission from SN 2012bz, which has a significant contribution in the UV/optical afterglow light curve, accounting for all of the flux at 141 ks, where the blackbody is peaking in the UV/optical energy range. Additionally my measurement for the expansion speed of 42400 kms^{-1} between 5900 and 141 ks, agree well with the measurement of the expansion velocity from FeII(5169) for SN 2012bz in Schulze et al. (2014) at $t \sim 3$ days.

6.4.2.2 GRB 171205

For GRB 171205, the broken power-law model provided the best fit for most light curves, with the exception of the V band. The limited number of observations in the V band makes this conclusion less robust. The initial power-law segment index, α_1, is close to zero for all bands, exhibiting variations mostly within 3σ, though the $UVM2$ band's index deviates by about 4σ. The α_2 segment shows significant variations across different light curves. Notably, there's a trend suggesting that the break time decreases with increasing energy, which could be indicative of an evolving component, possibly a blackbody. This could also account for the large UV excess at earlier times, reminiscent of GRB 060218.

While my light curves alone don't offer conclusive evidence for the emission process due to their inconsistency with solely synchrotron emission, my analyses do reveal the significance of introducing a blackbody component in the X-ray SED. The thermal component was a significant component in all the optical–X-ray SEDs I modelled. my findings on reddening echo the limited impact of the host galaxy's reddening, a conclusion consistent across different extinction curves. The rapid increase of the thermal component from 4×10^{11} cm to 5×10^{14} cm in a span of 35000 s is particularly striking.

Izzo et al. (2019) made similar observations and attributed the thermal component to the hot cocoon produced by a mildly-relativistic GRB jet with continued energy injection expanding into the circumstellar medium. They drew this inference from both the thermal component's characteristics and the high expansion velocities from the broad line absorption features $v \sim 100000$ kms^{-1} at 0.975 days past the GRB trigger time. Furthermore, they argue that the high velocity material and elemental mixing indicate that the injection spans a period exceeding the shock breakout timescale. If I take the average velocity from my study, at 0.362 ± 0.1 c, this translates to 108600 ± 30000 kms^{-1}, which aligns well with the finding in Izzo et al. (2019), providing further credence to their model.

Building on their conclusions, my study offers further validation for this model and highlights the need for multi-wavelength observations to truly discern the underlying emission processes. The results from my analysis of GRB 171205 exhibit striking parallels with those from GRB 060218. For GRB 060218, the photospheric radius over time was described by:

$$R_{BB} = \Big((233 \pm 6) + (1.0 \pm 0.1)(t - t_0)^{0.68 \pm 0.01}\Big) \times 10^{11}\,\mathrm{cm} \tag{6.9}$$

Despite the relatively large uncertainties in my GRB 171205 results, given in Eq. 6.8, the profiles are remarkably similar, especially in terms of the power-law index and the magnitude of the terms. This suggests that there might be a shared underlying mechanism or structural characteristic between these GRBs.

While Izzo et al. (2019) provide a comprehensive understanding, my work accentuates the intricacies of the thermal component and its potential origins. It's essential to consider both studies in tandem to get a better understanding of GRB 171205's behaviour and the broader implications for GRB studies.

6.4.3 GRBs with a thermal component only in the X-ray emission

6.4.3.1 GRB 090618

A thermal component was observed in the X-ray spectrum by Page et al. (2011) and Starling et al. (2012), during the prompt emission and up to 2500 s past the GRB trigger. I was able to fit a blackbody plus power-law model to the SED at 1100 s and 1400 s. I also found that the SED can be fitted with a broken power-law model. When fitting a blackbody plus a broken power-law the implied blackbody component is too large $\sim 10^{15}$ cm. Therefore there are two ways that the UV/optical emission be explained: either it is produced by synchrotron emission with the cooling frequency between the optical and X-ray energies or synchrotron emission with no break plus a thermal component.

The parameters of the broken power-law were $\beta_1 = 0.45 \pm 0.05$, $\beta_2 = 0.95 \pm 0.04$. This was consistent for both SEDs, with a break energy $E_b = 0.29 \pm 0.10$. My results vary slightly from that in Cano et al. (2011) whom find $\beta_1 = 0.64 \pm 0.02$, $\beta_2 = 1.14 \pm 0.02$, $E_b = 1.6$ keV. The SEDs in Cano et al. (2011) were fitted with a slightly larger intrinsic absorption $N_H = 0.27 \times^{22}$ cm^{-2} and extinction $A_V = 0.3$.

Alternatively, the thermal component was measured at 1100 s as $T = 0.296 \pm 0.021$ keV, $R = 2.29 \pm 0.34 \times 10^{12}$ cm, with $\beta = 0.65 \pm 0.01$. The thermal component was also observed at 1400 s and the parameters were consistent with these. This suggests a thermal component that has cooled and stayed relatively the same size. Starling et al. (2012) measured the thermal component at $T = 0.51 \pm 0.08$ keV, $R = 2.64 \times 10^{12}$. They fixed the intrinsic absorption slightly higher than ours at $N_H = 0.3 \times 10^{22}$ cm. I do not have sufficient data to look further to see if this component had evolved further, but the absence of the thermal component at late times (>10 ks Page et al. (2011)) suggests it has moved to lower energies through cooling. These parameters are consistent with the thermal component being produced by the cooling emission from a shock breakout.

The UV/optical light curve of 090618 implies a shallow decay after the break in the light curve. Apart from $UVW2$ all indices, α, where below 2. It has been argued that the value of p can vary in a burst and Curran et al. (2010) showed the p follows a gaussian distribution, centred on p=2.36, with a width of 0.59. However some of the fitted indices still fell short of this, with $F_V \propto t^{-1.24\pm0.08}$ erg cm^{-2} s^{-1} $^{-1}$. This could be due to an additional component in the optical emission, creating a shallower decay slope. Even if the optical synchrotron emission is below the cooling frequency, this would imply from α_1 that $p = 1.2$.

6.4.3.2 GRB 101219B

I fitted the UVOT light curves up until I detected a significant excess in the optical emission from the supernova at 140 ks. All light curves were best fit by a broken power-law, with the exception of $UVW2$, which had less data than the others and was best fit by a single power-law. The break in the light curve seems to increase for higher energy emission, although the uncertainty in the break time is large. The filters with positive α_1 values, specifically U, $UVW1$, and $UVM2$, exhibit trends in their light curves that are suggestive of a plateau-like behaviour (or $\alpha \approx 0$) before 3000s. However, the large uncertainties, especially in $UVM2$ and $UVW2$, make it challenging to draw definitive conclusion.. A possible cause for an early plateau could be something similar to what produces the plateau in X-ray light curves such as continued engine activity emitted as UV/optical radiation or an additional emission component.

I measure the thermal component only in the X-ray SED, with $kT = 0.114$, $R = (5.96 \pm 3.23) \times 10^{12}$ cm, consistent with that in Starling et al. (2012) and Sparre et al. (2011). I attempted to fit the blackbody across the optical–X-ray

SED. However the implied blackbody radius was too large. A broken power-law model could not be fitted with the given degrees of freedom.

6.4.3.3 GRB 161219B

The UVOT light curves were best modeled with a broken power-law for all bands. There is no consistency between the modeled parameters, neither the segment power-law indices nor the break times. Many of the light curves had shallow slopes after the breaks, with V, $\alpha_2 = 1.02 \pm 0.19$, which implies $p = 1.02$, far lower than the expected $p = 2$. This could be due to the optical emission from SN 2016jca. However, the $UVW2$ band also has $\alpha_2 = 1.18 \pm 0.05$, suggesting that the emission in both the V and $UVW2$ bands could be produced by the same mechanism or a combination of synchrotron and an additional component.

Cano et al. (2017) found evidence for two separate thermal components in the NIR–X-ray SED. They measured a thermal component of $kT = 0.014$ keV, $R = 6 \times 10^{14}$ cm at $t - t_0 = 33$ ks. They also found a thermal component at $t - t_0 = 5.8$ days with $kT = 0.0032$ keV, $R = 3 \times 10^{14}$ cm, which rose to a maximum, $R = 3 - 4 \times 10^{15}$ cm at 15–20 days. Cano et al. (2017) attributed the thermal component at $t > 5$ days as being produced from radioactive heating (Arnett, 1982).

I examined the early X-ray spectrum at 400 s, as well as the optical–X-ray SED at 850, 1300, 5850, and 33000 s. The X-ray SED at 400 s is best fit with a power-law plus blackbody model, significantly improving the fit with F-test $p = 4.17 \times 10^{-9}$. For the optical–X-ray SEDs, the combination of a broken power-law with a blackbody yielded the best fit. This model showed a significant improvement over the alternative model (blackbody + power-law), with a p-value of 0.001 for the SEDs at 850 and 1300 s.

During my exploration of various models, including BB+PL, BB+BPL, PL, and BPL (as shown in Table 1), I found that the blackbody improved the fit in some cases, notably at 1300 s. However, even in these instances, the blackbody parameters were poorly constrained due to large errors. Given this uncertainty and the consistency of the broken power-law model across various time points, I conclude that the UVOT/X-ray emission is best described by a broken power-law model.

6.4.4 Influence of Redshift and Burst Characteristics

Based on thermal component detection, GRBs were classified into three categories: solely in XRT, in both UVOT and XRT, or in neither.

The redshift distribution revealed potential variations between the categories. To statistically evaluate these variations, an Analysis of Variance (ANOVA) test was employed (St et al., 1989). This test yielded a p-value close to 0.05, suggesting a potential influence of redshift on thermal component detectability. Higher redshift GRBs showed a trend towards XRT-only thermal detection, potentially due to cosmological dimming. As GRBs occur at greater distances, represented by higher redshifts, their UV emissions can become fainter and harder to detect due to the $(1+z)$ factor reducing the emitted photon energy reaching the observer, particularly when these emissions are intrinsically weak.

In Figure 6.26, the Tukey's Honest Significant Difference (HSD) pairwise comparisons for the redshift distributions are shown. The x-axis of the plot represents the estimated difference in average redshifts between two compared groups. For instance, a value of 0.2 on the x-axis indicates that one group has an average redshift that is 0.2 units higher than another group. Confidence intervals, depicted by the horizontal lines, signify the range within which I expect the true difference in means between each pair of categories to reside. Importantly, these values are differences in means and not the actual redshifts themselves, which is why some values extend beyond the observed redshift range.

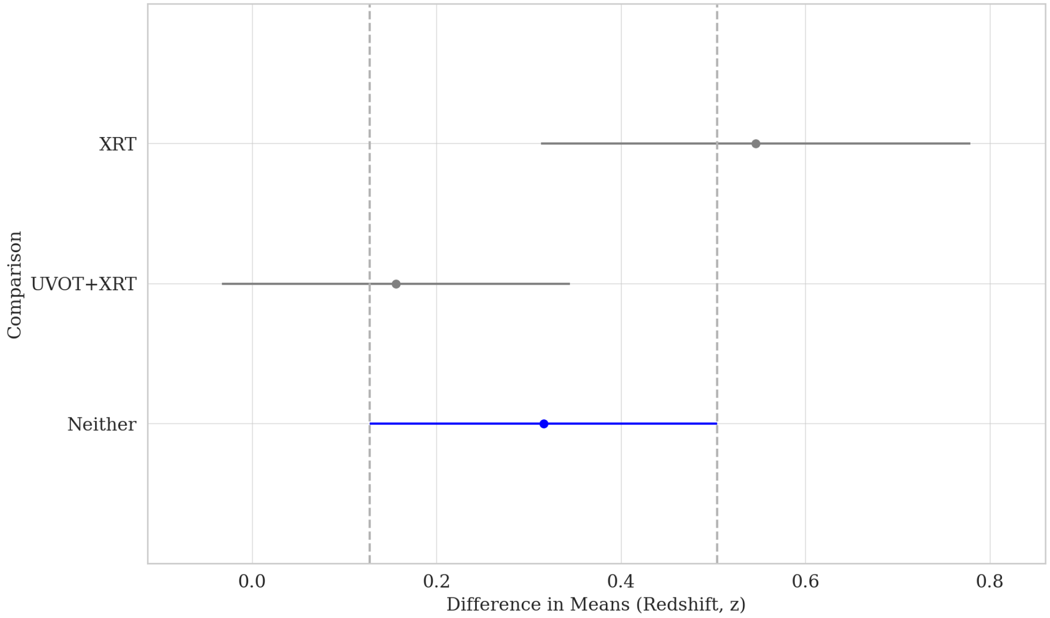

Figure 6.26: Tukey's HSD pairwise comparisons for redshift z distributions across the three thermal detection categories. If a confidence interval does not intersect the zero line, the difference is deemed statistically significant.

For the parameters E_{iso}, E_{peak}, and T_{90}, the ANOVA tests indicated no significant differences in their means across the categories. However, a visual inspection of the boxplots for E_{iso} reveals that GRBs in the "UVOT+XRT" category tend to have a median isotropic energy that is visibly lower than those in the "XRT" category. This observation suggests potential variations in E_{iso} distributions among the categories, even if the means are not statistically different. This could be indicative of the fact that weaker afterglows might be more conducive to the detection of the thermal component, ensuring it isn't overshadowed by the afterglow. A deeper exploration into the optical and X-ray luminosities at the times typically associated with thermal component detections could provide further insights into this hypothesis.

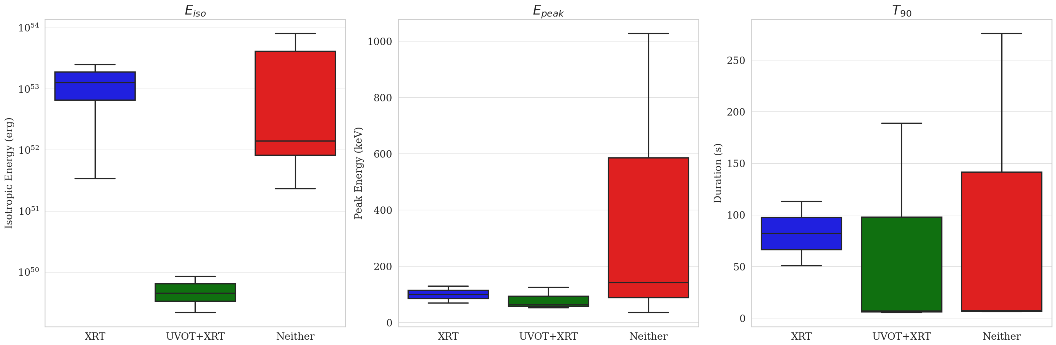

Figure 6.27: Multi-panel distribution plots of key GRB parameters across different thermal detection categories. From left to right, the plots showcase the distributions of isotropic energy ($E_{\rm iso}$), peak energy ($E_{\rm peak}$), and burst duration (T_{90}). The categories represent GRBs where thermal components are detected solely in XRT, in both UVOT and XRT, or in neither. The boxplots provide insights into the median, interquartile range, and potential outliers for each parameter within the respective categories.

After a thorough examination of the thermal detection across the categories, a correlation analysis was performed to understand the potential relationship between redshift and the likelihood of thermal detection. Specifically, a point-biserial correlation was used to quantify the association between redshift (a continuous variable) and thermal detection (a binary variable: detected or not detected). The results indicated a weak inverse correlation, suggesting that as redshift increases, there might be a slightly reduced likelihood of thermal detection. However, it's essential to interpret these findings with caution, as the correlation, while indicative, is weak and does not imply causation. More detailed analyses or larger datasets could provide clearer insights into this potential relationship.

Correlation analyses further elucidated these patterns. A weak inverse correlation was observed between redshift and thermal detection, with correlation coefficients hinting at an increased likelihood of XRT-only thermal detection for higher redshift GRBs. In contrast, $E_{\rm peak}$ showed a weak positive correlation, suggesting that bursts with elevated peak energies might more frequently exhibit thermal components in both UVOT and XRT.

Despite these nuanced findings, a cautious interpretation is imperative.

The correlations, while indicative, are not robust enough to imply causation. There's a clear need for more expansive datasets or complementary methodologies to refine these insights.

6.4.5 Detectability and Implications of Thermal Components in GRBs

My results indicate that approximately 72.7% of GRBs with associated supernovae in my sample exhibited thermal components within the first 50-ks. This is a lower limit, suggesting that while the majority of my observed GRBs show these thermal components, there may be more that remain undetected due to various reasons.

However, it's crucial to address the non-detection of thermal components in some GRBs. For instance, the absence of a detectable thermal component does not necessarily mean it isn't there. My findings hint at a potential influence of redshift on the detectability of thermal components. Notably, GRB091127 and GRB030831A, with redshifts of 0.49 and 0.479 respectively, lacked detectable thermal components. This brings us to my second question.

The absence of a detectable thermal component in certain bursts, especially those at higher redshifts, poses intriguing questions. Could the thermal components be inherently weaker in these GRBs, or is it a question of detectability due to their redshift? Interestingly, for some bursts where the thermal component was not straightforwardly detected, I was able to fit a blackbody shape to the model that better described the emission. However, the fitted parameters were often poorly constrained or unphysical. For example, in the case of GRB091127, fitting with a broken power-law + blackbody model gave us a velocity that far exceeds the speed of light, implying unphysical conditions.

From Table. 6.22 it can be seen that all GRBs modeled with a power-law (indicative of non-detection of the thermal component) exhibit luminosities that are orders of magnitude higher than those modeled with a blackbody, with the exception of GRB 180728. This stark difference in luminosity suggests

Table 6.22: Luminosities of selected GRBs at specified post-burst times. The GRBs are modeled either with a power-law or a blackbody (BB). The provided luminosities are within the energy range of $UVM2$ (4.8-6.4 eV) in the rest frame.

GRB	Model	Time (s)	Luminosity ($\times 10^{39}$ ergs/s)
130427A	Power-law	1878	9.6569×10^6
130831A	Power-law	707	3.3133×10^7
091127	Power-law	3300	3.4933×10^6
180728	Power-law	8000	2.2606×10^4
060218	BB	7500	3.1125
100316D	BB	33000	5.2962×10^5
171205A	BB	35000	1.2655×10^3

that the afterglow's brightness is indeed a significant factor that can mask the presence of a thermal component, making it undetectable.

The fact that non-detection GRBs have such high luminosities, combined with the knowledge that detected thermal components have much lower luminosities, lends credence to the hypothesis that thermal components might be universally present in all GRBs. However, their detection is contingent on the relative brightness of the afterglow. If the afterglow is too bright, it can suppress the thermal component's visibility.

GRB 180728 stands out due to its relatively lower luminosity, even though there was no detection of a thermal component. However, it's essential to note that the data for this GRB is limited. I only have access to a single SED at 8000s and lack window-timed X-ray data at earlier times. This means there's a possibility that a thermal component was present in the X-ray at early times, but I didn't have the data to observe it. Such constraints underscore the need for comprehensive data collection to make accurate detections and interpretations. While afterglow brightness is a significant factor, the availability and timing of the data also play a crucial role in the detectability of thermal components.

In conclusion, the data supports the hypothesis that the overwhelming brightness of the afterglow in some GRBs might overshadow the thermal component, making it challenging to detect. This could imply that even non-detection GRBs might possess these thermal components, but their visibility is compromised by the dominant afterglow.

6.5 Conclusion

My comprehensive analysis of GRBs has shed light on the presence and nuances of thermal components across various observation bands. These components, or their apparent absence, offer valuable insights into the intricate physical processes behind these astrophysical phenomena.

Four GRBs in my sample did not exhibit detectable thermal components in either the X-ray or UV/optical spectra. Among these, GRB 130427A displayed a potent synchrotron component. For GRB 130831A and GRB 091127, introducing a blackbody component didn't significantly refine the spectral fit. GRB 180728, however, presented a detectable thermal component, but only at a specific observational time (8000 s), but for unrealistic physics parameters.

GRB 120422 and GRB 171205 both demonstrated thermal components in their UV/optical spectra, highlighting that specific GRBs possess processes that impact their afterglow across both X-ray and UV/optical bands. The nature of the thermal component for GRB 171205, especially the observed high velocities, aligns closely with the hot cocoon model generated by a relativistic GRB jet. This model is consistent with findings by Izzo et al. (2019), further supported by my measured velocities for GRB 171205. Conversely, for GRB 060218, the thermal emission seems to originate from a shock breakout. The discrepancies between these two GRBs accentuate the diverse mechanisms behind GRB emissions.

GRB 090618, GRB 101219B and GRB 161219B showcased thermal components exclusively in their X-ray spectra, emphasising the variability of thermal components across GRBs.

An essential discovery from my study is the potential influence of redshift on the detectability of thermal components. There appears to be a trend where higher redshift GRBs primarily manifest thermal detection in the XRT spectrum. Cosmological dimming might be contributing to this trend, making UV emissions from distant GRBs more challenging to perceive.

From my results, approximately 72.7% of GRBs with associated supernovae in my sample showed thermal components within the first 50-ks. This figure is, however, a lower limit. The non-detection of thermal components in some GRBs raises intriguing questions about their actual presence and potential masking by other factors.

My luminosity analyses, as presented in Table 6.22, indicate that the non-detection GRBs often possess luminosities orders of magnitude higher than those with detected thermal components, with the notable exception of GRB 180728. This significant luminosity discrepancy suggests that the afterglow's brilliance can potentially eclipse the thermal component, rendering it undetectable. Such a masking effect raises the possibility that thermal components might universally exist in all GRBs, but their detection is contingent on the relative luminosity of the afterglow.

To conclude, my findings underscore the multifaceted nature of GRBs and the factors influencing the visibility of thermal components. While the overwhelming brightness of the afterglow can obscure the thermal component in some GRBs, other factors like data availability and timing also play a pivotal role in its detectability.

Chapter 7

General Conclusions

The culmination of this doctoral research has led to a deeper understanding of the intricacies of GRBs and their associated phenomena. The work carried out across multiple chapters provides a comprehensive perspective on the early UV/optical emission, thermal components, and the underlying physics of these astrophysical marvels. This final chapter aims to weave together the key findings from the preceding chapters, emphasising the significance and implications of the results obtained.

7.1 Thermal Components and UV/Optical Emission in GRBs

From the detailed analysis in Chapter 3, the exploration of GRB 060218's early UV/optical emission unearthed a series of compelling insights. The study conclusively determined the presence of synchrotron afterglow radiation in the initial phase, followed by a transition to Rayleigh-Jeans spectral shape indicative of a cooling thermal process. The proposed model, which accounted for the UV/optical and X-ray blackbody emissions from an expanding region, advanced our understanding of GRB 060218 and similar low-luminosity GRBs (LLGRBs). This model's strength lay in its ability to bridge the gap between the early UV/optical synchrotron signatures and the late synchrotron radio emissions. The findings of Chapter 3 also underscored the need for rapid UV/optical observations in LLGRBs to capture the transient afterglow before it's dominated by thermal emissions.

Chapter 4 further solidified our understanding of the thermal emissions in GRBs. Delving into GRB 100316D's UV/optical/X-ray emissions, the study proposed that the observed multi-wavelength thermal component originates from a cooling envelope post-shock breakout. This observation was fortified by the consistent blackbody component observed across different epochs, which aligned well with the behaviour exhibited by GRB 060218. Moreover, the study rectified inconsistencies in datasets and demonstrated the necessity of considering both the blackbody and power-law components for an accurate representation of the Spectral Energy Distribution (SED).

7.2 Implications of Neutron Star Mergers and Kilonovae

Chapter 5 was pivotal in consolidating the link between neutron star mergers and short gamma-ray bursts. The simultaneous observation of a gamma-ray burst and a gravitational wave was revolutionary, underscoring the power of multi-messenger astronomy. The spherically outflowing blackbody model introduced in this chapter was instrumental in elucidating the intricate dynamics of UV and optical/near-IR emissions in post-merger scenarios. The model's ability to capture the subtle nuances, especially the early UV emissions, emphasised its potential in refining kilonova models. Furthermore, the discovery of a substantial opaque wind surrounding the merger and the extensive effective blackbody radius highlighted the dynamic interplay of multiple processes, from early tidal stripping to post-merger nucleosynthesis, shaping the observed emissions.

7.3 Redshift Influence and the Universality of Thermal Components

Chapter 6 was a testament to the complex nature of GRBs and the myriad of factors that influence the visibility of thermal components. The research indicated a potential trend with redshift, where higher redshift GRBs predominantly show thermal detection in the XRT spectrum, possibly due to cosmological dimming. The analysis also proposed that the overwhelming luminosity of some GRBs could overshadow the thermal component, suggesting that these components might be universally present across GRBs but remain undetected due to the dominance of the afterglow. This chapter emphasised the significance of multi-wavelength observations, capturing GRB emissions across different bands, to unveil the hidden layers of these cosmic phenomena.

7.4 Overall Significance and Future Directions

This thesis has provided a comprehensive exploration of GRBs, from their early UV/optical emissions to their underlying thermal components. The findings have implications that extend beyond the specific GRBs studied, offering insights into the broader class of GRBs and associated phenomena. The models and methodologies employed can serve as a blueprint for future investigations, with the potential to further refine our understanding of these cosmic enigmas.

While this research has advanced our understanding of the thermal emissions in GRBs, particularly focusing on faint GRBs, where the thermal emission is often outshone by brighter afterglows, it also opens several avenues for future inquiry. We have established methods to detect and analyse thermal components in these faint events, raising questions about their similarities to more luminous GRBs. Do these faint GRBs exhibit thermal properties consistent with those observed in their brighter counterparts? Addressing this question could significantly refine our models of thermal processes in GRBs.

Additionally, this thesis has contributed to the understanding of the connection between neutron star mergers, kilonovae, and short GRBs. However, many questions remain, especially concerning the consistency of kilonovae production in neutron star mergers and whether thermal emissions are universally present in short GRBs resulting from different types of compact object mergers.

Looking forward, future research should aim to expand the sample size of GRBs with detectable thermal emissions to determine the universality of these characteristics. Increased observations from facilities like LIGO will also be crucial in understanding the broader implications of compact object mergers. Each new discovery will not only test our existing models but also refine our theoretical frameworks, furthering our ability to predict and understand the behaviour of GRBs within the broader context of high-energy astrophysics.

Bibliography

Junaid Aasi, BP Abbott, Richard Abbott, Thomas Abbott, MR Abernathy, Kendall Ackley, Carl Adams, Thomas Adams, Paolo Addesso, RX Adhikari, et al. Advanced ligo. *Classical and quantum gravity*, 32(7):074001, 2015.

Jea Abadie, BP Abbott, Richard Abbott, Matthew Abernathy, Timothee Accadia, Fausto Acernese, Carl Adams, Rana Adhikari, Parameswaran Ajith, Bruce Allen, et al. Predictions for the rates of compact binary coalescences observable by ground-based gravitational-wave detectors. *Classical and Quantum Gravity*, 27(17):173001, 2010.

B. P. Abbott, R. Abbott, T. D. Abbott, F. Acernese, K. Ackley, C. Adams, T. Adams, P. Addesso, R. X. Adhikari, V. B. Adya, and et al. Multi-messenger Observations of a Binary Neutron Star Merger. *The Astrophysical Journal Letters*, 848:L12, October 2017. doi: 10.3847/2041-8213/aa91c9.

B. P. Abbott, R. Abbott, T. D. Abbott, S. Abraham, F. Acernese, K. Ackley, C. Adams, V. B. Adya, C. Affeldt, and et al. Prospects for observing and localizing gravitational-wave transients with advanced ligo, advanced virgo and kagra. *Living Reviews in Relativity*, 23(1), Sep 2020. ISSN 1433-8351. doi: 10.1007/s41114-020-00026-9. URL `http://dx.doi.org/10.1007/s41114-020-00026-9`.

Benjamin P Abbott, Rich Abbott, TD Abbott, Fausto Acernese, Kendall Ackley, Carl Adams, Thomas Adams, Paolo Addesso, RX Adhikari, VB Adya, et al. Gw170817: observation of gravitational waves from a binary neutron star inspiral. *Physical Review Letters*, 119(16):161101, 2017.

Fet al Acernese, M Agathos, K Agatsuma, D Aisa, N Allemandou, A Allocca, J Amarni, P Astone, G Balestri, G Ballardin, et al. Advanced virgo: a second-generation interferometric gravitational wave detector. *Classical and Quantum Gravity*, 32(2):024001, 2014.

Rémi Adam, Peter AR Ade, N Aghanim, Y Akrami, MIR Alves, F Argüeso, M Arnaud, F Arroja, Mark Ashdown, J Aumont, et al. Planck 2015 results-i. overview of products and scientific results. *Astronomy & Astrophysics*, 594: A1, 2016.

C. Alard and R. H. Lupton. A Method for Optimal Image Subtraction. *ApJ*, 503:325–331, August 1998. doi: 10.1086/305984.

L. Amati, F. Frontera, M. Tavani, J. J. M. in't Zand, A. Antonelli, E. Costa, M. Feroci, C. Guidorzi, J. Heise, N. Masetti, E. Montanari, L. Nicastro, E. Palazzi, E. Pian, L. Piro, and P. Soffitta. Intrinsic spectra and energetics of BeppoSAX Gamma-Ray Bursts with known redshifts. *Astronomy & Astrophysics*, 390:81–89, July 2002. doi: 10.1051/0004-6361:20020722.

K. A. Arnaud. XSPEC: The First Ten Years. In George H. Jacoby and Jeannette Barnes, editors, *Astronomical Data Analysis Software and Systems V*, volume 101 of *Astronomical Society of the Pacific Conference Series*, page 17, January 1996.

W David Arnett. Type i supernovae. i-analytic solutions for the early part of the light curve. *Astrophysical Journal, Part 1, vol. 253, Feb. 15, 1982, p. 785-797.*, 253:785–797, 1982.

D. Band, J. Matteson, L. Ford, B. Schaefer, D. Palmer, B. Teegarden, T. Cline, M. Briggs, W. Paciesas, G. Pendleton, G. Fishman, C. Kouveliotou, C. Meegan, R. Wilson, and P. Lestrade. BATSE observations of gamma-ray burst spectra. I - Spectral diversity. *Astrophys. J.*, 413:281–292, August 1993. doi: 10.1086/172995.

S. D. Barthelmy, L. M. Barbier, J. R. Cummings, E. E. Fenimore, N. Gehrels, D. Hullinger, H. A. Krimm, C. B. Markwardt, D. M. Palmer, A. Parsons, G. Sato, M. Suzuki, T. Takahashi, M. Tashiro, and J. Tueller. The Burst Alert Telescope (BAT) on the SWIFT Midex Mission. *Space Science Reviews*, 120:143–164, October 2005. doi: 10.1007/s11214-005-5096-3.

Krzysztof Belczynski, Rosalba Perna, Tomasz Bulik, Vassiliki Kalogera, Natalia Ivanova, and Donald Q. Lamb. A study of compact object mergers as short gamma-ray burst progenitors. *The Astrophysical Journal*, 648 (2):1110–1116, Sep 2006. ISSN 1538-4357. doi: 10.1086/505169. URL `http://dx.doi.org/10.1086/505169`.

E. Berger. A short gamma-ray burst “no-host” problem? investigating large progenitor offsets for short grbs with optical afterglows. *The Astrophysical Journal*, 722(2):1946–1961, Oct 2010. ISSN 1538-4357. doi: 10.1088/0004-637x/722/2/1946. URL `http://dx.doi.org/10.1088/0004-637X/722/2/1946`.

S. I. Blinnikov, I. D. Novikov, T. V. Perevodchikova, and A. G. Polnarev. Exploding Neutron Stars in Close Binaries. *Soviet Astronomy Letters*, 10: 177–179, April 1984.

J. S. Bloom, S. R. Kulkarni, and S. G. Djorgovski. The observed offset distribution of gamma-ray bursts from their host galaxies: A robust clue to the nature of the progenitors. *The Astronomical Journal*, 123(3):1111–1148, mar 2002. doi: 10.1086/338893. URL `https://doi.org/10.1086/338893`.

J. S. Bloom, D. A. Perley, H.-W. Chen, N. Butler, J. X. Prochaska, D. Kocevski, C. H. Blake, A. Szentgyorgyi, E. E. Falco, and D. L. Starr. A Putative Early-Type Host Galaxy for GRB 060502B: Implications for the Progenitors of Short-Duration Hard-Spectrum Bursts. *Astrophys. J.*, 654:878–884, January 2007. doi: 10.1086/509114.

J.S. Bloom, D.A. Frail, and R. Sari. The Prompt Energy Release of Gamma-Ray Bursts using a Cosmological k-Correction. *The Astrophysical Journal*, 121:2879–2888, June 2001.

H.E. Bond. Iauc 6665: 1987a; 1997bq. *Circular No. 6665 Central Bureau for Astronomical Telegrams INTERNATIONAL ASTRONOMICAL UNION*, 1997.

A. A. Breeveld, P. A. Curran, E. A. Hoversten, S. Koch, W. Landsman, F. E. Marshall, M. J. Page, T. S. Poole, P. Roming, P. J. Smith, M. Still, V. Yershov, A. J. Blustin, P. J. Brown, C. Gronwall, S. T. Holland, N. P. M. Kuin, K. McGowan, S. Rosen, P. Boyd, P. Broos, M. Carter, M. M. Chester, B. Hancock, H. Huckle, S. Immler, M. Ivanushkina, T. Kennedy, K. O. Mason, A. N. Morgan, S. Oates, M. de Pasquale, P. Schady, M. Siegel, and D. vanden Berk. Further calibration of the Swift ultraviolet/optical telescope. *Mon. Not. R. astr. Soc.*, 406:1687–1700, August 2010. doi: 10.1111/j.1365-2966.2010.16832.x.

A. A. Breeveld, W. Landsman, S. T. Holland, P. Roming, N. P. M. Kuin, and M. J. Page. An Updated Ultraviolet Calibration for the Swift/UVOT. In J. E. McEnery, J. L. Racusin, and N. Gehrels, editors, *American Institute of Physics Conference Series*, volume 1358 of *American Institute of Physics Conference Series*, pages 373–376, August 2011. doi: 10.1063/1.3621807.

AA Breeveld, W Landsman, ST Holland, P Roming, NPM Kuin, and MJ Page. An updated ultraviolet calibration for the swift/uvot. In *AIP Conference Proceedings*, volume 1358, pages 373–376. American Institute of Physics, 2011.

O. Bromberg, E. Nakar, and T. Piran. Are Low-luminosity Gamma-Ray Bursts Generated by Relativistic Jets? *Astrophys. J.*, 739:L55, October 2011. doi: 10.1088/2041-8205/739/2/L55.

O. Bromberg, E. Nakar, T. Piran, and R. Sari. An Observational Imprint of the Collapsar Model of Long Gamma-Ray Bursts. *Astrophys. J.*, 749:110, April 2012. doi: 10.1088/0004-637X/749/2/110.

Peter J Brown, Peter WA Roming, Peter Milne, Filomena Bufano, Robin Ciardullo, Nancy Elias-Rosa, Alexei V Filippenko, Ryan J Foley, Neil Gehrels, Caryl Gronwall, et al. The absolute magnitudes of type ia supernovae in the ultraviolet. *The Astrophysical Journal*, 721(2):1608, 2010.

Filomena Bufano, Elena Pian, Jesper Sollerman, Stefano Benetti, Giuliano Pignata, Stefano Valenti, Stefano Covino, Paolo d'Avanzo, Daniele Malesani, Enrico Cappellaro, et al. The highly energetic expansion of sn 2010bh associated with grb 100316d. *The Astrophysical Journal*, 753(1):67, 2012.

E. Margaret Burbidge, G. R. Burbidge, William A. Fowler, and F. Hoyle. Synthesis of the Elements in Stars. *Reviews of Modern Physics*, 29(4):547–650, January 1957. doi: 10.1103/RevModPhys.29.547.

D. N. Burrows, J. E. Hill, J. A. Nousek, A. Wells, A. Short, M. Turner, O. Citterio, G. Tagliaferri, and G. Chincarini. The Swift X-Ray Telescope. In G. R. Ricker and R. K. Vanderspek, editors, *Gamma-Ray Burst and Afterglow Astronomy 2001: A Workshop Celebrating the First Year of the HETE Mission*, volume 662 of *American Institute of Physics Conference Series*, pages 488–490, April 2003. doi: 10.1063/1.1579408.

S. Campana, V. Mangano, A. J. Blustin, P. Brown, D. N. Burrows, G. Chincarini, J. R. Cummings, G. Cusumano, M. Della Valle, D. Malesani, P. Mészáros, J. A. Nousek, M. Page, T. Sakamoto, E. Waxman, B. Zhang, Z. G. Dai, N. Gehrels, S. Immler, F. E. Marshall, K. O. Mason, A. Moretti, P. T. O'Brien, J. P. Osborne, K. L. Page, P. Romano, P. W. A. Roming, G. Tagliaferri, L. R. Cominsky, P. Giommi, O. Godet, J. A. Kennea, H. Krimm, L. Angelini, S. D. Barthelmy, P. T. Boyd, D. M. Palmer, A. A. Wells, and N. E. White. The association of GRB 060218 with a supernova and the evolution of the shock wave. *Nature*, 442:1008–1010, August 2006. doi: 10.1038/nature04892.

Z. Cano, D. Bersier, C. Guidorzi, S. Kobayashi, A. J. Levan, N. R. Tanvir, K. Wiersema, P. D'Avanzo, A. S. Fruchter, P. Garnavich, A. Gomboc, J. Gorosabel, D. Kasen, D. Kopač, R. Margutti, P. A. Mazzali, A. Melandri, C. G. Mundell, P. E. Nugent, E. Pian, R. J. Smith, I. Steele, R. A. M. J. Wijers, and S. E. Woosley. XRF 100316D/SN 2010bh and the Nature of Gamma-Ray Burst Supernovae. *Astrophys. J.*, 740:41, October 2011a. doi: 10.1088/0004-637X/740/1/41.

Z. Cano, D. Bersier, C. Guidorzi, R. Margutti, K. M. Svensson, S. Kobayashi, A. Melandri, K. Wiersema, A. Pozanenko, A. J. van der Horst, G. G. Pooley, A. Fernandez-Soto, A. J. Castro-Tirado, A. de Ugarte Postigo, M. Im, A. P. Kamble, D. Sahu, J. Alonso-Lorite, G. Anupama, J. L. Bibby, M. J. Burgdorf, N. Clay, P. A. Curran, T. A. Fatkhullin, A. S. Fruchter, P. Garnavich, A. Gomboc, J. Gorosabel, J. F. Graham, U. Gurugubelli, J. Haislip, K. Huang, A. Huxor, M. Ibrahimov, Y. Jeon, Y. B. Jeon, K. Ivarsen, D. Kasen, E. Klunko, C. Kouveliotou, A. Lacluyze, A. J. Levan, V. Loznikov, P. A. Mazzali, A. S. Moskvitin, C. Mottram, C. G. Mundell, P. E. Nugent, M. Nysewand er, P. T. O'Brien, W. K. Park, V. Peris, E. Pian, D. Reichart, J. E. Rhoads, E. Rol, V. Rumyantsev, V. Scowcroft, D. Shakhovskoy, E. Small, R. J. Smith, V. V. Sokolov, R. L. C. Starling, I. Steele, R. G. Strom, N. R. Tanvir, Y. Tsapras, Y. Urata, O. Vaduvescu, A. Volnova, A. Volvach, R. A. M. J. Wijers, S. E. Woosley, and D. R. Young. A tale of two GRB-SNe at a common redshift of z=0.54. *Monthly Notices of the Royal Astronomical Society*, 413(1):669–685, May 2011b. doi: 10.1111/j.1365-2966.2010.18164.x.

Z. Cano, S.-Q. Wang, Z.-G. Dai, and X.-F. Wu. The Observer's Guide to the Gamma-Ray Burst-Supernova Connection. *ArXiv e-prints*, April 2016.

Z Cano, L Izzo, A de Ugarte Postigo, Cristina Carina Thöne, T Krühler, KE Heintz, D Malesani, S Geier, C Fuentes, T-W Chen, et al. Grb

161219b/sn 2016jca: A low-redshift gamma-ray burst supernova powered by radioactive heating. *Astronomy & Astrophysics*, 605:A107, 2017.

Zach Cano. A new method for estimating the bolometric properties of ibc supernovae. *Monthly Notices of the Royal Astronomical Society*, 434(2): 1098–1116, 2013.

Zach Cano, D Bersier, Cristiano Guidorzi, Raffaella Margutti, Karl Mikael Svensson, Shiho Kobayashi, Andrea Melandri, Klass Wiersema, A Pozanenko, Alexander J van der Horst, et al. A tale of two grb-sne at a common redshift of z= 0.54. *Monthly Notices of the Royal Astronomical Society*, 413 (1):669–685, 2011.

M Capalbi, M Perri, B Saija, F Tamburelli, and Lorella Angelini. The swift xrt data reduction guide. *Version*, 1:28, 2005.

R Carrasco. gemini multi object spectrograph gmos. `http://www.lna.br/SAGDWorkshop/Apres/SAGDW_RCarrasco_GMOS.pdf`, 2011. Accessed: 2018-05-15.

Ross P. Church, Andrew J. Levan, Melvyn B. Davies, and Nial Tanvir. Implications for the origin of short gamma-ray bursts from their observed positions around their host galaxies. *Monthly Notices of the Royal Astronomical Society*, 413(3):2004–2014, 05 2011. ISSN 0035-8711. doi: 10.1111/j.1365-2966.2011.18277.x. URL `https://doi.org/10.1111/j.1365-2966.2011.18277.x`.

Michael F. Corcoran. The heasarc calibration database. ,, Cited on: (01/12/17) 2017. https://heasarc.gsfc.nasa.gov/docs/heasarc/caldb/.

E. Costa, F. Frontera, J. Heise, M. Feroci, J. in't Zand, F. Fiore, M. N. Cinti, D. Dal Fiume, L. Nicastro, M. Orlandini, E. Palazzi, M. Rapisarda#, G. Zavattini, R. Jager, A. Parmar, A. Owens, S. Molendi, G. Cusumano, M. C. Maccarone, S. Giarrusso, A. Coletta, L. A. Antonelli, P. Giommi, J. M.

Muller, L. Piro, and R. C. Butler. Discovery of an X-ray afterglow associated with the γ-ray burst of 28 February 1997. *Nature*, 387:783–785, June 1997. doi: 10.1038/42885.

D. A. Coulter, R. J. Foley, C. D. Kilpatrick, M. R. Drout, A. L. Piro, B. J. Shappee, M. R. Siebert, J. D. Simon, N. Ulloa, D. Kasen, B. F. Madore, A. Murguia-Berthier, Y. C. Pan, J. X. Prochaska, E. Ramirez-Ruiz, A. Rest, and C. Rojas-Bravo. Swope Supernova Survey 2017a (SSS17a), the optical counterpart to a gravitational wave source. *Science*, 358(6370):1556–1558, December 2017. doi: 10.1126/science.aap9811.

D. Crampton, J. M. Fletcher, I. Jean, R. G. Murowinski, K. Szeto, C. G. Dickson, I. Hook, K. Laidlaw, T. Purkins, J. R. Allington-Smith, and R. L. Davies. Gemini multi-object spectrograph GMOS: integration and tests. In M. Iye and A. F. Moorwood, editors, *Optical and IR Telescope Instrumentation and Detectors*, volume 4008 of *SPIE*, pages 114–122, August 2000. doi: 10.1117/12.395420.

P. A. Curran, P. A. Evans, M. de Pasquale, M. J. Page, and A. J. van der Horst. On the Electron Energy Distribution Index of Swift Gamma-ray Burst Afterglows. *Astrophys. J. L.*, 716:L135–L139, June 2010. doi: 10.1088/2041-8205/716/2/L135.

G Cusumano, S Barthelmy, N Gehrels, S Hunsberger, S Immler, F Marshall, D Palmer, and T Sakamoto. Grb 060218: Swift-bat detection of a possible burst. *GRB Coordinates Network*, 4775:1, 2006.

M. De Pasquale, M. J. Page, D. A. Kann, S. R. Oates, S. Schulze, B. Zhang, Z. Cano, B. Gendre, D. Malesani, A. Rossi, E. Troja, L. Piro, M. Boër, G. Stratta, and N. Gehrels. The 80 Ms follow-up of the X-ray afterglow of GRB 130427A challenges the standard forward shock model. *ArXiv e-prints*, February 2016.

RWP Drever. Gravitational radiation edited by n. deruelle and t. piran, 1983.

M. R. Drout, A. M. Soderberg, A. Gal-Yam, S. B. Cenko, D. B. Fox, D. C. Leonard, D. J. Sand, D.-S. Moon, I. Arcavi, and Y. Green. The First Systematic Study of Type Ibc Supernova Multi-band Light Curves. *ApJ*, 741: 97, November 2011. doi: 10.1088/0004-637X/741/2/97.

D. Eichler, M. Livio, T. Piran, and D. N. Schramm. Nucleosynthesis, neutrino bursts and gamma-rays from coalescing neutron stars. *Nature*, 340:126–128, July 1989. doi: 10.1038/340126a0.

S W K Emery, M J Page, A A Breeveld, P J Brown, N P M Kuin, S R Oates, and M De Pasquale. The early optical afterglow and non-thermal components of GRB 060218. *Monthly Notices of the Royal Astronomical Society*, 484(4):5484–5498, 02 2019. ISSN 0035-8711. doi: 10.1093/mnras/stz373. URL `https://doi.org/10.1093/mnras/stz373`.

ESO. The fringing pattern. `https://www.eso.org/sci/facilities/lasilla/instruments/efosc/inst/fringing.html`, 2013. Accessed: 2018-06-02.

R.C. Essick. Ligo/virgo g298048: Fermi gbm trigger 524666471/170817529: Ligo/virgo identification of a possible gravitational-wave counterpart. *Gamma Ray Coordinates Network Circular 21505*, 2017.

P. A. Evans, S. B. Cenko, J. A. Kennea, S. W. K. Emery, N. P. M. Kuin, O. Korobkin, R. T. Wollaeger, C. L. Fryer, K. K. Madsen, F. A. Harrison, Y. Xu, E. Nakar, K. Hotokezaka, A. Lien, S. Campana, S. R. Oates, E. Troja, A. A. Breeveld, F. E. Marshall, S. D. Barthelmy, A. P. Beardmore, D. N. Burrows, G. Cusumano, A. D'Aì , P. D'Avanzo, V. D'Elia, M. de Pasquale, W. P. Even, C. J. Fontes, K. Forster, J. Garcia, P. Giommi, B. Grefenstette, C. Gronwall, D. H. Hartmann, M. Heida, A. L. Hungerford, M. M. Kasliwal, H. A. Krimm, A. J. Levan, D. Malesani, A. Melandri, H. Miyasaka, J. A. Nousek, P. T. O'Brien, J. P. Osborne, C. Pagani, K. L. Page, D. M. Palmer, M. Perri, S. Pike, J. L. Racusin, S. Rosswog, M. H. Siegel, T. Sakamoto,

B. Sbarufatti, G. Tagliaferri, N. R. Tanvir, and A. Tohuvavohu. Swift and nustar observations of gw170817: detection of a blue kilonova. *Science*, 358 (6370):1565–1570, dec 2017. doi: 10.1126/science.aap9580. URL `https://doi.org/10.1126%2Fscience.aap9580`.

Y.-Z. Fan, T. Piran, and D. Xu. The interpretation and implication of the afterglow of GRB 060218. *Journal of Cosmology and Astroparticle Physics*, 9:013, September 2006. doi: 10.1088/1475-7516/2006/09/013.

E. E. Fenimore, J. J. M. in 't Zand, J. P. Norris, J. T. Bonnell, and R. J. Nemiroff. Gamma-Ray Burst Peak Duration as a Function of Energy. *Astrophys. J. L.*, 448:L101, August 1995. doi: 10.1086/309603.

Rodrigo Fernández, Daniel Kasen, Brian D. Metzger, and Eliot Quataert. Outflows from accretion discs formed in neutron star mergers: effect of black hole spin. *Monthly Notices of the Royal Astronomical Society*, 446 (1):750–758, 11 2014. ISSN 0035-8711. doi: 10.1093/mnras/stu2112. URL `https://doi.org/10.1093/mnras/stu2112`.

Robert Filgas, Jochen Greiner, Patricia Schady, Thomas Kruehler, Adria C Updike, Sylvio Klose, Marco Nardini, David Alexander Kann, Andrea Rossi, Vladimir Sudilovsky, et al. Grb 091127: The cooling break race on magnetic fuel. *Astronomy & Astrophysics*, 535:A57, 2011.

W. Fong and E. Berger. The locations of short gamma-ray bursts as evidence for compact object binary progenitors. *The Astrophysical Journal*, 776(1): 18, Sep 2013. ISSN 1538-4357. doi: 10.1088/0004-637x/776/1/18. URL `http://dx.doi.org/10.1088/0004-637X/776/1/18`.

W. Fong, E. Berger, and D. B. Fox. Hubble space telescopeobservations of short gamma-ray burst host galaxies: Morphologies, offsets, and local environments. *The Astrophysical Journal*, 708(1):9–25, Dec 2009. ISSN 1538-4357. doi: 10.1088/0004-637x/708/1/9. URL `http://dx.doi.org/10.1088/0004-637X/708/1/9`.

W. Fong, E. Berger, R. Margutti, B. A. Zauderer, E. Troja, I. Czekala, R. Chornock, N. Gehrels, T. Sakamoto, D. B. Fox, and et al. A jet break in the x-ray light curve of short grb 111020a: Implications for energetics and rates. *The Astrophysical Journal*, 756(2):189, Aug 2012. ISSN 1538-4357. doi: 10.1088/0004-637x/756/2/189. URL `http://dx.doi.org/10.1088/0004-637X/756/2/189`.

DA Frail, SR Kulkarni, L Nicastro, M Feroci, and GB Taylor. The radio afterglow from the γ-ray burst of 8 may 1997. *Nature*, 389(6648):261–263, 1997.

A. S. Fruchter, E. Pian, S. E. Thorsett, L. E. Bergeron, R. A. González, M. Metzger, P. Goudfrooij, K. C. Sahu, H. Ferguson, M. Livio, M. Mutchler, L. Petro, F. Frontera, T. Galama, P. Groot, R. Hook, C. Kouveliotou, D. Macchetto, J. van Paradijs, E. Palazzi, H. Pedersen, W. Sparks, and M. Tavani. The Fading Optical Counterpart of GRB 970228, 6 Months and 1 Year Later. *Astrophys. J.*, 516:683–692, May 1999. doi: 10.1086/307136.

C. L. Fryer and P. Mészáros. Neutrino-driven Explosions in Gamma-Ray Bursts and Hypernovae. *Astrophys. J. L.*, 588:L25–L28, May 2003. doi: 10.1086/375412.

T. J. Galama, P. M. Vreeswijk, J. van Paradijs, C. Kouveliotou, T. Augusteijn, H. Böhnhardt, J. P. Brewer, V. Doublier, J.-F. Gonzalez, B. Leibundgut, C. Lidman, O. R. Hainaut, F. Patat, J. Heise, J. in't Zand, K. Hurley, P. J. Groot, R. G. Strom, P. A. Mazzali, K. Iwamoto, K. Nomoto, H. Umeda, T. Nakamura, T. R. Young, T. Suzuki, T. Shigeyama, T. Koshut, M. Kippen, C. Robinson, P. de Wildt, R. A. M. J. Wijers, N. Tanvir, J. Greiner, E. Pian, E. Palazzi, F. Frontera, N. Masetti, L. Nicastro, M. Feroci, E. Costa, L. Piro, B. A. Peterson, C. Tinney, B. Boyle, R. Cannon, R. Stathakis, E. Sadler, M. C. Begam, and P. Ianna. An unusual supernova in the error box of the γ-ray burst of 25 April 1998. *Nature*, 395:670–672, October 1998. doi: 10.1038/27150.

TJ Galama, PJ Groot, J Van Paradijs, C Kouveliotou, RG Strom, RAMJ Wijers, N Tanvir, J Bloom, M Centurion, J Telting, et al. Optical follow-up of grb 970508. *The Astrophysical Journal Letters*, 497(1):L13, 1998.

N. Gehrels, G. Chincarini, P. Giommi, K. O. Mason, J. A. Nousek, A. A. Wells, N. E. White, S. D. Barthelmy, D. N. Burrows, L. R. Cominsky, K. C. Hurley, F. E. Marshall, P. Mészáros, P. W. A. Roming, L. Angelini, L. M. Barbier, T. Belloni, S. Campana, P. A. Caraveo, M. M. Chester, O. Citterio, T. L. Cline, M. S. Cropper, J. R. Cummings, A. J. Dean, E. D. Feigelson, E. E. Fenimore, D. A. Frail, A. S. Fruchter, G. P. Garmire, K. Gendreau, G. Ghisellini, J. Greiner, J. E. Hill, S. D. Hunsberger, H. A. Krimm, S. R. Kulkarni, P. Kumar, F. Lebrun, N. M. Lloyd-Ronning, C. B. Markwardt, B. J. Mattson, R. F. Mushotzky, J. P. Norris, J. Osborne, B. Paczynski, D. M. Palmer, H.-S. Park, A. M. Parsons, J. Paul, M. J. Rees, C. S. Reynolds, J. E. Rhoads, T. P. Sasseen, B. E. Schaefer, A. T. Short, A. P. Smale, I. A. Smith, L. Stella, G. Tagliaferri, T. Takahashi, M. Tashiro, L. K. Townsley, J. Tueller, M. J. L. Turner, M. Vietri, W. Voges, M. J. Ward, R. Willingale, F. M. Zerbi, and W. W. Zhang. The Swift Gamma-Ray Burst Mission. *Astrophys. J.*, 611:1005–1020, August 2004. doi: 10.1086/422091.

G. Ghisellini, G. Ghirlanda, and F. Tavecchio. Puzzled by GRB 060218. *Mon. Not. R. astr. Soc.*, 375:L36–L40, February 2007a. doi: 10.1111/j.1745-3933.2006.00270.x.

G. Ghisellini, G. Ghirlanda, and F. Tavecchio. Did we observe the supernova shock breakout in GRB 060218? *Mon. Not. R. astr. Soc.*, 382:L77–L81, November 2007b. doi: 10.1111/j.1745-3933.2007.00396.x.

A. Goldstein, P. Veres, E. Burns, M. S. Briggs, R. Hamburg, D. Kocevski, C. A. Wilson-Hodge, R. D. Preece, S. Poolakkil, O. J. Roberts, and et al. An ordinary short gamma-ray burst with extraordinary implications: Fermi -gbm detection of grb 170817a. *The Astrophysical Journal*, 848(2):L14, Oct

2017. ISSN 2041-8213. doi: 10.3847/2041-8213/aa8f41. URL `http://dx.doi.org/10.3847/2041-8213/aa8f41`.

J. Goodman. Are gamma-ray bursts optically thick? *Astrophys. J. l*, 308: L47–L50, September 1986. doi: 10.1086/184741.

J. Gorosabel, V. Larionov, A. J. Castro-Tirado, S. Guziy, L. Larionova, A. Del Olmo, M. A. Martínez, J. Cepa, B. Cedrés, A. de Ugarte Postigo, M. Jelínek, O. Bogdanov, and A. Llorente. Detection of optical linear polarization in the SN 2006aj/XRF 060218 non-spherical expansion. *Astronomy & Astrophysics*, 459:L33–L36, December 2006. doi: 10.1051/0004-6361:20066391.

J. Greiner, W. Bornemann, C. Clemens, M. Deuter, G. Hasinger, M. Honsberg, H. Huber, S. Huber, M. Krauss, T. Krühler, A. Küpcü Yoldas, H. Mayer-Hasselwander, B. Mican, N. Primak, F. Schrey, I. Steiner, G. Szokoly, C. C. Thöne, A. Yoldas, S. Klose, U. Laux, and J. Winkler. GROND Commissioned at the 2.2-m MPI Telescopeon La Silla. *The Messenger*, 130:12–14, December 2007.

J. Greiner, W. Bornemann, C. Clemens, M. Deuter, G. Hasinger, M. Honsberg, H. Huber, S. Huber, M. Krauss, T. Krühler, A. Küpcü Yoldaş, H. Mayer-Hasselwander, B. Mican, N. Primak, F. Schrey, I. Steiner, G. Szokoly, C. C. Thöne, A. Yoldaş, S. Klose, U. Laux, and J. Winkler. GROND–a 7-Channel Imager. *Publications of the Astronomical Society of the Pacific*, 120:405, April 2008. doi: 10.1086/587032.

EW Guenther, S Klose, P Vreeswijk, E Pian, and J Greiner. Grb 060218/sn 2006aj, high resolution spectra. *GCN Circular*, 4863, 2006.

S Guiriec, C Kouveliotou, DH Hartmann, J Granot, K Asano, P Mészáros, R Gill, N Gehrels, and J McEnery. A unified model for grb prompt emission from optical to γ-rays; exploring grbs as standard candles. *The Astrophysical Journal Letters*, 831(1):L8, 2016.

Sylvain Guiriec, Valerie Connaughton, Michael S Briggs, Michael Burgess, Felix Ryde, Frédéric Daigne, Peter Mészáros, Adam Goldstein, Julie McEnery, Nicola Omodei, et al. Detection of a thermal spectral component in the prompt emission of grb 100724b. *The Astrophysical Journal Letters*, 727(2): L33, 2011.

F. A. Harrison, S. A. Yost, R. Sari, E. Berger, T. J. Galama, J. Holtzman, T. Axelrod, J. S. Bloom, R. Chevalier, E. Costa, A. Diercks, S. G. Djorgovski, D. A. Frail, F. Frontera, K. Hurley, S. R. Kulkarni, P. McCarthy, L. Piro, G. G. Pooley, P. A. Price, D. Reichart, G. R. Ricker, D. Shepherd, B. Schmidt, F. Walter, and C. Wheeler. Broadband Observations of the Afterglow of GRB 000926: Observing the Effect of Inverse Compton Scattering. *Astrophys. J.*, 559:123–130, September 2001. doi: 10.1086/322368.

Stephen W Hawking and Werner Israel. *Three hundred years of gravitation*. Cambridge University Press, 1989.

J. Heise, J. I. Zand, R. M. Kippen, and P. M. Woods. X-Ray Flashes and X-Ray Rich Gamma Ray Bursts. In E. Costa, F. Frontera, and J. Hjorth, editors, *Gamma-ray Bursts in the Afterglow Era*, page 16, 2001. doi: 10.1007/10853853_4.

J. Hjorth, J. Sollerman, P. Møller, J. P. U. Fynbo, S. E. Woosley, C. Kouveliotou, N. R. Tanvir, J. Greiner, M. I. Andersen, A. J. Castro-Tirado, J. M. Castro Cerón, A. S. Fruchter, J. Gorosabel, P. Jakobsson, L. Kaper, S. Klose, N. Masetti, H. Pedersen, K. Pedersen, E. Pian, E. Palazzi, J. E. Rhoads, E. Rol, E. P. J. van den Heuvel, P. M. Vreeswijk, D. Watson, and R. A. M. J. Wijers. A very energetic supernova associated with the γ-ray burst of 29 March 2003. *Nature*, 423:847–850, June 2003. doi: 10.1038/nature01750.

Jens Hjorth and Joshua S. Bloom. *The Gamma-Ray Burst - Supernova Connection*, pages 169–190. Cambridge University Press, 2012.

P. Hoflich. Asphericity Effects in Scattering Dominated Photospheres. *Astronomy & Astrophysics*, 246:481, June 1991.

R. A. Hulse and J. H. Taylor. Discovery of a pulsar in a binary system. *The Astrophysical Journal Letters*, 195:L51–L53, January 1975. doi: 10.1086/181708.

Bryan Irby. Heasoft. ,, Cited on: (01/12/17) 2017. https://heasarc.gsfc.nasa.gov/lheasoft/.

C. M. Irwin and R. A. Chevalier. Jet or Shock Breakout? The Low-Luminosity GRB 060218. *Mon. Not. R. astr. Soc.*, May 2016. doi: 10.1093/mnras/stw1058.

L Izzo, A de Ugarte Postigo, K Maeda, Cristina Carina Thöne, DA Kann, Massimo Della Valle, Ana Sagués Carracedo, MJ Michałowski, P Schady, S Schmidl, et al. Signatures of a jet cocoon in early spectra of a supernova associated with a γ-ray burst. *Nature*, 565(7739):324–327, 2019.

H-Th Janka, K Langanke, Andreas Marek, G Martínez-Pinedo, and B Müller. Theory of core-collapse supernovae. *Physics Reports*, 442(1-6):38–74, 2007.

Hans-Thomas Janka. Natal kicks of stellar mass black holes by asymmetric mass ejection in fallback supernovae. *Monthly Notices of the Royal Astronomical Society*, 434(2):1355–1361, 07 2013. ISSN 0035-8711. doi: 10.1093/mnras/stt1106. URL `https://doi.org/10.1093/mnras/stt1106`.

W. A. Joye and E. Mandel. New Features of SAOImage DS9. In H. E. Payne, R. I. Jedrzejewski, and R. N. Hook, editors, *Astronomical Data Analysis Software and Systems XII*, volume 295 of *Astronomical Society of the Pacific Conference Series*, page 489, 2003.

P. M. W. Kalberla, W. B. Burton, D. Hartmann, E. M. Arnal, E. Bajaja, R. Morras, and W. G. L. Pöppel. The Leiden/Argentine/Bonn (LAB) Survey of Galactic HI. Final data release of the combined LDS and IAR surveys with improved stray-radiation corrections. *Astronomy & Astrophysics*, 440: 775–782, September 2005. doi: 10.1051/0004-6361:20041864.

Y. Kaneko, R. D. Preece, M. S. Briggs, W. S. Paciesas, C. A. Meegan, and D. L. Band. The Complete Spectral Catalog of Bright BATSE Gamma-Ray Bursts. *Astrophys. J. S.*, 166:298–340, September 2006. doi: 10.1086/505911.

DA Kann, S Klose, B Zhang, Daniele Malesani, E Nakar, A Pozanenko, AC Wilson, NR Butler, Pall Jakobsson, S Schulze, et al. The afterglows of swift-era gamma-ray bursts. i. comparing pre-swift and swift-era long/soft (type ii) grb optical afterglows. *The Astrophysical Journal*, 720(2):1513, 2010.

Daniel Kasen, N. R. Badnell, and Jennifer Barnes. Opacities and spectra of ther-process ejecta from neutron star mergers. *The Astrophysical Journal*, 774(1):25, Aug 2013. ISSN 1538-4357. doi: 10.1088/0004-637x/774/1/25. URL `http://dx.doi.org/10.1088/0004-637X/774/1/25`.

Daniel Kasen, Rodrigo Fernández, and Brian D. Metzger. Kilonova light curves from the disc wind outflows of compact object mergers. *Monthly Notices of the Royal Astronomical Society*, 450(2):1777–1786, Apr 2015. ISSN 0035-8711. doi: 10.1093/mnras/stv721. URL `http://dx.doi.org/10.1093/mnras/stv721`.

Ray W Klebesadel, Ian B Strong, and Roy A Olson. Observations of gamma-ray bursts of cosmic origin. *The Astrophysical Journal*, 182:L85, 1973.

C. Kouveliotou. Iauc 6660: Grb 970508. *Circular No. 6660 Central Bureau for Astronomical Telegrams INTERNATIONAL ASTRONOMICAL UNION*, 1997.

Chryssa Kouveliotou, Charles A Meegan, Gerald J Fishman, Narayana P Bhat, Michael S Briggs, Thomas M Koshut, William S Paciesas, and Geoffrey N Pendleton. Identification of two classes of gamma-ray bursts. *The Astrophysical Journal*, 413:L101–L104, 1993.

J. H. Krolik and E. A. Pier. Relativistic motion in gamma-ray bursts. *Astrophys. J.*, 373:277–284, May 1991. doi: 10.1086/170048.

S. R. Kulkarni, D. A. Frail, M. H. Wieringa, R. D. Ekers, E. M. Sadler, R. M. Wark, J. L. Higdon, E. S. Phinney, and J. S. Bloom. Radio emission from the unusual supernova 1998bw and its association with the γ-ray burst of 25 April 1998. *Nature*, 395:663–669, October 1998. doi: 10.1038/27139.

Alexander Kusenko and Gino Segrè. Pulsar velocities and neutrino oscillations. *Physical Review Letters*, 77(24):4872–4875, Dec 1996. ISSN 1079-7114. doi: 10.1103/physrevlett.77.4872. URL `http://dx.doi.org/10.1103/PhysRevLett.77.4872`.

J. M. Lattimer and D. N. Schramm. The tidal disruption of neutron stars by black holes in close binaries. *Astrophys. J.*, 210:549–567, December 1976. doi: 10.1086/154860.

L.-X. Li. Shock breakout in Type Ibc supernovae and application to GRB 060218/SN 2006aj. *Mon. Not. R. astr. Soc.*, 375:240–256, February 2007. doi: 10.1111/j.1365-2966.2006.11286.x.

Li-Xin Li and Bohdan Paczyński. Transient events from neutron star mergers. *The Astrophysical Journal*, 507(1):L59–L62, Nov 1998. ISSN 0004-637X. doi: 10.1086/311680. URL `http://dx.doi.org/10.1086/311680`.

Liang Li, En-Wei Liang, Qing-Wen Tang, Jie-Min Chen, Shao-Qiang Xi, Hou-Jun Lü, He Gao, Bing Zhang, Jin Zhang, Shuang-Xi Yi, Rui-Jing Lu, Lian-Zhong Lü, and Jian-Yan Wei. A Comprehensive Study of Gamma-Ray Burst Optical Emission. I. Flares and Early Shallow-decay Component. *The Astrophysical Journal*, 758(1):27, October 2012. doi: 10.1088/0004-637X/758/1/27.

E.-W. Liang, B.-B. Zhang, M. Stamatikos, B. Zhang, J. Norris, N. Gehrels, J. Zhang, and Z. G. Dai. Temporal Profiles and Spectral Lags of XRF

060218. *Astrophys. J. L.*, 653:L81–L84, December 2006. doi: 10.1086/510516.

J Lucey. Flat fielding. `https://community.dur.ac.uk/physics.astrolab/flat_fielding.html`, 2016. Accessed: 2018-05-20.

M. Lyutikov and R. Blandford. Electromagnetic Outflows and GRBs. In R. Ouyed, editor, *Beaming and Jets in Gamma Ray Bursts*, page 146, 2002.

A. I. MacFadyen and S. E. Woosley. Collapsars: Gamma-Ray Bursts and Explosions in "Failed Supernovae". *The Astrophysical Journal*, 524:262–289, October 1999a. doi: 10.1086/307790.

A. I. MacFadyen and S. E. Woosley. Collapsars: Gamma-Ray Bursts and Explosions in "Failed Supernovae". *Astrophys. J.*, 524:262–289, October 1999b. doi: 10.1086/307790.

A. I. MacFadyen, S. E. Woosley, and A. Heger. Supernovae, Jets, and Collapsars. *Astrophys. J.*, 550:410–425, March 2001. doi: 10.1086/319698.

K. Maeda, T. Nakamura, K. Nomoto, P. A. Mazzali, F. Patat, and I. Hachisu. Explosive Nucleosynthesis in Aspherical Hypernova Explosions and Late-Time Spectra of SN 1998bw. *Astrophys. J.*, 565:405–412, January 2002. doi: 10.1086/324487.

R N Manchester, G B Hobbs, A Teoh, and M_ Hobbs. The australia telescope national facility pulsar catalogue. *The Astronomical Journal*, 129(4):1993, 2005.

CB Markwardt, SD Barthelmy, JC Cummings, D Hullinger, HA Krimm, and A Parsons. The swift bat software guide. *NASA/GSFC, Greenbelt, MD*, 6, 2007.

Philip Massey. A user's guide to ccd reductions with iraf. *National Optical Astronomy Observatory*, 1997.

P. A. Mazzali, K. Nomoto, F. Patat, and K. Maeda. The Nebular Spectra of the Hypernova SN 1998bw and Evidence for Asymmetry. *Astrophys. J.*, 559:1047–1053, October 2001. doi: 10.1086/322420.

P. A. Mazzali, J. Deng, K. Nomoto, D. N. Sauer, E. Pian, N. Tominaga, M. Tanaka, K. Maeda, and A. V. Filippenko. A neutron-star-driven X-ray flash associated with supernova SN 2006aj. *Nature*, 442:1018–1020, August 2006. doi: 10.1038/nature05081.

Paolo A Mazzali, Koji S Kawabata, Keiichi Maeda, Ken'ichi Nomoto, Alexei V Filippenko, Enrico Ramirez-Ruiz, Stefano Benetti, Elena Pian, Jinsong Deng, Nozomu Tominaga, et al. An asymmetric energetic type ic supernova viewed off-axis, and a link to gamma ray bursts. *Science*, 308(5726): 1284–1287, 2005.

P. Mészáros and M. J. Rees. Optical and Long-Wavelength Afterglow from Gamma-Ray Bursts. *Astrophys. J.*, 476:232–237, February 1997.

P. Meszaros, M. J. Rees, and H. Papathanassiou. Spectral properties of blast-wave models of gamma-ray burst sources. *Astrophys. J.*, 432:181–193, September 1994. doi: 10.1086/174559.

Peter Meszaros and MJ Rees. Relativistic fireballs and their impact on external matter-models for cosmological gamma-ray bursts. *Astrophysical Journal, Part 1 (ISSN 0004-637X), vol. 405, no. 1, p. 278-284.*, 405:278–284, 1993.

B. D. Metzger, G. Martínez-Pinedo, S. Darbha, E. Quataert, A. Arcones, D. Kasen, R. Thomas, P. Nugent, I. V. Panov, and N. T. Zinner. Electromagnetic counterparts of compact object mergers powered by the radioactive decay of r-process nuclei. *Monthly Notices of the Royal Astronomical Society*, 406(4):2650–2662, Jun 2010. ISSN 0035-8711. doi: 10.1111/j.1365-2966.2010.16864.x. URL `http://dx.doi.org/10.1111/j.1365-2966.2010.16864.x`.

Michał J MichałowskI, Dong Xu, Jamie Stevens, Andrew Levan, Jun Yang, Zsolt Paragi, Atish Kamble, An-Li Tsai, Helmut Dannerbauer, Alexander J Van Der Horst, et al. The second-closest gamma-ray burst: sub-luminous grb 111005a with no supernova in a super-solar metallicity environment. *Astronomy & Astrophysics*, 616:A169, 2018.

Jennifer Millard, David Branch, E Baron, Kazuhito Hatano, Adam Fisher, Alexei V Filippenko, RP Kirshner, PM Challis, Claes Fransson, Nino Panagia, et al. Direct analysis of spectra of the type ic supernova sn 1994i. *The Astrophysical Journal*, 527(2):746, 1999.

U. Munari and T. Zwitter. Equivalent width of NA I and K I lines and reddening. *A & A*, 318:269–274, February 1997.

E. Nakar. A Unified Picture for Low-luminosity and Long Gamma-Ray Bursts Based on the Extended Progenitor of llGRB 060218/SN 2006aj. *Astrophys. J.*, 807:172, July 2015. doi: 10.1088/0004-637X/807/2/172.

E. Nakar and R. Sari. Relativistic Shock Breakouts - A Variety of Gamma-Ray Flares: From Low-luminosity Gamma-Ray Bursts to Type Ia Supernovae. *Astrophys. J.*, 747:88, March 2012. doi: 10.1088/0004-637X/747/2/88.

Ehud Nakar and Anthony L Piro. Supernovae with two peaks in the optical light curve and the signature of progenitors with low-mass extended envelopes. *The Astrophysical Journal*, 788(2):193, 2014.

J. P. Norris, G. F. Marani, and J. T. Bonnell. Connection between Energy-dependent Lags and Peak Luminosity in Gamma-Ray Bursts. *Astrophys. J.*, 534:248–257, May 2000. doi: 10.1086/308725.

J. A. Nousek, C. Kouveliotou, D. Grupe, K. L. Page, J. Granot, E. Ramirez-Ruiz, S. K. Patel, D. N. Burrows, V. Mangano, S. Barthelmy, A. P. Beardmore, S. Campana, M. Capalbi, G. Chincarini, G. Cusumano, A. D. Falcone, N. Gehrels, P. Giommi, M. R. Goad, O. Godet, C. P. Hurkett, J. A. Kennea,

A. Moretti, P. T. O'Brien, J. P. Osborne, P. Romano, G. Tagliaferri, and A. A. Wells. Evidence for a Canonical Gamma-Ray Burst Afterglow Light Curve in the Swift XRT Data. *Astrophys. J.*, 642:389–400, May 2006. doi: 10.1086/500724.

S. R. Oates, M. J. Page, P. Schady, M. de Pasquale, T. S. Koch, A. A. Breeveld, P. J. Brown, M. M. Chester, S. T. Holland, E. A. Hoversten, N. P. M. Kuin, F. E. Marshall, P. W. A. Roming, M. Still, D. E. vanden Berk, S. Zane, and J. A. Nousek. A statistical study of gamma-ray burst afterglows measured by the Swift Ultraviolet Optical Telescope. *Mon. Not. R. astr. Soc.*, 395: 490–503, May 2009. doi: 10.1111/j.1365-2966.2009.14544.x.

F. Olivares E., J. Greiner, P. Schady, A. Rau, S. Klose, T. Krühler, P. M. J. Afonso, A. C. Updike, M. Nardini, R. Filgas, A. Nicuesa Guelbenzu, C. Clemens, J. Elliott, D. A. Kann, A. Rossi, and V. Sudilovsky. The fast evolution of SN 2010bh associated with XRF 100316D. *Astronomy & Astrophysics*, 539:A76, March 2012. doi: 10.1051/0004-6361/201117929.

Bohdan Paczyński. Gamma-ray bursters at cosmological distances. *The Astrophysical Journal*, 308:L43–L46, 1986.

KL Page, RLC Starling, G Fitzpatrick, SB Pandey, JP Osborne, P Schady, S McBreen, S Campana, TN Ukwatta, C Pagani, et al. Grb 090618: detection of thermal x-ray emission from a bright gamma-ray burst. *Monthly Notices of the Royal Astronomical Society*, 416(3):2078–2089, 2011.

E Pian, L Amati, LA Antonelli, RC Butler, E Costa, G Cusumano, J Danziger, M Feroci, F Fiore, F Frontera, et al. Bepposax detection and follow-up of grb980425. *Arxiv preprint astro-ph/9903113*, 1999.

E. Pian, P. A. Mazzali, N. Masetti, P. Ferrero, S. Klose, E. Palazzi, E. Ramirez-Ruiz, S. E. Woosley, C. Kouveliotou, J. Deng, A. V. Filippenko, R. J. Foley, J. P. U. Fynbo, D. A. Kann, W. Li, J. Hjorth, K. Nomoto, F. Patat, D. N. Sauer, J. Sollerman, P. M. Vreeswijk, E. W. Guenther, A. Levan,

P. O'Brien, N. R. Tanvir, R. A. M. J. Wijers, C. Dumas, O. Hainaut, D. S. Wong, D. Baade, L. Wang, L. Amati, E. Cappellaro, A. J. Castro-Tirado, S. Ellison, F. Frontera, A. S. Fruchter, J. Greiner, K. Kawabata, C. Ledoux, K. Maeda, P. Møller, L. Nicastro, E. Rol, and R. Starling. An optical supernova associated with the X-ray flash XRF 060218. *Nature*, 442:1011–1013, August 2006. doi: 10.1038/nature05082.

T. Piran. The physics of gamma-ray bursts. *Reviews of Modern Physics*, 76: 1143–1210, October 2004. doi: 10.1103/RevModPhys.76.1143.

Tsvi Piran. Gamma-ray bursts and the fireball model. *arXiv preprint astro-ph/9810256*, 1998.

L. Piro. Iauc 6660: Grb 970508. *Circular No. 6656 Central Bureau for Astronomical Telegrams INTERNATIONAL ASTRONOMICAL UNION*, 1997.

T. S. Poole, A. A. Breeveld, M. J. Page, W. Landsman, S. T. Holland, P. Roming, N. P. M. Kuin, P. J. Brown, C. Gronwall, S. Hunsberger, S. Koch, K. O. Mason, P. Schady, D. vanden Berk, A. J. Blustin, P. Boyd, P. Broos, M. Carter, M. M. Chester, A. Cucchiara, B. Hancock, H. Huckle, S. Immler, M. Ivanushkina, T. Kennedy, F. Marshall, A. Morgan, S. B. Pandey, M. de Pasquale, P. J. Smith, and M. Still. Photometric calibration of the Swift ultraviolet/optical telescope. *Mon. Not. R. astr. Soc.*, 383:627–645, January 2008. doi: 10.1111/j.1365-2966.2007.12563.x.

R. D. Preece, M. S. Briggs, R. S. Mallozzi, G. N. Pendleton, W. S. Paciesas, and D. L. Band. The BATSE Gamma-Ray Burst Spectral Catalog. I. High Time Resolution Spectroscopy of Bright Bursts Using High Energy Resolution Data. *Astrophys. J. S.*, 126:19–36, January 2000. doi: 10.1086/313289.

J. L. Racusin, E. W. Liang, D. N. Burrows, A. Falcone, T. Sakamoto, B. B. Zhang, B. Zhang, P. Evans, and J. Osborne. Jet Breaks and Energetics of Swift Gamma-Ray Burst X-Ray Afterglows. *Astrophys. J.*, 698:43–74, June 2009. doi: 10.1088/0004-637X/698/1/43.

M. J. Rees and P. Mészáros. Refreshed Shocks and Afterglow Longevity in Gamma-Ray Bursts. *The Astrophysical Journal Letters*, 496(1):L1–L4, March 1998. doi: 10.1086/311244.

P. W. A. Roming, T. E. Kennedy, K. O. Mason, J. A. Nousek, L. Ahr, R. E. Bingham, P. S. Broos, M. J. Carter, B. K. Hancock, H. E. Huckle, S. D. Hunsberger, H. Kawakami, R. Killough, T. S. Koch, M. K. McLelland, K. Smith, P. J. Smith, J. C. Soto, P. T. Boyd, A. A. Breeveld, S. T. Holland, M. Ivanushkina, M. S. Pryzby, M. D. Still, and J. Stock. The Swift Ultra-Violet/Optical Telescope. *Space Science Reviews*, 120:95–142, October 2005. doi: 10.1007/s11214-005-5095-4.

E. S. Rykoff, F. Aharonian, C. W. Akerlof, M. C. B. Ashley, S. D. Barthelmy, H. A. Flewelling, N. Gehrels, E. Göğüş, T. Güver, Ü. Kiziloğlu, H. A. Krimm, T. A. McKay, M. Özel, A. Phillips, R. M. Quimby, G. Rowell, W. Rujopakarn, B. E. Schaefer, D. A. Smith, W. T. Vestrand, J. C. Wheeler, J. Wren, F. Yuan, and S. A. Yost. Looking Into the Fireball: ROTSE-III and Swift Observations of Early Gamma-ray Burst Afterglows. *The Astrophysical Journal*, 702(1):489–505, September 2009. doi: 10.1088/0004-637X/702/1/489.

R. Sari, R. Narayan, and T. Piran. Cooling Timescales and Temporal Structure of Gamma-Ray Bursts. *Astrophys. J.*, 473:204, December 1996. doi: 10.1086/178136.

R. Sari, T. Piran, and R. Narayan. Spectra and Light Curves of Gamma-Ray Burst Afterglows. *Astrophys. J. L.*, 497:L17–L20, April 1998. doi: 10.1086/311269.

R. Sari, T. Piran, and J. P. Halpern. Jets in Gamma-Ray Bursts. *Astrophys. J. L.*, 519:L17–L20, July 1999. doi: 10.1086/312109.

Re'em Sari and Peter Mészáros. Impulsive and Varying Injection in Gamma-

Ray Burst Afterglows. *The Astrophysical Journal Letters*, 535(1):L33–L37, May 2000. doi: 10.1086/312689.

S. Y. Sazonov, A. A. Lutovinov, and R. A. Sunyaev. An apparently normal γ-ray burst with an unusually low luminosity. *Nature*, 430:646–648, August 2004. doi: 10.1038/nature02748.

P. Schady, M. J. Page, S. R. Oates, M. Still, M. de Pasquale, T. Dwelly, N. P. M. Kuin, S. T. Holland, F. E. Marshall, and P. W. A. Roming. Dust and metal column densities in gamma-ray burst host galaxies. *Mon. Not. R. astr. Soc.*, 401:2773–2792, February 2010. doi: 10.1111/j.1365-2966.2009.15861.x.

Patricia Schady, Tom Dwelly, Mat J Page, Thomas Krühler, Jochen Greiner, Samantha R Oates, Massimiliano De Pasquale, Marco Nardini, PWA Roming, A Rossi, et al. The dust extinction curves of gamma-ray burst host galaxies. *Astronomy & Astrophysics*, 537:A15, 2012.

E. F. Schlafly and D. P. Finkbeiner. Measuring Reddening with Sloan Digital Sky Survey Stellar Spectra and Recalibrating SFD. *Astrophys. J.*, 737:103, August 2011. doi: 10.1088/0004-637X/737/2/103.

Edward F. Schlafly and Douglas P. Finkbeiner. Measuring reddening with sloan digital sky survey stellar spectra and recalibrating sfd. *The Astrophysical Journal*, 737(2):103, Aug 2011. ISSN 1538-4357. doi: 10.1088/0004-637x/737/2/103. URL `http://dx.doi.org/10.1088/0004-637X/737/2/103`.

D. J. Schlegel, D. P. Finkbeiner, and M. Davis. Maps of Dust Infrared Emission for Use in Estimation of Reddening and Cosmic Microwave Background Radiation Foregrounds. *Astrophys. J.*, 500:525–553, June 1998. doi: 10.1086/305772.

S. Schulze, S. Klose, G. Björnsson, P. Jakobsson, D. A. Kann, A. Rossi, T. Krühler, J. Greiner, and P. Ferrero. The circumburst density profile around GRB progenitors: a statistical study. *Astronomy & Astrophysics*, 526:A23, February 2011. doi: 10.1051/0004-6361/201015581.

S Schulze, D Malesani, A Cucchiara, Nial R Tanvir, T Krühler, A de Ugarte Postigo, Georgios Leloudas, J Lyman, D Bersier, K Wiersema, et al. Grb 120422a/sn 2012bz: Bridging the gap between low-and high-luminosity gamma-ray bursts. *Astronomy & Astrophysics*, 566:A102, 2014.

K. Serkowski, D. S. Mathewson, and V. L. Ford. Wavelength dependence of interstellar polarization and ratio of total to selective extinction. *Astrophys. J.*, 196:261–290, February 1975. doi: 10.1086/153410.

S. J. Smartt, T.-W. Chen, A. Jerkstrand, M. Coughlin, E. Kankare, S. A. Sim, M. Fraser, C. Inserra, K. Maguire, K. C. Chambers, M. E. Huber, T. Krühler, G. Leloudas, M. Magee, L. J. Shingles, K. W. Smith, D. R. Young, J. Tonry, R. Kotak, A. Gal-Yam, J. D. Lyman, D. S. Homan, C. Agliozzo, J. P. Anderson, C. R. Angus, C. Ashall, C. Barbarino, F. E. Bauer, M. Berton, M. T. Botticella, M. Bulla, J. Bulger, G. Cannizzaro, Z. Cano, R. Cartier, A. Cikota, P. Clark, A. De Cia, M. Della Valle, L. Denneau, M. Dennefeld, L. Dessart, G. Dimitriadis, N. Elias-Rosa, R. E. Firth, H. Flewelling, A. Flörs, A. Franckowiak, C. Frohmaier, L. Galbany, S. González-Gaitán, J. Greiner, M. Gromadzki, A. Nicuesa Guelbenzu, C. P. Gutiérrez, A. Hamanowicz, L. Hanlon, J. Harmanen, K. E. Heintz, A. Heinze, M.-S. Hernandez, S. T. Hodgkin, I. M. Hook, L. Izzo, P. A. James, P. G. Jonker, W. E. Kerzendorf, S. Klose, Z. Kostrzewa-Rutkowska, M. Kowalski, M. Kromer, H. Kuncarayakti, A. Lawrence, T. B. Lowe, E. A. Magnier, I. Manulis, A. Martin-Carrillo, S. Mattila, O. McBrien, A. Müller, J. Nordin, D. O'Neill, F. Onori, J. T. Palmerio, A. Pastorello, F. Patat, G. Pignata, Ph. Podsiadlowski, M. L. Pumo, S. J. Prentice, A. Rau, A. Razza, A. Rest, T. Reynolds, R. Roy, A. J. Ruiter, K. A. Rybicki, L. Salmon, P. Schady, A. S. B. Schultz, T. Schweyer, I. R. Seitenzahl, M. Smith, J. Sollerman, B. Stalder, C. W. Stubbs, M. Sullivan, H. Szegedi, F. Taddia, S. Taubenberger, G. Terreran, B. van Soelen, J. Vos, R. J. Wainscoat, N. A. Walton, C. Waters, H. Weiland, M. Willman, P. Wiseman, D. E. Wright, Ł. Wyrzykowski, and O. Yaron. A kilonova as the electromagnetic counterpart to a gravitational-wave source. *Nature*, 551 (7678):75–79, Oct 2017. ISSN 1476-4687. doi: 10.1038/nature24303. URL `http://dx.doi.org/10.1038/nature24303`.

C Snodgrass and C Benoît. Automatic removal of fringes from efosc images. *The Messenger*, 152:pp–14, 2013.

A. M. Soderberg, E. Berger, M. Kasliwal, D. A. Frail, P. A. Price, B. P. Schmidt, S. R. Kulkarni, D. B. Fox, S. B. Cenko, A. Gal-Yam, E. Nakar, and K. C. Roth. The Afterglow, Energetics, and Host Galaxy of the Short-Hard Gamma-Ray Burst 051221a. *Astrophys. J.*, 650:261–271, October 2006a. doi: 10.1086/506429.

A. M. Soderberg, S. R. Kulkarni, E. Nakar, E. Berger, P. B. Cameron, D. B. Fox, D. Frail, A. Gal-Yam, R. Sari, S. B. Cenko, M. Kasliwal, R. A. Chevalier, T. Piran, P. A. Price, B. P. Schmidt, G. Pooley, D.-S. Moon, B. E. Penprase, E. Ofek, A. Rau, N. Gehrels, J. A. Nousek, D. N. Burrows, S. E. Persson, and P. J. McCarthy. Relativistic ejecta from X-ray flash XRF 060218 and the rate of cosmic explosions. *Nature*, 442:1014–1017, August 2006b. doi: 10.1038/nature05087.

J. Sollerman, A. O. Jaunsen, J. P. U. Fynbo, J. Hjorth, P. Jakobsson, M. Stritzinger, C. Féron, P. Laursen, J.-E. Ovaldsen, J. Selj, C. C. Thöne, D. Xu, T. Davis, J. Gorosabel, D. Watson, R. Duro, I. Ilyin, B. L. Jensen, N. Lysfjord, T. Marquart, T. B. Nielsen, J. Näränen, H. E. Schwarz, S. Walch, M. Wold, and G. Östlin. Supernova 2006aj and the associated X-Ray Flash 060218. *Astronomy & Astrophysics*, 454:503–509, August 2006. doi: 10.1051/0004-6361:20065226.

M Sparre, Jesper Sollerman, JPU Fynbo, D Malesani, P Goldoni, A de Ugarte Postigo, S Covino, V d'Elia, H Flores, François Hammer, et al. Spectroscopic evidence for sn 2010ma associated with grb 101219b. *The Astrophysical journal letters*, 735(1):L24, 2011.

Lars St, Svante Wold, et al. Analysis of variance (anova). *Chemometrics and intelligent laboratory systems*, 6(4):259–272, 1989.

R. L. C. Starling, K. Wiersema, A. J. Levan, T. Sakamoto, D. Bersier, P. Goldoni, S. R. Oates, A. Rowlinson, S. Campana, J. Sollerman, N. R. Tanvir, D. Malesani, J. P. U. Fynbo, S. Covino, P. D'Avanzo, P. T. O'Brien, K. L. Page, J. P. Osborne, S. D. Vergani, S. Barthelmy, D. N. Burrows, Z. Cano, P. A. Curran, M. de Pasquale, V. D'Elia, P. A. Evans, H. Flores, A. S. Fruchter, P. Garnavich, N. Gehrels, J. Gorosabel, J. Hjorth, S. T. Holland, A. J. van der Horst, C. P. Hurkett, P. Jakobsson, A. P. Kamble, C. Kouveliotou, N. P. M. Kuin, L. Kaper, P. A. Mazzali, P. E. Nugent, E. Pian, M. Stamatikos, C. C. Thöne, and S. E. Woosley. Discovery of the nearby long, soft GRB 100316D with an associated supernova. *Mon. Not. R. astr. Soc.*, 411:2792–2803, March 2011. doi: 10.1111/j.1365-2966.2010.17879.x.

RLC Starling, Kim L Page, A Pe'Er, Andrew P Beardmore, and Julian P Osborne. A search for thermal x-ray signatures in gamma-ray bursts–i. swift bursts with optical supernovae. *Monthly Notices of the Royal Astronomical Society*, 427(4):2950–2964, 2012.

J. H. Taylor and J. M. Weisberg. A new test of general relativity - Gravitational radiation and the binary pulsar PSR 1913+16. *The Astrophysical Journal*, 253:908–920, February 1982. doi: 10.1086/159690.

K. Toma, K. Ioka, T. Sakamoto, and T. Nakamura. Low-Luminosity GRB 060218: A Collapsar Jet from a Neutron Star, Leaving a Magnetar as a Remnant? *Astrophys. J.*, 659:1420–1430, April 2007. doi: 10.1086/512481.

E. Troja, A. R. King, P. T. O'Brien, N. Lyons, and G. Cusumano. Different progenitors of short hard gamma-ray bursts. *Monthly Notices of the Royal Astronomical Society: Letters*, 385(1):L10–L14, 03 2008. ISSN 1745-3925. doi: 10.1111/j.1745-3933.2007.00421.x. URL `https://doi.org/10.1111/j.1745-3933.2007.00421.x`.

E Troja, T Sakamoto, C Guidorzi, JP Norris, A Panaitescu, S Kobayashi, N Omodei, JC Brown, DN Burrows, PA Evans, et al. Broadband study of grb 091127: a sub-energetic burst at higher redshift? *The Astrophysical Journal*, 761(1):50, 2012.

T. N. Ukwatta, K. S. Dhuga, M. Stamatikos, C. D. Dermer, T. Sakamoto, E. Sonbas, W. C. Parke, L. C. Maximon, J. T. Linnemann, P. N. Bhat, A. Eskandarian, N. Gehrels, A. U. Abeysekara, K. Tollefson, and J. P. Norris. The lag-luminosity relation in the GRB source frame: an investigation with Swift BAT bursts. *Mon. Not. R. astr. Soc.*, 419:614–623, January 2012. doi: 10.1111/j.1365-2966.2011.19723.x.

J. van Paradijs, C. Kouveliotou, and R. A. M. J. Wijers. Gamma-Ray Burst Afterglows. *Ann. Rev. of Astronomy & Astrophysics*, 38:379–425, 2000. doi: 10.1146/annurev.astro.38.1.379.

JA Van Paradijs, M Pettini, NR Tanvir, JS Bloom, H Pedersen, HU Noerdgaard-Nielsen, M Linden-Voernle, J Melnick, G van de Steene, M Bremer, et al. Discovery of transient optical emission from the error box of the gamma-ray burst of february 28, 1997. *Nature*, 386:686–689, 1997.

F. J. Virgili, E.-W. Liang, and B. Zhang. Low-luminosity gamma-ray bursts as a distinct GRB population: a firmer case from multiple criteria constraints. *Mon. Not. R. astr. Soc.*, 392:91–103, January 2009. doi: 10.1111/j.1365-2966.2008.14063.x.

F. J. Virgili, C. G. Mundell, V. Pal'shin, C. Guidorzi, R. Margutti, A. Melandri, R. Harrison, S. Kobayashi, R. Chornock, A. Henden, A. C. Updike, S. B. Cenko, N. R. Tanvir, I. A. Steele, A. Cucchiara, A. Gomboc, A. Levan, Z. Cano, C. J. Mottram, N. R. Clay, D. Bersier, D. Kopač, J. Japelj, A. V. Filippenko, W. Li, D. Svinkin, S. Golenetskii, D. H. Hartmann, P. A. Milne, G. Williams, P. T. O'Brien, D. B. Fox, and E. Berger. GRB 091024A and the

Nature of Ultra-long Gamma-Ray Bursts. *Astrophys. J.*, 778:54, November 2013. doi: 10.1088/0004-637X/778/1/54.

V. Šimon, R. Hudec, and G. Pizzichini. The color evolution of the optical afterglow of GRB 030329 and the implications for the underlying supernova SN 2003dh. *Astronomy & Astrophysics*, 427:901–905, December 2004. doi: 10.1051/0004-6361:20041548.

Xiang-Gao Wang, Bing Zhang, En-Wei Liang, Rui-Jing Lu, Da-Bin Lin, Jing Li, and Long Li. Gamma-Ray Burst Jet Breaks Revisited. *The Astrophysical Journal*, 859(2):160, June 2018. doi: 10.3847/1538-4357/aabc13.

E. Waxman, P. Mészáros, and S. Campana. GRB 060218: A Relativistic Supernova Shock Breakout. *Astrophys. J.*, 667:351–357, September 2007. doi: 10.1086/520715.

K. Wiersema, S. Savaglio, P. M. Vreeswijk, S. L. Ellison, C. Ledoux, S.-C. Yoon, P. Møller, J. Sollerman, J. P. U. Fynbo, E. Pian, R. L. C. Starling, and R. A. M. J. Wijers. The nature of the dwarf starforming galaxy associated with GRB 060218/SN 2006aj. *A & A*, 464:529–539, March 2007. doi: 10.1051/0004-6361:20066273.

R. Willingale, P. T. O'Brien, J. P. Osborne, O. Godet, K. L. Page, M. R. Goad, D. N. Burrows, B. Zhang, E. Rol, N. Gehrels, and G. Chincarini. Testing the Standard Fireball Model of Gamma-Ray Bursts Using Late X-Ray Afterglows Measured by Swift. *Astrophys. J.*, 662:1093–1110, June 2007. doi: 10.1086/517989.

J. Wilms, A. Allen, and R. McCray. On the Absorption of X-Rays in the Interstellar Medium. *The Astrophysical Journal*, 542(2):914–924, October 2000. doi: 10.1086/317016.

C. Winkler. INTEGRAL: Overview and mission concept. *Astrophys. J. S.*, 92: 327–332, June 1994. doi: 10.1086/191973.

S. E. Woosley. Gamma-ray bursts from stellar mass accretion disks around black holes. *Astrophys. J.*, 405:273–277, March 1993a. doi: 10.1086/172359.

S. E. Woosley. Gamma-ray bursts from stellar mass accretion disks around black holes. *Astrophys. J.*, 405:273–277, March 1993b. doi: 10.1086/172359.

S. E. Woosley and A. Heger. The Supernova Gamma-Ray Burst Connection. In S. S. Holt, N. Gehrels, and J. A. Nousek, editors, *Gamma-Ray Bursts in the Swift Era*, volume 836 of *American Institute of Physics Conference Series*, pages 398–407, May 2006. doi: 10.1063/1.2207927.

S. E. Woosley, A. Heger, and T. A. Weaver. The evolution and explosion of massive stars. *Reviews of Modern Physics*, 74:1015–1071, November 2002. doi: 10.1103/RevModPhys.74.1015.

B. Zhang and P. Mészáros. Gamma-Ray Bursts: progress, problems & prospects. *International Journal of Modern Physics A*, 19:2385–2472, 2004. doi: 10.1142/S0217751X0401746X.